MEASUREMENTS OF TIME-DEPENDENT FREE-SURFACE VISCOPLASTIC FLOWS DOWN STEEP SLOPES

PAR

Steve COCHARD

ingénieur mécanicien diplômé EPF
de nationalité suisse et originaire de Montreux (VD)

EPFL

ÉCOLE POLYTECHNIQUE
FÉDÉRALE DE LAUSANNE

Suisse
2007

Abstract

THE objective of this thesis was to increase our understanding of gravity-driven geophysical flows by developping a new platform to simulate avalanches of fluid in the laboratory.

To simulate flow avalanches in the laboratory, we created a unique experimental setup consisting of a metallic frame supporting a reservoir, an inclined aluminum plane, and a horizontal run-out zone. At 6-m long, 1.8-m wide, and 3.5-m high, the structure is probably the largest laboratory setup of its kind in the world. In a dam-break experiment, up to 120 liters of fluid can be released from the reservoir down the 4-m long inclined plane. We precisely control initial and boundary conditions.

To measure the free-surface profile, a novel imaging system consisting of a high-speed digital camera coupled to a synchronized micro-mirror projector was developed. The camera records how regular patterns projected onto the surface are deformed when the free surface moves. We developed algorithms to post-process the image data, determine the spreading rate, and generate whole-field 3-dimensional shape measurements of the free-surface profile. We compute the phase of the projected pattern, unwrap the phase, and then apply a calibration matrix to extract the flow thickness from the unwrapped phase.

56 different flow configurations, with a wide range of inclinations, were finally tested with Newtonian and viscoplastic fluids. For each test, the evolution of the free surface was recorded in 3 dimensions. Different flow regimes were observed, which depend on: the plane inclination, the setup geometry, the volume, and characteristics of the fluid. Partial agreements were found between theoretical models and our results.

Keywords: experimental fluid mechanics; gravity-driven geophysical flows; non-Newtonian fluids; dam-break; free surface; fringe-projection.

Résumé

A FIN de mieux prévenir les dangers des écoulements géophysiques gravitaires, une nouvelle plate-forme de mesure spermettant de simuler les avalanches de fluide en laboratoire a été développée.

L'installation s'inspire de l'expérience dite de 'rupture de barrage'. Elle consiste en un plan incliné de 4 m de long, surmonté d'un réservoir. Lors de la rupture de barrage, les 120 l de fluide contenus dans le réservoir sont libérés par l'ouverture d'une porte et s'écoulent le long du plan incliné. Un plan horizontal est situé à la base du plan incliné et force le fluide à s'arrêter. Le principal avantage avec l'expérience en laboratoire est que les conditions limites et aux bords sont parfaitement contrôlées.

Pour mesurer la déformation de la surface libre, un nouveau système d'imagerie a été mis au point. Un projecteur est synchronisé à une caméra rapide. Celle-ci enregistre la manière dont des franges lumineuses sont déformées par le passage du fluide. Nous avons développé des algorithmes pour calculer la hauteur du fluide en fonction de la déformation de ces franges. La technique consiste tout d'abord à retrouver la phase du signal lumineux, puis à dérouler cette phase et enfin, à l'aide d'une matrice établie lors d'une calibration, de calculer la hauteur du fluide. La surface libre du fluide est mesurée avec une précision de l'ordre du demi-millimètre sur une surface de $1,4 \times 1.4$ m² à une fréquence de 48 Hz.

56 configurations d'écoulements, avec des fluides Newtonien et viscoplastiques, ont ensuite été testées pour différentes inclinaisons. Pour chaque test, l'évolution de la surface libre a été enregistrée en trois dimensions. Plusieurs régimes ont été observés en fonction: de l'inclinaison du plan, de différentes géométries de barrage, du volume de départ, et des caractéristiques du fluide. Plusieurs comparaisons ont finalement été menées entre nos résultats expérimentaux et des modèles théoriques.

Mots-clés : mécanique des fluides expérimentale, écoulement géophysique gravitaire, fluide non-Newtonien, rupture de barrages, surface-libre, projection de franges.

Acknowledgements

I would like to express my sincere gratitude to Prof. C. Ancey for having supervised my work during this thesis and for his precious support.

To everyone at the LHE, I express my appreciation for their time and assistance, and in particular: Mr. C. Perrinjaquet for his help with everything experimental; Mr. N. Andreini, Mr. M. Reintchler and Mr. S. Wiederseiner for their useful and thought-provoking discussions on gravity-driven flows; Mr. M. Teuscher without whom the experimental setup would not be the largest of its kind in the world and Mr. D. Bouffard for sharing ideas to improve anything.

I would like to extend my gratitude to Prof. P. Jacquot (EPFL-STI-NAM) and Ass. Prof. M. Liebling (UCSB) for introducing me to the method of fringe projection to measure large objects, Mr. P. Loech (EPFL-ENAC-LESO) for lending a hand on countless occasions and Mr. M. Heim (Mathworks) for providing me with beta versions of Matlab to resolve some hardware conflicts.

I am very grateful to Prof. N. Balmforth, Prof. P. Jacquot and Prof. J. McElwaine for their participation in the thesis committee and taking the time to read through the manuscript and attend the private defence. Their comments and suggestions have been greatly appreciated. I would also like to thank Dr. M. Farhat for presiding over the committee.

I reserve my deepest thanks to my wife Séverine for her love and support. I am also grateful to my parents, Shirley, my family and friends for their constant encouragements.

Contents

CHAPTER 1

Introduction

E VERY year, gravity-driven geophysical flows such as debris flows, snow ava-
lanches, pyroclastic flows kill hundreds of people and cause considerable dam-
age to infrastructure. To prevent these casualties, there is a rising demand for
models that predict flow characteristics such as speed, spreading rate, flow path
or impact pressure. These flows are strongly time-dependent and involve non-
Newtonian material. The purpose of this thesis is to better understand time-
dependant free-surface viscoplastic flows down steep slopes by carrying out exper-
imental observations in the laboratory.

A large number of models to describe gravity-driven geophysical flow have
been proposed over the last 30 years. Most of them rely on a set of equations
which is similar to the Saint-Venant equations of motion used in hydraulics to
calculate flash floods [Iverson, 1997, Ancey, 2001]. Two major problems arise
with this approach, which may undermine the results value: first, the rheological
proprieties of the fluids are usually unknown. *Ad hoc* rheological laws use non-
measurable empirical parameters. Second, the flows are strongly time-dependent
while the Saint-Venant equations are valid, in principle, for regimes close to a
steady regime. The performances, which may be quite poor, of current models
have engaged the scientific community to develop more complex rheological laws
and more sophisticated numerical models [Iverson, 2003, Salm, 2004].

We adopted a different approach. The governing equations used for modelling
gravity-driven flows are not intrinsic to the phenomena. They are a versatile set of
equations used for describing various flow conditions ranging from flash floods to
rockfalls and volcano lava flows. They are not related to a unique setting; they have
been used for describing both large-scale flows (e.g., rivers) and small-scale (e.g.,

in the laboratory, flume experiments) flows. Essentially, our idea is to simulate avalanches of fluid in the laboratory, which makes it possible to investigate them repeatedly in a well-controlled environment, with particular interest devoted to the free-surface profile and the spreading rate.

With the experiments carried out so far, there is no clear evidence that there are scaling problems with gravity-driven flows. Furthermore and probably more fundamentally, the equations currently used for modelling natural flows hold for any scale. So, in this respect, it is shrewder to take benefit from this scale invariance and conduct experiments on the laboratory scale, where probing can be performed at lower cost and more extensively than in the field.

To simulate avalanches of fluids, we created a unique experimental setup consisting of a metallic frame supporting a reservoir, an inclined aluminum plane, and a horizontal run-out zone. At 5.5-m long, 1.8-m wide, and 3.5-m high, the structure is likely to be the largest laboratory setup of its kind in the world. In a dam-break experiment, up to 120 l of fluid are released from the reservoir down the 4.5-m long plane. We precisely control initial conditions, such as the fluid volume, density, and rheological characteristics, and boundary conditions, such as plane angle and surface roughness. The inclined plane enables the fluid to accelerate vigorously at early times. The run-out is kept in a horizontal position to force the fluid to come to a halt. The typical experimental procedure is quite simple: first, the fluid is poured into a reservoir closed by a sluice gate. This gate is opened within 0.8 s, thanks to two pneumatic jacks, and unleashes the fluid onto the steep plane. The fluid then accelerates vigorously, at times finds a pseudo equilibrium state, where the velocity is nearly constant, and eventually decelerates quite rapidly. Compared to true gravity-driven geophysical flows, we are able to fully control the initial and boundary conditions, the nature of the flowing material (e.g., rheological properties), and the flow geometry. We can also measure all what is needed to test the efficiency and reliability of governing equations worked out for describing highly complex, non-equilibrium, nonlinear flows.

To measure the free-surface profile, we developed a novel imaging system. The system consists of a high-speed digital camera coupled to a synchronized micro-mirror projector. The camera records how regular patterns projected onto the surface are deformed when the free surface moves. We developed algorithms to post-process the image data, determine the spreading rate, and generate whole-field three-dimensional shape measurements of the free-surface profile. We compute the phase of the projected pattern, unwrap the phase, and then apply a calibration matrix to extract the flow thickness from the unwrapped phase. The free surface is reconstructed with an accuracy of half one millimetre over a surface of 1.4 x 1.4 m^2 at a frame rate of 48 Hz —a major achievement.

Post-processing data from a typical three minute experiment required almost

a week of computational time on a single processor. To accelerate computation time, we run the post-processing on a cluster of two Mac Pro computers with eight processor cores built for this purpose. This parallel setup reduced processing time to one day, enabling us to conduct more experiments and apply more complex processing algorithms.

With this setup, we can acquire high-accuracy data related to the dam-break problem, which can then be used to test the various analytical and numerical models developed to compute the spreading of a viscoplastic material under time-dependent flow conditions.

56 different flow configurations were finally tested. For each test, the evolution of the free surface was recorded in 3 dimensions. We observed different flow regimes depending on: the characteristic of the flow, the plane inclination, the volume of fluid and the setup geometry (channel or plane). We then compared our experimental results with some analytical and numerical models.

CHAPTER 2

Experimental Setup

To accurately measure the surge's free-surface variations with time, we have developed a new imaging system, consisting of a digital camera coupled with a synchronized micro-mirror projector. The object's surface is imaged into a camera and patterns are projected onto the surface under an angle of incidence that differs from the imaging direction. From the deformed pattern recorded by the camera, the phase can be extracted and, by using unwrapping algorithms, the height can be computed and the free surface reconstructed. We were able to measure the free surface of the flow keeping the accuracy below 1 mm over a surface of 1.4 $\times$ 1.4 m^2. The proposed system in its entirety is innovative and more efficient than most methods used to date in practical applications, it is based on state-of-the-art thechniques and components that have been adapted to the purpose of this study.

2.1   Introduction

The objective of this chapter is to describe the experimental procedures used for reconstructing three-dimensional, time-dependent profiles of flow depth. To give the reader an overview of the experimental setting, we will describe the experimental facilities and procedures that we used to generate surges down an inclined plane (see Section 2.2). Tracking the free surface of a rapid surge remains delicate, especially when speed and accuracy are sought. Various techniques have been used in recent years. For instance, Iverson et al. [2004] used parallel laser sheets to reconstruct rapid granular avalanches down irregular topography; Pouliquen and Forterre [2002] used a Moiré technique, while Eaket et al. [2005] employed high-speed stereoscopy for the same purpose.

Here, we will present an image-processing technique based on pattern projection. In itself, the technique is not new [e.g., see Desmangles, 2003], but we think that the particular application described herein is innovative given the number of technical problems that must be sorted out for it to be operated in dam-break experiments. Various strategies can be applied to reconstruct three-dimensional, time-dependent free surfaces. Pattern projection turns out to be very convenient in terms of cost, robustness, accuracy, and versatility. A key point concerns the computation of flow depth. In Sections 2.3.2 and 2.3.3, we will show how to use fringe deformation to reconstruct a three-dimensional profile. The basic idea underpinning our developments is that in terms of signal processing, free-surface variations entail fringe deformations, viz phase shift and, possibly, amplitude modulation. Section 2.4 is devoted to phase mapping; the different algorithms used will be outlined there. Usually, a phase map is calculated using a three- or four-image algorithm (as described in Section 2.4.1); for fast flows, we use a one-image algorithm (see Sections 2.4.2 and 2.4.3). The phase, defined in the interval $[0, 2\pi)$, is then unwrapped as explained in Section 2.5. Back computation (recovering flow depth from phase shift) will be presented in Section 2.6: we will show how the flow depth can be deduced from the unwrapped phase signal. Finally, we will give an example of its application in Section 2.7.

2.2   Facility and procedures

2.2.1   Overview

Figure 2.1 gives a view of the experimental setup, while Figure 2.2 shows the upper inclined plane, the reservoir, and the gate. Typically, an experiment is run as follows. An amount of fluid is placed in a reservoir at the top of an inclined plane. The fluid is suddenly released by opening the dam's sluice gate. Using a

high-speed digital camera, we then record how a fringe pattern projected on the flow surface is deformed, which makes it possible to measure the flow depth at any place on the surface.
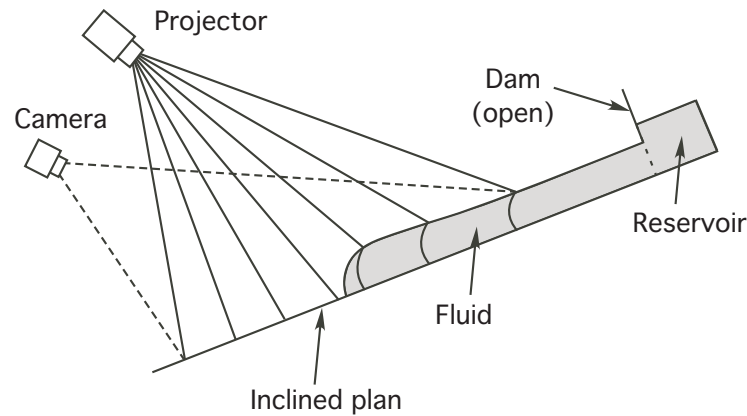

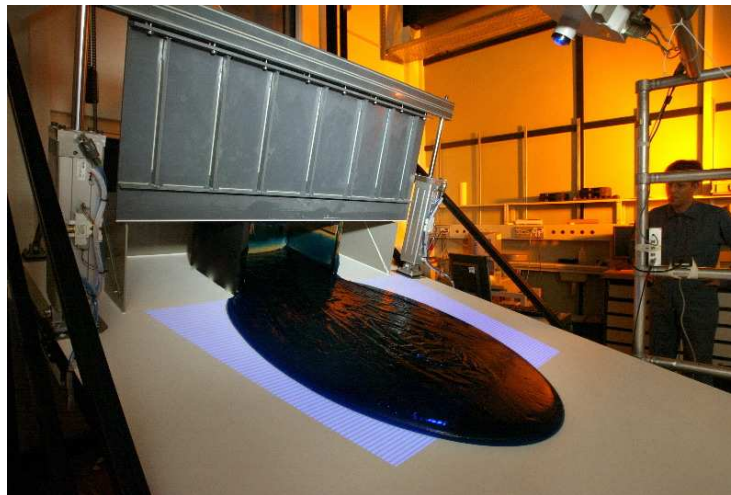Figure 2.1: The experimental setup and the measurement system.

Figure 2.2: View on the sluice gate and the reservoir at the channel inlet.

More specifically, our system worked in the following way: a micro-mirror projector[1] projected periodic fringe patterns of incoherent light onto the surface, as

---

[1]a modified z-Snapper provided by ViALUX, Chemnitz, Germany.

explained in Section 2.3.3. We placed the digital camera[2] above the flow, but with an incidence angle that differed from the projection angle. This camera recorded how the projected fringes were deformed by the free surface. In terms of signal processing, fringe deformation is equivalent to a phase offset, which can be shown to be directly proportional to the local flow thickness. Thus, measuring flow depth boils down to measuring phase offset.

2.2.2   Experimental facility

The facility was made up of a metal frame supporting an inclined plane, a horizontal plane (run-out zone), and a reservoir, as sketched in Figure 2.3. This structure was 6 m long, 1.8 m wide, and 4 m high. The 4-m-long aluminium inclined plane could be inclined from 0° to 45°, powered by an electric motor. Its slope angle was accurately measured by a digital clinometer with a precision of 0.1°. The 6-mm-thick aluminium plate was supported by a frame made of profiled aluminium beams (of section 40×80 mm^2) to ensure rigidity.

Different PVC channels were positioned on the inclined plane in order to limit the lateral spreading of the fluid in the cross-stream direction. As for the inclined plane, the channels could be inclined from 0° to 45° and could have different widths and shapes.

A PVC reservoir of varying volume and shape was positioned at the top of the inclined plane behind the dam wall. The maximum capacity of the reservoir was 120 kg. The dam wall was composed of a 1.6×0.8 m^2 ultralight carbon plate. Two pneumatic jacks lifted the sluice gate by 30 cm within 0.8 s. An ultralight dam wall was needed to reduce dam-wall inertia, plane vibration, and jerk. The two jacks were quickly raised by injecting air pressured at 7 MPa. Two electromagnetic sensors were located at the tip of each jack to control its position, reset the clock and start the acquisition process.

The carbon dam wall was 4 cm thick. To be able to close the dam gate, the canal was cut at this position. To avoid the material to flow out through this opening, two PVC spring-loaded valves closed the opening once the gate opened.

The run-out plane had two functions: first—and this is the most important point—the flowing material was forced to undergo a transition from a flow regime to a deposition (run-out) regime. Second, it collected the fluid flowing from the inclined plane, which made cleaning easier. The 1.5-m-long, 1.8-m-wide run-out plane was maintained in a horizontal position and was connected to the inclined plane by a sealing plastic band. The projector and the camera were fixed on another frame, which was independent of the main frame.

---

[2]a Basler A202k/C, 1004×1004 Pixels Camera Link 'k', monochrome, provided by Qualimat-est, Geneva, Switzerland.
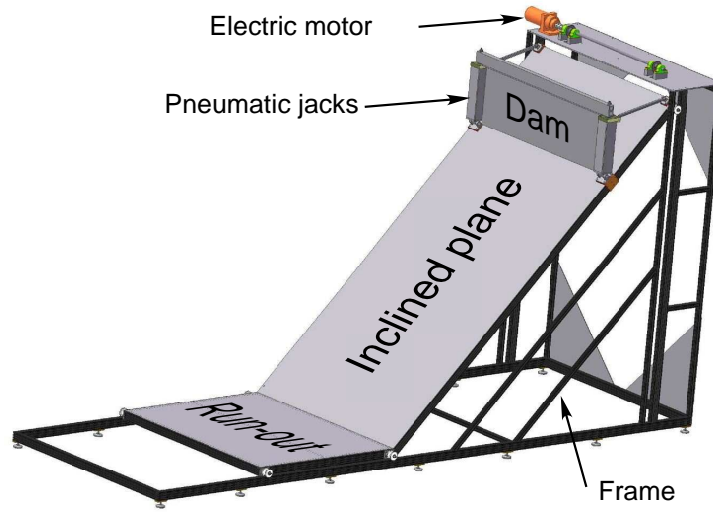
Figure 2.3: Schematic perspective of the facility.

2.2.3 Experimental procedure

A typical experimental run can be split into four stages.

1. The viscoplastic fluid used to-date is a stable polymeric gel; Carbopol Ultrez 10 (see Section 3.1). The fluid is prepared 1 or 2 days before experiments and stocked in a 60-l drum. Polymer chains are mixed into a sodium-hy-droxide/water solution at a given pH. This solution is left to rest for a long time so that all polymer chains have time to unroll and form a dispersion (repulsive interactions between chains). To ensure good light contrast, titanium dioxide (TiO_2) is added to whiten the Carbopol (see Section A.1).

   The Newtonian fluid used is a glucose syrup. 75 kg of sugar are melted down 3 days before the test at 130°C. When all the glucose is liquefied the mass is cooled down to 20°C and poured into the reservoir. To ensure a good temperature homogeneity, the syrup is let at rest in the reservoir overnight (see Section A.2.1).

2. The fluid is gently poured into the reservoir, while the inclined plane is kept in the horizontal position. The upper plane is then inclined at a given value and its position is checked using a digital clinometer. The free surface is smoothed out to horizontal by hand.

3. Once all the devices are installed, the measurement system is calibrated, as explained at length in Section 2.6. A few minutes before starting the test,

we collect a fluid sample and test it using a Bohlin CVOR rheometer to characterize its rheological properties (see Section 3.3).

4. We lift up the sluice gate and the material starts accelerating and flowing. The surge motion is imaged by the digital camera. When there is no significant motion, we stop recording images. The material is then removed from the flume and the plane is carefully cleaned.

2.3   Measurement system

2.3.1   How to measure the free-surface variations with time?

For dam-break experiments, the crux of the problem lies in properly measuring the free-surface evolution. Three criteria guided our choice among various systems. First, we needed a noninvasive system to avoid disturbing the free boundary. Second, global methods that are able to capture the flow surface within a single pass were preferred over scanning methods, which are not well suited to providing snapshots. Third, we wished to develop a method that would allow high acquisition rates.

The method chosen involved projecting patterns onto the fluid surface. This method is described in Section 2.3.2.

Three global systems were considered:

1. A method involving projecting patterns onto the fluid surface. Pattern deformation is recorded by a camera. This method is described in Section 2.3.2.

2. A stereoscopic system, with two cameras scrutinizing the same surface. This method performs well with surfaces of varying color and contrast since colored pixels can be used as reference points and tracked [Eaket et al., 2005]. The height is computed by taking the difference between two successive images recorded by the two cameras. Since our fluids are monochromatic, this method was discarded.

3. A system based on the time of flight of emitted photons. Photons are emitted by a source, a number of which are back-scattered by the surface. The time between their emission and reception provides an estimate of the distance travelled [Niclass et al., 2005]. This method performs well solely for static objects, but should be a promising technique for our purpose in the coming years given the rapid progress in this field.

2.3.2 Projecting patterns

Measuring the shape of an object using pattern projection can be broken down into three steps:

1. A periodic given pattern is projected onto an object.

2. The object surface is imaged into a camera under an angle of incidence that differs from the imaging direction.

3. The surface height is retrieved from the image.

For the sake of simplicity, two parallel lines are projected onto a surface, as shown in Figure 2.4 [Bateman et al., 2006].

The height difference Δh can be then expressed as

$$\Delta h = \frac{\Delta p}{\tan \alpha}, \tag{2.1}$$

where $\Delta p = p_p - p_a$ is the difference between p_p the projected lines onto the object and p_a the apparent line on the surface viewed by the camera; α is the angle between the projected lines and the camera. The distance p_p is measured in a plane containing the camera and the projector, and parallel to the reference surface. p_p could also be defined as the apparent line on the reference surface viewed by the camera.

This simple relationship emphasizes two points. First, the closer the projected lines p_p are, the greater the accuracy of Δh is. Second, the closer to 90° the angle α is, the better the accuracy of Δh is.
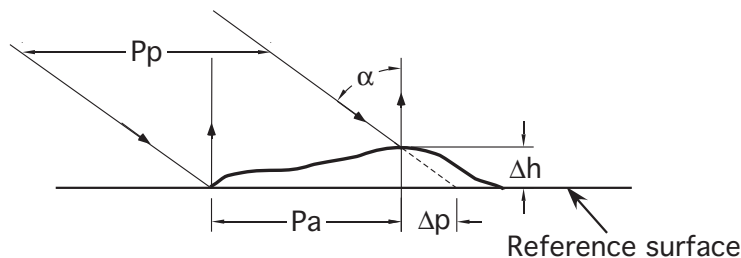
Figure 2.4: Projection of parallel lines on a surface and the retrieved height.

A problem with projecting lines is that any valuable information between two lines is lost, as illustrated by Figure 2.5. There is another technical problem related to the camera resolution: for two lines to be distinguished by the camera, there must be a minimum separation distance of three pixels, which imposes a lower bound on the accuracy of Δh according to equation (2.1).
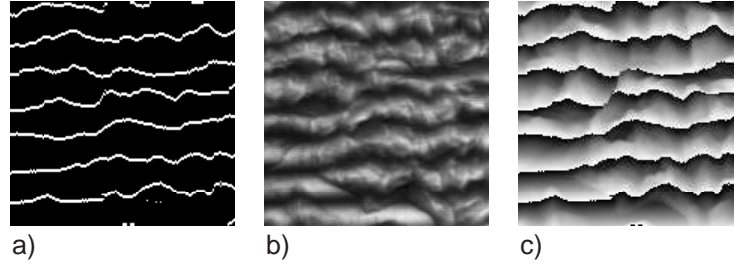
Figure 2.5: Comparison between: a) projection of lines, b) projection of fringes and c) the resulting phase map.

Another problem stems from computing the difference Δp when it becomes larger than one-half of the projected line spacing p_p since in that case, it is no longer associated with the closest reference line. This results in a negative value Δh, whereas a high positive value is expected. Figure 2.6 illustrates this loss of information: island 2 is embedded in island 1 and there is no convenient way of determining whether island 2 is located above or below island 1.
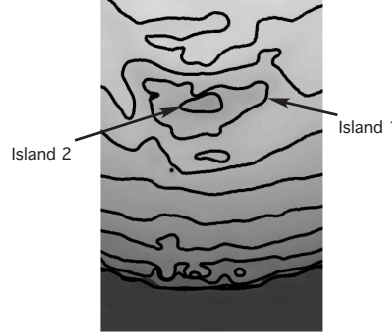
Figure 2.6: Loss of information due to looped line or islands. Is island 2 at a higher or lower elevation than island 1?

2.3.3   Projecting fringes

Instead of isolated lines, we can project cosine fringe patterns. Information theory would say that we are replacing a 1-bit system with an n-bit system, n being typically 8, 10, 12 or 16 depending on the performance of the camera and the projector. In our case, both the projector and the camera were 8-bit systems. Moreover, instead of relating height to light intensity, we can link height to the

fringe phase. The intensity observed at a given pixel (i, j) can be written as

$$I(i, j) = r(i, j)[A(i, j) + B(i, j) \cos \phi(i, j)], \tag{2.2}$$

where r is the reflectivity coefficient of the surface to be measured, A and B are called the background and modulation intensities, and ϕ denotes the phase. The phase varies within the interval $[0, 2\pi)$. The observed intensity I differs from the modulation intensity B. Ideally, we would like the background intensity A to be zero, but in practice this is not possible. Working with phase instead of intensity has the substantial advantage that altering surface reflectivity r does not influence the outcome.

We used an imaging system made up of a digital camera coupled with a synchronized micro-mirror projector working at a maximum rate of 48 Hz. The 1000 $\times$1000 px^2 CCD camera and the projector were synchronized by the frame grabber. The actual projection surface was 1.6$\times$1.6 m^2.

The projector was made up of 1024$\times$768 micro-mirrors that oscillated between two positions and onto which light was projected from a LED; for one position, light was reflected through the projector lens, while for the other position, light was not reflected. It was a binary system: for a given pixel, light was switched on or off. An 8-bit gray level was achieved by changing the projection duration of each micro-mirror. The main advantage of a micro-mirror projector (MMD) lies in its capacity to instantaneously project a given pattern. As mentioned in Section 2.3.1, achieving high resolution in time and space requires global acquisition and projection.

The 8-bit camera grabbed images, which are characterized by an intensity ranging from 0 (deep black) to 255 (white). For the phase to be properly retrieved from an image, a narrow range of 30 gray values is sufficient.

At its maximum rate, the camera recorded an image within 20.7 ms, while the fringes were projected for 20.3 ms. A time lag of 0.1 ms separated two images. Special attention was paid to ensure that projection occurred entirely within the acquisition time with no synchronization delay. The MMD is originally a 1-bit projection system, relative intensity is controlled by the projection duration and therefore any error (e.g., an error due to time discretization) may lead to significant errors in the post-treatment of images.

Capturing 48 images per second with a 1000$\times$1000 px^2 camera (i.e., 48 MB/s) during time intervals as long as 10 min requires a CameraLink connection between the camera and the frame grabber. To store the huge amount of data within a short interval of time, we integrated four hard disks in parallel into a RAID-0 system. The acquisition program was entirely developed using LabView.

2.4   Phase mapping

The phase map is a graphical representation (density plot) of the $\phi(i,j)$ functions [see Equation 2.2]. Optic convention is used here: high values (2π) are in white, whereas lower values (0) are in black.

Most algorithms used for retrieving phase from an image or a series of images are based on one the following methods:

1. Temporal phase mapping, where the phase map is retrieved using many images taken at different times:

   - phase-shifting, see Section 2.4.1.

2. Spatial phase mapping, where the phase map is reconstructed using the spacial information contained in one images:

   - Fourier transform, see Section 2.4.2, and the Hilbert transform [Onodera et al., 2005];
   - local wave retrieval, see 2.4.3;
   - wavelets [Watkins, 2007, Colonna de Lega, 1997].

The phase map is also often referred to as the *wrapped phase*, which explains why we speak of unwrapping techniques when recovering flow depth from phase shift.

To enhance accuracy, we must adapt our unwrapping algorithm with respect to fluid velocity. In the earlier moments of a run (typically 1–2 s), the flows accelerated vigorously and a one-image algorithm was used. After the flow had sufficiently slowed down, a three- or four-image algorithm was used.

Note also that for the phase map to be retrieved from the grabbed image(s), the images should not be saturated. If the grabbed images contained saturated pixels, this resulted in a loss of information and the creation of additional frequencies in the phase map.

2.4.1   Phase shifting

The principle of phase shifting consists in projecting $N \geqslant 3$ images of a fringe pattern shifted by $(i-1)2\pi/N$, with $i = 1\dots N$ [Colonna de Lega and Jacquot, 1996, Lehmann, 1997]. The phase can be analytically computed from the series of images using a least square approach [Hung et al., 2000]. An example with a

series of $N = 4$ images is given in Figure 2.7, with the following intensities

$$\begin{cases} I_1(i,j) &=& A + B\cos\phi(i,j), \\ I_2(i,j) &=& A + B\cos(\phi(i,j) + \frac{\pi}{2}), \\ I_3(i,j) &=& A + B\cos(\phi(i,j) + \pi), \\ I_4(i,j) &=& A + B\cos(\phi(i,j) + \frac{3\pi}{2}), \end{cases}$$

where

$$\phi = f(I_1, I_2, I_3, I_4) = \arctan\frac{I_4 - I_2}{I_1 - I_3}. \tag{2.3}$$
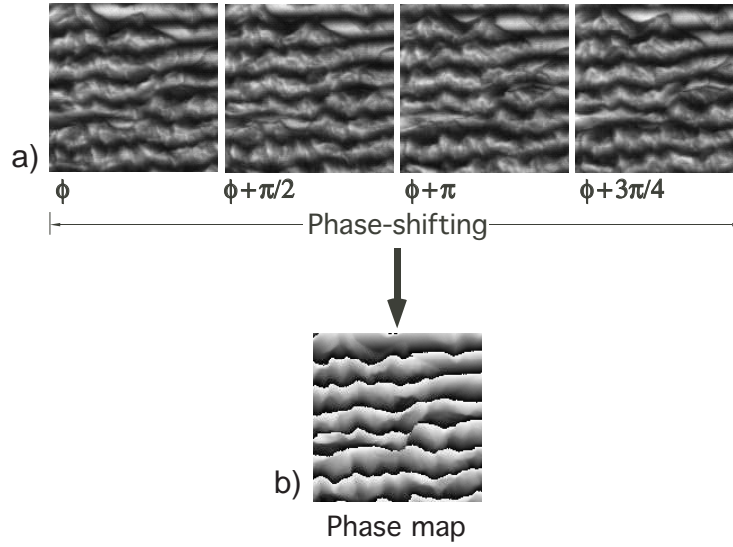
Figure 2.7: Phase shifting: a) with 4 images and b) the resulting phase map.

A phase map can be extracted from any new image using the $N - 1$ preceding images.

Three-fringe patterns can be projected at the same time using a red-green-blue (RGB) color coding. An independent phase map can be extracted from each new image. The idea is attractive, but requires a complicated and expensive setting [Jeong and Kim, 2002].

The method based on three or four images is more appropriate when the fluid slows down and the relative motion between the first and the last images is less than 1 or 2 pixels. This method is not suitable at earlier times when the fluid is released because the displacement of the fluid between the first and the last images is too large. The resulting phase map is blurred and unusable. During the first instants of the test, the phase map must be computed with only one image; this computation can be done with a Fast Fourier Transform (FFT) algorithm, as

explained in Section 2.4.2, or with a local wave retrieval algorithm, as described in Section 2.4.3.

This method should be used as much as possible because it is the only one that gives the phase explicitly, whereas in other methods, the phase is assessed by extrapolation.

2.4.2   Fourier transformation profilometry (FTP)

Fourier transformation profilometry (FTP) was first introduced by Takeda et al. [1982]. The idea is to work in the frequency domain of the recorded images in order to filter out the projected frequency f_0 and to keep only the desired frequencies ϕ_0 which contain the information on the object [Su and Chen, 2001].

In FTP, one assumes that the variations of the background and modulation intensity A and B and the object frequency are slow compared with the projected frequency f_0.

Without loss of generality we fix that the projected frequency f_0 is in the i-direction only. Equation 2.2 is written as:

$$I(i,j) = a(i,j) + b(i,j)\cos[2\pi f_0 i + \phi_0(i,j)], \tag{2.4}$$

where

$$a(i,j) = r(i,j)A(i,j),$$

and

$$b(i,j) = r(i,j)B(i,j).$$

Following Takeda et al. [1982] we obtain:

$$I(i,j) = a(i,j) + c(i,j)\exp(2\pi\imath f_0 i) + \bar{c}(i,j)\exp(-2\pi\imath f_0 i), \tag{2.5}$$

with

$$c(i,j) = \frac{1}{2}b(i,j)\exp[\imath\phi_0(i,j)], \tag{2.6}$$

where $\bar{c}$ denotes the complex conjugate of c and $\imath$ the imaginary unit ($\sqrt{-1}$).

Next, equation (2.5) is Fourier transformed with respect to i:

$$\hat{I}(f,j) = \hat{a}(f,j) + \hat{c}(f - f_0, j) + \hat{\bar{c}}(f + f_0, j), \tag{2.7}$$

where the hat symbol denotes the Fourier transforms, while f is the frequency in the i-direction.

$\hat{c}(f - f_0), j)$ is translated by f_0 toward the origin to obtain $\hat{c}(f, j)$ as sketched in Figure 2.8. In our case f_0 is computed using a reference image (without ϕ_0).
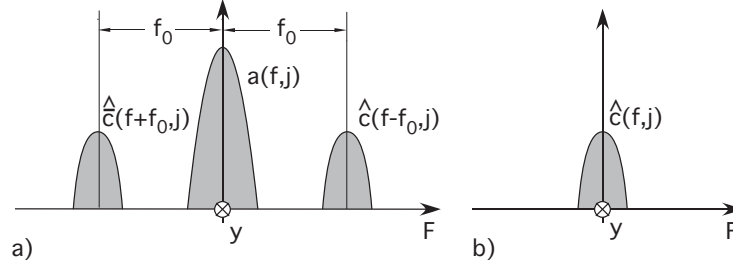
Figure 2.8: Frequency map: a) of a grabbed image, b) with only the frequency of the projected cosine shifted to zero.

$c(i, j)$ is then obtained by computing the inverse Fourier transform of $\hat{c}(f, j)$ with respect to f. The complex logarithm of (2.6) gives:

$$\log[c(i,j)] = log[\frac{1}{2}b(i,j)] + \imath\phi_0(i,j). \tag{2.8}$$

The phase ϕ_0 of the object lies now in the imaginary part.

In the remaining subsection we explain how the FTP was implemented in our setup.

A cosine fringe pattern with 45° inclinations is projected onto the surface of the reference plane during the calibration procedure, as shown in Figure 2.9(a) (see also Section 2.6). Two-dimensional Fourier transform analysis is then carried out on the recorded images as follows:

1. In the frequency map, the central peak is removed. This central peak represents frequencies close to zero, which are related to the flat inclined plane.

2. The frequency f_0 of projected pattern is localized [see Figure 2.9(b)] (see below).

3. The frequency map is filtered out to keep only the desired values [see Figure 2.9(c))].

4. The frequency map is shifted from the frequency f_o to the center [see Figure 2.9 (c)].

5. An inverse FFT analysis is carried out on the frequency map. The argument of the (complex) inverse FFT output provides us with the phase map of the reference plane [see Figure 2.9(d)].

Apart from the shift over f_0, this procedure is the same as the Hilbert transform. Indeed, in the last couple of years, the Hilbert transform has been used
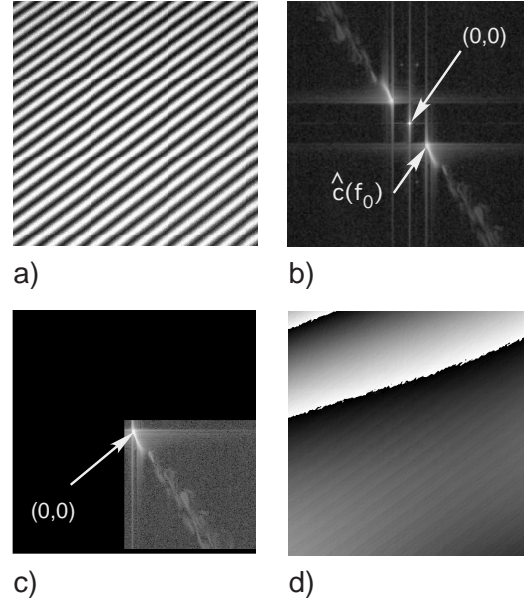
Figure 2.9: Reference plane: a) projected fringes, b) image in FFT domain with the frequency f_0 of the projected fringe, c) image filtered and shifted and d) reference plane phase map.

in interferometry to retrieve the phase from a single image [Onodera et al. [2005], Sticker et al. [2001], Larkin et al. [2001] and Hitzenberger et al. [2001]]. The development of demodulation technique using the discrete Hilbert transform seems a promising method.

The same procedure is then repeated, during the test, with the recorded images except that the frequency map is shifted by the value f_0, which was computed during the calibration procedure. Figure 2.10 shows a typical example, which can be compared with the images obtained when using the reference plane (Figure 2.9). The wrapped phase is then obtained by subtracting the new phase and the phase of the reference plane [see Figure 2.10 (d)]. The resulting phase is the difference between the object phase and the reference-plane phase. Section 2.5.4 will show that unwrapping the difference between the object-phase and reference-phase maps is equivalent to taking the difference of the unwrapped phases.

Concerning point 1 in the description immediately above, a delicate task is to properly remove the central peak. Since it is present on every image, the simplest strategy to remove it is to normalize the intensity by subtracting the mean intensity, as follows

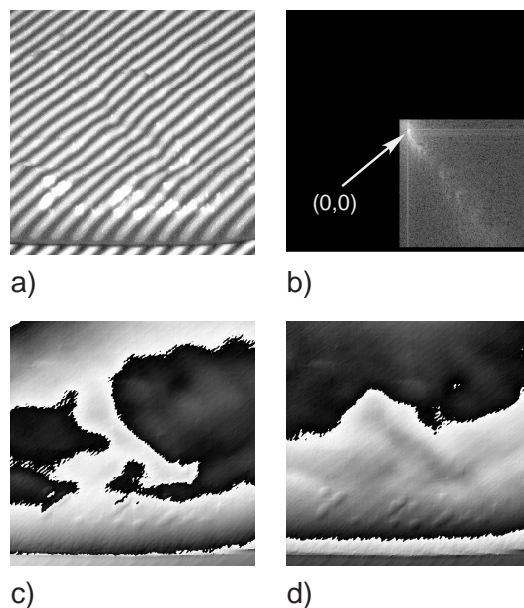$$I = I_1 - \frac{1}{N} \sum_{n=1}^{N} I_n,$$

Figure 2.10: Object: a) projected fringes, b) object image filtered and shifted in Fourier domain c) resulting phase map, and d) difference between the object phase map and the reference plane phase map.

where I_i is the intensity of image i $(i = 1 \ldots N)$ obtained during the calibration procedure (see Section 2.4.1) by shifting $N \geqslant 3$ fringe patterns by $(i-1)2\pi/N$.

Su and Chen [2001] discussed the influence of sampling in FTP. They emphasized that the recorded images as well as Discrete Fourier Transform (DFT) are digital, whereas FTP theory is based on continuous Fourier transform. This difference between theory and experimental treatment induces errors at high frequency values. We are attempting to implement methods for reducing errors that arise at high frequencies; note that this issue remains of secondary importance in our context because the typical wavelength of the free surface is quite long in comparison with the period related to these high frequencies.

FTP efficiency depends highly on filtering, i.e., how many frequencies must be kept or discarded. An experienced user can easily find frequencies that must be removed in order to enhance map accuracy. Making this process automatic is, however, quite difficult. It is almost impossible to know in advance when a phase-shifting algorithm can be used as a replacement for FTP. To solve this problem, we project 45°-inclined fringes with a phase shift of $2(i-1)\pi/N$, with $i = 1 \ldots N$. Both phase-shifting and FTP algorithms can then be used depending on the quality of their respective phase map.

As illustrated in Figure 2.11(a), this method encounters serious problems when

the projection pattern is parallel to a shadowed region. In this case, there is no real possibility to differentiate a dark area arising from shadow from the dark area that results from the projection. Erroneous frequencies are introduced, which result in an incorrect wrapped phase, as highlighted in Figure 2.11(b). Furthermore, if the light pattern crosses the shadow area perpendicularly, the wrapped phase remains of fair quality. All the information contained in a shadowed region is lost (see Section 2.5).

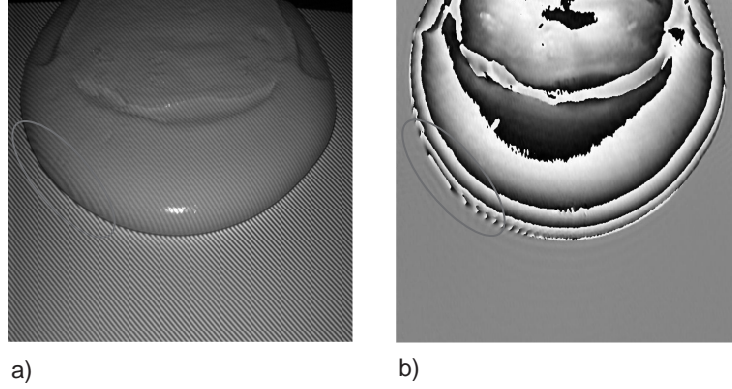a)   b)

Figure 2.11: Fringe projection at 45°: a) grabbed image, b) phase map computed with FTP. The phase map exhibits erroneous frequencies on the bottom left corner (area marked with the ellipsis).

In a nontelecentric setup (see Section 2.6), the fringe frequency changes with the incidence angle of the camera. The frequency f_0 is no longer represented by a sharp peak in the frequency map, but by something that is a bit more diffuse, as illustrated in Figure 2.12.

2.4.3   Local wave retrieval

Different methods have been developed to date to retrieve the phase of a signal, using one image and a local algorithm (Ransom and Kokal [1986], Marcy [1983], Ichioka and Inuiya [1972]). We decided to work with Liebling's algorithm [Liebling et al., 2004].

In local wave retrieval methods, one assumes that locally, only the value of the phase ϕ changes, while the background and modulation intensities A and B remain constant. The basic idea is then to divide an image into small windows and to estimate the phase in each of those windows by assuming that, in a given window, only the phase ϕ changes. Empirically, one observes that results are improved
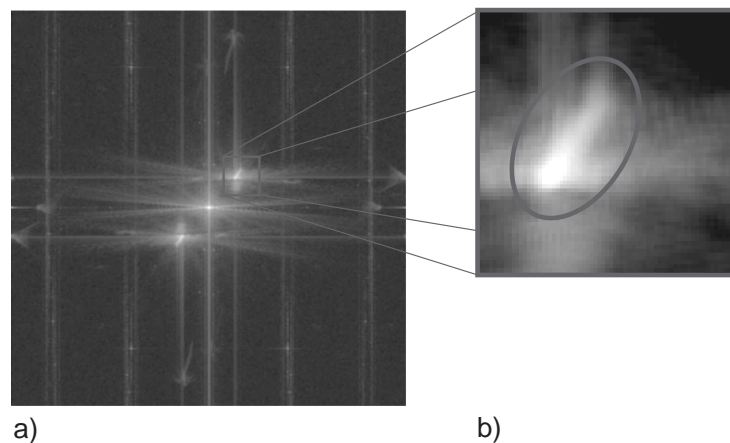
Figure 2.12: Image in the FFT domain with the frequency f_0 of the projected fringe in a nontelecentric setup: a) overview, b) close-up of the diffuse peak f_0.

when small phase steps and windows of sizes ranging from two to four periods are used.

As for FTP, the resulting phase map is defined as the difference between the object-phase and the reference-phase maps.

A major advantage of this method lies in the fact that any image can be used as a reference image. As explained in Section 2.4.2, projecting fringes parallel to a shadowed region introduces errors in the wrapped phase. The influence of a shadowed region can be minimized using a projection pattern perpendicular to it. In our setup, a shadowed region appeared at the front of the surge. An ideal projection image would have patterns perpendicular to all shadowed areas. In our setup, a symmetric image was used, as shown in Figure 2.13 (a). The axis of symmetry of the projection was aligned with the symmetry axis of the surge. This simple projection pattern tended to minimize the area where cosine fringe and shadow areas were parallel.

When this method is used with a symmetric projection, special attention should be paid to the calibration procedure since a sudden deviation in the unwrapped phase is likely to appear near the axis of symmetry (see Figure 2.14).

2.5 Phase unwrapping

Once we had obtained the phase map, we unwrapped it. The principle of phase unwrapping is quite easy to understand in one-dimensional problems. Let us consider that we have a phase signal ϕ defined over the interval $[0, 2\pi)$ and we
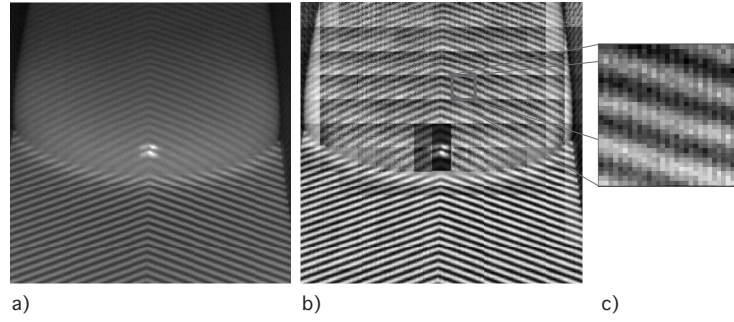
Figure 2.13: a) Grabbed image, b) local wave retrieval using window, c) close-up
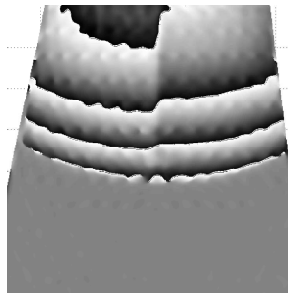of one window.

Figure 2.14: Phase computed using the local wave retrieval algorithm.

want to unwrap it. Whenever the signal goes out from the interval $[0, 2\pi)$, we add or subtract 2π to it depending on the derivative $\partial_x \phi$, as shown in Figure 2.15.
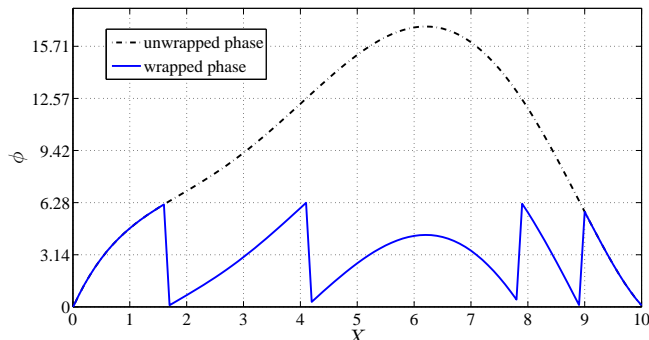

Figure 2.15: Example of phase unwrapping in 1D.

Without noise and shadow, 2D phase unwrapping would have a single solution. The phase could be computed at any point if the phase gradient $\nabla \psi$ and the true phase ψ at some initial point $\mathbf{r_0}$ were known, independently of the integration path C.

$$\psi(\mathbf{r}) = \int_C \nabla\psi \cdot \mathbf{dr} + \psi(\mathbf{r_o}). \tag{2.9}$$

Noise and shadow produce residues in the phase map which makes Equation 2.9 path-dependent. Residues can be seen as discontinuities in the phase map. In Figure 2.16 the integrations, from A to B, along the upper path and the bottom one give different results.

Any unwrapping algorithm tends to provide a proper *approximate* solution φ of the true phase map ψ.

2.5.1 Noise and shadow

The point is that noise blurs the sharp frontiers of the phase ϕ whenever ϕ approaches π (modulo π). Figure 2.17 shows a typical example of noise disturbance.

Ideally, to retrieve the phase ϕ from the observed intensity I [see Equation (2.2)], we would like to have the modulation intensity B equal to 255 (for an 8-bit system) and the background intensity A equal to the mean value of B (127.5). In practice, B varies between 30 and 120. In order to increase B, two solutions are available:

- the acquisition time is increased so that more light is received by the camera;

- the gain of the camera is increased to make it more light-sensitive.
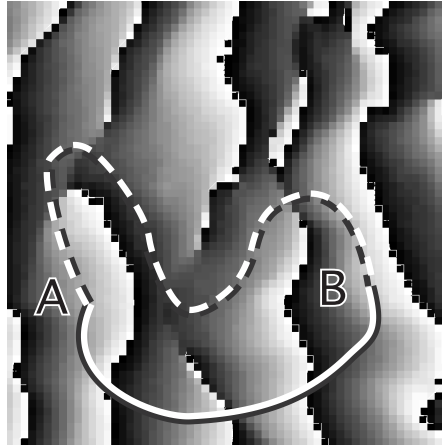
Figure 2.16: The integrations, from A to B, along the upper path (dash line) and the bottom one (continuous line) give different results.

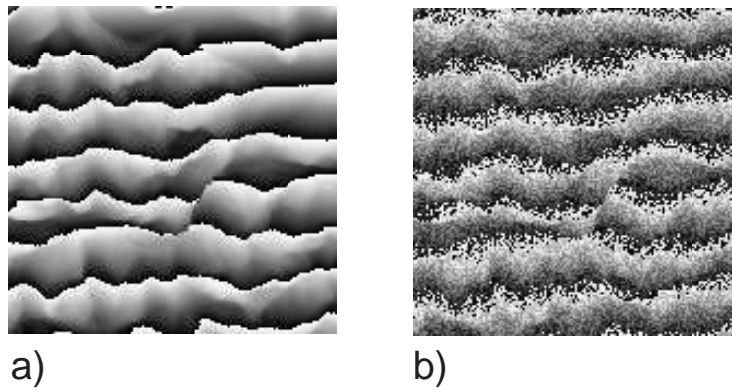a)   b)

Figure 2.17: Phase map: a) original, b) with noise.

In both cases, noise is increased. Indeed, when taking an image, a camera records the trajectory of the filmed object. If the displacement is relatively short, the picture looks sharp. In the converse case, if the typical displacement length exceeds three pixels, the image is blurred. In the latter case, the reconstructed phase is noisy. In short, we have two alternatives:

- if the acquisition time is long enough, the recorded image is blurred, but the modulation intensity B is relatively high. The intensity A should be equal to the mean value of B ;

- if the acquisition time is short, the resulting image is sharp, but at the same time is characterized by lower B values.

A tradeoff must be found. To obtain high modulation intensity B while keeping a short acquisition time, we can increase light intensity or increase the gain of the camera. The camera gain is increased by increasing the gain of the charge amplifier, so that fewer photons are needed to capture an image. However, this is at the expense of an increased noise level.

Shadowed regions appear when the plane surface is not entirely covered by the projected image or when part of this surface is hidden to the camera, as sketched in Figs. 2.18 and 2.19. All the information in the shadowed or hidden parts is lost. In order to obtain high-quality results, care must be taken to avoid such regions, while trying to keep the angle between the projecting and acquiring directions as close as possible to 90°. Again, a compromise must be found between the extent of shadowed areas and the mismatch of incidence angles.
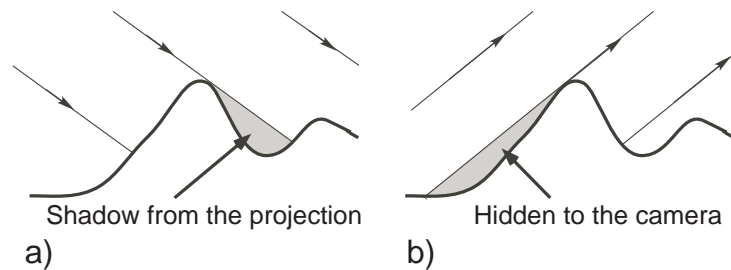

Figure 2.18: a) Shadow from the projector, b) parts hidden from the camera.

2.5.2 Residues

Without residue, phase unwrapping would be path-independent and therefore independent of the unwrapping algorithm. This highlights two points: first, the
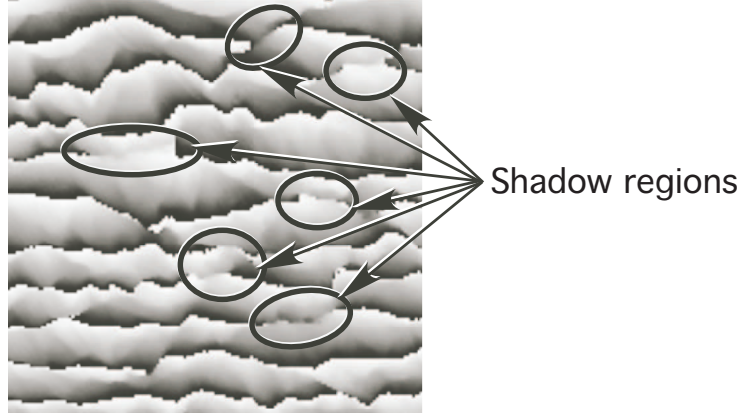
Figure 2.19: Shadow regions on an image.

acquisition procedure should be improved to reduce the noise and avoid any shadow part while keeping a good sensitivity (see Equation 2.1). Second, the relative number of residues in the phase map gives a valuable information on the 'quality' of the phase map and can help improve the acquisition procedure and determine which unwrapping algorithm should be used (see Section 2.5.3).

A sufficient condition for path independence is to check that the integral of the gradient of the wrapped phase ϕ along any simple closed path is equal to zero:

$$\oint \nabla\phi(\mathbf{r}) \cdot \mathbf{dr} = 0. \tag{2.10}$$

If this condition is not fulfilled, the unwrapped phase is path-dependent and the closed path encompasses a residue. This condition can be written for our purpose as:

$$\begin{aligned} q_{i,j} &= \mathcal{W}[\phi(i, j+1) - \phi(i,j)] \\ &+ \mathcal{W}[\phi(i+1, j+1) - \phi(i, j+1)] \\ &- \mathcal{W}[\phi(i+1, j+1) - \phi(i+1, j)] \\ &- \mathcal{W}[\phi(i+1, j) - \phi(i,j)], \end{aligned} \tag{2.11}$$

where $\mathcal{W}$ is the wrapping function:

$$\varphi = \mathcal{W}(\phi) = \phi + 2k\pi, \tag{2.12}$$

where k is an integer function that forces $0 < \varphi < 2\pi$. Equation 2.11 defines a residue map. The values of the residues are equal to some integers $n_{i,j}$ modulo 2π. In practice, the value of the charge $n_{i,j}$ is equal to ± 1. An example is given by Figure 2.20. In this case, as already illustrated in Figure 2.16, the result is path dependent.

All 2D unwrapping algorithms use different strategies to approximate a solution φ of the true phase map ψ.
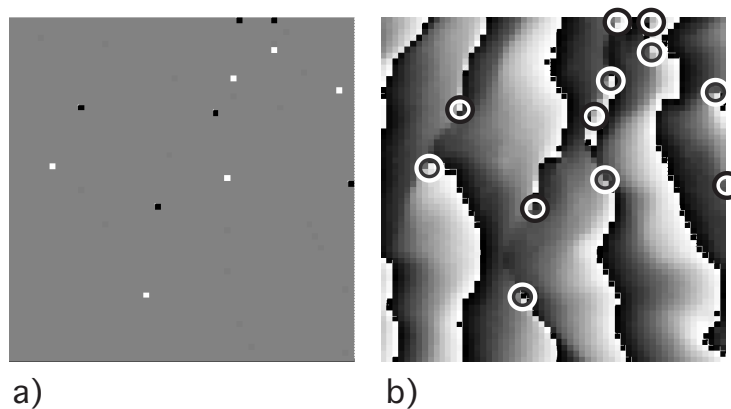
Figure 2.20: a) Residues map and b) residues on the phase map.

2.5.3 2-dimensional phase unwrapping algorithms

To date, different methods can provide approximations to two-dimensional un-wrapping problems. For instance, the book of Ghiglia and Pritt (1998) reviewed different approaches to phase unwrapping and provided eight C++ routines illus-trating these strategies. On the whole, there are two different approaches to phase unwrapping: one is based on path-following methods or local methods, while the other is based on minimum-norm methods or global methods. The path-following method starts at a given point in the phase map and computes the neighboring points by following a predefined path. The main problem arises in choosing the best path to avoid shadowed or noisy parts. Minimum-norm methods minimize the squared error ϵ of the phase gradients in the least-square sense:

$$\epsilon^2 = \int W(\nabla\varphi - \mathbf{g})^2 \mathrm{d}A, \tag{2.13}$$

with

$$\mathbf{g} = \nabla\psi + \mathbf{n}, \tag{2.14}$$

where $\mathrm{d}A$ is an elemental area, $\mathbf{g}$ the measured gradients which is the true gradient $\nabla\psi$ corrupted by noise $\mathbf{n}$. The square difference can be weighted by different functions W.

Ghiglia and Pritt ranked different algorithms by sorting them from the simplest and fastest ones to more complex and slower ones.

1. Goldstein's branch cut algorithm, *path-following* [Goldstein et al., 1988].

2. Quality-guided algorithm, *path-following*, [Roth, 1995].

3. Unweighted least-squares algorithm, *minimum-norm*, [Takajo and Takahashi, 1988].

4. Preconditioned conjugated gradient (PCG) algorithm, *minimum-norm*.

5. Mask-cut algorithm, *path-following*, [Parti et al., 1990].

6. Multigrid algorithm, *minimum-norm*, [Pritt, 1996].

7. Flynn's minimum discontinuity algorithm, *path-following*, [Flynn, 1997].

8. Minimum L^p-norm algorithm, *minimum-norm*, [Ghiglia and Romero, 1996].

As is usually the case, the best results are not systematically obtained with the most sophisticated algorithms. Even if the last two algorithms turn out to be the most robust ones, it is worth trying them all whenever we test a new configuration. After many trials, we opted for the path-following algorithm methods because their calculation time is much shorter than the minimum-norm one for usually better or equivalent results. Incidentally, note that all these algorithms have tunable parameters, which substantially influence not only the running time, but also the quality of the results.

In the following sections, the 4 path-following algorithms are summarized.

Goldstein's branch cut algorithm

The idea behind the algorithm of Goldstein, Zebker and Werner is to connect the nearby residues of opposite polarity with branch cuts so that they are balanced [Goldstein et al., 1988]. Residues can also be balanced by connecting them with branch cuts to the image border. The algorithm attempts to minimize the sum of the cut lengths. The integration path cannot cross a branch cut. The branch cuts of the example given in Figure 2.16 are represented in Figure 2.21.

Quality-guided path following

Let us define the *quality map* as the map that measures the statistical variance of the phase derivatives[3] [Pritt, 1996]. The phase derivative variance is defined by:

$$z_{i,j} = \frac{\sqrt{\sum \left(\triangle^x{}_{m,n} - \overline{\triangle^x}_{i,j} \right)^2} + \sqrt{\sum \left(\triangle^y{}_{m,n} - \overline{\triangle^y}_{i,j} \right)^2}}{k^2}, \qquad (2.15)$$

---

[3]Other quality maps can be defined such as the *pseudo-correlation map* or the *maximum phase gradient map*. Only the *phase derivative variance* is discussed here as it had proved to be the most valuable map for our purpose.
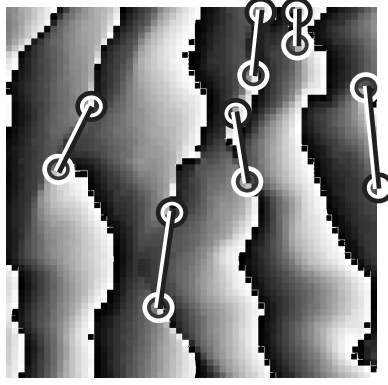
Figure 2.21: Branch cuts defined by Goldstein's algorithm.

where for each sum the index (m, n) range over the $k \times k$ window centered at pixel (i, j). The terms $\triangle^x{}_{m,n}$ and $\triangle^y{}_{m,n}$ are the partial derivatives of the phase (i.e., the wrapped phase difference).

$$\triangle^x{}_{m,n} = \mathcal{W}[\phi(m+1, n) - \phi(m, n)]$$

$$\triangle^y{}_{m,n} = \mathcal{W}[\phi(m, n+1) - \phi(m, n)]$$

The terms $\overline{\triangle^x}_{m,n}$ and $\overline{\triangle^y}_{m,n}$ are the averages of the partial derivatives in the $k \times k$ window. Equation 2.15 is the root-mean-square measure of the variance of the partial derivatives in the x and y directions. In practice, the phase derivative variance is computed in 3×3 windows. The phase derivative variance map of Figure 2.16 is given in Figure 2.22, where the dark regions represent the decorrelated phase due to shadow or noise.

A comparison of the quality map (see Figure 2.22) with the phase map (see Figure 2.16) and the residues map (see 2.20) shows that the corrupted phases and the residues tend to have low-quality value. The approach of the quality-guided path following algorithm is to chose the integration path that follows the high-quality pixels and avoids the low-quality pixels. The methods relies on the assumption that a good quality map will guide the integration path without encircling any unbalances residues. Even if there is no direct relationship between the quality map and the position of the residues, this method is surprisingly robust in practice.

Mask-cut algorithm

The mask-cut algorithm is an 'hybrid' algorithm between the Goldstein's algorithm and the quality map algorithm. The underlying idea is to use the quality map to guide the placement of the branch cuts [Parti et al., 1990]. The resulting

Figure 2.22: The quality map defined by the phase derivative variance map where the dark regions represent the low quality value due to shadow or noise.

algorithm combines the advantages of both algorithms: the quality map is used to guide the unwrapping process while the branch cuts ensure that no unwrapping errors are introduced by encircling unbalanced residues.

Flynn's minimum discontinuity algorithm

Phase unwrapping has been introduced at the beginning of this section as the process of assigning an integer multiple of 2π to each region to minimize the discontinuities across the fringe lines. The additions of an integer multiple to each region 'lifts' that region into place.

Flynn [1997] proposed an algorithm, which employs a clever scheme for detecting lines of discontinuity which does not necessarily lie on fringe lines. The algorithm identifies the lines of discontinuity that are joined into loops, and then it essentially adds the appropriate multiple of 2π to the pixel enclosed by the loop if this action removes more discontinuities than it adds. This process is performed iteratively, reducing the discontinuities at each stage, until no more loops can be identified. A quality map can be used to weight jump counts and guide the placement of the discontinuities.

Flynn's algorithm works particularly well when the phase map presents some loop patterns. In our practical case, we had well defined loops in the phase map as we unwrapped the difference of the object phase map and the reference phase map as explained in Section 2.5.4. Those loops may be cut if the inclined canal is used and the algorithm does not converge toward the right unwrapped phase.

Empirical procedure

Experience has demonstrated that, for our particular setup, the best procedure to unwrap the phase map is to:

1. Choose a couple of arbitrary phase maps at different times.

2. Compute the residues maps to estimate the quality of the phase maps.

3. Unwrap the phase maps using Goldstein's algorithm to have valuable reference unwrapped phase maps.

4. Compare:

   - the quality-guided path following algorithm and the mask-cut one with Goldstein's unwrapped phase maps for the inclined canal setup;

   - the quality-guided path following algorithm, the mask-cut one and Flynn's one with Goldstein's unwrapped phase maps for the inclined plane setup.

5. Chose the most appropriate one.

6. Unwrap all the results.

2.5.4   Phase difference

A good way to reduce computation time is to unwrap the difference of the two phase maps instead of computing the difference of the respective unwrapped phase, as shown in Figure 2.23. The resulting map shows fewer 2π jumps, which makes the reconstruction of the unwrapped phase easier, faster, and more accurate. Unwrapping the difference of the object phase map and the reference phase map provides the same results as taking the difference of the unwrapped phases.

2.5.5   Wavelet filtering

Before transforming the image pixels i, j and the unwrapped phase φ into a metric Cartesian coordinates system x, y and a height z respectively, the unwrapped phase map was filtered. To filter the phase map, we used a *bior 3.7* wavelet at level 4 with a thresholding method, which penalized the low coefficients [Misiti et al., 2007].
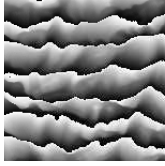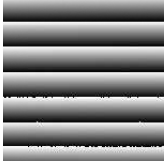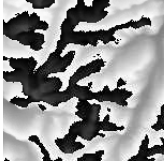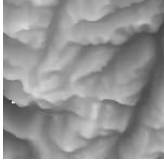
Figure 2.23: Unwrapping the difference of the object phase map and the reference phase map is equal to the difference of the unwrapped phases.

2.6   Calibration

The calibration procedure computed a matrix $M_{ij\varphi}$ to transform the image pixels i, j and the unwrapped phase φ into a metric Cartesian coordinate system x, y and a height z respectively.

Equation 2.1 gives the height as a function of the angle α and the distance between two lines P_p. The following assumption underlies this equation: projection and acquisition must be telecentric, which is not the case in our setup [Chen and Quan, 2005].

Figure 2.24 shows how the angle α between the projection angle and the camera angle varies in a nontelecentric setup: $\alpha_1 \neq \alpha_2$.

The same also holds for the projected lines P_p and the apparent line P_a seen by the camera; $P_1 \neq P_2$.

Theoretically, knowing the relative position of the camera, the projector, and the inclined plane as well as the projection and camera angles makes it possible to modify Equation (2.1) by including a height correction factor for each position [Desmangles, 2003]. This method involves accurately measuring the position of each element of the setup, which is time-consuming. Moreover, it does not take optical deformation into account. For these reasons we decided to use a more practical calibration procedure, which was based on a modified version of the virtual calibration-plane method proposed by Xiaoling et al. [2005].

The underlying idea of the calibration procedure is to position a calibration plate at different heights z and project the pattern to be used during the test. Each image of the calibration plate gives a relation between the pixel i, j and the
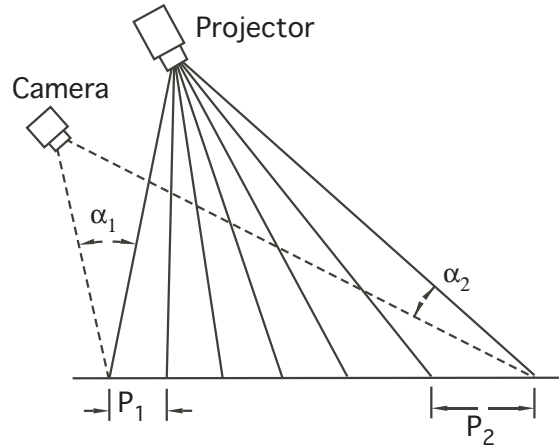
Figure 2.24: Variation in the angle α for a nontelecentric setup.

Cartesian coordinate system x, y as well as a relation between the computed phase ϕ and the height z.

To calibrate this measurement system, we proceeded as follows:

1. Well-defined patterns such as squares were projected onto the inclined plane to adjust the focus of the projector and camera.

2. We checked that the recorded images from the camera properly included the zone of interest. Light power and projection resolution were optimized by fitting the size of the projected images with the plane size. An intensity profile was taken on the grabbed images to ensure that its values ranged from 0 to 255 and that no part was saturated.

3. We related the Cartesian coordinates x, y, z of the plane with a grid i, j, each cell representing a pixel of the unwrapped phase. To that end, we designed a calibration plate, i.e., a simple plane surface, over which we marked gray disks, 2 cm in diameter spaced 10 cm apart. The upper surface of this plane corresponded to elevation $z_0 = 0$. All fringe patterns, which were used in experimental runs, were then projected on this calibration plane [see Figure 2.25(a)]. The modulation of the reference plane was obtained by averaging the calibration projections, [see figure 2.25(b)], while the position of the circle centers were found using a least-square method. [see Figure 2.25 (c)].

4. The wrapped phase was referred to as ϕ_{z_0} [see figure 2.25(d)]. A relation between the plane xy_{z_0} and the camera coordinates ij was obtained using a piecewise linear interpolation function.

5. Any circle that was partially contained in the image was removed because
   its center could not be accurately located (information was partly lost). If it
   were kept, it would introduce distortion.

a)   b)

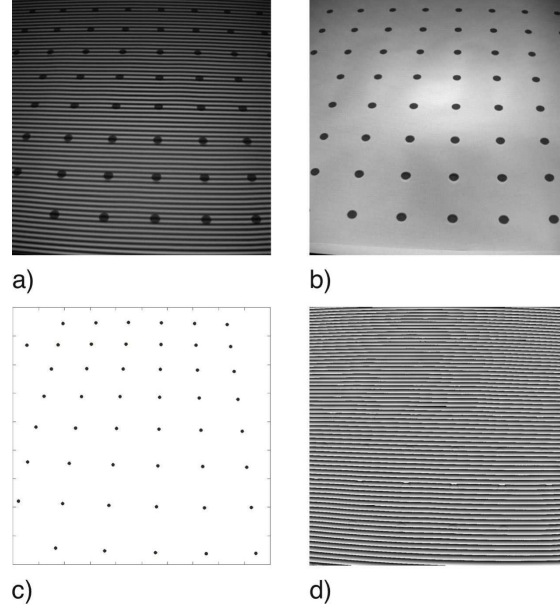c)   d)

Figure 2.25: a) Projection of the fringe on the calibration plate, b) modulation
with the calibration circles, c) position of the circle in the camera pixel coordinates
and d) phase map of the calibration plane.

The same procedure was repeated k times with the calibration plate placed
over the inclined plane at an elevation z_k, with $k = 1, 2, \ldots K$; (see Figure 2.26) in
practice, we used K values as high as 7. A relation between the plane $xy_{z_k}(k =
1, 2, ..., K)$ and the camera coordinates ij was obtained using a piecewise linear
interpolation. The corresponding wrapped phase ϕ_{z_k} was computed and the phase
difference $\phi_{z_k} - \phi_{z_0}$ was unwrapped and denoted by φ_{z_k}. φ_{z_k} was not unique since
$\phi_{z_k} - \phi_{z_0} \in [0, 2\pi)$. z_k was a function of $\varphi_{z_k} = \psi_{z_k} + j\pi$, with $j = 1, 2, ...$ A
way of finding j is explained in Section 2.6.1. Once $\phi_{z_k} = \varphi_{z_k} + j\pi$ was defined, a
piecewise linear interpolation method was used to complete the z-axis calibration.
The unwrapped phases $\varphi_k (k = 1, 2, ..., K)$ at elevation $z_k (k = 1, 2, ..., K)$ were
considered as reference phases. With the reference phases φ_k and their elevations
z_k, every pixel height (z-axis coordinate) was obtained by linearly interpolating φ_k
and z_k.

We ended up with a calibration matrix $M_{ij\varphi}$, which related the value of the
unwrapped phase φ_k in the pixel coordinate system ij with the elevation z_k in the
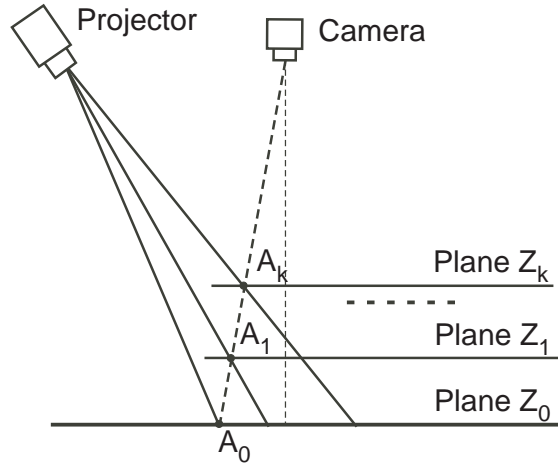
Figure 2.26: Calibration with virtual planes z_k.

plane coordinate system xy. Figure 2.27 shows the matrix $M_{ij\varphi}$ with five surfaces φ_k, which represented five different elevations z_k: 5, 25, 45, 65, and 85 mm. The dots represent the position of the circle centers located on the calibration plane.
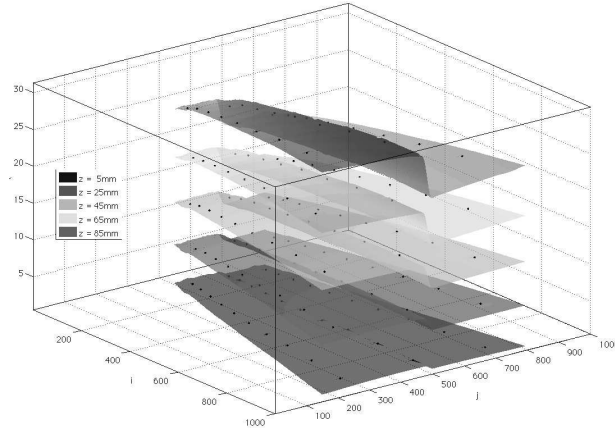
Figure 2.27: Calibration matrix $M_{ij\phi}$ with five reference planes $z - k$. The dots represent the position of the circle centers on the calibration plane.

The steps, which appear in the middle of each surface φ_k, result from a symmetric projected pattern, which was not aligned with the x-direction of the calibration plane. For the camera, the projection angles on either side of the symmetry axis were different, which led to contrasted sensitivity to flow depth [see Equation 2.1]. A closer look at Figure 2.28(a) shows that the axis of symmetry of the

projected pattern was not vertical; the projection angle was slightly different on either side of that line. This leads to a step-shaped variation in the phase map [see Figure 2.28(b)] as well as in the unwrapped phase map [see Figure 2.28 (c)]. As expected, the calibration process resulted in the surface not showing any step [Figure 2.28 (d)].
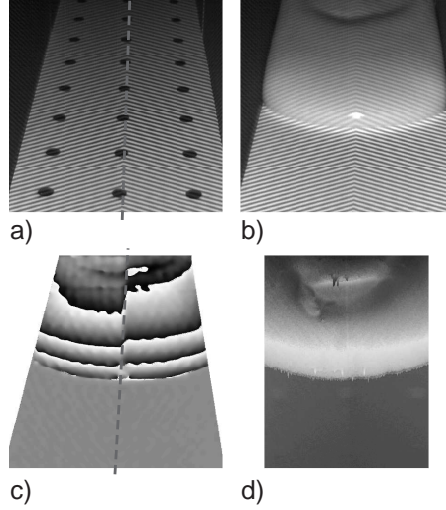

Figure 2.28: Projection of a symmetric pattern not aligned with the reference plane, a) grabbed image of the reference plane with the axis of symmetry in the dotted line, b) grabbed image of the sluice, c) phase map with a step on the axis of symmetry, d) the resulting surface without any step.

Compared to classical ways of calibration, this method reduces the hardware requirement of the system. It also simplifies the process of grabbing and processing data. Better accuracy is achieved by increasing the number of virtual calibrating planes z_k. The standard deviation error, when five planes are used, is on the order of 1%.

2.6.1 Temporal phase unwrapping

A problem arose with our setup: two calibration planes with two different heights may still have the same phase ϕ_{z_k}. To get around this problem, we used Temporal Phase Unwrapping (TPU). This technique is presented at length by Huntley and Saldner [1997]. It involves unwrapping a phase with high sensitivity by means of other phases with lower sensitivity.

First, a series of phase-shifted images (see Section 2.4.1) is projected with a projected period p_{p1}, which is longer or equal to the plane length. In this case,

the phase ϕ_1 is equal to the unwrapped phase φ_1. The unwrapped phase φ_1 is contained within the interval $[0, 2\pi)$ and the accuracy of the measure is low. We know from Equation 2.1 that the measurement accuracy can be increased when a series of images is projected with a smaller period. We choose to project a second series of phase-shifted images, but with a period p_{p2} set to half the length p_{p1}, having twice the accuracy, the unwrapped phase φ_2 is contained in the interval $[0, 4\pi)$. To avoid complex unwrapping algorithms (see Section 2.5) to compute φ_2, we use the TPU method:

1. ϕ_1 is computed from the first series of phase-shifted images: $\phi_1 = \varphi_1 \in [0, 2\pi)$.

2. φ_1 is multiplied by 2 and the result is denoted by ψ_1. ψ_1 belongs to the interval $[0, 4\pi)$.

3. ϕ_2 is computed from the second series of phase-shifted images. $\phi_2 \in [0, 2\pi)$.

4. The unwrapped phase φ_2 is directly calculated by adding 0 or 2π to ϕ_2 so that $\phi_2 + (0 \text{ or} 2\pi) = \psi_1 + \epsilon$. ϵ is the residual error: $\varphi_2 = \psi_1 + \epsilon$.

Once that φ_2 is computed, the period of a new series of phase-shifted images with a period p_{p3} is set to half the length p_{p2}. The accuracy of the new unwrapped phase φ_2 lies within the interval $[0, 8\pi)$. This process can be repeated n times until the desired accuracy is reached, as illustrated by Figure 2.29.

2.6.2 Computational time

The mean time spent from acquiring an image to obtaining a three-dimensional surface takes nearly 5 min on a Dual-Core Intel Xeon processor at 2.66 GHz under Mac OS X:

- on average, a one-image algorithm for retrieving the phase takes 1'30" (see Section 2.4.2 and 2.4.3) and less than 10" with a phase-shifting algorithm;

- phase unwrapping takes 30" to 1 min depending on the complexity and the quality of the object phase (see Section 2.5);

- transforming the unwrapped phase map into an image in a Cartesian coordinate system takes about 1'30, depending on the number of virtual planes z_k used (see Section 2.6).

Given that a typical experimental test lasted at least 3 min (usually from 3 min to 12 h) and we operated a camera at 45 fps, we ended up with a minimum of 8'100 images. The total computational time would therefore be 270 hours (11.25
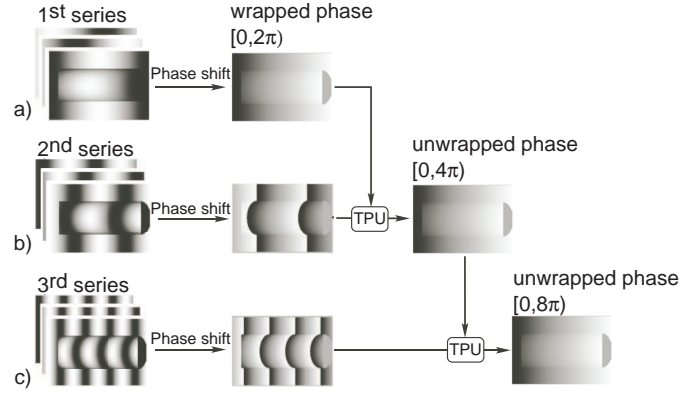
Figure 2.29: Temporal phase unwrapping: a) a series of phase-shifted images is projected with a projected period P_{p1} longer or equal to the plane length. ϕ_1 is equal to the unwrapped phase φ_1. b) a second series of phase-shifted images is projected, but with a period P_{p2} set to half the length P_{p1}. ϕ_2 is computed. The unwrapped phase φ_2 is directly calculated by adding 0 or 2π to ϕ_2 so that $\phi_2 + (0$ or $2\pi) = 2\phi_1 + \epsilon$. c) This processes is repeated with a new series of images.

days), which would make the method of limited interest when conducting many experiments. In order to speed up calculation, we used the *Distributed Computing Toolbox* from Matlab, with a grid of 8 CPUs, which made it possible to reduce the computational time to one day.

2.7   Examples

Here, we provide the results obtained when releasing a 40-l volume of Carbopol Ultrez 10 at a solid concentration of 0.3% down a 30-cm wide channel. The bed inclination was 12° with respect to the horizontal and the channel cross-section was rectangular.

Figure 2.30 (a) represents the grabbed image of the flow taken at time $t_1 = 1$ s. The wrapped phase was obtained by a local wave retrieval algorithm. Figure 2.30 (b) illustrates the same flow but at time $t_2 = 52.0$ s. The phase was computed using a 4-image algorithm.

2.8   Conclusion

In order to accurately measure the three-dimensional flow depth profiles in the dam-break problem, a new experimental facility and new processes have been built.
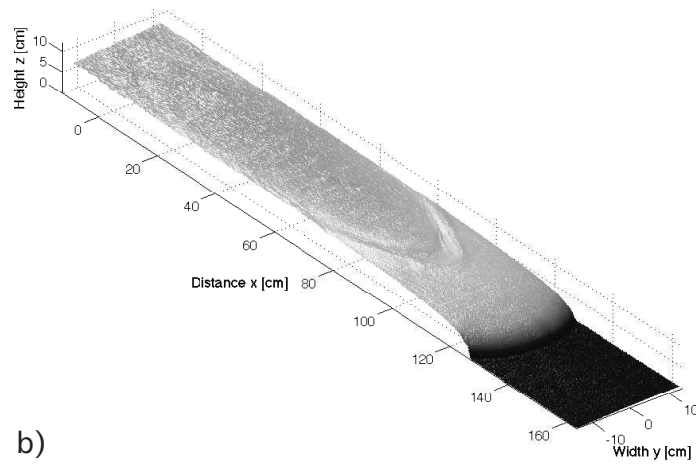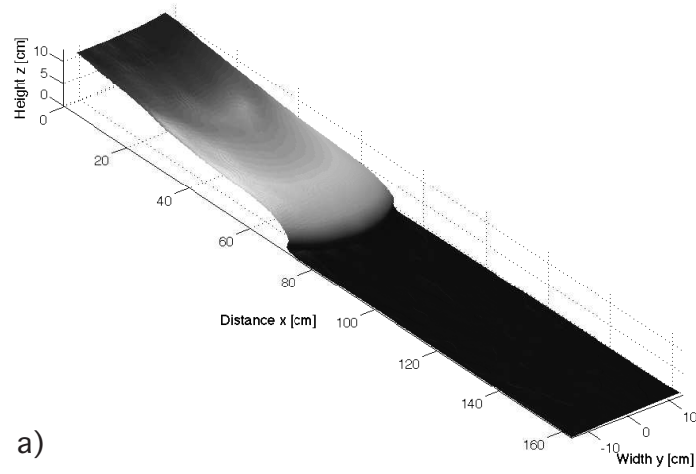
Figure 2.30: Free surface at: a) $t_1 = 1.0$ s, b) $t_1 = 52.0$ s.

Three-dimensional flow-depth profiles are measured using a high-speed digital camera, which records how a fringe pattern projected onto the flow surface is deformed. This technique has never been used to measure large moving objects such as a surge down an inclined plane. Many innovative solutions have been developed to sort out the numerous technical problems that arise when a fast and deformable material flows. Various methods, algorithms, and techniques ranging from airborne Synthetic Aperture Radar to biomedical imaging have been combined to obtain a high-accuracy measurement system.

Our system allowed us to measure the surface height of a 1.4×1.4 m^2 surge withan uncertainty of the order of 1 mm at a frame rate of 48 Hz. With this tool, we can acquire high-accuracy data related to the dam-break problem, which can then be used to test the various numerical models developed to compute the spreading of a non-Newtonian material in time-dependent flow conditions.

Rheological characterization of viscoplastic materials

V ISCOPLASTIC materials are characterised by a yield stress, which means that they behave like solids when the shear stress does not exceed the yield stress and like fluids for shear stress in excess of the yield stress. Viscoplasticity is one possible model to reproduce the fact that geophysical materials can flow under some circumstances, while they behave as solids when they are not sufficiently stressed.

3.1   Introduction

Two plastic theories are commonly used to describe rapid gravity driven geophysical flows such as avalanches and debris flows: Coulomb plasticity and viscoplasticity [Ancey, 2007]. Ideal coulomb material are two-phase material for which pore pressure and friction plays a key role in the bulk dynamics. Viscoplastic materials typically behave as a single-phase fluid on the macroscopic scale and exhibit a viscous behaviour after yielding. Determining the rheological behaviour of geophysical materials remains difficult because they encompass coarse, irregular particles over a very wide range of size. Consequently, the true nature of plastic behaviour for geophysical flows is still vigorously debated.

Even if this study focuses on the behaviour of viscoplastic fluids down steep slope, the experimental setup can be used with any kind of material.

Two fluids were tested on the experimental setup with different configurations:

- a viscoplastic fluid: a stable polymeric gel, Carbopol® Ultrez™ 10 carbomer polymer from Noveon, Inc. provided by Gattefossé AG, Luzern, Switzerland[1]. If not specified otherwise, 'Carbopol' refer to 'Carbopol Ultrez 10';

- a glucose syrup used as a Newtonian fluid (see Appendix A).

In this chapter, the rheology of viscoplastic material will first be discussed in Section 3.2. The experimental procedure used to measure the flow curve, yield stress and thixotropy will then be described in Section 3.3. The preparation of both fluids is explained in Appendix A.

3.2   Viscoplastic material

Viscoplastic materials are defined by a yield stress. The yield stress τ_c is the critical shear stress that must be exceeded before irreversible deformation and flow occur. Once the yield stress is exceeded, the material exhibits viscous liquid behaviour. For applied stresses below the yield stress, the material deforms as an elastic body. An elastic material is deformed under stress, but then returns to its original shape when the stress is removed.

One very popular equation to model viscoplastic materials is the *Bingham model* [Bingham, 1922]:

$$\tau = \tau_c + K\dot{\gamma}, \tag{3.1}$$

where τ_c is the yield-stress and K the *consistency*.

---

[1]From now on the ® and ™ decoration are dropped.

The *Herschel-Bulkley model* [Herschel and Bulkley, 1926] is more adapted to take into account the non-linear shearing effect (Ostwald [1925] and de Waele [1923]):

$$\tau = \tau_c + K\dot{\gamma}^n, \tag{3.2}$$

where n is a power-law index that gauges the degree of shear thinning or thickening. In most practical cases $n < 1$. If $n = 1$ the Herschel-Bulkley model is equivalent to the Bingham one. If $n = 1$ and $\tau_c = 0$ the fluid is Newtonian.
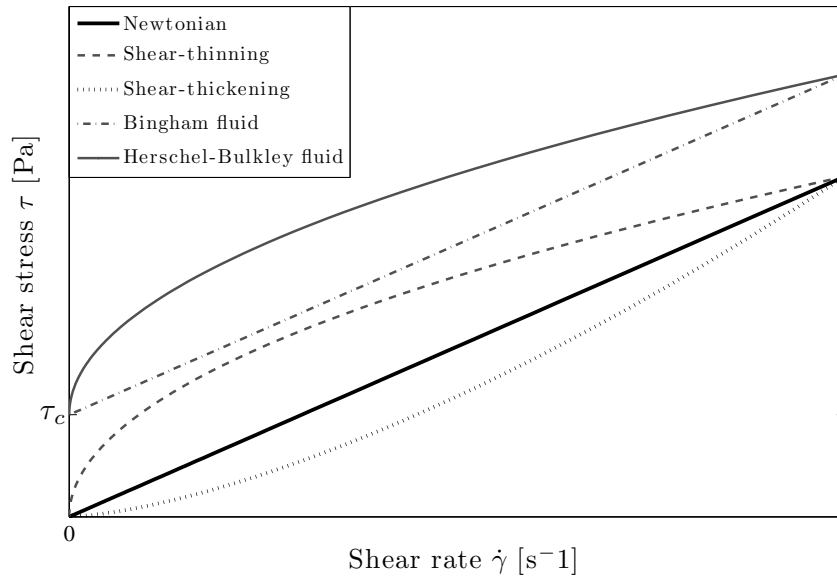

Figure 3.1: Newtonian fluid and idealized Non-Newtonian fluids.

3.2.1 Yield stress

For both, Bingham and Herschel-Bulkley models, the flow curve crosses the shear stress-axis at the yield-stress τ_c for a shear rate $\dot{\gamma}$ equal to zero. The yield stress cannot be measured directly but is extrapolated from the flow curve. The following question arises: how close to zero should the shear rate be measured in order to have a good approximation of the yield stress? De Kee and Chan Man Fong [1993] give a surprising response: "the measurement of the yield stress... is the measure of the experimenter's patience". In other words [Cheng, 1986]: "the magnitude of any measured yield stress depends on the time of the measurement", because viscoelastic and thixotropic effects can mask other features. James et al.

[1987] demonstrated that a variation in the yield stress by more than an order of magnitude can be obtained depending on how it is measured.

To determine the duration of the observation/experiment vs a characteristic time of the material deformation, Reiner [1964] defines the Deborah number[2] De as:

$$De = \frac{T_r}{T_{obs}} \tag{3.3}$$

where T_r is a characteristic relaxation time and T_{obs} the duration of the observation/experiment. De is zero for a Newtonian fluid and is infinite for a solid. The yield stress is directly related to the Deborah number.

A myth?

In 1985, Barnes and Walters [1985] came up with a provocative article in which they concluded that the yield stress is a myth and does not exist. If we recall Herodotus' motto '$\pi\alpha\nu\tau\alpha \ \rho\epsilon\iota$', everything flows, then the statement from Barnes and Walters becomes obvious; if the measurement time is long enough a shear rate will always be recorded. This property is no restricted to viscoplastic materials but to all materials [Barnes, 2000] and explains the creeping behaviour of solids[3]. Every solid exhibits a Newtonian viscosity plateau at very low stresses.

Piau [2007] measured, with MRI-rheometery technique, and compared results for different concentration of Carbopol 940 and 980 at very low shear rate and found, instead of a yield stress, two Newtonian plateau. Figure 3.2 represents the flow curve of a viscoplastic material showing an asymptotic Newtonian behaviour at very low and very high shear rate [Roberts et al., 2001].

Figure 3.3 illustrates the same phenomena but in a viscosity/shear stress diagram where the two Newtonian plateau are also visible [Malkin, 1995].

Slip or wall depletion

In some cases, the Carbopol polymer chains can be repelled from the walls because of various physico-chemical forces arising between the polymer chains and the walls, e.g., electrostatic and steric forces. Because of molecules' migration, a very narrow layer of water is created between the walls and the gel. The water layer acts as a lubricator and the Carbopol gel slips over it. Figure 3.4 sketches the flow velocity of Carbopol with and without slip.

---

[2]In the Judges 5:5 in the old Testament of the Bible, prophetess Deborah stated that:*The mountains flowed before the Lord.*

[3]a plastic deformation of the material over time under a stress which is below the limit of elasticity
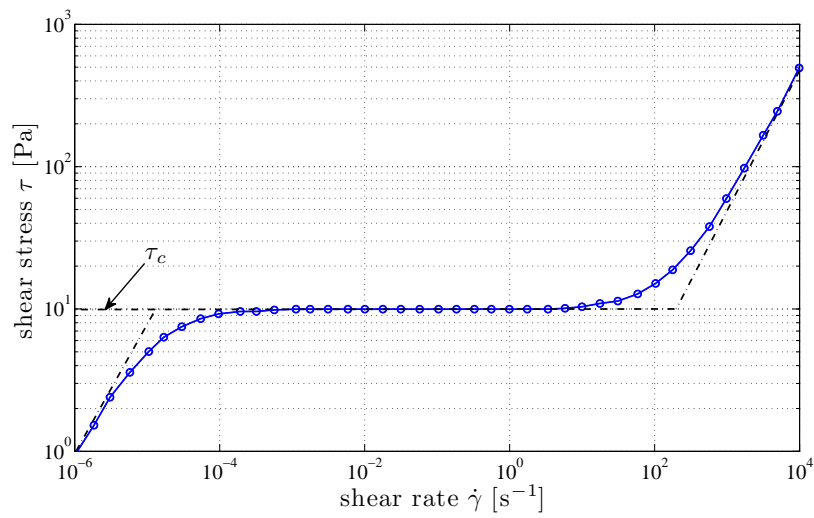
Figure 3.2: Viscoplastic material showing an asymptotic Newtonian behaviour at very low and very high shear rate, respectively as dashed lines, and the apparent yield stress τ_c. Replotted form Barnes [1999].
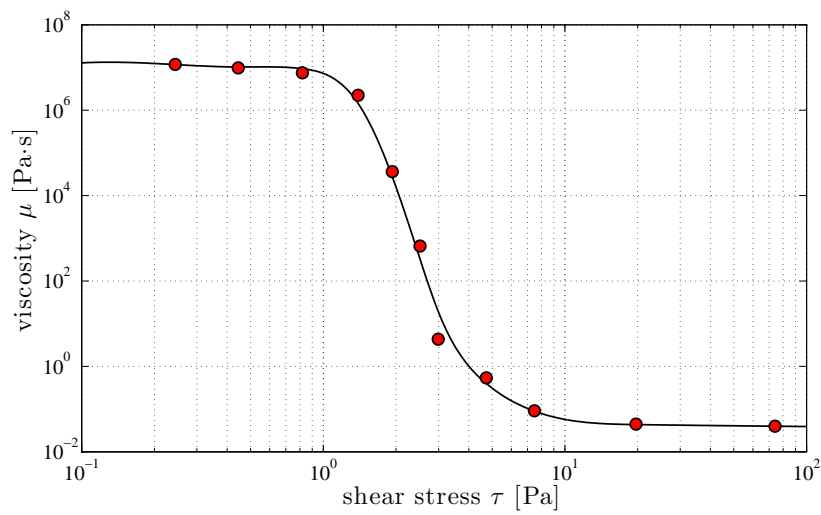

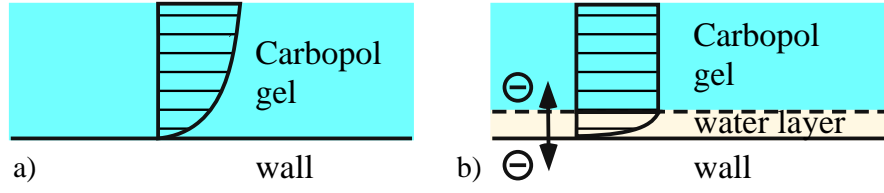Figure 3.3: Viscosity versus shear stress data for a 10% suspension of bentonite. Replotted form Malkin [1995].

Figure 3.4: Velocity of a layer of Carboplol, a) without slip, b) with slip.

When measuring the flow curve, great attention should be paid to avoid slip. If slip occurs, the measured flow curve provides erroneous results. Figure 3.5 shows measurement made by Gregory and Mayers [1993] with and without slip. The result with slip shows a pseudo yield stress and a pseudo Newtonian region which, can lead to a wrong evaluation of the flow curve.
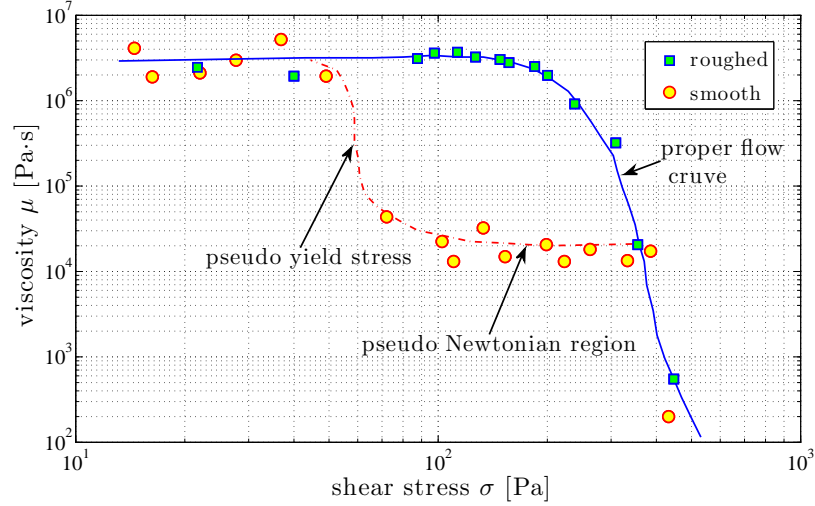

Figure 3.5: Viscosity vs. shear stress for a printing ink, measured in a parallel plate geometry with smooth and roughened pates. Data from Gregory and Mayers [1993].

Slip should be avoided not only when determining the flow curve with the rheometer but also during the experiments on the inclined plane.

Barnes [1995] propose two solutions to avoid slip by altering the physical and chemical character of the walls:

1. By roughening the walls [Barnes and Nguyen, 2001].

2. By coating the walls [Wu and Kwak, 1999].

Yield stress and thixotropy

Coussot et al. [2002] provided evidence for an interplay between yield stress and thixotropy. Møller et al. [2006] concluded that yield stress and thixotropy of a fluid have the same physical origin. The measurement of the yield stress not only depends on the duration of the experiment, but also on the history of the fluid deformation. The following model was proposed

$$\mu = \mu_0(1 + \lambda^n), \tag{3.4}$$

where λ represents the degree of jamming, and satisfies

$$\frac{\mathrm{d}\lambda}{\mathrm{d}t} = \frac{1}{T} - \alpha\lambda\dot{\gamma}, \tag{3.5}$$

where T and α are material dependent constants, $\dot{\gamma}$ the shear rate and t the time.

3.2.2 Methods to measure the yield stress

Even if in the previous section the yield stress has been questioned as a physical property, the concept of a yield stress still remains very useful for a wide range of applications.

From now on, 'yield stress' will refer to the apparent yield stress as defined by Figure 3.2. A practical definition of the yield stress will be given in Section 3.3.1

Yield stress determination by creep test

Figure 3.6 illustrates the results of a sample under creep tests with different stress values. For stress values under the yield stress, the sample is not flowing and the curves overlay and tend to a plateau. The strain increases proportionally to the applied stress values, so the compliance J stays constant. For stresses in excess of the yield stress, the sample flows, and the compliance increases.

Sequential creep measurements are made at selected stress increments. The lowest stress, which leads to a departure form the plateau, defines the yield stress. As already discussed, the integration time is a key factor since the yield stress depends on the measurement time.

Yield stress measurement by stress ramp

Figure 3.7 shows the response of a viscoplastic sample under a stress ramp. Initially the sample acts as an elastic material. The measured viscosity appears to
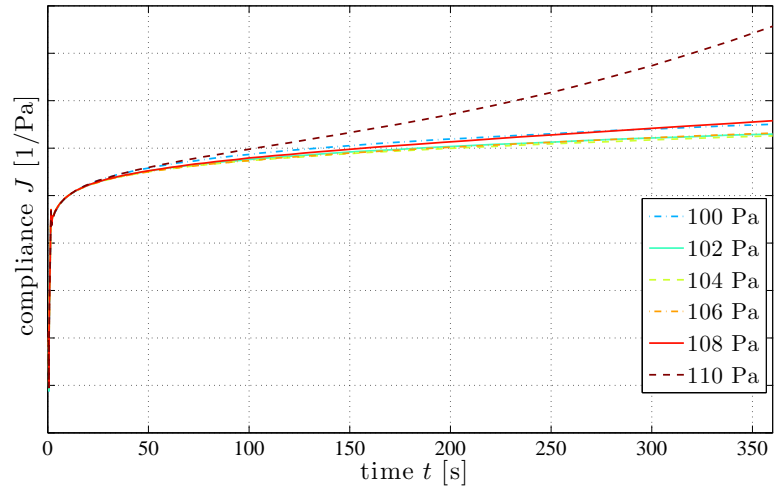
Figure 3.6: Creep test of Carbopol Ultrez 10 at a concentration of 0.4%. The yield stress is between 108 and 110 Pa. The test was preformed with the Couette rheometer described in Section 3.3.2.

increase, as more stress is applied to the sample, the more the sample resist. Once the yield stress is reached, the sample starts to flow and the viscosity falls rapidly. The stress measured at the peak of viscosity can be described as the yield stress of the sample.

Mendes and Dutra's method (2004)

Mendes and Dutra [2004] proposed another method, which involves plotting

$$\frac{\mathrm{d}\ln\tau}{\mathrm{d}\ln\dot\gamma} = \frac{\dot\gamma}{\tau}\frac{\mathrm{d}\tau}{\mathrm{d}\dot\gamma}, \tag{3.6}$$

as a function of τ. The yield stress position is given by a sharp peak in the curve. An example is provided in Figures 3.8 and 3.9.
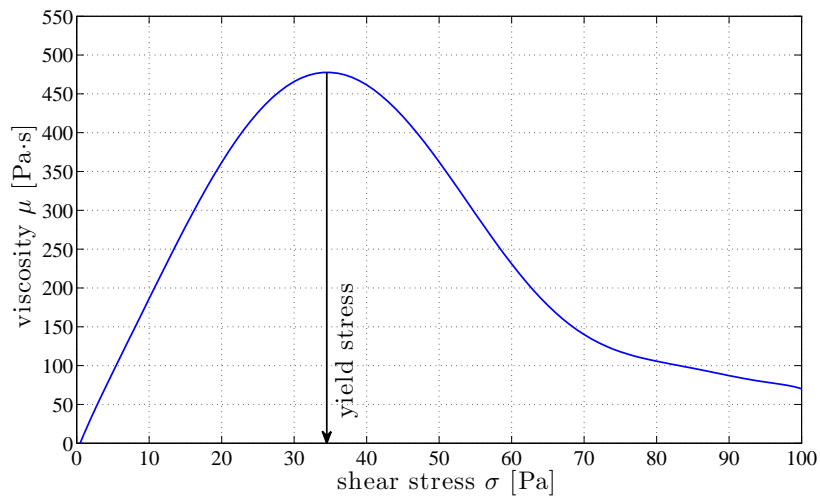
Figure 3.7: Sketch of the determination of the yield stress using a stress ramp. The yield stress is determined by the peak of viscosity. Here the yield stress is equal to 34 Pa.
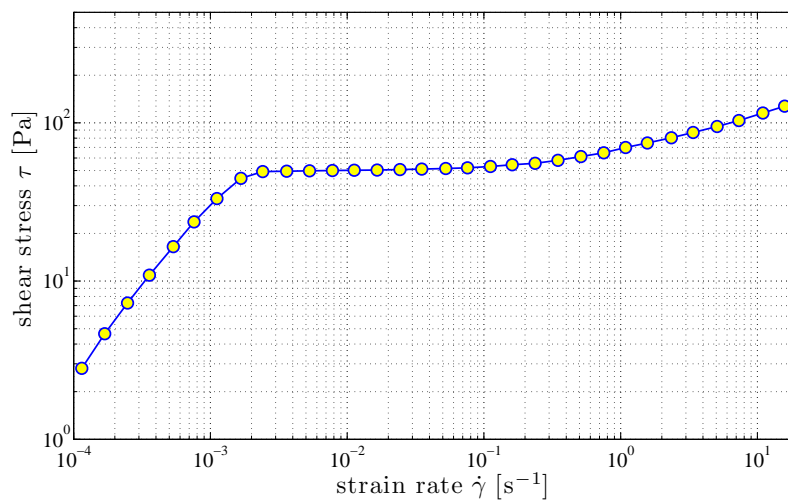

Figure 3.8: Flow curve of Mayonnaise sample. After Mendes and Dutra [2004].
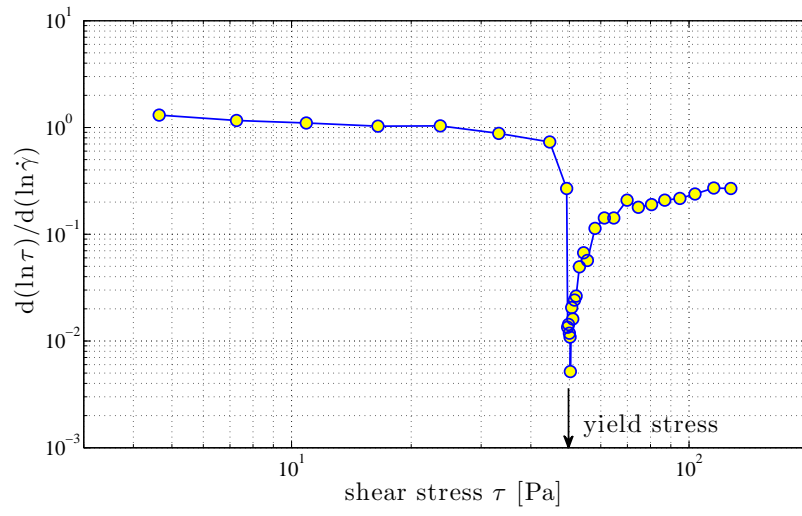
Figure 3.9: Estimation of the yield stress of a Mayonnaise sample (see Figure 3.8). After Mendes and Dutra [2004].

3.3 Rheology of Carbopol Ultrez 10

The rheological proprieties of Carbopol depend on

- the concentration of Carbopol;

- the pH of the solution;

- the 'quality' of the water, e.g., ions concentrations;

- the fluid preparation. A technical description of how both fluids, the Carbopol gel and the glucose syrup, were prepared can be found in Appendix A.

Carbopol was used at four different concentrations during this study. Table 3.3 summarizes the concentration of the different components used and presents the parameters of the Herschel-Bulkley model.

Concentration	0.25%	0.30%	0.35%	0.40%
Ultrez 10 [gr]	150.00±0.05	180.00±0.05	210.00±0.05	240.00±0.05
NaOH [gr]	62.20±0.05	74.64±0.05	87.09±0.05	99.53±0.05
H_2O [kg]	59.79±0.04	59.07±0.04	58.92±0.04	58.77±0.04
Solution [kg]	60.00±0.04	60.00±0.04	60.00±0.04	60.00±0.04
τ_c [Pa]	78±1	89±1	102±1	109±1
K [Pa·s^{-n}]	32.1±2.3	47.68±1.7	58.91±1.7	75.84±1.9
n [-]	0.388±0.023	0.415±0.021	0.505±0.027	0.579±0.033

Table 3.1: Rheological results for the different Carbopol concentrations used during this study.

Sodium Hydroxide Anhydrous Pellets RPE-ACS-ISO[4] were used as NaOH, and demineralized water as H_2O.

3.3.1 Measurement of the yield stress

After having used different protocols to measure the yield stress, it appeared that the *creep test* was the best choice to determine the value of the yield stress. It has been seen in Section 3.2.1 that the value of the yield stress depends on the measurement time. Here the integration time is set arbitrary to 6 min. In this study, the value found after 6 minutes defines the 'yield stress'.

The test is conducted as follows, using a coaxial cylinder geometry:

---

[4]provided by Reactolab SA, Servion, Switzerland

- the sample is sheared under a constant stress for 6 minutes and the curve compliance J/time t is recorded;

- the same test is repeated with higher stresses until the curve diverges from the previous ones. The stress increment is 1 Pa.

Figure 3.6 shows the results of a series of creep tests for a sample of Carbopol at a concentration of 0.40% (only the pair values of the stress are presented in order to reduce the number of curves and facilitate the reading of the figure).

3.3.2 Couette rheometer

To determine the flow curve of the viscoplastic gel a Couette flow rheometer was used (see Figure 3.10).
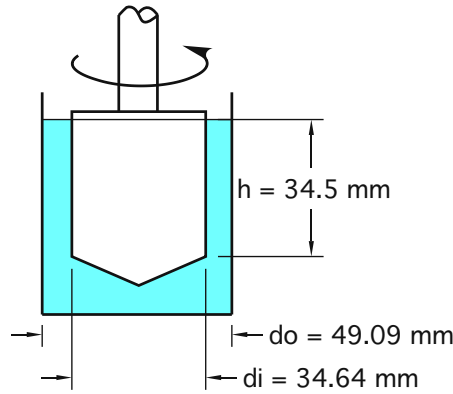
Figure 3.10: Coaxial cylinder rheometer.

The imposed stress started 10 Pa over the yield stress and covered one order of magnitude by step of 2 Pa.

Inverse problem

The Couette inverse problem can be express as

$$\omega(\tau) = (A\dot{\gamma})(\tau) = \frac{1}{2} \int_{\beta\tau}^{\tau} \frac{\dot{\gamma}(S)}{S} \mathrm{d}S, \qquad (3.7)$$

where $\beta = r_i/r_o$ is the ratio of the radius of the inner and outer cylinders, A the integral operator and $S(r) = \tau(r_i/r)^2$ represents the distribution of shear rate.

To recover the shear rate $\dot{\gamma}$ from the rotational velocity $\omega(\tau)$ a least-square approach is used. Instead of solving $\omega = A\dot{\gamma}$, an attempt is made to minimize

the residual $\|\omega - A\dot{\gamma}\|$, usually with an additional constraint on the norm of $\|\dot{\gamma}\|$ or its derivative, to control the smoothness of the solution. We used Tikhonov's regularisation method proposed by Yeow et al. [2000] and modified by Ancey. The advantages of this method are its robustness against computation inaccuracies and measurement errors, its versatility, its fast convergence when the function to be recovered behaves reasonably well, and the relative facility of its implementation. The drawbacks are that it relies on an arbitrary selection of the regularization operator (even though specific procedures have been established [Calvetti et al., 2000]) and its limited capacity to retrieve irregular functions. Figure 3.11 shows 3 flow curves for Carbopol at a concentration of 0.3% obtained with 3 different regularization operators.
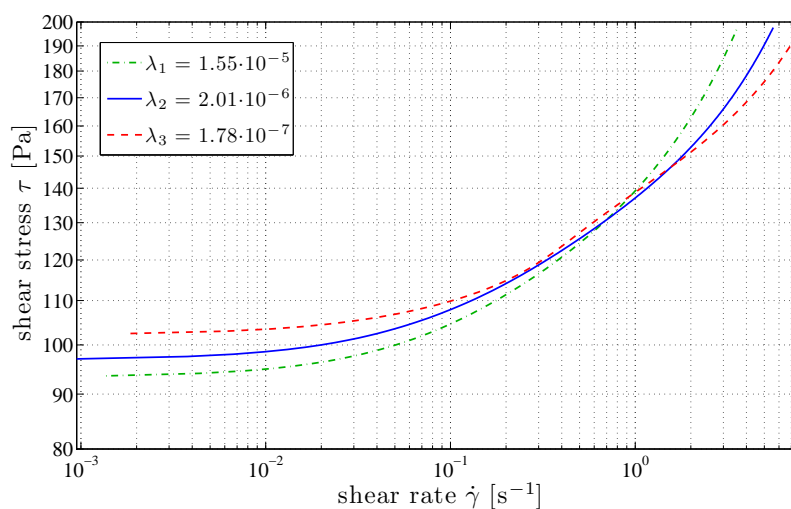
Figure 3.11: Flow curves obtained with different regularisation operator λ.

3.3.3 Herschel-Burkley

To determine the parameters τ_c, K and n of the Herschel-Bulkley model

$$\tau = \tau_c + K\dot{\gamma}^n, \tag{3.8}$$

τ_c was set to the value determined by the creep test while k and n were computed using a least-square approach. Figure 3.12 gives an example of results obtained for Carbopol Ultrez 10 at a concentration of 0.30%:

- dashed line: the results form the Couette rheometer using Tikhonov's regu-
  larisation;

- dash-dot line: the best fit with the parameters τ_c, K and n free ($\tau = 96.78 + 47.87\dot{\gamma}^{0.5435}$;

- solid line: the best fit when τ_c is fixed ($\tau = 90.02 + 47.65\dot{\gamma}^{0.4459}$).
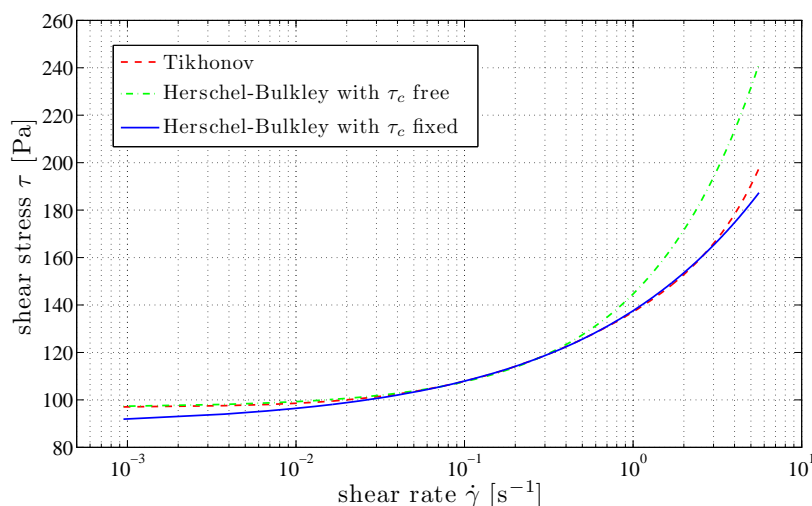

Figure 3.12: Herschel-Bulkley model for a sample of Carbopol at a concentration of 0.30%.

3.3.4   Slip condition

Slip can ruin our results, both in our search for a reliable flow curve and during the dam-break experiments.

Slip on the rheometer

Ultrez 10 slips on smooth steel sufrace such as the rheometer tools. To ensure a no-slip condition on the surface of the cylinders, both inner and outer cylinders were covered with water resistant sandpaper 180.

Coating the cylinder with PVP K-90[TM] high-molecular-weight polyvinyl-pyrrolidone from International Specialty Products, Inc.[5] as recommended by Wu et al. [1999], had proved, in our case, to be disastrous. Not only the flow curves obtained were below the ones given with the sandpaper, but they were also fluctuating.

---

[5]provided by ISP Switzerland AG, Baar, Switzerland

A 6-blade vane also proved not to be the solution. The vane drilled a hole in the sample and once the hole created, the Carbopol could not fill it back in because of its yield stress.

The use of sandpaper with the parallel plates geometry were tested, but with poor results. The accuracy of the gap is a key factor in the parallel plate geometry and the sandpaper made its measurement difficult. With calibration oil the measurement error was about 20%.

Slip on the inclined plane/channel

The inclined plane was made of a 6-mm-thick aluminium plate. The channel was built with PVC. Carbopol Ultrez 10 slips on both material. To get rid of slip on the experimental setup,

- the aluminium inclined plane was painted with Krautol Zink- und Alugrund 3363 paint[6];

- the PVC channel was first coated with Dupli-Color Plastic Primer[7] before being painted with Krautol Zink- und Alugrund 3363 paint in order to have the same surface as on the inclined plane.

To check that no slip is taking place during the dam-break experiment, a sample of Carbopol was placed on the surface of plane/channel, outside the measurement area and above a coloured line and let for the duration of the test. If the sample had not moved during the test we can be confident that no wall repellency occurred. For 3 runs, we measured slip. The corresponding tests were deleted and redone.

3.3.5   Thixotropy

To evaluate thixotropy, a typical hysteresis loop test has been performed; a linear shear rate ramp is applied from zero to a maximum value and then is inversed to return to zero. This procedure is then repeated again and again until a constant loop behaviour is obtained. The area between the upper and lower curve is a measure of thixotropy. Figure 3.13 shows the 1st response to the up-ramp and 6th one to the down ramp for a 120-s ramp and a 180-s ramp. Barnes [1997] resumes this procedure: "a test where both shear rate and time are changed simultaneously, on a material where the response is itself a function of both shear rate and time–as thixotropy obviously is–is bad experimentation, because the response cannot then be resolved into the separate effects arising from both variable". Nevertheless, it can be observed that the curves are close to each other (within the measurement

---

[6]provided by Selma AG, Schwerzenbach, Switzerland
[7]provided by Motip Dupli AG, Volketswil, Switzerland

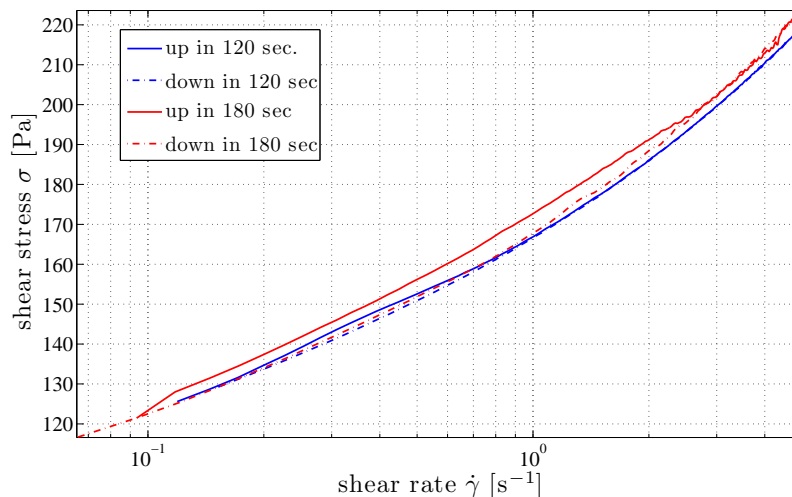error) and that the loop area is small which in turn shows that Carbopol Ultrez 10 is non-thixotropic.

Figure 3.13: Hysteresis loops for carbopol Ultrez 10 at a concentration of 0.30%. The up-curve represent the first response to an increasing shear ramp while the down-curve the response to the sixth decreasing shear ramp.

A second test consists of a 10-s creep test followed by a recovery period done with a 40-mm serrated parallel plate geometry to reduce inertia. The applied stress is above the yield stress. The time to reach equilibrium gives an indication on the thixotropy of the sample. Figure 3.14 shows a 120 and a 150-Pa creep test for a sample of Ultrez 10 at a concentration of 0.30%. The equilibrium is reached, for both tests, in approximately 1 s when the stress is applied and in less than 1 s when the stress is removed. The short time to reach equilibrium shows that Carbopol is non-thixotropic.
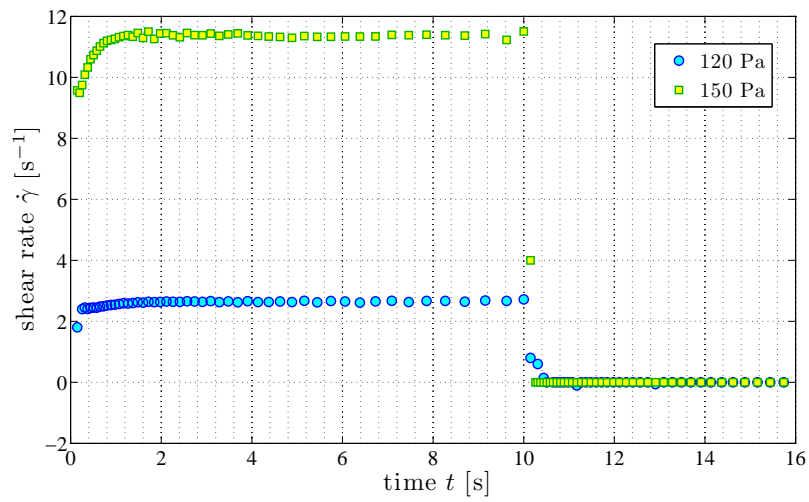
Figure 3.14: Creep test and recovery period on a sample of Carbopol with a 40-mm serrated parallel on a sample of Carbopol at a concentration C of 0.30%.

3.4 Conclusion

This study focuses on the behaviour of viscoplastic fluids down steep slopes as is a common model to describe rapid gravity driven geophysical flows. Viscoplastic materials typically behave as single-phase fluids on the macroscopic scale and exhibit a viscous behaviour after yielding.

Two fluids were tested:

- glucose syrup as a typical Newtonian fluid;

- Carbopol Ultrez 10 as a viscoplastic gel.

Even if the yield stress concept had been demonstrated erroneous, the viscoplastic approach is still valuable if the range of shear rate encountered in the flow is within the same range of shear rate used to derive the material rheological characteristics. During a dam break, the flow experiences different regimes, as explained in Chapter 4. The shear rates during these different flow regimes are within the range of the shear rate measured with the rheometer, except during the run-out regime. The run-out regime is characterized by low velocity and shear stress comparable with the extrapolated value of the yield stress. During the run-out regime channelization process occurs and a better model could be obtained by a better understanding of the physical mechanisms leading to yield stress, e.g., by introducing a thixotropy formulation.

To guaranty the quality of the results on the inclined plane and of the rheometer, slip on the bottom walls has to be avoided. To ensure a no-slip condition on the surface of the rheometer cylinders, both inner and outer cylinders were covered with water resistant sandpaper 180. Slip was prevented from the inclined plane and channel by coating the wall with a special painting.

CHAPTER 4

Dam breaks

THE dam break experiment is the prototypical flow configuration used for investigating gravity-driven flows. The dam break consists in the sudden release of a given volume of material down a slope. A precisely measured amount of fluid is placed in a reservoir at the top of an inclined plane. The fluid is then suddenly released by the instantaneous opening of the dam's gate and flows down the inclined plane, as sketched in Figure 4.1. The initial conditions (volume of fluid, rheological characteristics, density, etc) and the boundary conditions (slope angle, surface roughness, topography) of the dam break can easily be imposed.

Essentially, our idea was to test the dam break equations under extreme conditions in a well-controlled environment—the laboratory—where both the initial and boundary conditions are prescribed. Here, 'extreme conditions' means that we focus our attention on time-dependent flows (surges with a front) mobilizing Newtonian or non-Newtonian fluids, experiencing different stages from release to run-out: acceleration (balance between inertia and pressure gradient), a nearly fully developed regime (flow at equilibrium), and deposition (predominance of dissipation processes).
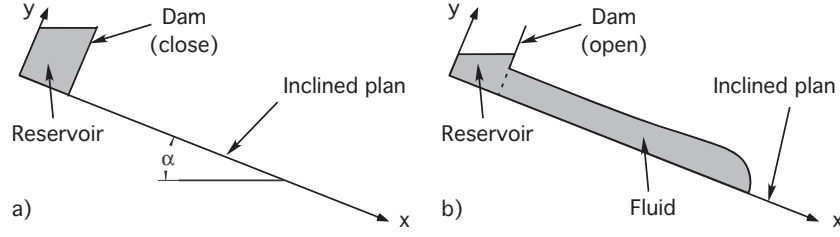
Figure 4.1: Dam break model, a) the gate is closed and the fluid is contained by the reservoir, b) the dam is opened and the fluid flows down the inclined plan.

4.1   Introduction

A growing number of models based on the shallow-water equations are currently used to describe natural flows such as flash floods [Hogg and Pritchard, 2004], floods with sediment transport [Pritchard, 2005], snow avalanches [Bartelt et al., 1999], debris flows [Iverson, 1997, Huang and García, 1997], lava flows [Griffiths, 2000], subaqueous avalanches [Parker et al., 1986]. The shallow-water equations were originally worked out by Saint Venant [1871] to compute flood propagation along rivers. Their use was gradually extended to strongly time-dependent flows such as waves induced by a dam break [Ritter, 1892]. In the derivation of these models, a number of assumptions are used, the most important of which are: the long-wave approximation (no significant curvature of the free surface), hydrostatic pressure, blunt velocity profile, and no change in the bulk composition or rheology. Furthermore, in these models, the bottom shear stress is computed using either empirical expressions (e.g., Chézy friction) or non-Newtonian constitutive equations, with the difficult question of parameter estimation remaining.

The Saint-Venant equations are composed, in their non-conservative form, of:

- a continuity equation:

$$\frac{\partial h}{\partial t} + \frac{\partial hu}{\partial x} = 0$$

- a momentum equation:

$$\underbrace{\frac{\partial u}{\partial t} + u\frac{\partial u}{\partial x}}_{\text{inertia}} = \underbrace{g\sin\alpha}_{\text{gravity}} - \underbrace{g\cos\alpha\frac{\partial h}{\partial x}}_{\substack{\text{pressure} \\ \text{gradient}}} + \underbrace{\frac{\tau_p}{\rho h}}_{\substack{\text{rheological} \\ \text{behaviour}}}$$

where: $h(x,t)$ is the height of the flow, $u(x,t)$ the velocity of the flow in function of position x and time t. g is gravity acceleration, ρ is the density of the fluid,

α the angle path and $\tau_p(u, h)$ is a friction law, which depends on u and h. Many empirical laws were proposed to relate τ_p with the flow variables u and h depending on the rheological behaviour.

In the dam break problem, a slide of viscoplastic material can be broken down into a plug zone, or unsheared zone, in the upper part of the flow where the material behaves as a solid and a sheared layer, in the lower part where the material yields and behaves as a liquid. The plug zone slides along the shear layer on the 'yield surface'. We can identify three flow regimes, as sketched in Figure 4.2:

- The inertial regime [Figure 4.2 (a)]: the dominant balance is between inertia and pressure gradient: $\rho \frac{\partial u}{\partial t} \sim \frac{\partial h}{\partial x}$. The bulk mass presents a strong curvature and most of the mass is sheared and behaves as a liquid. Rheological behaviour is of lower importance.

- The hydrodynamic regime [Figure 4.2 (b)]: the dominant balance is between gravity acceleration and viscosity: $\tau_p \sim \rho g h \sin \alpha$. The flow has slowed down and the variations of velocity are small, the inertial term can be neglected. Liu and Mei [1990] explained how the yield stress, in steady flow, affects the free surface profile.

- The run-out regime [Figure 4.2 (c)]: the dominant balance is between pressure gradient and viscosity (and sometimes the gravity acceleration): $\tau_p \sim \rho g h \frac{\partial h}{\partial x}$ [Coussot et al., 1996]. Matson and Hogg [2007] predicted that the final arrested state is approached asymptotically, i.e., never stops.
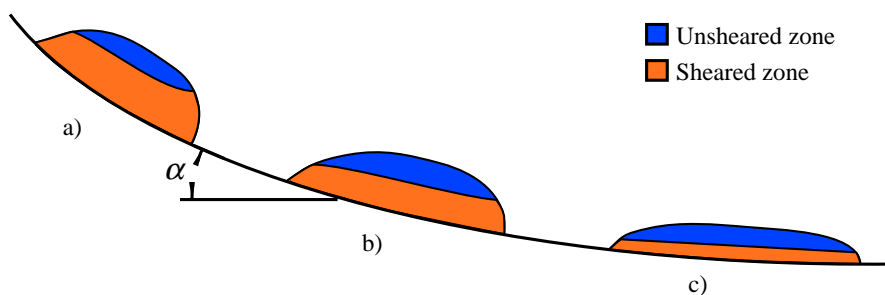
Figure 4.2: Three flow regimes can be identified: a) inertial regime, b) viscosity regime and c) run-out regime

.

Piau [1996] claimed that the Saint-Venant equations were not valid at the front because the assumption of low curvature of the free surface is no longer valid. He proposed a new model, which predicts that the front is always totally sheared, as shown in Figure 4.3, except when it comes to a rest.
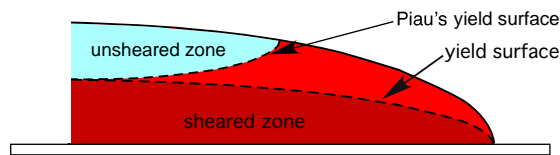
Figure 4.3: Piau's model: the front zone is sheared due to 3D effects.

Although the Saint-Venant equations, adapted to geophysical flows, provide sound results conceerning the spreading rate and bulk velocity, when the slope angle is small ($<5°$), they are not suited to explain the dynamics of free-surface flows down slopes with higher angles. They are also not suited to predict the first instants of the flow just after the break of the dam.

The theoretical approach, based on the Saint-Venant equations, has proven to be valuable, but is not sufficient to explain the dynamics of gravity-driven-flows. In order to develop new analytical and numerical models, we need to better understand the phenomena and one way to achieve this goal is to measure the free-surface of the flow as well as its spreading rate.

In this chapter, theoretical results will first be recalled starting from the local governing equations (see Section 4.2.1). A classification of different flow regimes is then discussed in Section 4.2.5. Solutions of the dam break problem are given for Newtonian fluids in viscous regime in Section 4.2.7 and for Herschel-Bulkley fluid in Section 4.2.8. For fast flows, when no dominant balance takes place between the different forces, the flow-depth averaged equations are used and described, for Newtonian fluids in in Section 4.2.10 and for Herschel-Bulkley fluids in Section 4.2.11. The experimental results are finally presented, for Newtonian fluids in a channel in Section 4.4, for Carbopol down a channel in section 4.5 and for Carbopol down an inclined plane in Section 4.6.

Experiments

Few experimental setups were built to measure the profile depth and the spreading rate of non-Newtonian fluids down inclined plane or channel. Different setups of different size and shape were built to measure the flow profile of non-Newtonian materials in steady or unsteady regime. Some examples included:

- The United States Geological Survey (USGS) built a 95-m-long, 2-m-wide, and 1.2-m-deep flume with a 31° slopes [Iverson et al., 1992]. Up to 20 m^3 of material placed behind a steel gate could be released. The flow depth was measured ultrasonically at given places along the flume;

- Iverson et al. [2004] also used a 1-m long, 0.2-m wide flume with two distinct

topographies to release 300 cm^3 of sand at a slope angle of 31.6°. Parallel laser sheets measured the deformation along lines;

- Chanson et al. [2006] used a 2-m long, 0.34-m wide flume with a slope of 15° to test up to 4 kg of thixotropic fluids. The free-surface elevation was measured using a CCD camera and a series of laser sheets;

- Debiane [2000] used a 3-m long, 30-cm wide canal to test viscoplastic material in the dam break problem. The height of the surge is measured using ultrasonic devices while the position of the front is recorded using a high speed camera mounted on a carriage;

- Kern et al. [2004] used a 34-m-long, 2.5-m-wide canal to test the rheology of snow. The velocity profile was measured using optoelectrionic sensors.

  Some natural site were also equipped with monitoring systems to acquire data on avalanche features (e.g., velocity, flow depth, mass balance). The Ryggfon site in Norway (managed by the Norwegian Institute of Geotechnics) and the Vallée de la Sionne in Switzerland (managed by the Schnee und Lawinen Forschung institute at Davos) are typical examples of field test sites in Europe to test snow avalanches. Acquiring data on high-speed phenomena remains a challenge. Classic methods such as image processing techniques give useful information on the shape and velocity of the avalanche, but cannot track the internal structure. Non-intrusive methods (e.g., Doppler radar) give access to it, but their signals remain inextricably difficult to decipher. Static sensors for measuring impact pressure or snow density are also of common use, but yield information at fixed places and their signals are also difficult to interpret.

4.2   Dam breaks

The dam break consists in the sudden release of a given volume of material down a slope. In this section we will describe two-dimensional models for the dam breaks of Newtonian and viscoplastic fluids. We will first recall the governing equations and the assumptions made to solve the problem using two different approaches:

- the slow motion approach, for hydrodynamic regimes [Balmforth et al., 2002, Liu and Mei, 1990, Nakaya, 1975];

- the Saint-Venant approach, with a depth-averaged formulation of the equations [Hunt, 1982, Huang and García, 1997, Piau, 1996].

4.2.1   Governing equations

The local governing equations are given by the Navier-Stokes equations, which are composed of a continuity equation:

$$\frac{\partial u}{\partial x} + \frac{\partial v}{\partial y} = 0, \tag{4.1}$$

and momentum equations:

$$\rho \left(\frac{\partial u}{\partial t} + u\frac{\partial u}{\partial x} + v\frac{\partial u}{\partial y} \right) = \rho g \sin\theta - \frac{\partial p}{\partial x} + \frac{\partial^2 u}{\partial x^2} + \frac{\partial^2 u}{\partial y^2}, \tag{4.2}$$

$$\rho \left(\frac{\partial v}{\partial t} + u\frac{\partial v}{\partial x} + v\frac{\partial v}{\partial y} \right) = -\rho g \cos\theta - \frac{\partial p}{\partial y} + \frac{\partial^2 v}{\partial x^2} + \frac{\partial^2 v}{\partial y^2}. \tag{4.3}$$

The variation of height h can be computed by integrating Equation 4.1:

$$\int_{y=0}^{h} \left(\frac{\partial u}{\partial x} + \frac{\partial v}{\partial y} \right) \mathrm{d}y = 0.$$

From this equation and the boundary condition equations (see Equation 4.7), the variation of height h becomes:

$$\frac{\partial h}{\partial t} + \frac{\partial h\overline{u}}{\partial x} = 0, \tag{4.4}$$

where $\overline{u} = \int_{y=0}^{h} u(x,\ y,\ t)\mathrm{d}y/h$ is the mean velocity through a flow section. To close this, $\bar{u}$ must be determined.

With the boundary conditions, the momentum equations can also be computed, the results are given by Equation 4.33 and 4.34 for Herschel-Bulkley fluids.

4.2.2   Initial conditions

At the start of the test the fluid is at rest in the reservoir (see Figure 4.4), the initial condition takes the following form:

$$h = H[1 - (L - x)\sin(\alpha)] \text{ and } u = 0 \text{ for } 0 \le x \le L, \tag{4.5}$$

$$h = 0 \text{ and } u = 0 \text{ for } x > L, \tag{4.6}$$

$h_0 = h(L/2)$ is the height the flow would have in an horizontal reservoir.

The continuity equation becomes:

$$\int_{0}^{x_f} h(x,\ t)\mathrm{d}x = Lh_0,$$

where x_f is the front position.
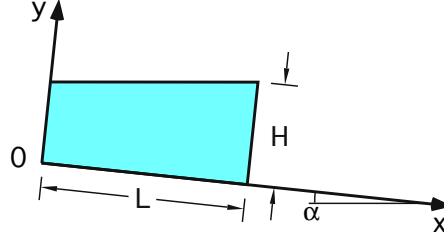
Figure 4.4: Initial conditions.

4.2.3 Boundary conditions

In the dambreak problem, the boundary conditions take the following form:

- at the free surface:

$$v|_h = \frac{\mathrm{d}h}{\mathrm{d}t} = \frac{\partial h}{\partial t} + u|_h \frac{\partial h}{\partial t}; \tag{4.7}$$

- at the bottom, $y = 0$: $u = v = 0$.

The stress equilibrium at the boundary is given by:

$$-p_a\mathbf{n} + (-p\mathbf{1} + \boldsymbol{\sigma}) \cdot \mathbf{n} + \gamma\frac{1}{R}\mathbf{n} = 0, \tag{4.8}$$

where $\mathbf{n} = (-\partial_x h, \ 1)/\sqrt{1 + (\partial_x h)^2}$ is the normal vector to the free-surface, p_a the atmospheric pressure, $R = \partial_{xx} h/[1 + (\partial_x h)^2]^{3/2}$ the radius of curvature, γ the surface tension, $\boldsymbol{\sigma} = 2\mu[\nabla\mathbf{u}]$ the stress tensor where $[\nabla\mathbf{u}]$ is the symmetric part of the velocity gradient, and ∂_x denote the partial derivative $\frac{\partial}{\partial x}$. We assume that the surrounding air does not interact with the flow. The boundary conditions lead to:

- a condition on the normal component of the stress:

$$-p_a - (-p\mathbf{n} + \boldsymbol{\sigma} \cdot \mathbf{n}) \cdot \mathbf{n} + \gamma\frac{1}{R} = 0,$$

  which becomes

$$p - p_a + \gamma\frac{\partial_{xx} h}{[1 + (\partial_x h)^2]^{\frac{3}{2}}} - \frac{2\mu}{1 + (\partial_x h)^2}\left[\partial_y v + (\partial_x h)^2 \partial_x u - \partial_x h(\partial_y u + \partial_x v)\right] = 0; \tag{4.9}$$

- a condition on the tangential component of the stress:

$$(-p\mathbf{n} + \boldsymbol{\sigma} \cdot \mathbf{n}) \cdot \mathbf{t} = 0$$

with $\mathbf{t} = (1, \ \partial_x h)/\sqrt{1 + (\partial_x h)^2}$ the vector tangent to the free surface,

$$[1 - (\partial_x h)^2](\partial_x v + \partial_y u) + 2\partial_x h(\partial_y v - \partial_x u) = 0. \qquad (4.10)$$

Surface tension can be neglected when the curvature is small, or when its effects are small compared to the fluid pressure.

4.2.4   Dimensionless formulation

In this section the following dimensionless variables will be used:

$$\hat{u} = \frac{u}{U}, \quad \hat{v} = \frac{v}{V}, \quad \hat{x} = \frac{x}{L}, \quad \hat{y} = \frac{y}{H}, \quad \hat{t} = \frac{t}{T} = \frac{t}{L/U}, \quad \hat{p} = \frac{p}{\rho g H \cos(\alpha)}.$$

In addition to the length scale ratio ϵ, we introduce the following dimensionless numbers: the *flow Reynolds number* Re, the *Froude number* Fr and the *capillarity number* Ca:

$$\epsilon = \frac{H}{L}, \qquad \mathrm{Re} = \frac{UH}{\mu/\rho}, \qquad \mathrm{Fr} = \frac{U}{\sqrt{gH\cos\theta}}, \quad \text{and} \quad \mathrm{Ca} = \frac{\mu U}{\gamma}.$$

We also introduce the *Kapitza number* Γ as the ratio between the surface tension γ/R and the kinematic pressure:

$$\Gamma = \frac{\gamma}{R}\frac{1}{\rho U^2} = \frac{\gamma}{\rho U^2 H} = \frac{1}{\mathrm{ReCa}}.$$

Governing equations

Substituting the dimensionless variables into the governing equations leads to:

$$\frac{\partial \hat{u}}{\partial \hat{x}} + \frac{\partial \hat{v}}{\partial \hat{y}} = 0, \qquad (4.11)$$

$$\epsilon \mathrm{Re}\frac{\mathrm{d}\hat{u}}{\mathrm{d}\hat{t}} = \frac{\mathrm{Re}}{\mathrm{Fr}^2}\left(\tan\theta - \epsilon\frac{\partial \hat{p}}{\partial \hat{x}}\right) + \epsilon^2\frac{\partial^2 \hat{u}}{\partial \hat{x}^2} + \frac{\partial^2 \hat{u}}{\partial \hat{y}^2}, \qquad (4.12)$$

$$\epsilon^2 \mathrm{Re}\frac{\mathrm{d}\hat{v}}{\mathrm{d}\hat{t}} = -\frac{\mathrm{Re}}{\mathrm{Fr}^2}\left(1 + \frac{\partial \hat{p}}{\partial \hat{y}}\right) + \epsilon^3\frac{\partial^2 \hat{v}}{\partial \hat{x}^2} + \epsilon\frac{\partial^2 \hat{v}}{\partial \hat{y}^2}. \qquad (4.13)$$

4.2.5   Flow regimes

The momentum equation expresses a balance between gravity acceleration, inertial terms, pressure gradient, and viscous dissipation, whose order of magnitude are, respectively, $\rho \sin\alpha$, $\rho U^2/L$, p/L and $\eta U/H^2$. Depending on the dominant balances between those terms different flow regimes occur. We describe here four regimes which can be achieved:

1. *Inertial regime*, the dominant balance is between inertia and pressure gradient. We then have
$$U = \sqrt{gH \cos \alpha}.$$
The regime occurs when: $\epsilon \mathrm{Re} \gg 1$ and $\mathrm{Fr} = O(1)$. In this regime, the rheological effect can be neglected and the governing equations become the Euler equations.

2. *Viscous regime*, the dominant balance is between pressure gradient and viscous stresses within the bulk. We obtain
$$U = \frac{\rho g \cos \alpha H^3}{\eta L}.$$
Inertial terms must be low compared to the pressure gradient and the slope must be shallow ($\tan \alpha \ll \epsilon$). This imposes the following constraint: $\epsilon \mathrm{Re} \ll 1$ and $\mathrm{Fr}^2 = O(\epsilon \mathrm{Re}) \ll 1$. This regime is achieved for slow flows on gentle slopes ($\alpha \ll 1$). This regime will be further described in Section 4.2.6.

3. *Visco-inertial regime*, where inertia and viscous contributions are nearly equal. In this case we have
$$U = \frac{1}{\epsilon} \frac{\eta}{\rho H}.$$
The pressure gradient has to be low compared to the viscous stress, which entails the following conditions $\eta \gg \epsilon \rho \sqrt{gH^3}$. We then have $\epsilon \mathrm{Re} \sim 1$ and $\mathrm{Fr} = \eta/(\rho \epsilon \sqrt{gH^3}) \gg 1$.

4. *Hydrodynamic regime*, where the dominant balance is between viscous contributions and gravity acceleration. We obtain
$$U = \frac{\rho g \sin \alpha H^2}{\eta}.$$
Inertia must be negligible, which means that $\epsilon \ll 1$. We then have $\mathrm{Re} = O(\mathrm{Fr}^2)$ and $\tan \alpha \gg \epsilon$.

This classification of regimes into four groups holds for Newtonian fluids. It can also describe non-Newtonian flows for which the bulk viscosity does not vary significantly with shear rate over a sufficiently wide range of shear rate. If the latest assumption is not valid, further dimensionless groups (e.g., the *Bingham number* $\mathrm{Bi} = \frac{\tau_c F}{\mu U}$) must be introduced, which results in a more complex classification.

Analytical solutions can be computed for some regimes. In Section 4.2.6, solutions for the viscous regime are discussed. When there is no dominant balance,

the full governing equations have to be solved, which is a difficult task, even numerically (see Section 4.2.12). To simplify the problem, the flow-depth averaged equations can be used. The nearly steady-state regime is discussed in Section 4.2.9.

In this study, the experimental results are compared with:

- the viscous regime solutions in the case of horizontal channel for both Newtonian and viscoplastic fluids (see Section 4.4 for Newtonian fluids and Section 4.5.1 for viscoplastic gels);

- the flow-depth averaged solution in the case of an inclined channel for both Newtonian and viscoplastic fluids (see Section 4.4 for Newtonian fluids and Section 4.5.2 for viscoplastic gels) and a viscous regime solution for Newtonian fluids.

- computational fluid dynamics (CFD) results in the case of dam breaks on an inclined plane (see Section 4.6 for viscoplastic gels).

4.2.6   Viscous regime

In the viscous regime we have: $O(\text{Re}) = O(\text{Fr}) = 1$, which is satisfied if we take $U = gH^2 \sin \alpha/(\mu/\rho)$, with $\alpha \neq 0$. To order ϵ^0, we get:

$$\frac{\partial^2 \hat{u}}{\partial \hat{y}^2} = -1, \tag{4.14}$$

$$\frac{\hat{p}}{\hat{y}} = -1, \tag{4.15}$$

with $\hat{p} = 0$ at the free surface. Returning to physical variables, we have

$$u(x,\, y,\, t) = \frac{\rho g \sin \theta}{2\mu} y(2h - y), \tag{4.16}$$

$$v(x,\, y,\, t) = 0, \tag{4.17}$$

$$p(x,\, y,\, t) = \rho g \cos \theta (h - y), \tag{4.18}$$

$$\bar{u}(x,\, t) = \frac{1}{3} \frac{\rho g h^2 \sin \theta}{\mu}. \tag{4.19}$$

The equation of motion is then

$$\frac{\partial h}{\partial t} + \frac{\partial h \bar{u}}{\partial x} = 0, \text{or} \tag{4.20}$$

$$\frac{\partial h}{\partial t} + \frac{1}{3} \frac{\rho g \sin \theta}{\mu} \frac{\partial h^3}{\partial x} = 0, \text{or}$$

$$\frac{\partial h}{\partial t} + \frac{\rho g h^2 \sin \theta}{\mu} \frac{\partial h}{\partial x} = 0,$$

which is a non-linear diffusion equation of the form $\partial_t h + c(h)\partial_x h = 0$ with $c(h) = \rho g h^2 \sin\theta/\mu$ or $\partial_t h + \partial_x f(h) = 0$ with $f(h) = \rho g h^3 \sin\theta/(3\mu)$.

4.2.7   Viscous regime solutions for a Newtonian fluid

In 1974, Nakaya [1974] proposed a solution to the dam break problem on gentle slopes for Newtonian fluids with the assumption that surface tension can be neglected. Eight years later, Huppert [1982a] came up with the same solution for horizontal beds which was generalized to slopes the same year [Huppert, 1982b]. His solution have been widely tested over the years [Didden and Maxworthy, 1982, McCarthy and Seymour, 1993]. Debiane [2000] proposed a set of simplified equations for engineering applications: based on Huppert's solution for an horizontal bed, and based on the solution proposed by Hunt [1994] for an inclined bed (see Section 4.2.10).

Nakaya's solution for an horizontal bed

The hydrodynamic regime is reached after a time t_1

$$t_1 = \left(\frac{q^4 \rho^3}{g^2 \mu^3}\right)^{\frac{1}{7}}, \tag{4.21}$$

where q is the flow section, μ the viscosity and ρ is the density of the fluid.

The height of the surge is given by

$$h(x,t) = \eta_f^{2/3}\left(3q^2\frac{\nu}{g}\right)^{\frac{1}{5}}\phi\left(\frac{\eta}{\eta_f}\right)t^{-\frac{1}{5}} \qquad \forall\, x < x_f \tag{4.22}$$

where h is the depth of the surge as shown in Figure 4.5, $\nu = \frac{\mu}{\rho}$ is the dynamic viscosity, and

$$\eta = \left(\frac{1}{3}g\frac{q^3}{\nu}\right)^{-\frac{1}{5}}xt^{-\frac{1}{5}}. \tag{4.23}$$

where η_f is the value of η at $x = x_f(t)$

$$\eta_f = \left[\frac{1}{5}\left(\frac{3}{10}\right)^{\frac{1}{3}}\pi^{\frac{1}{2}}\Gamma\left(\tfrac{1}{3}\right)\Gamma^{-1}\left(\tfrac{5}{6}\right)\right]^{-\frac{3}{5}} \cong 1.411\ldots \tag{4.24}$$

The function $\phi(\chi)$ is illustrated by Figure 4.6 and defines the shape of the free surface

$$\phi(\chi) = \left(\frac{3}{10}\right)^{\frac{1}{3}}\left(1 - \chi^2\right)^{\frac{1}{3}}. \tag{4.25}$$
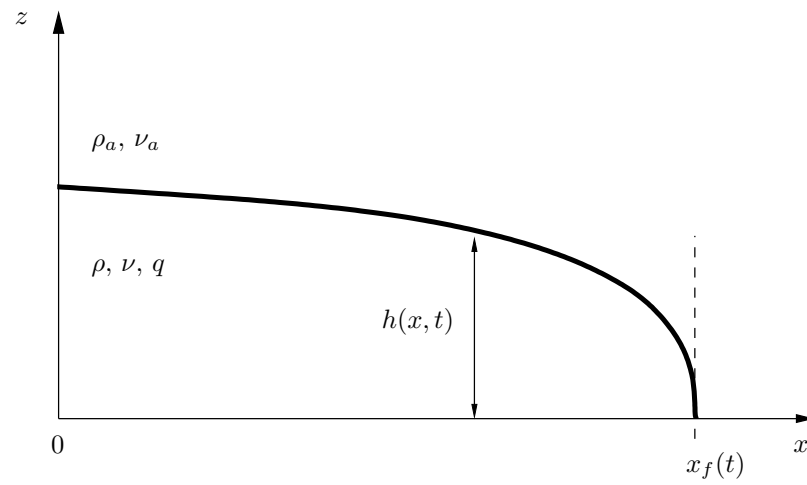
Figure 4.5: Sketch of the flow surge with its coordinate system.
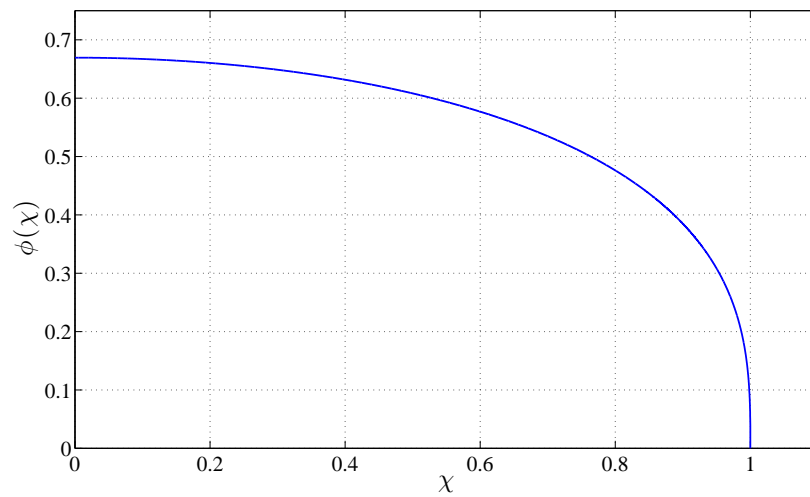
Figure 4.6: The depth profile of viscous flows in dimensionless numbers.

The front position is finally given by:

$$x_f(t) = \eta_f \left(\frac{1}{3}g\frac{q^3}{\nu}\right)^{\frac{1}{5}} t^{\frac{1}{5}}. \tag{4.26}$$

Debiane's solution for an horizontal bed

Debiane made the same assumptions as Huppert, but the resolution is slightly different. The following dimensionless numbers are defined

$$\hat{h} = \frac{h}{H}, \qquad \hat{x} = \frac{x}{L}, \qquad \hat{t} = t\frac{\rho g H^3}{12\mu L^2}, \qquad \hat{x}_f = \frac{x_f}{L} \tag{4.27}$$

with H the flow depth in the reservoir at time $t = 0$ and L the reservoir length along the x-axis (see Figure 4.4). He also defined a new dimensionless Reynolds number:

$$Re = \frac{\rho H^{\frac{5}{2}} g^{\frac{1}{2}}}{\mu L}. \tag{4.28}$$

His solution takes the form

$$\hat{h} = \hat{h}\left(\hat{x}, \hat{t}, Re\right), \qquad \hat{x}_f = \hat{x}_f\left(\hat{t}, Re\right).$$

For a time $\hat{t} > 0.037 + 3.61 \cdot 10^{-4} Re^2$, the front position x_f is

$$\hat{x}_f\left(\hat{t}\right) = 1.862\left(\hat{t} + 0.069 - 3.61 \cdot 10^{-4} Re^2\right)^{\frac{1}{5}}, \tag{4.29}$$

and

$$\hat{h}\left(\hat{x}, \hat{t}\right) = \frac{1}{0.841\hat{x}_f\left(\hat{t}\right)}\left[1 - \left(\frac{\hat{x}}{\hat{x}_f(\hat{(t)})}\right)^2\right]^{\frac{1}{3}} \qquad \forall\, \hat{x} < \hat{x}_f. \tag{4.30}$$

Huppert's solution for an inclined bed

The same assumptions are made as those used for the horizontal bed. The flow profile then takes the form:

$$h(x, t) = \left(\frac{\nu}{g\sin\alpha}\right)^{\frac{1}{2}} x^{\frac{1}{2}} t^{-\frac{1}{2}} \qquad \forall\, x < x_f, \tag{4.31}$$

while the front position is given by

$$x_f(t) = \left(\frac{9q^2 g\sin\alpha}{4\nu}\right)^{\frac{1}{3}} t^{\frac{1}{3}}. \tag{4.32}$$

It should be stressed that the flow profile given by Equation 4.31 ends abruptly at height $h = h_f(t) = 1.5\, q\, x_f^{-1}$ for $x = x_f$, which is physically not correct. To predict the flow profile at the surge front, an equation accounting for the surface tension has to be added. The new set of equations has no analytical solution.

4.2.8   Viscous regime solutions for Herschel-Bulkley fluids

For viscoplastic fluids, the yield surface ($\sigma_{xy} = \tau_c$) separates the flow into two layers: the bottom layer which is sheared ($\sigma_{xy} > \tau_c$) and the upper layer or plug layer ($\sigma_{xy} < \tau_c$). Balmforth and Craster [1999] demonstrated that the shear stress in the plug layer is indeed close to zero but nonzero, which resolves a number of paradoxes raised about viscoplastic solutions [Adams et al., 1997, Lipscomb and Denn, 1984].

The solution given by Balmforth et al. [2007] for viscoplastic dam breaks in horizontal cases is based on the assumption that the flow is sufficiently slow for inertia to be negligible. The governing equations can be reduced to a single equation for the fluid depth $h(x,t)$:

$$\partial_t h = \left(\frac{\rho g}{K}\right)^{1/n} \frac{\partial}{\partial x}\left[\frac{n|\partial_x h|^{1/n-1} Y^{1+1/n}}{(n+1)(2n+1)}\left[(1+2n)h - nY\right]\partial_x h\right], \qquad (4.33)$$

where

$$Y = h - \frac{\tau_c}{\rho g|\partial_x h|}, \qquad (4.34)$$

is a pseudo-yield surface.

The following dimensionless variables are introduced:

$$\hat{x} = \frac{x}{L}, \qquad \hat{z} = \frac{z}{H}, \qquad \hat{h} = \frac{h}{H}, \qquad \hat{Y} = \frac{Y}{H}, \qquad \hat{t} = \frac{t}{\frac{L}{H}\left(\frac{KL}{\rho g H^2}\right)^{1/n}}.$$

and rewrite Equation 4.33 in a non-dimensional form with only two parameters; B and n:

$$\partial_{\hat{t}}\hat{h} = \frac{\partial}{\partial \hat{x}}\left[\frac{n|\partial_{\hat{x}}\hat{h}|^{1/n-1}\hat{Y}^{1+1/n}}{(n+1)(2n+1)}\left[(1+2n)\hat{h} - n\hat{Y}\right]\partial_{\hat{x}}\hat{h}\right] \qquad (4.35)$$

$$\hat{Y} = \hat{h} - \frac{B}{\partial_{\hat{x}}\hat{h}}, \qquad (4.36)$$

and where B is the Bingham number,

$$B = \frac{\tau_c L}{\rho g H^2}. \qquad (4.37)$$

Figures 4.7 gives the numerical solutions of Equation 4.35 for $B = 0.1$ and $n = 1$.
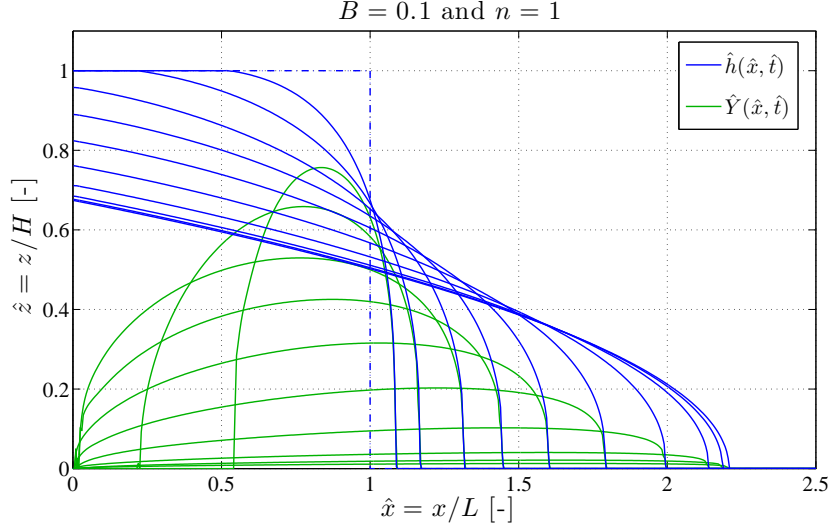
Figure 4.7: Height $\hat{h}$ and pseudo-yield surface $\hat{Y}$, for $B = 0.1$ and $n = 1$. The time $\hat{t} =$0.1, 0.4, 1.6, 3.6, 8, 20, 60, 200, 420, and 720. The dash-dot line show the initial conditions.

4.2.9 Flow-depth averaged equations

To solve fast-moving free-surface problem, a common method is to depth-average the local equation of motions. This method leads to the Saint-Venant equations, also referred to as the boundary layer approximation, the long-wave approximation, or the lubrication approximation. The Saint-Venant approach involves integrating the momentum and mass balance equations over depth. The Saint-Venant equations are composed of

- a continuity equation:

$$\frac{\partial h}{\partial t} + \frac{\partial h\overline{u}}{\partial x} = 0, \tag{4.38}$$

- a momentum equation:

$$\rho\Big(\frac{\partial h\bar{u}}{\partial t} + \frac{\partial h\overline{u^2}}{\partial x}\Big) = \bar{\rho}gh\sin\alpha - g\cos\alpha\frac{\partial h}{\partial x} + \frac{h\partial\bar{\sigma}_{xx}}{\partial x} - \tau_b, \tag{4.39}$$

where: $h(x,t)$ is the height of the flow, $\bar{u}(x,t)$ the depth-average velocity of the flow, $\bar{\rho}$ is the depth-average density, α the slope angle and τ_b is the bottom shear stress. The pressure is to first order hydrostatic:

$$p = \rho g(h - y)cos\alpha.$$

Any depth-averaged function is defined as:

$$\bar{f}(x,t) = \frac{1}{h(x,t)} \int_0^{h(x,t)} f(x,y,t)\mathrm{d}y.$$

To close the system we use the Boussinesq momentum coefficient which links the mean velocity $\bar{u}$ to the mean square velocity

$$\overline{u^2} = \frac{1}{h} \int_0^h u^2(y)\mathrm{d}y = \beta \bar{u}^2, \tag{4.40}$$

where most of the time the parameter β is set to unity.

Analytical solutions can be obtained for the Saint-Venant by seeking self-similar solutions or by the method of characteristics.

4.2.10   Flow-depth average solutions for Newtonian fluids

Debiane's solution for an inclined channel

The solution given by Debiane follows the kinematic-wave approach used by Hunt [1994]. A perturbation method is utilized to work out analytical solution for the body and head (outer and inner solutions, respectively).

The dimensionless variables introduced by Debiane are

$$\hat{h} = \frac{h}{H}, \qquad \hat{x} = \frac{x}{L}, \qquad \hat{t} = t\frac{\rho g H^3 \cos\alpha}{12\mu L^2}, \qquad \hat{x}_f = \frac{x_f}{L}. \tag{4.41}$$

The final solution is then made up of inner and outer solutions (see Figure 4.8).

The free surface is given by

$$\hat{h}_i\left(\hat{x},\hat{t}\right) = \left(\frac{\hat{x}}{12\hat{L}\hat{t}}\right)^{\frac{1}{2}}, \tag{4.42}$$

which is identical to Equation 4.31.

The front position for the outer solution is given by

$$\hat{x}_{Fk}\left(\hat{t}\right) = \left(\frac{27}{4}\hat{L}\left(2-\hat{L}\right)^2\right)^{\frac{1}{3}} \hat{t}^{\frac{1}{3}}. \tag{4.43}$$

By substituting Equation 4.43 into Equation 4.42 the height of the front is computed as

$$\hat{h}_{Fk}\left(\hat{t}\right) = \left(\frac{2-\hat{L}}{16\hat{L}\hat{t}}\right)^{\frac{1}{3}}. \tag{4.44}$$
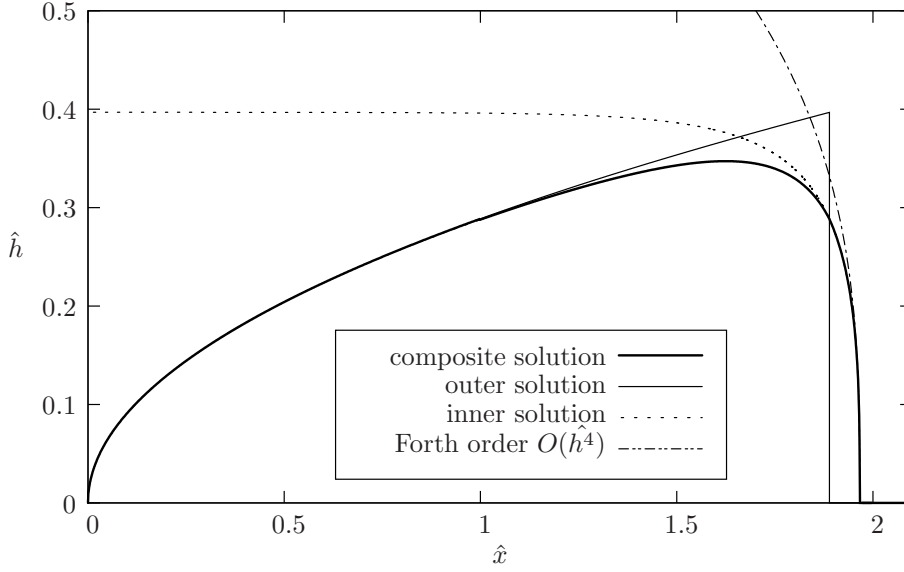
Figure 4.8: Solution of Debiane for $\hat{L} = 1$ at time $\hat{t} = 1$.

This solution does not have a physical meaning at the front of the surge. Using a perturbation method, Hunt [1994] introduced an inner solution, which is more accurate to describe the front shape.

$$\hat{L}\left(\hat{x} - \hat{x}_{Fk}\left(\hat{t}\right)\right) = \hat{h} + \frac{\hat{h}_{Fk}\left(\hat{t}\right)}{2} \ln\left(\frac{\hat{h}_{Fk}\left(\hat{t}\right) - \hat{h}}{\hat{h}_{Fk}\left(\hat{t}\right) + \hat{h}}\right) + (\ln(4) - 1)\frac{\hat{h}_{Fk}\left(\hat{t}\right)}{2}. \quad (4.45)$$

By choosing $\hat{h} = 0$ we obtain the position of the front

$$\hat{x}_f(\hat{t}) = \hat{x}_{Fk}(\hat{t}) + (\ln(4) - 1)\frac{\hat{h}_{Fk}\left(\hat{t}\right)}{2\hat{L}}. \quad (4.46)$$

Equation 4.45 can be estimated using a 4th order development $O(\hat{h}^4)$ and the result is

$$\hat{h} \approx \left[3\hat{h}_{Fk}^2\hat{L}\left(\hat{x}_f - \hat{x}\right)\right]^{\frac{1}{3}}, \quad (4.47)$$

which is only correct close to the front. Finally a composed solution is obtained

$$\hat{h}\left(\hat{x}, \hat{t}\right) = \begin{cases} \hat{h}_i + \hat{h}_e - \hat{h}_{Fk} & \hat{\xi} \leq 0 \\ \hat{h}_e & \hat{\xi} \geq 0 \end{cases} \quad (4.48)$$

with $\hat{\xi} = \hat{x} - \hat{x}_{Fk}$.

4.2.11 Flow-depth averaged solutions for Herschel-Bulkley fluids

Huang and García [1998] considered two partial differential equations to supplement the governing Equations 4.38 and 4.39, one for the plug layer and another one for the sheared layer.

The outer solution is given in an implicit form by

$$x = \left[\rho g h^n (h - h_y) \frac{\sin \alpha}{K} \right]^{1/n} t, \tag{4.49}$$

$$A = \frac{n}{2n+1} \left[\frac{\rho g (h_f - h_y) \sin \alpha}{K} \right]^{1/n} \left(\frac{n+1}{n} h_f^2 + \frac{1}{n+1} h_f h_y + \frac{n}{n+1} h_y^2 \right) t, \tag{4.50}$$

$$x_f = \frac{2n+1}{n} \left(\frac{n+1}{n} h_f + \frac{1}{n+1} h_y + \frac{n}{n+1} \frac{h_y^2}{h_f} \right)^{-1} A, \tag{4.51}$$

$$\frac{x}{x_f} = \frac{h(h - h_y)^{1/n}}{h_f (h_f - h_y)^{1/n}}, \tag{4.52}$$

$$\frac{\mathrm{d} x_f}{\mathrm{d} t} = \frac{n}{2n+1} \left[\frac{\rho g (h_f - h_y)^{n+1} \sin \alpha}{K} \right]^{1/n} \left(1 + \frac{n}{n+1} \frac{h_y}{h_f} \right), \tag{4.53}$$

where A is the flow volume V divided by the reservoir width D, x_f the front position, h_f the front height and h_y the yield depth:

$$h_y = \frac{\tau_c}{\rho g \sin \alpha}. \tag{4.54}$$

The inner solution takes the form

$$\left(\frac{h_i \phi - h_y}{h_f - h_y} \right)^{(n+1)/n} = \frac{\left(1 - \frac{n}{2n+1} \frac{h_f - h_y}{h_f} \right) \phi}{\left(1 - \frac{n}{2n+1} \frac{h_i - \frac{h_y}{\phi}}{h_i} \right)}, \tag{4.55}$$

with the boundary condition given by

$$\int_{-\infty}^{0} (h_f - h_i) \mathrm{d} \xi = \int_{0}^{\delta} h_i \mathrm{d} \xi, \tag{4.56}$$

where

$$\phi = 1 - \frac{\mathrm{d} h_i}{\mathrm{d} \xi}, \tag{4.57}$$

and where $\xi = x - x_f$. A composite solution h_c is obtained by adding the inner and outer solutions and subtracting their common matching term h_f:

$$h_c = h + h_i - h_f. \tag{4.58}$$

4.2.12 Computational fluid dynamics

In Section 4.6, the dam-break results for a viscoplastic gel down an inclined plane are compared with computational fluid dynamics (CFD) simulations. The CFD code used at LHE is an extension of a three-dimensional incompressible Navier-Stokes solver with a free surface developed by Griebel et al. [1998]. A Chorin's projection scheme is used in combination with a level-set representation of the free surface. A shear-rate dependent viscosity function is introduced to take the rheological properties of the fluid into account. Numerically this gives rise to a stiff problem, which requires the use of an implicit solver for the viscous terms.

4.3 Measurement campaigns

This study hinged on three measurement campaigns:

1. Approximately 55 kg of Glucose syrups were released down a 30-cm wide canal with slope angles of 0°, 6°, 12°, 18°, and 24° to validate the experimental setup. The results are presented in Section 4.4.

2. 23 and 43 kg of Carbopol at 4 different concentrations were tested in the 30-cm wide canal with slope angle of 0°, 6°, 12°, 18°, and 24°. The test results are given in Section 4.5.

3. 43 kg of Carbopol at 4 different concentrations tested on the inclined plane for slope angle of 0°, 6°, 12° and 18°. Section 4.6 presents the results.

4.3.1 Setup

The canal and the inclined plane are sketched in Figure 4.9 with their associated coordinates system. The reservoir had a length L of 51 cm and a width D of 30 cm. The carbon dam gate was 4 cm thick. The canal, when in place, had the same width D as the reservoir.
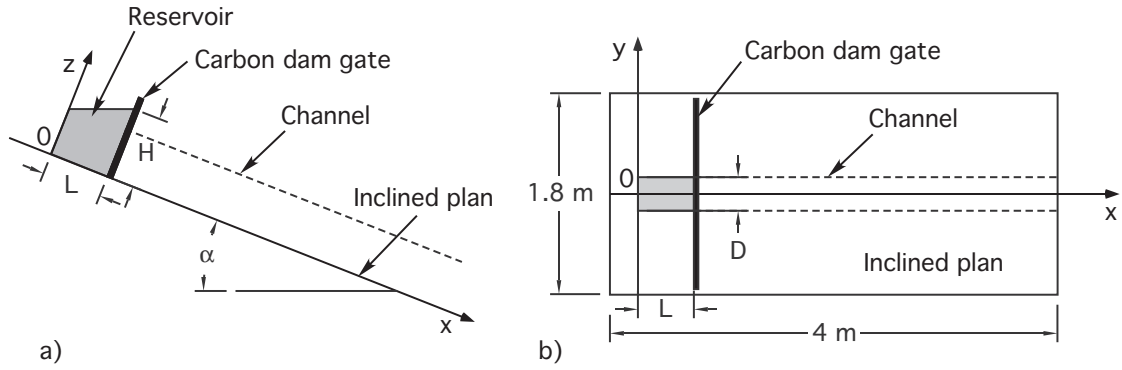
Figure 4.9: Sketch of the experimental setup with its coordinate system, a) side-view b) top-view.

4.3.2   Reproducibility and accuracy of the experiments

In this section, the accuracy of the measurement setup is discussed with a focus on the experimental procedure. To evaluate the reproductibility of the procedure some experiments had been repeated with the same initial and boundary conditions.

Two examples are presented here to illustrate the confidence we gained in our setup. Both examples were obtained with 43 kg of Carbopol at a concentration of 0.30%: the first one on the inclined plane with 12° slope and the second one in the 30-cm wide horizontal channel.

Once the free surface of the flow surge computed (see Chapter 2), the flow depth profile at the centerline is extracted for each time step as well as the contact line (see Figure 4.10). The front position was then detected using a threshold of 0.5 cm.

Reproductibility of the experiments on the inclined plane

Two tests, with the same initial and boundary conditions, are presented in this section. A mass of 43 kg of Cabopol at a concentration of 0.30% was released twice down the inclined plane. The plane had a slope of 12°. Figure 4.11 shows both front positions x_f during the 60 first seconds as well as the difference Δx_f between them. Δx_f is contained between 2.5 and 6 mm and should be compared with the area of measurement, which is 1.2×1.3 m. Both tests give similar front positions.

Figure 4.12 shows the flow profile at $y = 0$ for both test. The difference between both sets of profiles $\Delta z(x, t)$ is in the order of 3 mm. The profiles are similar in both cases. The contact lines for both test are presented in Figure 4.13.
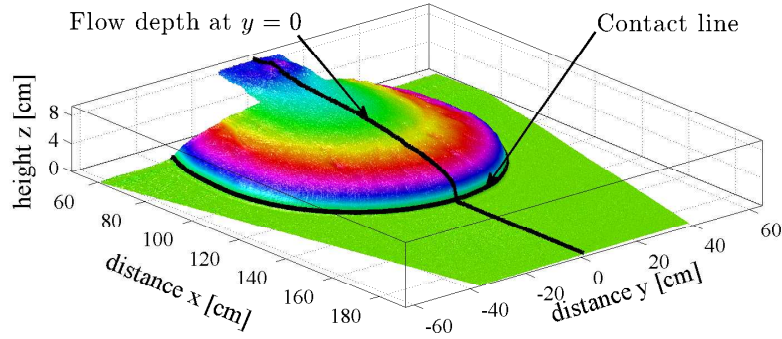
Figure 4.10: 3D view of 43 kg of Ultrez 10 at a concentration C of 0.25% down a 6° slope at time t= 900 s.
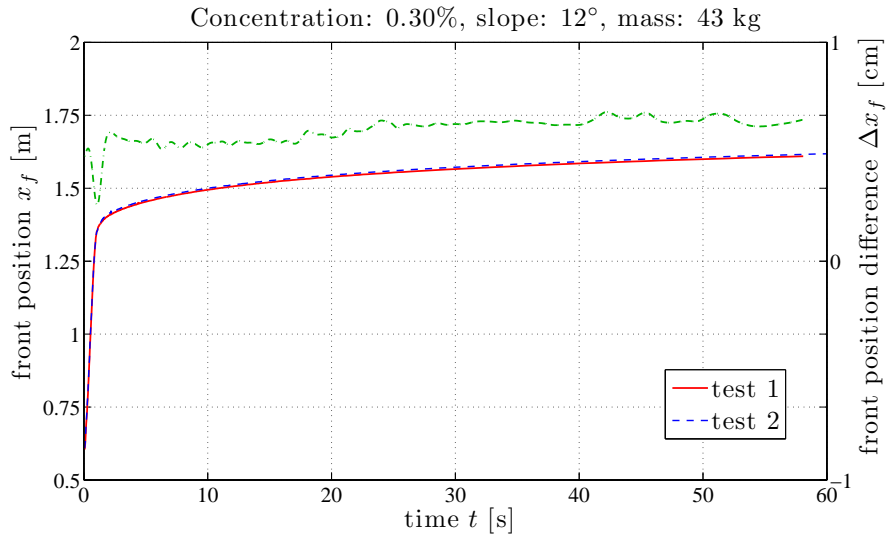
Figure 4.11: Front positions x_f and difference between them. Two tests were performed with mass $m = 43$ kg, inclined plane slope angle $\alpha = 12°$ and Ultrez 10 concentration $C = 0.30\%$.

Concentration:0.30%, slope: 12°, mass: 43kg
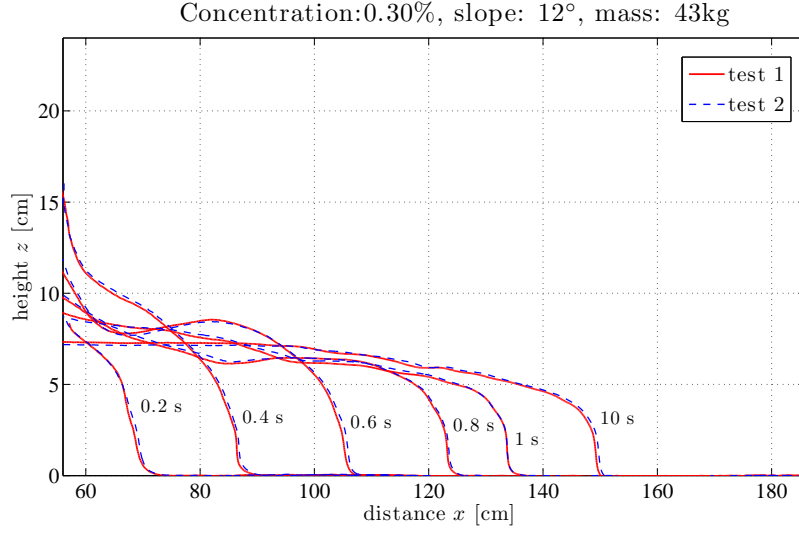
Figure 4.12: Flow depths h for two tests with mass $m = 43$ kg, inclined plane slope angle $\alpha = 12°$ and Ultrez 10 concentration $C = 0.30\%$.

To test our system, we also checked if the surge presented a symmetry with respect to its center line. As the setup was symmetric, the flow had to be symmetric. In this example the flow is perfectly symmetric with respect to the axis $y = 0$. The maximum difference measured in the y-direction is less than half one millimeter.

Reproductibility of the experiments in the channel case

For the second comparison, 43 kg of Carbopol at a concentration of 0.30% were released twice in the 30-wide channel. The channel was set to an horizontal position.

For the second test, the free surface of the fluid was **not** flattened as prescribed by the procedure. Figures 4.14 and 4.15 show the position of the front x_f as a function of time for both tests as well as the difference between the two front positions. The difference is less than 1.5 cm after 8 hours. The maximum difference is found at the beginning of the test where its value reaches 6 cm and then decreases with time to reach an almost constant value after 4 hours. During the first instant of the test, the fluid is in the inertial regime and flow is driven by the pressure term $\frac{\partial h}{\partial x}$. This highlights the importance of the initial conditions.

In practice, it is difficult to guarantee horizontal free-surface in the reservoir with viscoplastic materials as it had to be flattened out by hand.
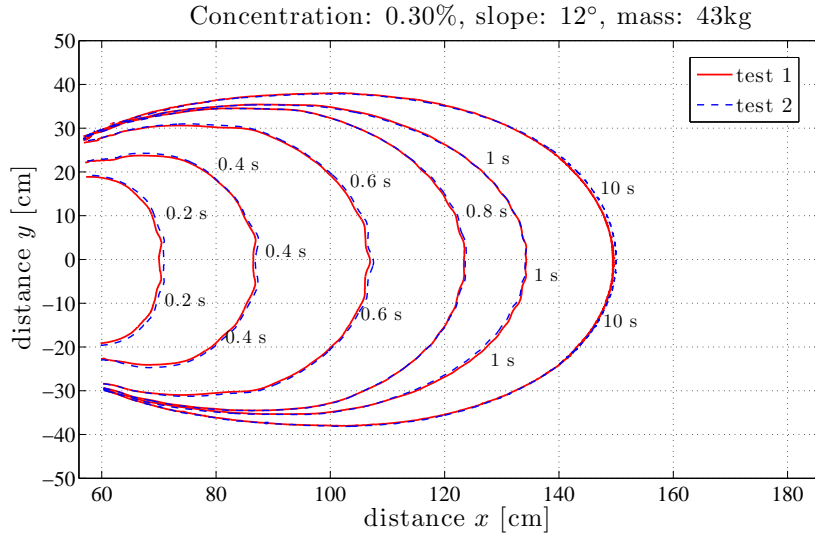
Figure 4.13: Position of the contact lines for two tests with mass $m = 43$ kg, inclined plane slope angle $\alpha = 12°$ and Ultrez 10 concentration $C = 0.30\%$.
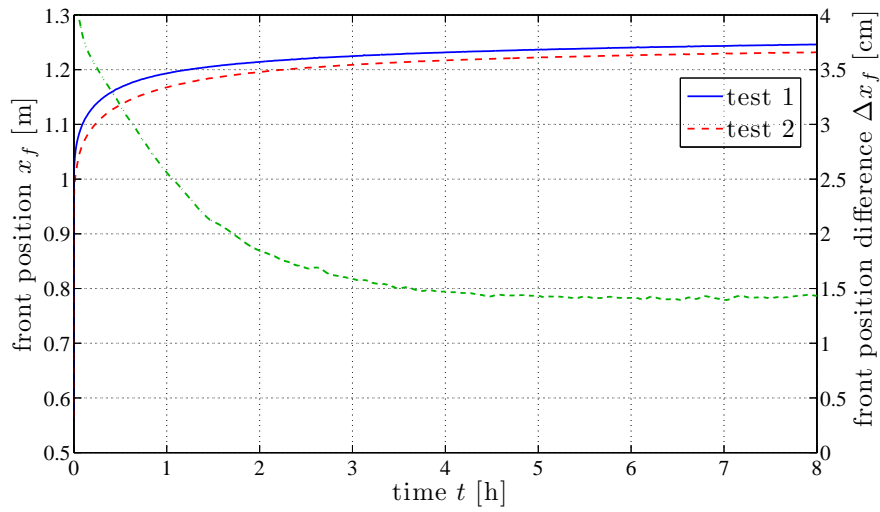
Figure 4.14: Front positions x_f as a function of time and difference between them, for two tests with mass $m = 43$ kg, channel slope angle $\alpha = 0°$ and Ultrez 10 concentration $C = 0.30\%$.
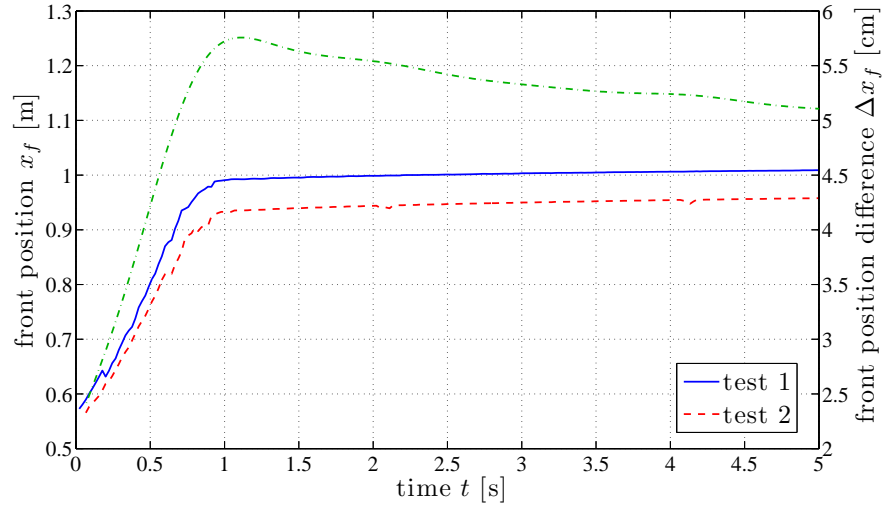
Figure 4.15: Zoom on the first 5 seconds of Figure 4.14.

Figure 4.16 shows the flow profiles for both tests. The delay of 'test 2' is clearly visible. Nevertheless the profiles for both tests are similar.
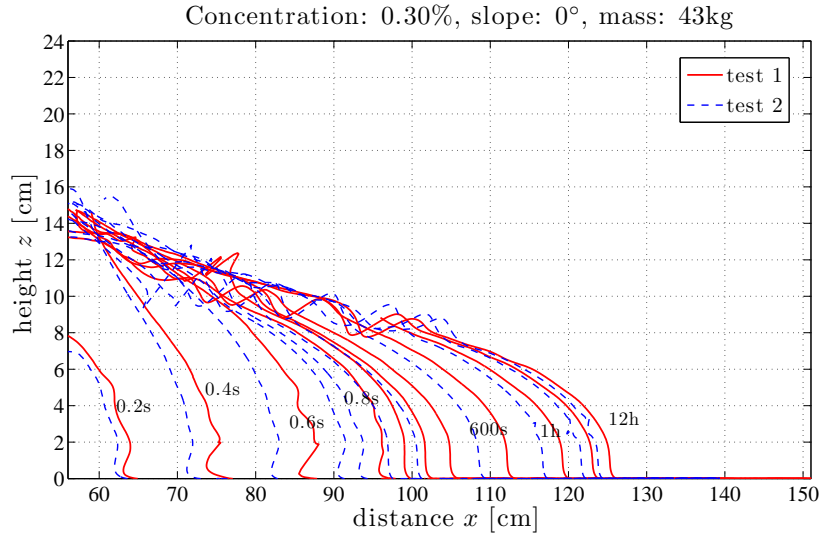
Figure 4.16: Flow profiles of two tests with mass $m = 43$ kg, channel slope angle $\alpha = 0°$ and Ultrez 10 concentration $C = 0.30\%$.

Summary

When the experimental procedure is correctly followed the reproducibility of two tests is in the order of half one centimeter. To obtain valuable results the handling of the boundary conditions is a key point. If similar boundary conditions are achieved then similar results are recorded. The smoothing of the free-surface in the reservoir has to be done with great care.

The precision of our measurement system is in the order of half one millimeter on a 1.4×1.4 m^2 with a frame rate of 48 Hz and the precision of the experimental procedure is in the order of half one centimeter. The overall measurement precision of the moving free-surface of a surge of approximately 40 kg is bellow one centimeter. Our setup is, to our knowledge, the more precise avalanche simulator built to date.

4.4 Experimental dam breaks with glucose syrup down a channel

For preliminary experiments, we tested our setup with Newtonian fluids. In this section the experimental results obtained with glucose syrup are compared with analytical solutions.

5 dam break experiments with glucose syrup were carried out with slope ranging from 0° to 24° (see Table 4.1). The syrup was prepared as described in Section A.2.1.

α [°]	mass [kg]	h_0 [cm]	H [cm]	μ [Pa s]	ρ [kg m^{-3}]	Figures
0	56.1	25.8	25.8	345	1420	4.17 and 4.18
6	56.7	26.1	28.8	352	1420	B.4 and B.5
12	57.0	26.2	31.6	352	1420	B.6 and B.7
18	57.6	26.5	34.8	345	1420	4.19 and 4.20
24	50.8	23.4	34.7	345	1420	B.10 and B.11

Table 4.1: Experimental parameters: h_0 is the flow depth when the canal is in horizontal position while H is the flow depth at the dam gate when the canal is inclined.

4.4.1 Front position

Figures 4.17 and 4.18 illustrate front positions obtained experimentally and the theoretical ones predicted by Huppert [1982a] and Debiane [2000] for horizontal case. Figure 4.19 and 4.20 show the same results, but for an 18° slope. The remaining cases are presented in Appendix B.

To take into account the opening duration (30 cm within 0.8 s), an artificial delay of 0.5 s was imposed on all experimental data. For each experiment, two fits of the function $y(x) = At^n$ are made. For the first fit, both A and n vary, the resulting values are called, respectively, A_2 and n_2. For the second fit, the parameter A is free, and called A_1 while n is fixed, and called n_1. n_1 has the value given by theory: $n_1 = 1/5$ for the horizontal case and $n_1 = 1/3$ for the inclined case. A and n values are presented in Figure 4.22.

For the horizontal case (see Figure 4.17 and 4.18), both theoretical predictions are similar except close to $t = 0$. For early times, Debiane predicted a front position different from zero. The experiment data can be fit with a power-law function $x = At^n$ for a time greater than approximately 5 s with $n_2 = 0.21$ and $A_2 = 0.618$. Equation 4.21 predicted that the hydrodynamic regime should be

reached after 0.3 s. The front position varies, as predicted, as a function of $t^{1/5}$, but with a delay. The difference between the predicted value of A by Huppert and the one computed from the experimental data is 12%. This may be explained by the friction exerted by side walls, during the first instants of the test, when the flow depth is of the same order as the canal width.
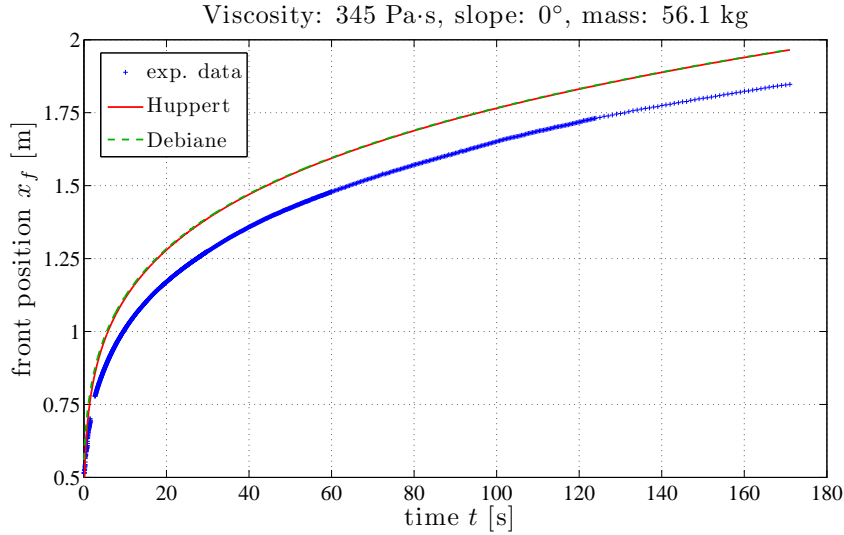
Figure 4.17: 56.1 kg of glucose syrup with a viscosity of 345 Pa·s on a slope of 0°. Both prediction by Huppert and Debiane are superimposed on the upper curve while the lower curve is the experimental data

For the channel inclined at 18°, figures 4.19 and 4.20 present the experimental front positions as well as those predicted by theory. As for the horizontal case, the experimental front positions exhibits a delay, which can be explained by side-wall effect. During the first instants, the flow depth is comparable to its width and the wall friction can no longer be neglected. The hypothesis of a 2D flow is not valid.

For the inclined channel, the predicted regime is achieved after a much greater time than for horizontal case. When the inclination is small, the hydrodynamic regime is a balance between gravity, pressure gradient, and viscosity. At first, when the flow profile curvature is still large, pressure gradient dominates gravity acceleration and the front position varies, as in the horizontal case, with $t^{1/5}$. After a while, when the fluid has stretched enough, gravity becomes equal to and then larger than the pressure term, the dominant balance is then between gravity acceleration and viscosity. In that case, the front velocity is a function of $t^{1/3}$. For larger slope angles, the balance between pressure gradient and viscosity is also observed, but for shorter times, the pressure gradient rapidly becomes smaller than
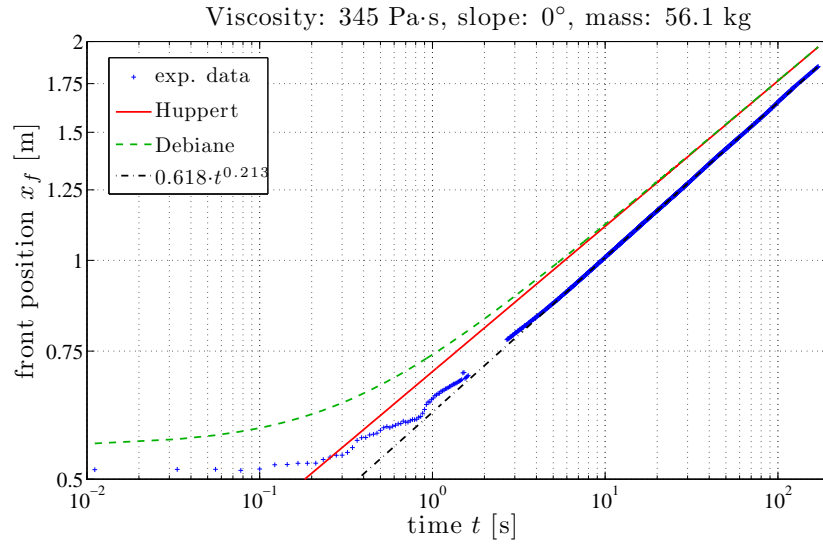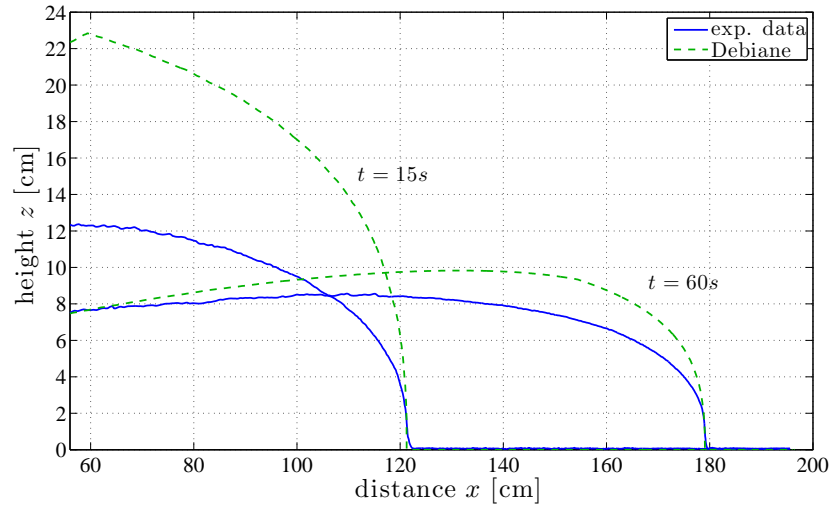
Figure 4.18: 56.1 kg of glucose syrup with a viscosity of 345 Pa·s on a slope of 0°.
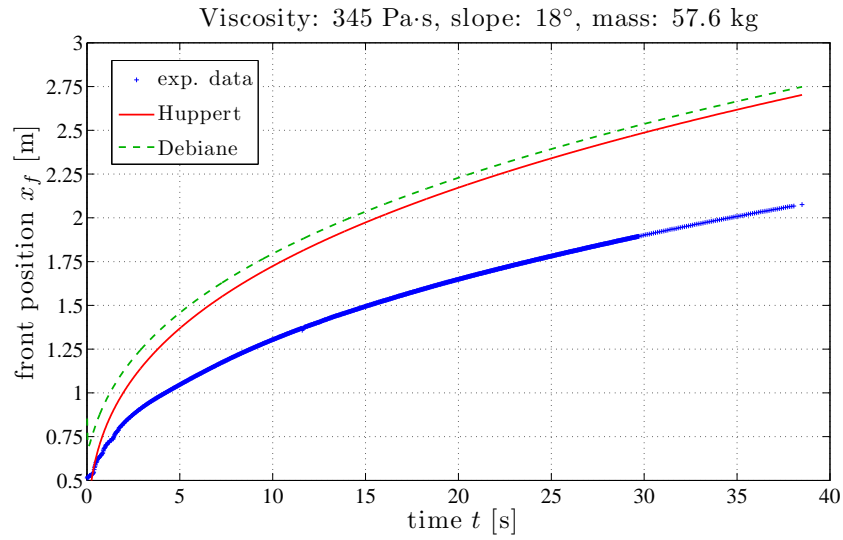
Figure 4.19: 57.6 kg of glucose syrup with a viscosity of 345 Pa·s on a slope of 18°.
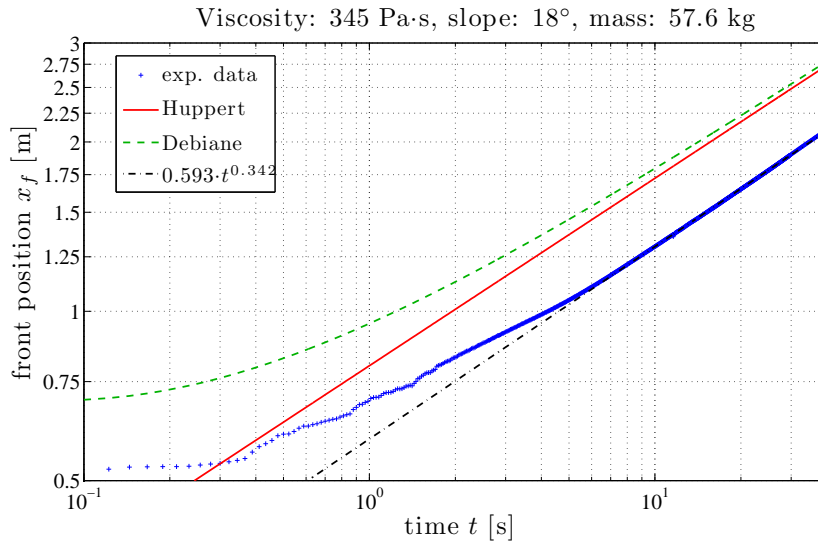
Figure 4.20: 56.1 kg of glucose syrup with a viscosity of 345 Pa·s on a slope of 18°.

gravity acceleration.

Three regimes are illustrated in Figure 4.21. First, the front follows the dash-dot line $t^{1/5}$ where the dominant balance is between pressure gradient and viscosity. This regime lasts longer for smaller inclinations than for larger ones. Second, the balance is between pressure gradient, gravity and viscosity. The front positions no longer follows the dash-dot line $t^{1/5}$, but does not yet follow the dashed line $t^{1/3}$. Third, the dominant balance is between gravity acceleration and viscosity and the regime is the one predicted by theory. Again, it takes more time to reach this regime at lower slope angle.

Figure 4.22 shows the coefficient A and n, which came up in the function $f(t) = At^n$, where $f(t)$ is the front position as a function of time. In the upper subplot, the experimental value of A is underestimated in comparison with the theoretical one. This is due to the delay observed in the experiments, which appears during the first instants of the flow when the 2D hypothesis is wrong and the flow is slowed down by the friction on the side walls. The lower subplot shows the value of n. Both experimental values of n are close to the theoretical one. A better fit could have been made if the sections on which the measurement was taken were sufficiently long for the fluid to fully reach its hydrodynamic regime.
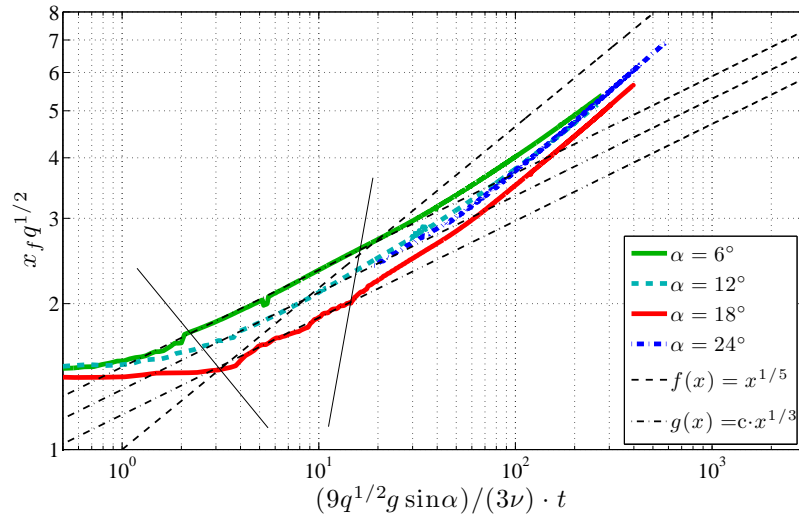
Figure 4.21: 56.1 kg of glucose syrup with a viscosity of 345 Pa·s on a slope of 18°. The narrow continuous are estimators of the flow regime changes.
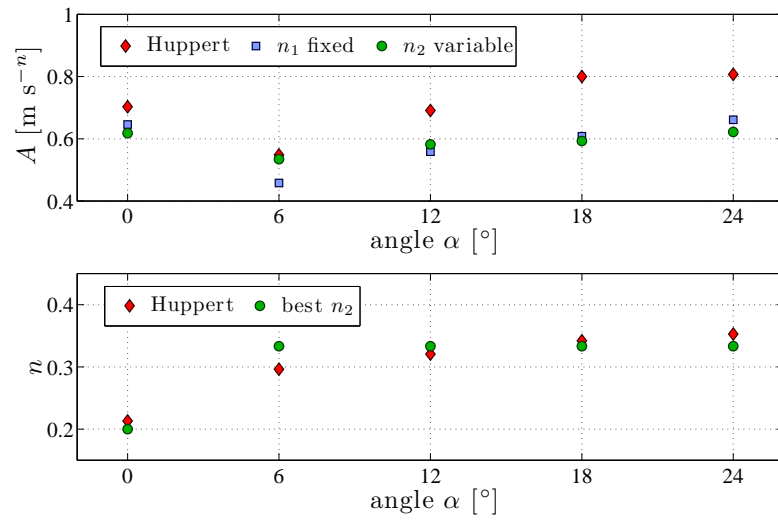
Figure 4.22: 56.1 kg of glucose syrup with a viscosity of 345 Pa·s on a slope of 18°.

4.4.2 Flow depth profile

Figure 4.23 to 4.25 show the flow depth profile at the centerline ($y = 0$) for inclination α equal to $0°$, $6°$, and $18°$. For each angle, two profiles are presented at two different times, the second being 4 times larger than the first one. In the previous section, we have seen that the experimental front position had a delay compared to the theoretical one, and thus, in order to compare the theoretical depth profile with the experimental one, the time of the theoretical results was adapted to fit the experimental results. The profiles are then compared for same front position, regardless of time.

For the horizontal channel (see Figure 4.23), the predictions of Huppert and Debiane closely approximate the experimental results. The theoretical depth at the front is slightly higher than the measured one, which is a consequence of neglecting surface tension.
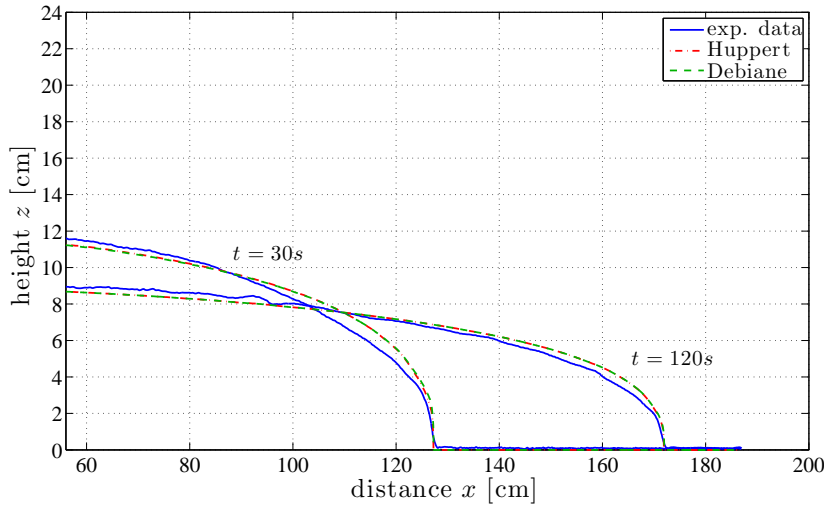
Figure 4.23: 56.1 kg of glucose syrup with a viscosity of 345 Pa·s on a slope of $0°$.

For the inclined channel (see Figures 4.24 and 4.25), the shape given by the theoretical solution does not match the experimental one for short times. The profile seems to be better predicted for longer times. This result could parallel the ones presented in Figure 4.21; the hydrodynamic regime (where the dominant balance is between gravity acceleration and viscosity) is not reached as quickly as predicted theoretically. An intermediate regime where the pressure term is larger than the viscosity first occurs. The profile proposed by Debiane does not take this intermediate regime into account. Hunt [1994] stressed that his model is valid

only when the front has travelled a distance 4 times greater than the length of the reservoir, i.e, here after 2 meters.

Figure 4.24: 56.1 kg of glucose syrup with a viscosity of 345 Pa·s on a slope of 6°.
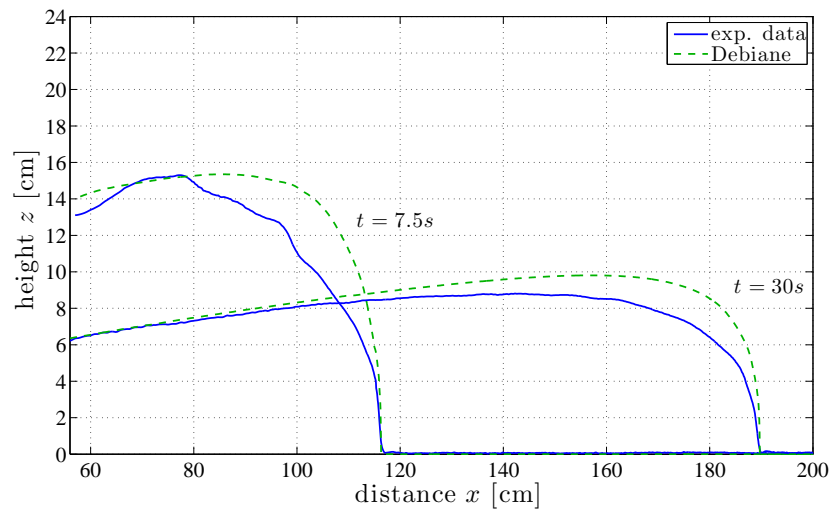
Figure 4.25: 56.1 kg of glucose syrup with a viscosity of 345 Pa·s on a slope of 18°.

4.4.3 Summary

Theory shows good agreements with experimental results. The front position is, as predicted, a function of t^n when the time t becomes sufficiently large. Nevertheless, a delay is always observed, with a relative difference of 12% in the horizontal case and up to 24% in the steepest cases. The delay can be partly explained by the tri-dimensional effects of the flow and the shear stress at the canal walls.

The theoretical flow depth profile over-predicts the flow height at the front for both horizontal and inclined channels. These differences are more pronounced for low slope angles than for steeper ones.

Three regime were monitored on the inclined channel:

- a pressure gradient/viscosity regime;

- a pressure gradient/gravity acceleration/viscosity regime;

- a gravity/viscosity regime.

4.5 Experimental dam breaks with Carbopol Ultrez 10 gel down a channel

35 dam break experiments with Carbopol Ultrez 10 were carried out to test the influence of the different parameters (see Table 4.2). The experiments were performed on 5 slope angles α for 2 masses m of Carbopol at 4 different concentrations C. The Carbopol was prepared as described in Section A.1.1.

Slope	0°		6°		12°		18°		24°
Mass	43 kg	23 kg	43 kg	23 kg	43 kg	23 kg	43 kg	23 kg	23 kg
0.25%	C.2	4.30	C.11	C.15	C.22	C.26	C.32	C.36	C.43
0.30%	C.3	C.6	C.12	C.16	C.23	C.27	C.33	C.37	C.44
0.35%	C.4	C.7	C.13	C.17	C.24	C.28	C.34	C.38	C.45
0.40%		C.8	C.14	C.18	C.25	C.29	C.35	C.39	C.46

Table 4.2: Figure reference numbers for experiments run with Carbopol Ultrez 10 down a canal. All the figures are presented in Appendix C except Figure 4.30, which is discussed in this chapter.

4.5.1   Horizontal channel

7 tests were carried out in the horizontal canal to measure the front velocity and the flow profile. Each of those 7 tests lasted 12 hours in order to measure the run-out behaviour and, if any, the stopping position. The flow did not come to rest in any of those 7 tests, as shown on Figures 4.26 and 4.27. After 12 hours the front velocity was between 3.5 mm/h ($C = 0.25\%$ and $m = 43$ kg) and 1.5 mm/h ($C = 0.40\%$ and $m = 23$ kg).

All tests presented the same behaviour for the front position x_f;

- first, the front accelerated rapidly to reach an almost constant velocity. For example, the front velocity was 55 cm/s for the test with $m = 43$ kg and $C = 0.25\%$. The flow is in the inertial regime;

- then the front slowed down drastically to reach velocities one order of magnitude slower. In the previous example, the velocity of the front dropped down to 6 cm/s;

- the front velocity kept on decreasing asymptotically toward zero. In our example the front velocity after 12 hours was below to 3.6 mm/s and still decreasing.

The gels with lower Ultrez 10 concentrations went faster than those with higher ones.

A complete run-out was observed on a 60-hours test. The test was done with 43 kg of Carbopol at a concentration of 0.30%. Not only a stop was observed, but also an inversion of the flow direction was recorded (see Figure 4.28). The front came to rest at time $t = 39$ hours. During the next 21 hours the front position withdrew of half one millimeter because the Carbopol had dried. Even if the relative moisture in laboratory was set to 70%, the Carbopol dried. The moisture could not be set to a higher value since some measurement tools are sensitive to a wet atmosphere.

During the run-out regime, the shear stress is comparable to the yield stress. The viscoplastic concept may, at these shear rates, not be valid anymore as explained in Chapter 3.

The experimental and theoretical flow profiles are compared in Figure 4.30 for 23 kg of Ultrez 10 at a concentration C of 0.35%. The predicted profile was computed using Balmforth's model (see Equation 4.34). The experimental front position is slower than the predicted one during the first period, which was unexpected as theory neglected inertia but still predicts a faster flow than the one observed. The flow shape is also not correctly predicted.

The evolutions of the front as predicted by theory and as measured in our experiment are different. The predicted front positions follow straight lines, in a
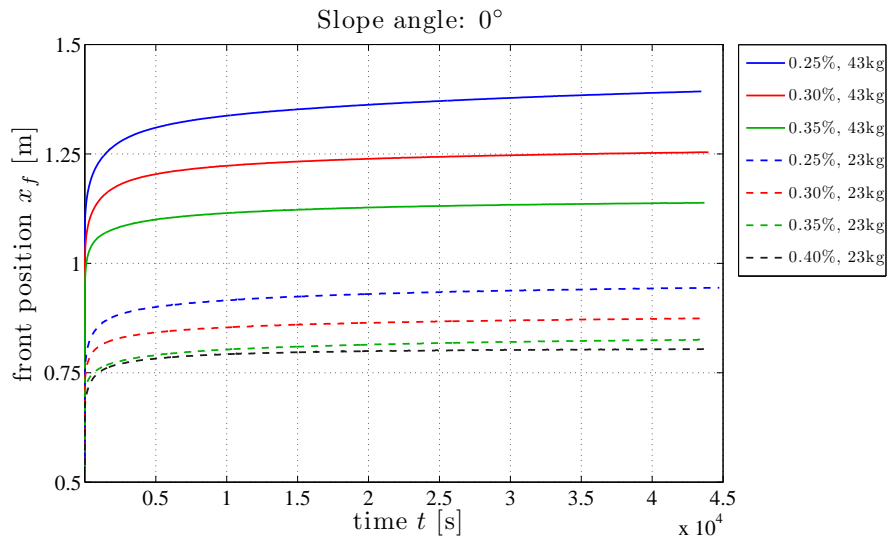
Figure 4.26: Front position as a function of time for 4 Carbopol concentration and 2 masses in the horizontal channel.
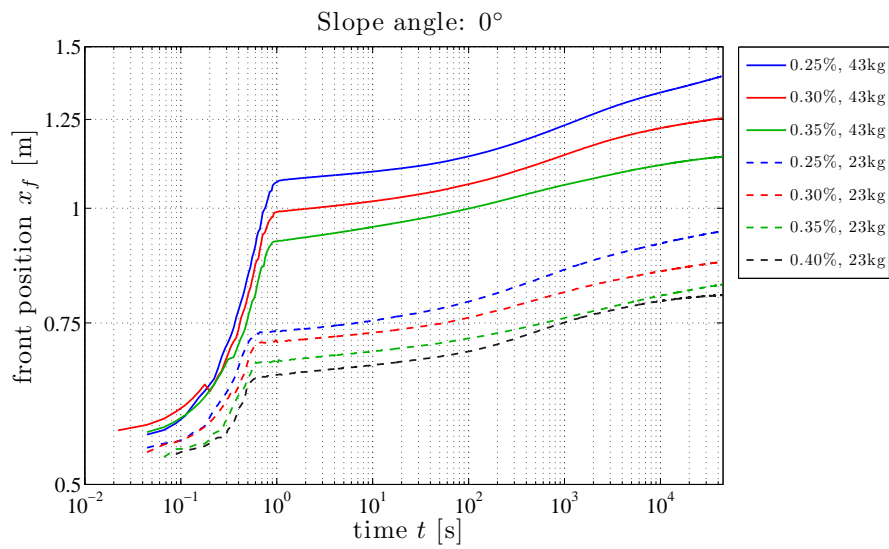
Figure 4.27: As Figure 4.26 but on semi-log graph.
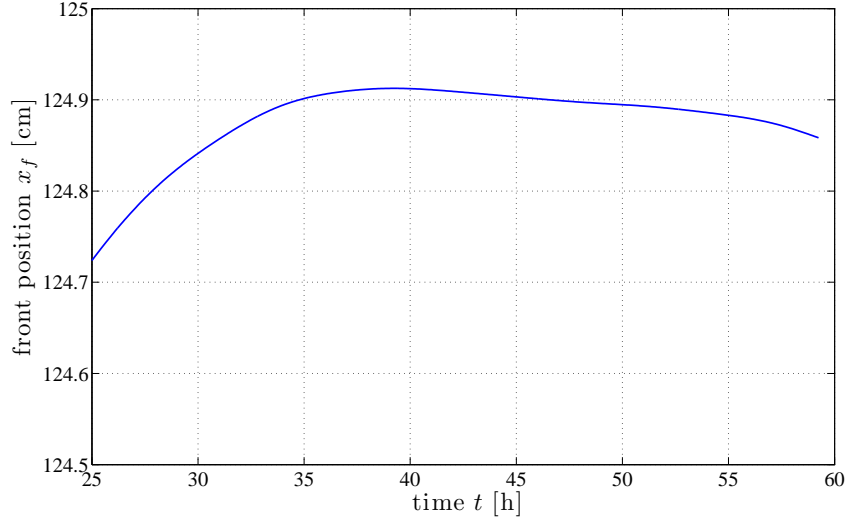
Figure 4.28: Front position between 25 and 60 hours for C =0.30% and m =43 kg. The front came to a rest after 39 hours. The position of the front then reverse due to the drying of the gel of Carbopol.

semi-log plot, during the first seconds and then smoothly decay toward a plateau. The measured positions, on the contrary, exhibit a strong acceleration before an abrupt break. After 1 s the fluid exponentially decelerates.

The shape of the flow is also not correctly predicted by the theory (see Figure 4.30). The experimental profile is much flatter than the theoretical one except at the front. The observed front is abrupt and, as in the presented example, presents two steps. These steps are a direct consequence of 3D effects. When the dam opened a 'new' vertical free-surface is created. The vertical and horizontal free-surfaces connect at the junction line (see Figure 4.31). The stress close to the junction line is below the yield stress so no flow occurs. The lower layers of the material exit the reservoir and carry the junction line away. A hollow formed behind the junction line.

Figures 4.32 to 4.35 show the formation of the hollow ($C = 0.30\%$ and $m = 43$ kg):

1. The bottom layers moved faster than the upper ones and the free surface, which was almost flat, started to bulge out. At time $t = 0.57$ s (see Figure 4.32), both the 'horizontal' and 'vertical' free surfaces merged. The layer of Ultrez 10 which was moved by the opening of dam gate ended up at a higher position than the fluid still in the reservoir. The free surfaces connect
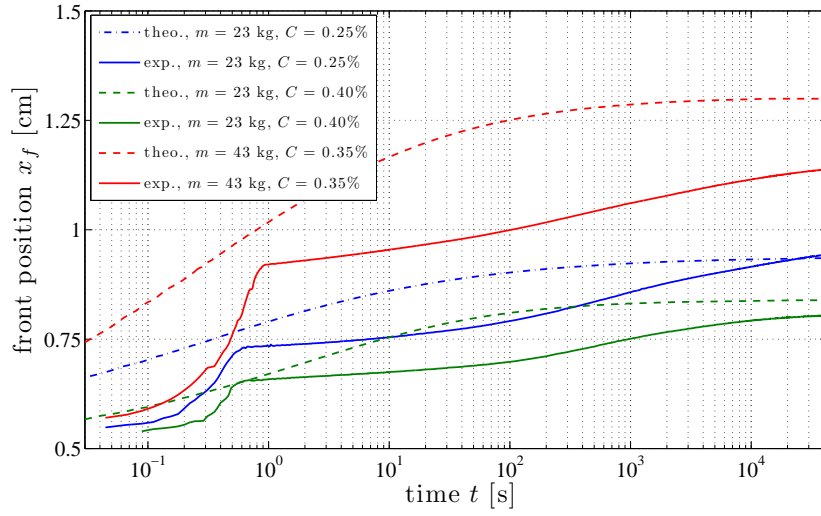
Figure 4.29: Front positions for different concentrations and masses; predicted in dashed lines and measured in continuous lines.
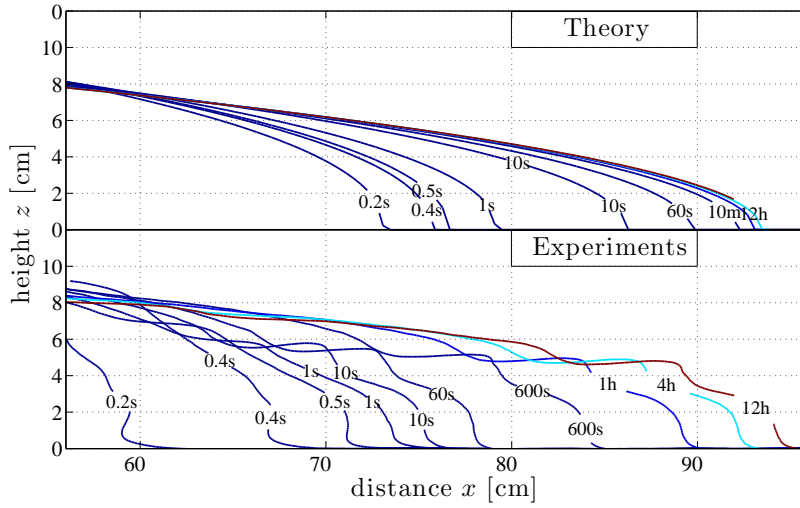
Figure 4.30: Flow profile for a test with $m = 23$ kg and $C = 0.25\%$; predicted profiles in dashed lines and measured ones in continuous lines.
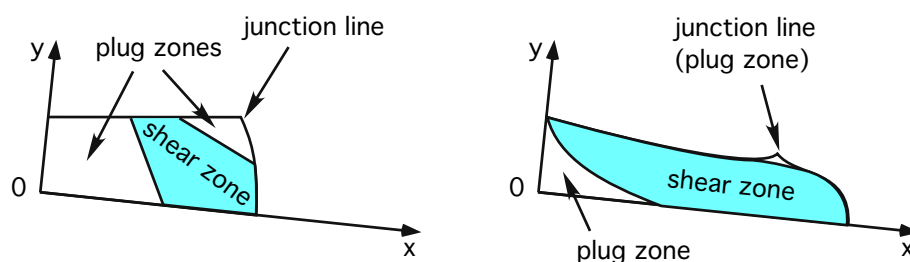
Figure 4.31: The interface between the 'vertical' and 'horizontal' is named the junction line (a). The junction line is embedded in a plug zone which is carried away for the reservoir by under sheared layer (b).

and let a visible *junction line* on the gel. This junction line then collapsed in its center as pointed out by the arrow in Figure 4.32.

2. A hollow formed just behind the junction line. At time 0.76 s (see Figure 4.33), the depression is clearly visible. The formation of the hollow is a 3D phenomenon as it resulted from the collapse of the junction line in its middle. The gel stuck on the channel walls while the middle of the junction line kept on moving.

3. At time $t = 1.4$ s, the depth of the depletion reached it maximum value (see Figure 4.34). From there on, the amplitude of the hollow decreased as the height of the flow decrease but relative amplitude stayed the same.

4. After 12 hours the depression was still visible as the stress in the upper layer was below the yield stress and no flow occurred. The deformation of the hole is a better indicator of the 3D phenomena than the front shape. The difference between the front positions at $y = 0$ and at $y = D/2 = 15$ is 3.5 cm while the difference between the position of the junction line at the same location is 11 cm.

4.5.2   Inclined channel

28 tests were carried out on the channel inclined from 6° to 24°. The front position for each test is presented in Appendix C.

As expected the surges reached higher velocity with higher slope angles. Figure 4.36 shows the front position as a function of time for different slope angles α for 23 kg of Carbopol at a concentration C of 0.25%. The surge front moved exponentially further for higher slope angles during its inertial regime. This can be
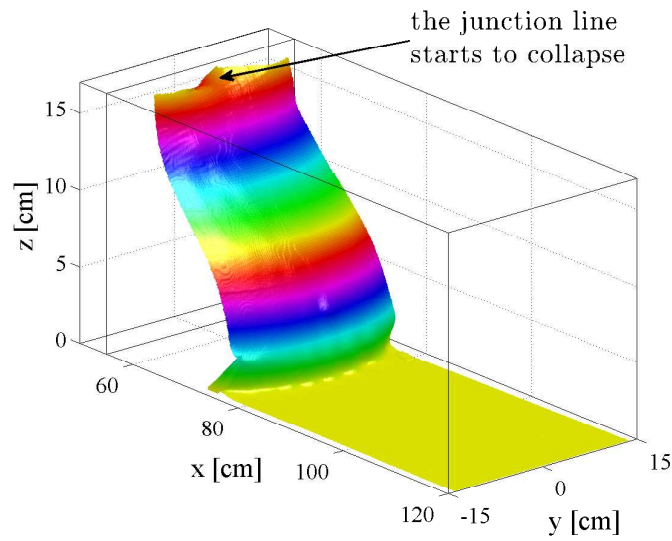
Figure 4.32: 3D view of a test with $C = 0.30\%$ and $m = 43$ kg at $t = 0.57$ s illustrating the collapse of the junction line.
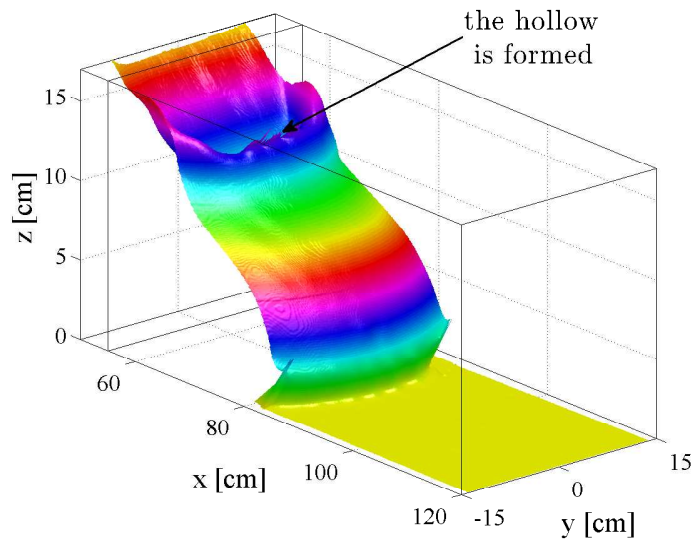
Figure 4.33: 3D view of a test with $C = 0.30\%$ and $m = 43$ kg at $t = 0.76$ s.
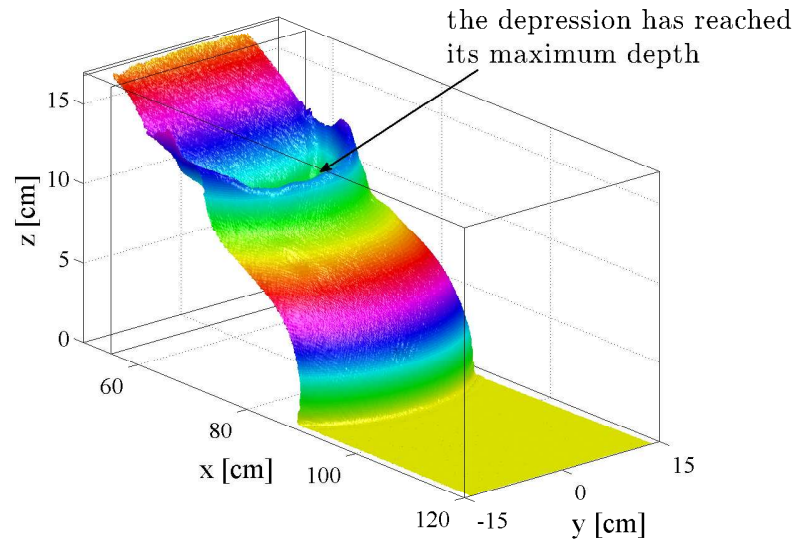
Figure 4.34: 3D view of a test with $C = 0.30\%$ and $m = 43$ kg at $t = 1.4$ s.
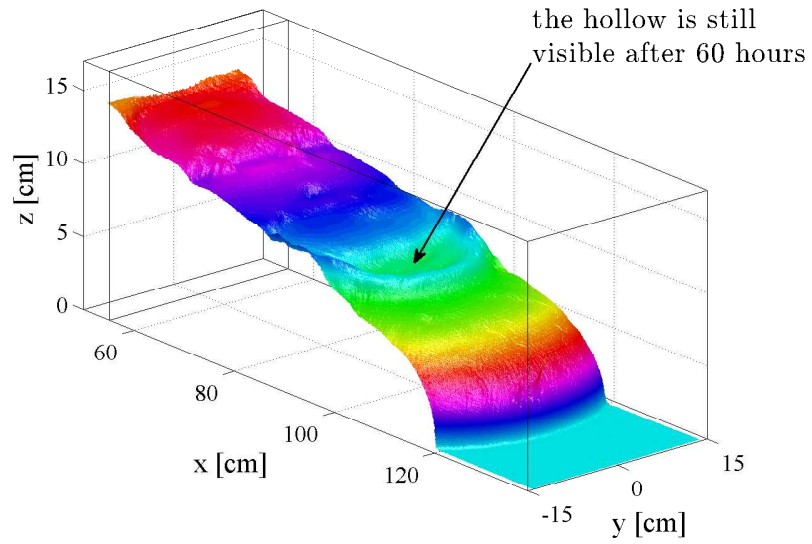
Figure 4.35: 3D view of a test with $C = 0.30\%$ and $m = 43$ kg at $t = 60$ hours.

described as the combined effect of a larger component of gravity acceleration in the flow direction ($g \cos \alpha$) on the one hand, and a larger pressure gradient ($\partial h / \partial x$) on the other hand. As for the horizontal test, the flow strongly decelerated once the inertial regime was over.
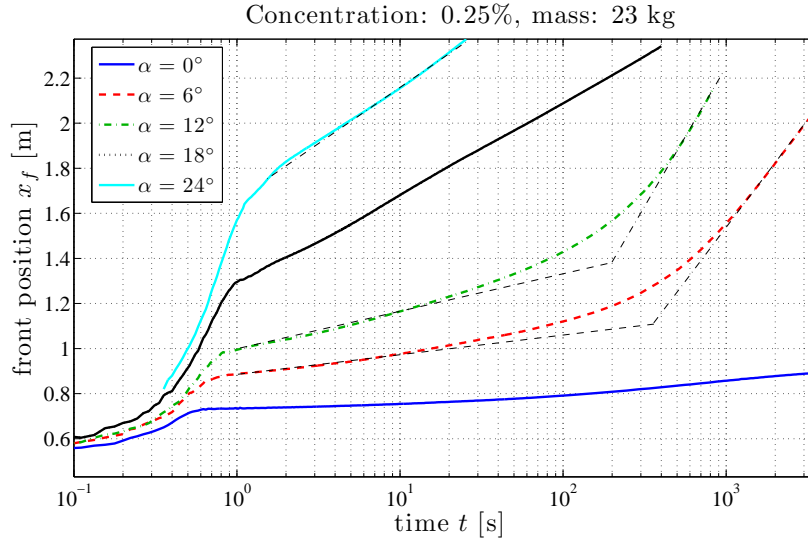
Figure 4.36: Front position as a function of time for 23 kg of Ultrez 10 at a concentration of 0.25% down different slope. Three regime can be identidied: the inertia regime, the pressure gradient/gravity acceleration (dashed lines), and the hydrodynamic regime (dash-dot lines).

Like in the Newtonian case, four regimes can be delimited in Figure 4.36 ($m = 23$ kg, $C = 0.25\%$):

1. The inertial regime, for $t \leqslant 1$ s.

2. The pressure gradient/gravity acceleration regime for $1 \leqslant t \leqslant 30$ s for slopes α of 6 and 12° and for $1 \leqslant t \leqslant 300$ s for slopes of 18 and 24 °.

3. A intermediate regime where the dominant balance is between pressure gradient, gravity acceleration and viscosity.

4. The hydrodynamic regime, for $t \geqslant 400$ and 10^4 s, for, respectively, $\alpha = 6$ and 12°. The hydrodynamic regime is not recorded for inclination of 18 and 24°.

The pressure-gradient/gravity and the hydrodynamic regime are suggested by light dashed lines.

As for the horizontal case, gels with lower Ultrez 10 concentration travel faster down the channel (see Figures 4.37 and 4.38).
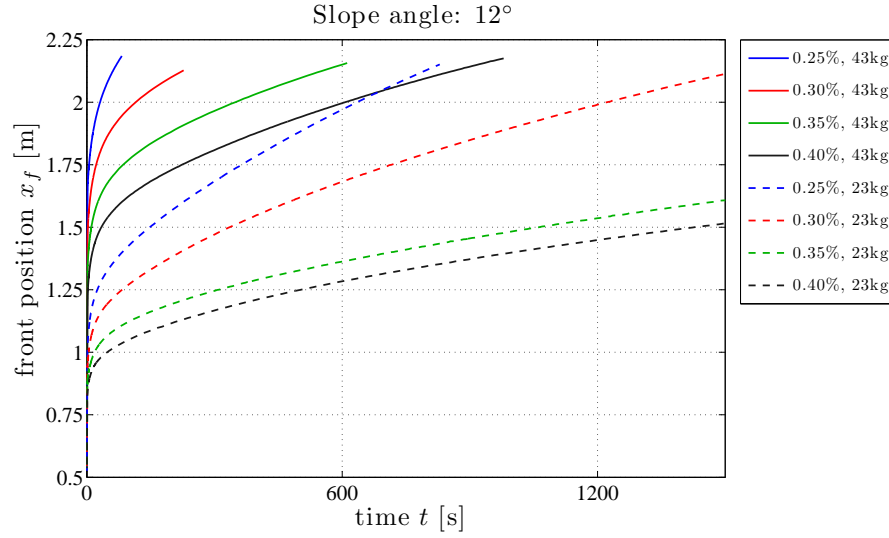
Figure 4.37: Comparison of the front positions x_f on a 12° inclined channel.
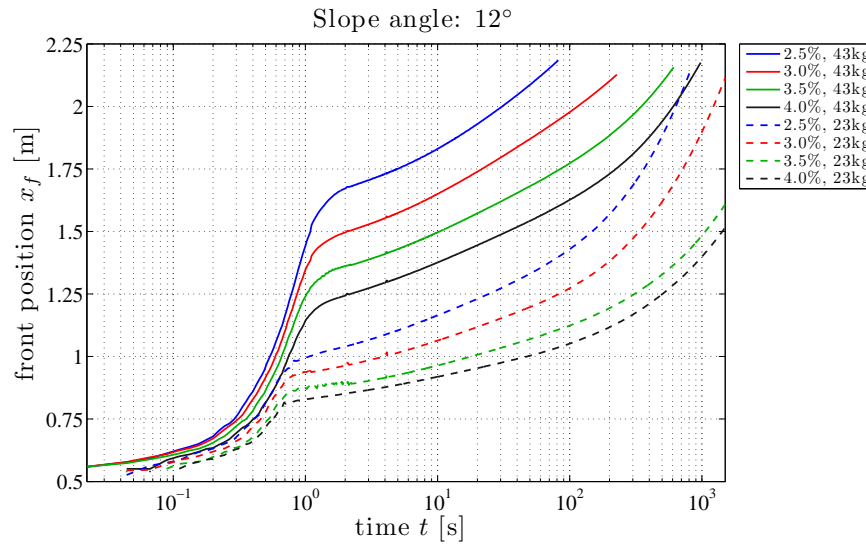
Figure 4.38: Comparison of the front positions x_f on a 12° inclined channel in a semi-log plot.

The experimental front position is compared in Figure 4.39 with the analytical solution of Huang and García [1998] (see Section 4.2.11) for 23 kg of Carbopol at a concentration C of 0.40% on a 12° slope. As it was the case for the horizontal channel, the experimental and theoretical curves are different. The experimental surge moves faster than the theoretical one during the inertial regime. The flow then slows down and exhibits a pressure gradient/viscosity balance regime (between 1 and approximately 60 s). The experimental curve is then below the predicted one. After 10^2 s, the theoretical plot starts to curve down and crosses the experimental plot at $t = 845$ s.
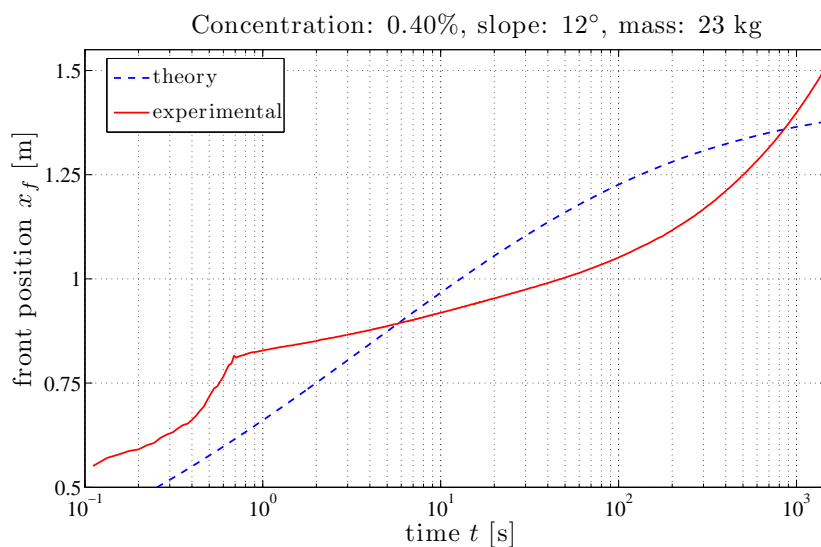
Figure 4.39: Comparison between the predicted front position and the measured one for 23 kg of Carbopol at a concentration C of 0.40% on a 12° slope.

As for the horizontal plane, a depression was created behind the junction line of the vertical and horizontal free-surfaces when the gate opened. For inclinations equal to or greater than 12°, some instabilities appear at the surface behind the depression when the material experienced was in hydrodynamic regime. Figure 4.40 shows an example of these instabilities for Carbopol at a concentration of 0.30% with a mass of 43 kg after 247 s. The initial instability started at the junction between the hollow and the wall. The following ones appeared together. They are more visible for gel with higher Carbopol concentration. The front does not show instabilities as the channalization observed on the inclined plane (see Section 4.6).
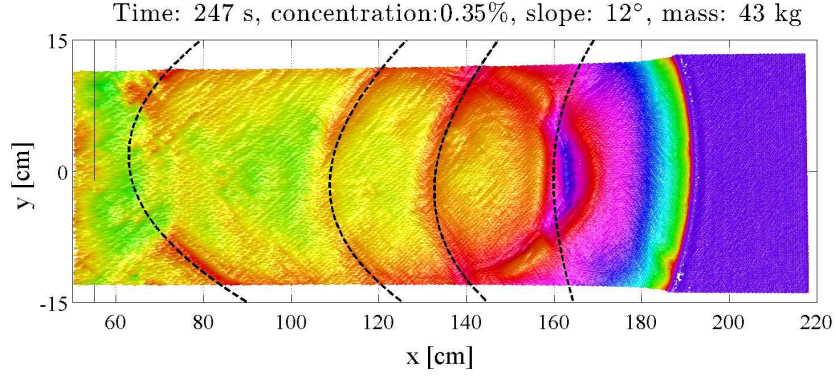
Figure 4.40: Instabilities for Carbopol at a concentration of 0.30% with a mass of 43 kg after 247 s on a slope of 12°.

4.5.3   Summary

Horizontal channel

The position and shapes of the front predicted by the theory do not follow the experimental results. Two main reasons for this difference are:

- the flow in the channel cannot be considered as a two-dimensional flow. As a matter of fact, in our setup, the channel is not wide enough to neglect the tri-dimensional effects and a two-dimensional model cannot correctly predict the flow. When releasing 43 kg of Ultrez 10, the height H is comparable with the width D of the channel. The deformation of the junction line (as describe in Figures 4.32 to 4.35) is a hallmark of tri-dimensional effects;

- the dam gate plays a key role. First, it takes some time to open (0.8 s) and does not disappear instantly when opening. Second, the gate hauled a layer of fluid upward. The layer has a velocity close to the velocity of the gate and modified the initial conditions. The fluid in the reservoir is modelled with an initial velocity $\mathbf{u} = 0$ in the theory, which is not exactly the case with our setup.

Inclined channel

As for the horizontal channel, the theoretical front position and flow profiles are not predicted properly because the flow in the channel cannot be considered as a two-dimensional flow. In our setup, the channel width is not large enough for the tri-dimensional effects to be ignored.

4 regimes were recorded on the inclined channel:

- an inertial regime;

- a pressure gradient/gravity acceleration regime;

- a regime where pressure gradient, gravity acceleration and viscosity play key roles;

- an hydrodynamic regime.

Some instabilities appear at the surface during the hydrodynamic regime for inclination of 12° or more.

4.6 Experimental dam breaks with Ultrez 10 down an inclined plane

16 tests were performed with 43 kg of Carbopol at concentrations of 2.5, 3.0, 3.5 and 0.40% on inclined plane with inclinations α of 0, 6, 12 and 18°. Table 4.3 summarize the different tests and their respective figures.

Slope	0°	6°	12°	18°
Mass	43 kg	43 kg	43 kg	43 kg
0.25%	D.2, D.3	D.10, D.11	D.18, D.19	D.26, D.27
0.30%	D.4, D.5	D.12, D.13	4.45, 4.46	D.28, D.29
0.35%	D.6, D.7	D.14, D.15	D.22, D.23	D.30, D.31
0.40%	D.8, D.9	D.16, D.17	D.24, D.25	D.32, D.33

Table 4.3: Figure reference numbers for experiments run with Ultrez 10 down a inclined plane.

4.6.1   Inclined plane

At the opening of the dam gate, the material contained in the reservoir flows and spreads down the inclined plane. The spreading along the x and y-axis depends of the fluid rheological proprieties, the plane inclination, the reservoir dimensions and the mass. During this last campaign, the same mass (43 kg) and the same reservoir dimensions were used in comparison with the inclined channel.

In the channel the principal flow direction is along the x-axis while on the inclined plane the fluid is not bounded by the channel walls and can spread. Figures 4.41 to 4.44 are snapshots of an experiment on a 12° inclined plane with a concentration C of 0.30%,

- at time $t = 0.19$ s, the dam gate started to open. The surge velocity was mainly in the x-direction;

- at time $t = 0.48$ s, the dam gate was still being lifted up. The opening height was still lower than the fluid height in the reservoir. The velocity in the x and y-direction are of the same order of magnitude;

- at time $t = 0.80$ s, the gate was fully opened. Both vertical and horizontal free surfaces had been connected approximately 0.6 s after the beginning of the test. The free surface in the reservoir presented a strong gradient, the fluid was still in the inertial regime;

- at time $t = 1.60$ s, the gel had slowed down drastically as shown by Figure 4.47 and reached the hydrodynamic regime. The free surface in the reservoir was flat.

The surge profiles and the front position for this experiment are summarized by Figure 4.45 and the contact lines are shown in Figure 4.46.

Two regimes are clearly visible from Figure 4.47: the inertial regime from 0 to 1 s and the hydrodynamic regime from 1 s. The front position accelerated during the first second before slowing down abruptly, and then slowed down exponentially. A third regime, the run-out regime, takes over the hydrodynamic regime when channelization can be observed (see Section 4.6.2). The example given here is for a 12° inclined plane with gels at different concentrations of Ultrez 10, but the same behaviour is observed for all inclinations.

Figures 4.48 and 4.49 present the contact lines at $t =$1.6 s for Ultrez 10 at different concentrations on a 12° inclined plane and the contact lines for a concentration of 0.30% down on different inclinations, respectively. Without surprise, the lower the Ultrez10 concentration is, the steeper the slope, the faster the flow (see Appendix D).
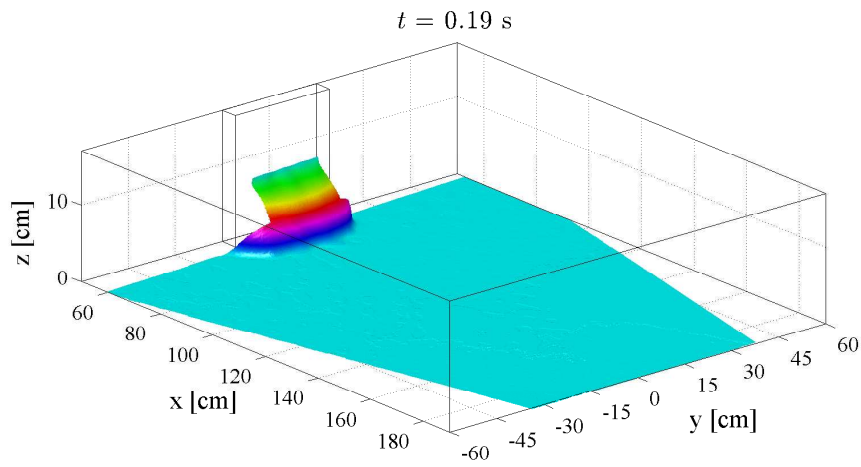
Figure 4.41: 3D view of 43 kg of Carbopol at a concentration of 0.30% down a 12° inclined plane as time $t =$0.19 s.
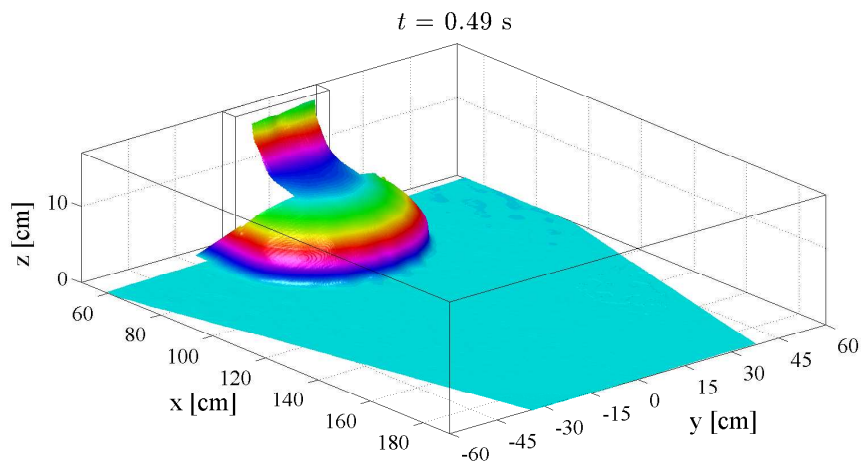
Figure 4.42: 3D view of 43 kg of Carbopol at a concentration of 0.30% down a 12° inclined plane as time $t =$0.48 s.
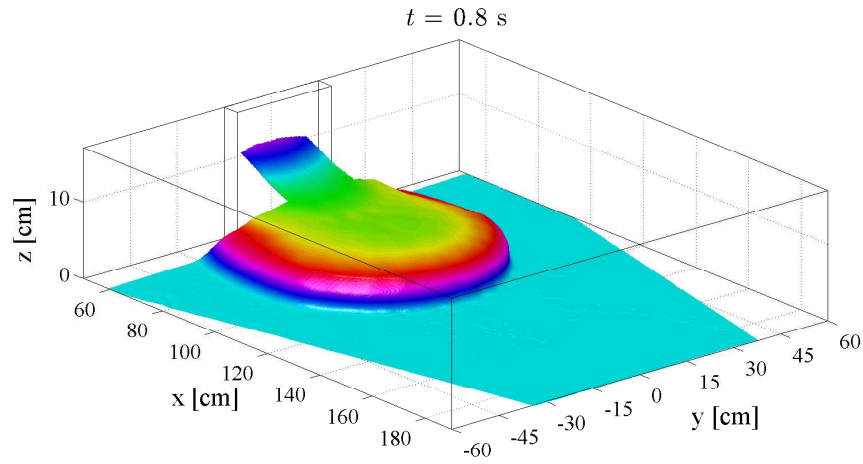
Figure 4.43: 3D view of 43 kg of Carbopol at a concentration of 0.30% down a 12°
inclined plane as time t =0.80 s.
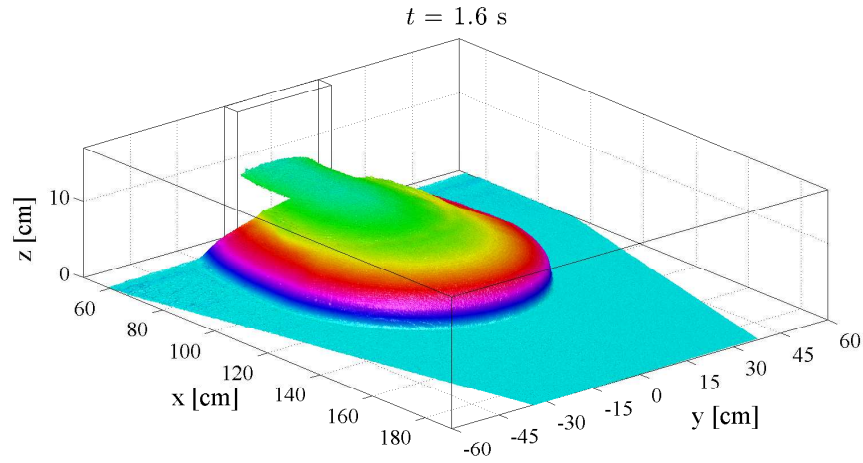
Figure 4.44: 3D view of 43 kg of Carbopol at a concentration of 0.30% down a 12°
inclined plane as time t =1.60 s.
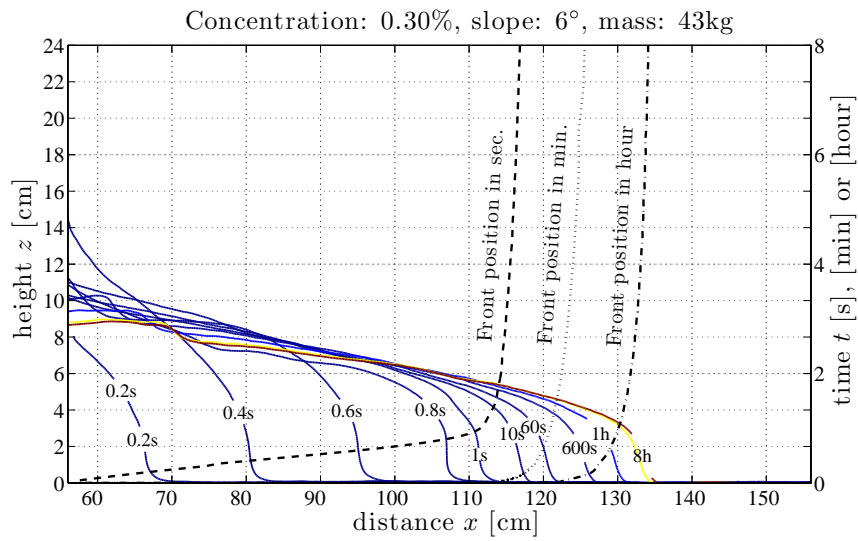
Figure 4.45: Surge profile and front position of Carbopol at a concentration of 0.30% down a 12° inclined plane.
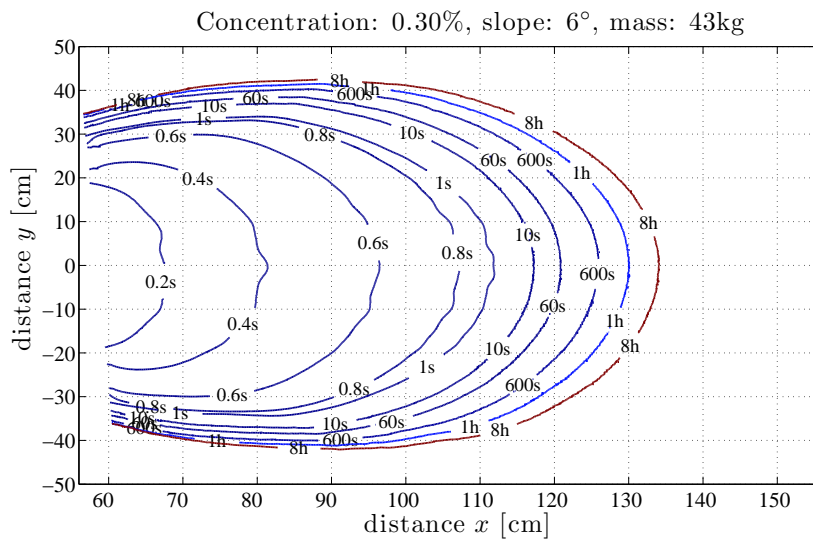
Figure 4.46: Contact line of Carbopol at a concentration of 0.30% down a 12° inclined plane.
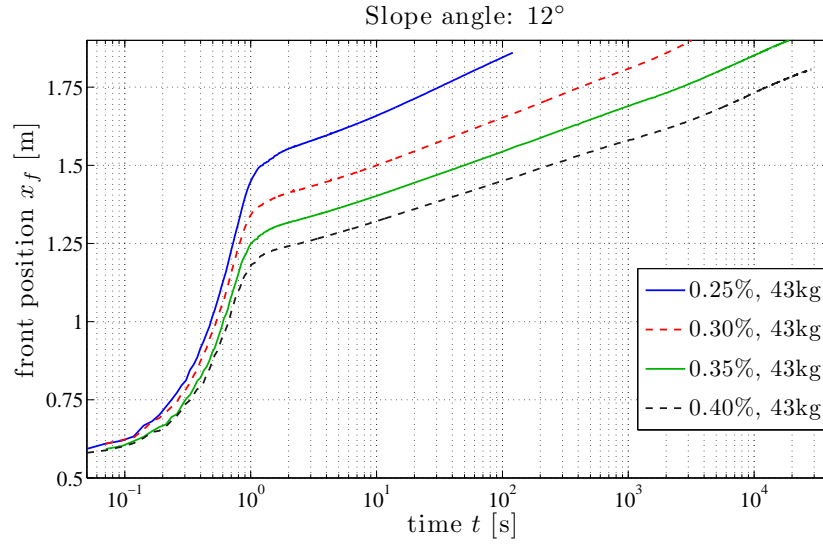
Figure 4.47: Front position for Carbopol at different concentration down a 12°
inclined plane.
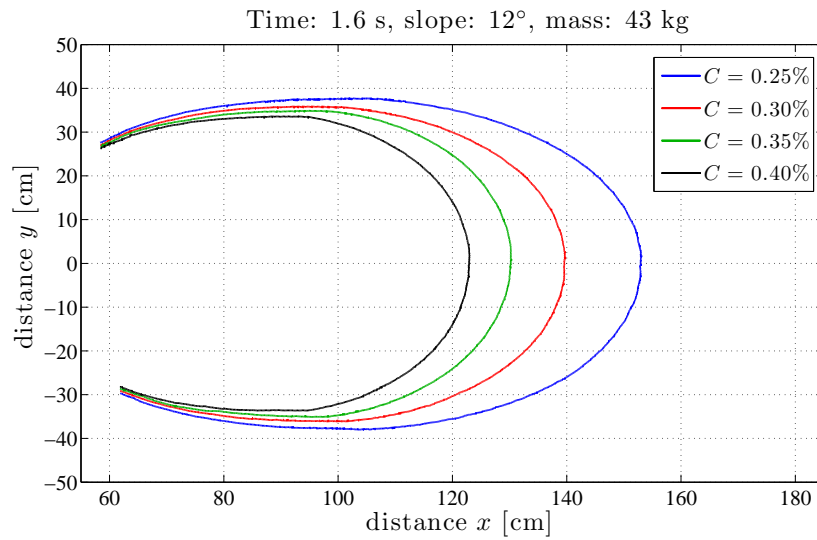
Figure 4.48: Contact line at time $t =$1.6 s for Carbopol at different concentration
down a 12° inclined plane.
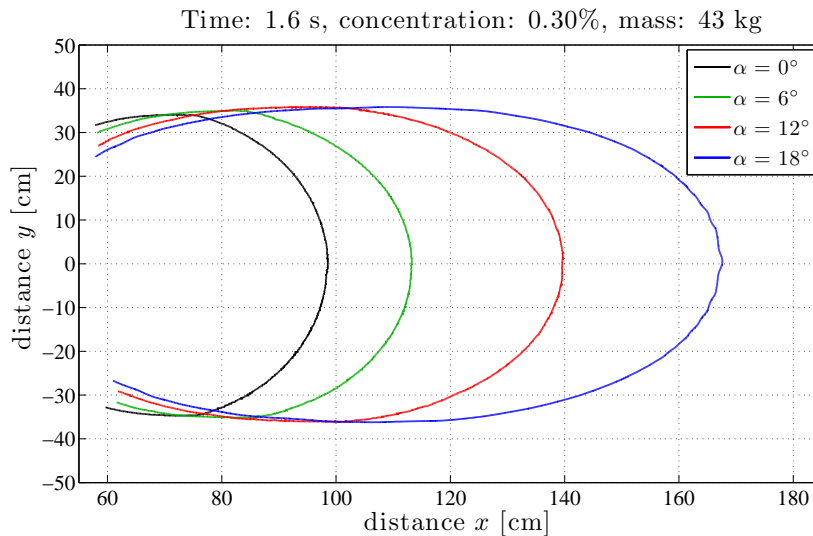
Figure 4.49: Contact line at time $t =$1.6 s for Carbopol at a concentration of 0.30% down inclined planes.

A comparison between the CFD code used at LHE (see Section 4.2.12) and an experiment with $C = 0.25\%$, $\alpha = 12°$ and $m = 43$ kg is presented in Figures 4.50 to 4.53 for time t equals to 0.5, 1.0, 2.0 and 5.0 s respectively [Rentschler and Ancey, 2007]. The CFD results is faster than the experimental result because the opening of the dam gate is not simulated, creating a larger opening than in reality. The CFC results then under-predict the front position. The width of the surge is also well predicted even if, like the front position, its position is closer to the reservoir than for experimental results. The height of the fluid remaining in the reservoir is over-predicted by the numerical model.

4.6.2 Surface structure formation

For all tests, surface structure formation was observed during the run-out regime (see Figure 4.54). Here, 'surface structure formation' means that several valleys formed in opposition to the occurrence of a single flowing channel in the middle of a plugged volume as described by Coussot et al. [2002] or Kerr et al. [2006]. The higher the Ultrez 10 concentration is, and the steeper plane inclination is, the deeper the channels. The valleys are symmetric around the y-axis and aligned with the flow directions. The surface structure formation starts in area where the shear stress is closed to the yield stress. If a plug region forms, the flow passes by and gains some velocity. By doing so, the shear stress increases and the
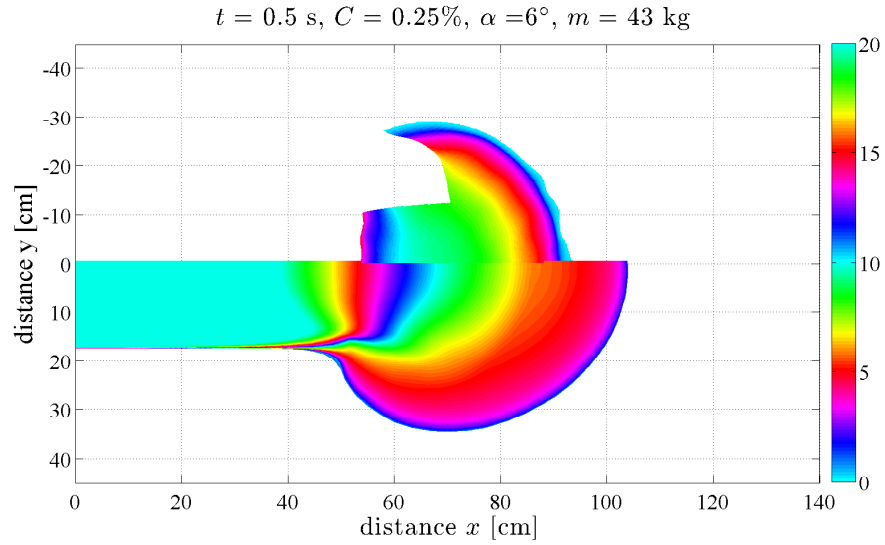
Figure 4.50: Comparison between experimental result (upper half) and CFD result (bottom half) for test with $C = 0.25\%$, $\alpha = 12°$ and $m = 43$ kg at $t = 0.5$ s.
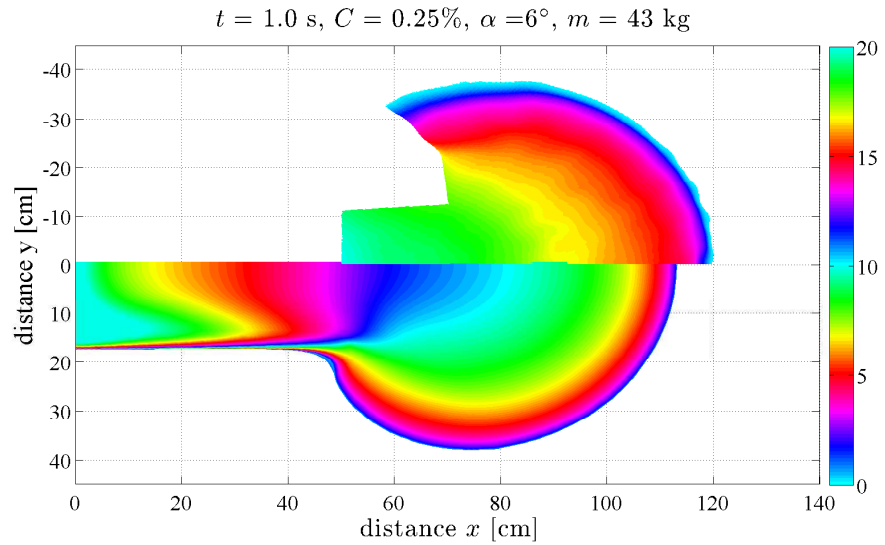
Figure 4.51: Comparison between experimental result (upper half) and CFD result (bottom half) for test with $C = 0.25\%$, $\alpha = 12°$ and $m = 43$ kg at $t = 1.0$ s.
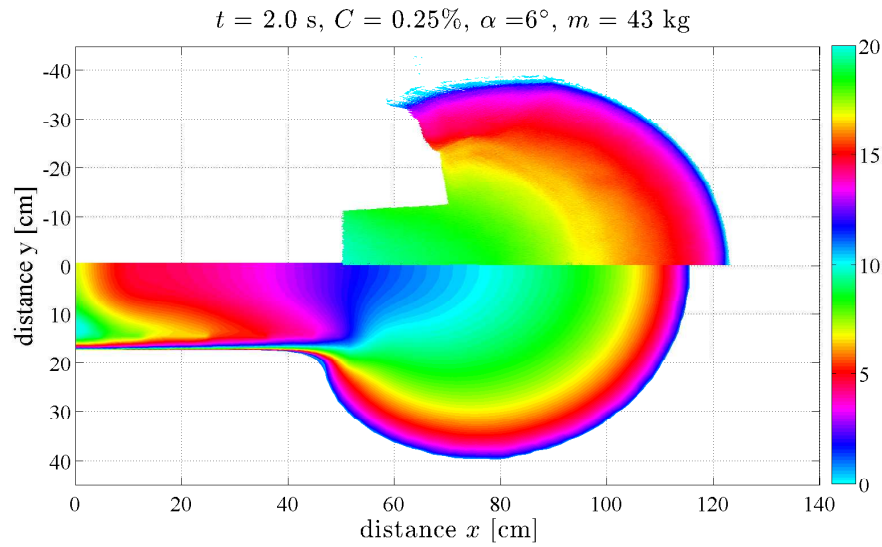
Figure 4.52: Comparison between experimental result (upper half) and CFD result (bottom half) for test with $C = 0.25\%$, $\alpha = 12°$ and $m = 43$ kg at $t = 2.0$ s.
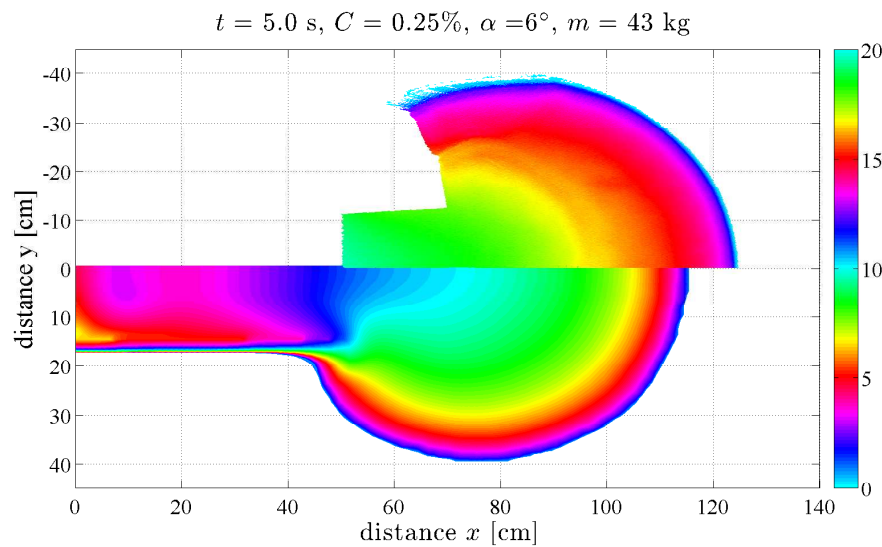
Figure 4.53: Comparison between experimental result (upper half) and CFD result (bottom half) for test with $C = 0.25\%$, $\alpha = 12°$ and $m = 43$ kg at $t = 5.0$ s.

viscosity decreases amplifying the surface structure formation process.

During the run-out regime, flow velocity was very low (the front moves at 0.5 mm/h for the test with $C = 0.25\%$ on an horizontal plane after 12 hours), but did not drop to zero.
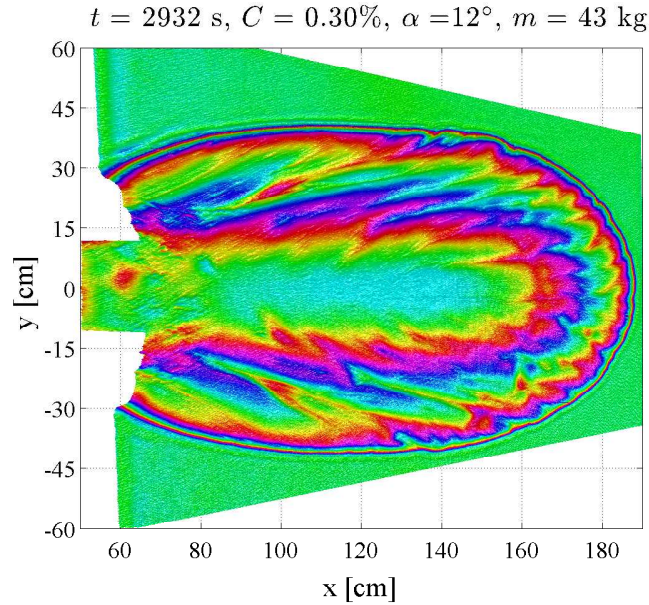
Figure 4.54: Top view of surface structure formation at time $t = 2932$ s of a test with $C = 0.25\%$ and $\alpha = 12°$.

4.6.3 Summary

Dam breaks on inclined planes showed three regimes,

1. Inertial regime. The gel left the reservoir with high velocity and spread down the inclined plane.

2. Hydrodynamic regime. The flow slowed down abruptly and then the front velocity decreased exponentially.

3. Run-out regime. The surge slowed down exponentially but did not stop even after 12 hours. During the run-out regime channelisation was observed and small channels appeared on the surface as illustrated by Figure 4.54.

4.7 Conclusion

Tests were repeated to gauge the reproducibility and precision of the experiments. The tests demonstrate that the handling of the boundary conditions, the smoothing of the free surface in the reservoir, is a key issue to obtain valuable results. If similar boundary conditions are achieved then similar results are recorded within an error of the order of 5 mm on a surface of 1.2 m^2.

Three measurement campaigns were carried out:

1. With glucose syrup as Newtonian fluid down inclined channels. This preliminary experiment was designed to test our setup. Analytical solutions were compared with experiments for horizontal and inclined channels. Viscous regime solutions proposed by Nakaya [1974], Huppert [1982a] and Debiane [2000] showed good agreements in the horizontal case even if the predicted front positions were faster than the recorded ones (see Section 4.2.7). Delay can be partly explained by tri-dimensional effects of the flow and the shear stress at the canal walls. Then comparisons were done between the depth-averaged equations proposed by Hunt [1984] together with Debiane [2000] and experimental results obtained with the inclined channel (see Section 4.2.10). The predicted front positions were also faster than the measured ones, which can be explained by the shear stress at the canal side walls.

2. With Carbopol as a viscoplastic fluid down inclined channels. Four flow regimes were observed:

   - an inertial regime during the first second;
   - a pressure gradient/gravity acceleration regime for t varying from 1 to 30-60 s;
   - an intermediate regime where the dominant balance is between pressure gradient, gravity acceleration and viscosity;
   - a hydrodynamic regime where the flow slows down exponentially;
   - a run-out regime where instabilities occur on the surface.

   For the horizontal case, the gravity acceleration term is perpendicular to the flow direction. The front position slows down exponentially toward zero. During the campaign, only one stop had been observed after 29 hours.

   Two theoretical approaches were compared with our experimental results: first, the viscous regime solution proposed by Balmforth et al. [2007], and second, the depth-averaged solution proposed by Huang and García [1998]. Both approaches were compared with experiments on channels inclined from

0 to 24° without success (see Section 4.2.8 and 4.2.11, respectively). For viscoplastic materials the width of our canal can not be neglected in comparison with the height of the flow and a two-dimensional approach is not valid.

3. With viscoplastic material down inclined planes. The material can spread on the inclined plane. Three regimes where recorded:

   - an inertial regime during the first second;
   - a hydrodynamic regime where the front velocity decreases exponentially;
   - a run-out regime with channelization.

The comparison with the computational fluid dynamics (CFD) developed at LHE are promising even if the predicted flow is slightly slower than the experimental results.

CHAPTER 5

Conclusion

THE objective of this thesis was to improve our understanding of gravity-driven geophysical flows by developping a new platform to simulate avalanches of fluid in the laboratory.

The governing equations used for modelling gravity-driven flows are not intrinsic to the phenomena. They are a versatile set of equations used for describing various flow conditions ranging from flash floods to rockfalls and volcano lava flows. They are not related to a unique setting; they have been used for describing both large-scale flows (e.g., rivers) and small-scale (e.g., in the laboratory, flume experiments) flows. The only varying element is energy dissipation, the expression of which is adjusted empirically depending on the flow features. Essentially, our idea was to test the shallow-flow equations under extreme conditions in a well-controlled environment—the laboratory—where both the initial and boundary conditions are prescribed. Here, 'extreme conditions' mean that we focus our attention on time-dependent flows (surges with a front) mobilizing Newtonian or non-Newtonian fluids, experiencing different stages from release to run-out: acceleration (balance between inertia and pressure gradient), a nearly fully developed regime (flow at equilibrium), and deposition (predominance of dissipation processes).

With the experiments carried out so far, there is no clear evidence that there are scaling problems with gravity-driven flows. Furthermore and probably more fundamentally, the equations currently used for modelling natural flows hold for any scale. So, in this respect, it is shrewder to take benefit from this scale invariance and conduct experiments on the laboratory scale, where probing can be performed at lower cost and more extensively than in the field.

In our laboratory, we built a platform equipped with two inclined planes: the

upper plane is 4-m long while the run-out plane is 1.5-m long. The upper plane is inclined at steep angles, enabling the fluid to go through different regimes. The run-out plane forces the flowing material to undergo a transition from a flow regime to a deposition (run-out) regime. The typical experimental procedure is quite simple: first, the fluid is poured into a box closed by a sluice gate. This gate is opened very fast (within 0.8 s) thanks to two pneumatic jackets and unleashes the fluid onto the steep plane. The fluid then accelerates vigorously, at times finds a pseudo equilibrium state, where the velocity is nearly constant, and eventually decelerates quite rapidly. Compared to true flow avalanches, we are able to fully control the initial and boundary conditions, the nature of the flowing material (e.g., rheological properties), and the flow geometry. We can also measure all what is needed to test the efficiency and reliability of governing equations worked out for describing highly complex, non-equilibrium, nonlinear flows.

Impediments to accurate measurements of the free surface evolution are, however, many because of the significant variations in its curvature and velocity.The deformation of the free-surface was used to follow the evolution of the flow and to determine the different regimes. To accurately measure the surge's free-surface variations with time, we have developed a new imaging system, consisting of a digital camera coupled with a synchronized micro-mirror projector. The object's surface is imaged into a camera and patterns are projected onto the surface under an angle of incidence that differs from the imaging direction. From the deformed pattern recorded by the camera, the phase can be extracted and, by using unwrapping algorithms, the height can be computed and the free surface reconstructed. We were able to measure the free surface of the flow to within 1 mm over a surface of 1.4×1.4 m^2 at a frequency of 45 Hz. The system is innovative and more efficient than most methods used to date in practical applications.

Carbopol Ultrez 10 was used as a viscoplastic material. Viscoplastic material are commonly described by the Herschel-Bulkley model ($\tau = \tau_c + K\dot{\gamma}^n$). This model is based on the concept of a yield stress τ_c. The yield stress τ_c is the critical shear stress that must be exceeded before flow occur. It is quite difficult to measure τ_c directly. Most of the time, τ_c is evaluated by extrapolating the flow curve to at $\dot{\gamma} = 0$. At very low shear rates the concept of yield stress was demonstrated erroneous since the yield-stress value depends on the measurement duration. Even through the yield stress is questioned as a physical property, the concept of yield stress remains very useful for a wide range of applications. We arbitrary chose to 'measure' the yield stress with a 6-min creep test. The test is conducted as follows, using a coaxial cylinder geometry:

- the sample is sheared under a constant stress for 6 minutes and the curve compliance J/time t is recorded. When not flow occurs the plot tends toward a plateau;

- the same test is repeated with higher stresses until the curve diverges from the previous ones. The stress increment is 1 Pa.

Slip appears when physico-chemical forces repelled the polymer chains from the walls and create a water layer. Because of molecules' migration, a very narrow layer of water is created between the walls and the gel. The water layer acts as a lubricator and the Carbopol gel slips over it. Slip can be avoid by roughening the surfaces or by coating them. We chose to roughen the geometries of the rheometer with sandpaper and to coat the inclined plane with a special paint. Nevertheless, to ensure that no slip occurred during the dam-break experiment, a sample of Carbopol was placed on the plane and let for the duration of the test. If the sample did not move during the test, we can be confident that not slip occurred.

During a test, the flow experienced different regimes depending on the balance between the driving forces, which are: inertia, gravity acceleration, pressure gradient, and viscous forces. Analytical solutions can be computed for some regimes. When the slope is gentle and the dominant balance is between pressure gradient and viscous stresses, a solution can be worked out for the viscous regime. When there is no dominant balance, the full governing equations have to be solved, which is a difficult task, even numerically. To simplify the problem, the flow-depth averaged equations can be used. Viscous regime and flow-depth averaged solutions are proposed for both, Newtonian and Herschel-Bulkley fluids down a channel. The tests on the inclined plane where compared with computational fluid dynamic simulations.

56 experiments were carried out with viscoplastic gels and Newtonian fluids on inclined channels and planes. For each test, the evolution of the free surface was recorded in three dimensions. We then compared our experimental results with both theoretical predictions: the viscous regime and the flow depth-averaged solutions.

- For Newtonian fluids down inclined channels, we observed three flow regimes:

    - a pressure gradient/viscosity regime;
    - a transition regime;
    - a gravity/viscosity regime.

  Viscous regime solutions proposed by Nakaya [1974], Huppert [1982a] and Debiane [2000] which were in good agreement wit our data for the horizontal case, although the predicted front positions were faster than the recorded ones. Delay can be partly explained by three-dimensional effects of the flow and the channel side wall friction. Then comparisons were done between the flow depth-averaged equations proposed by Hunt [1984] together with

Debiane [2000] and experimental results obtained with the inclined channel (see Section 4.2.10). The predicted front positions were also faster than the measured ones, which can be explained by the shear stress at the channel side walls.

- For viscoplastic gels down inclined channels, we observed four regimes:

    - an inertial regime;
    - a pressure gradient/gravity acceleration regime;
    - a transition regime where the dominant balance is between pressure gradient, gravity acceleration and viscosity;
    - a hydrodynamic regime where the flow slows down exponentially;
    - a run-out regime where instabilities occur on the surface.

For the horizontal case, the front velocity slows down exponentially toward zero. During the campaign, only one stop had been observed after 29 hours.

Two theoretical approaches were compared with our experimental results: first, the viscous regime solution proposed by Balmforth et al. [2007], and second, the flow depth-averaged solution proposed by Huang and García [1998]. The predicted solutions were compared with experiments on channels inclined from 0 to 24° without success. For viscoplastic materials, the width of our channel cannot be neglected in comparison with the height of the flow and a two-dimensional approach is not valid.

- For viscoplastic gels down inclined planes, we recorded three regimes:

    - an inertial regime;
    - a hydrodynamic regime;
    - a run-out regime with channelization.

The computational fluid dynamics (CFD) simulation overestimated the velocity of the front during the inertial regime and underestimated it during the viscous regime. The difference between the front velocities can be explained by the fact that the dam gate disappeared instantaneously at $t = 0$ s in the simulations. A more realistic implementation of the dam-gate opening is underway.

During the 56 experiments our setup:

- measured the free-surface of the surges very accurately over 1.2 m^2 surface;

- made reproducible tests easy;

- was very versatile. It recorded flow velocities ranging from 1 m/s to 0.5 mm/h;

- recorded long experiments. One test lasted 2.5 days (which was not limited by our setup);

- allowed parametric studies. To speed up calculation, we used a grid of 8 CPUs, which made possible the reduce of computational time from one week to one day, enabling us to conduct more experiments and apply more complex processing algorithms;

- was easily to handle by one experimentalist. The setup was design to be manipulated by just one person, which is an advantage when running long experimental campaigns.;

- proposed many algorithms to compute the free-surface height. This allow a fine tuning of the quality of the results depending on the quality of the grabbed images;

- created a large database which is accessible to the scientific community upon request[1].

Further investigations

The setup is fully operational. Additional campaigns should be carried out, as the platform was designed to allow for fast parametric studies. In my opinion we should further investigate:

- viscoplastic material on steeper slopes;

- viscoplastic material with different yield stresses;

- different reservoir sizes with different volumes of material;

- thixotropic materials;

- topographies. The inclined plane could be covered with different topographies to test the behaviour of non-Newtonian fluids with obstacles.

---

[1]The 3-dimensional results can be obtained by e-mailing the author at: steve.cochard@a3.epfl.ch.

APPENDIX A

Fluid preparation

Two different fluids were used on our setup:

- a glucose syrup, as a Newtonian fluid

- a stable polymeric gel, as a viscoplastic material.

Those fluids fulfill the following requirements. They are:

- non toxic, as the setup is open;

- reproducible;

- white or can be coloured in white to ensure a good reflectivity so the measurement system retrieve as much light as possible (see Sect 2.3.3);

- cheap, as each test can involve up to 120 l.

A.1 Viscoplastic fluid: Carbopol Ultrez 10

Carbopol Ultrez 10 polymer is an 'easy to disperse' crosslinked polyacrylic acid polymers synthesized in a toxicologically preferred cosolvent system of ethyl acetate and cyclohexane. Ultrez 10 is supplied as dry powder of tightly coiled acidic molecules. Once dispersed in water, the molecules begin to hydrate and partially uncoil [see Figure A.1(a)]. The solution is then acid (approx. pH of 3). To achieve maximum thickening from Carbopol polymer is by converting the acidic Carbopol polymer to a salt. This is easily achieved by neutralizing the Carbopol with a common base such as sodium hydroxide (NaOH) [Nov, 2002]. The polymers, once neutralised (pH of 7-8) and uncoiled, reach a volume one thousand bigger that their initial volume and modify the rheology of the solution.

Once neutralised Ultrez 10 behaves as a viscoplastic fluid. Its flow characteristics are equivalent to the Carbopol 940.
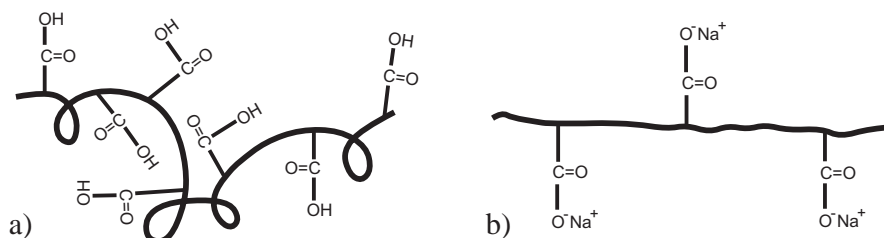
Figure A.1: Molecule of polymer; a) in coiled state and b) neutralised with NaOH and uncoiled.

A considerable amount of works had been published using Carbopol 940 as a viscoplastic material [e.g., see Roberts and Barnes [2001], Wu and Kwak [1999] or Atapattu et al. [1995]]. Unfortunately, Carbopol 940 proved to be cancerous. We therefore chose Carbopol Ultrez 10 which is safer, easier to handle and its proprieties are closed to those of Carbopol 940.

The advantages of using Ultrez 10 are listed:

- self-wetting polymer. The polymer is dispersed over the water-surface and wets itself within 30 minutes. Ultrez 10 is easy to handle;

- the yield stress and the 'viscosity' are adjusted by changing the concentration of polymer mixed in the water and the pH of the solution;

- Carbopol Ultrez 10 is not thixotropic. The shear stress does not depend on the history of the strain rate;

- the polymeric gel is not temperature dependent in our range of use. The laboratory has an air conditioning system, which ensures a room temperature between 19.5°C and 20.5°C and the gel is not heated during it preparation;

- very stable. It can be stored over long period of time without aging in a closed barrel;

- easy to clean;

- has no impact on environnement.

The drawbacks of using Ultrez 10 are:

- few experiment have been done with Ultrez 10. Most of the research works have been carried out with Carbopol 940. The internal mechanisms of the Ultrez 10 are poorly understood;

- very sensitive to ions concentrations and pH. The material change drastically its characteristics with those two parameters. A great care is necessary when filling the barrel with demineralized water;

- on one hand the Ultrez 10-water solution is acid and on the other hand the water-sodium hydroxide solution is basic, both solutions are potentially dangerous;

- the material dries if not confined. 99.5% of the mass of the gel is composed of water, so if the gel has a free-surface in contact with air it dries. The relative humidity in the laboratory is set to 70% to reduce this effect, but cannot be increased because some measurement devices were not designed to sustain higher humidity;

- surface interaction and slip.

A.1.1 Preparation of Carbopol Ultrez 10

The preparation of Carbopol Ultrez 10 can be broken down into 12 points:

1. A predefined quantity of Carbopol was gently dispersed over the surface of 40 l of demineralized water contained in a 65-l barrel.

2. The solution was let at rest for at least 2 hours, until the Carbopol had completely drowned.

3. 50 gr of titanium dioxide was then added as well as approx. 10 l of water to obtain a total of 50 kg. This extra water allowed Carbopol, which was deposited on the side of the barrel, just over the water surface, to wet. The solution was then left at rest for at least 2 hours.

4. The water-Carbopol solution was then gently mixed with a 613×103-mm diameter paint stirrer adjusted on a drilling machine. The solution was mixed from the bottom up, eliminating injection of air, until the bubbles formed on the surface disappeared.

5. The solution is left at rest for one night.

6. The right amount of sodium hydroxide (NaOH), for the given quantity of Carbopol (in our case 414.69 gr of NaOH per kg of Carbopol Ultrez 10), was dissolved in water. Water was then added until the mix weighted 10 kg.

7. The water-Carbopol solution was gently mixed until the TiO_2 which had deposited on the bottom of the barrel was dispersed and coloured the solution in white.

8. The water-sodium hydroxide was then poured into the water-Carbopol solution and the resulting solution was mixed from the bottom up at high rotation speed to blend it homogeneously. Once the chemical reaction started to occur and the fluid viscosity to increase the mixing is stopped.

9. The solution was left at rest at least 12 hours.

10. The barrel was weighed before the Carbopol was poured into the reservoir.

11. The barrel was weighed a second time to adapt the total mass which had been poured.

12. The pH and the rheology of Carbopol are tested on a sample.

13. The plane was inclined and the surface smoothed to the horizontal by hand and checked with a slope gauge.

14. approx. 80 gr of Carbopol were placed on the lower part of the inclined plane, outside the measurement area, just above a colour mark. The sample was left until the test was finished to ensure that no slip occured.

15. The test started when opening the dam sluice gate.

A.2   Newtonian fluid: glucose syrup

Oils and sugar syrups are two common Newtonian fluids with a large range of viscosity available. A glucose syrup was preferred over oil for the following reasons:

- glucose syrup can be cleaned up with hot water without recourse to solvents;

- the viscosity can be adjusted with the water content;

- many flow measurements have already been performed with glucose syrup;

- oils tend to diffuse thought PVC and carbon which are the main components of our canal.

The drawbacks of using glucose syrup are:

- the syrup has to be prepared as it can not be found for sale within the commerce for the desired viscosity (approx. 300–400 Pa s);

- the syrup is unstable and crystallises easily. Crystallisation is initiated by impurities. In order to whiten the solution, titanium dioxide (TiO_2) is added to the solution, the glucose crystal germinate around the small TiO_2 particles. The syrup, with added titanium dioxide crystallises within 2 days;

- the solution need to be heated up to 110°C to liquefy. Unfortunately the glucose colours dark when heated due to Maillard reactions [Bostan and Boyacioglu, 1997]. Coloration is an exponential function of time and temperature. It is important to cool down the solution as soon as it has reached the temperature of 110°C and not leave it in the oven;

- the viscosity is very dependent of the temperature as illustrated by Figure A.2. Around 20°C, the viscosity variation is more than 10% per degree Celsius.

Glucose syrup is easier to clean up and safer for the setup than oil, but is more delicate to prepare and manipulate.

A.2.1   Preparation of the glucose syrup

The syrup viscosity was set to 350 Pa at 20° so that the front of the surge was crossing the area of measurement (approx. 2.5 m) in a couple of minutes.

The syrup is obtained by heating white crystal glucose monohydrate and demineralized water. Glucose monohydrate is glucose anhydrous (or pure glucose) with 9.08% of water. From now on, 'glucose' refers to glucose monohydrate if not
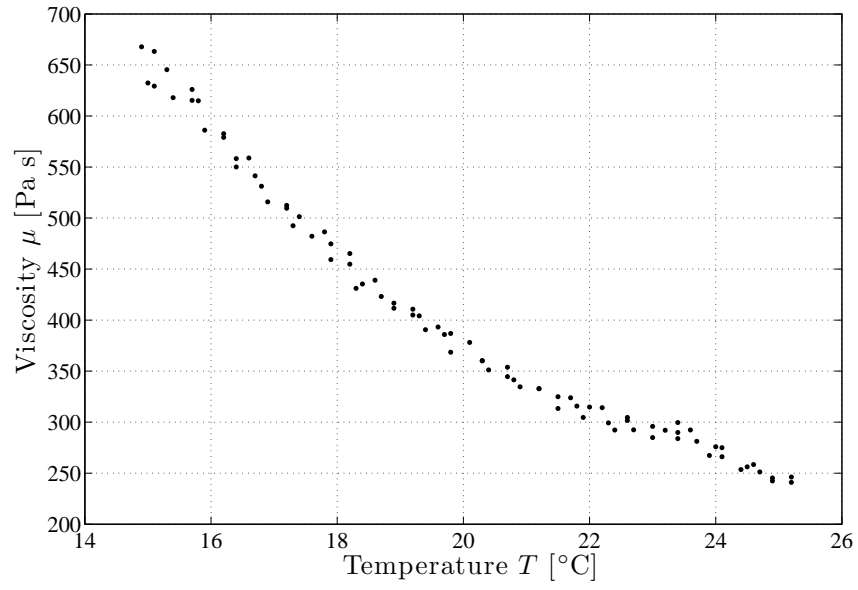
Figure A.2: Viscosity μ vs temperature T for a solution of 96% of mass of mono-hydrate glucose (approx. 87% of glucose anhydrous). At 20°C, the viscosity varies more than 10% per °C.

specified. Titanium is added and mixed with glucose before the solution is heated to ensure homogeneous colour.

Figure A.3 shows the viscosity μ as a function of the glucose concentration at 20°C [Debiane, 2000]. To reach a viscosity of 350 Pa, the syrup has to contain 96% in mass of glucose for 4% of water. At ambient temperature the maximum solubility of glucose in water is 50% in mass. At ambient temperature, the maximum possible concentration of glucose produces a solution with a viscosity of 0.012 Pa s (approx. 10 times greater than the viscosity of water). Glucose solubility increases rapidly with the temperature increase. A syrup with 96% of glucose (87% of glucose anhydrous) can only be obtained if the solution is heated to 110°C (see Figure A.4).
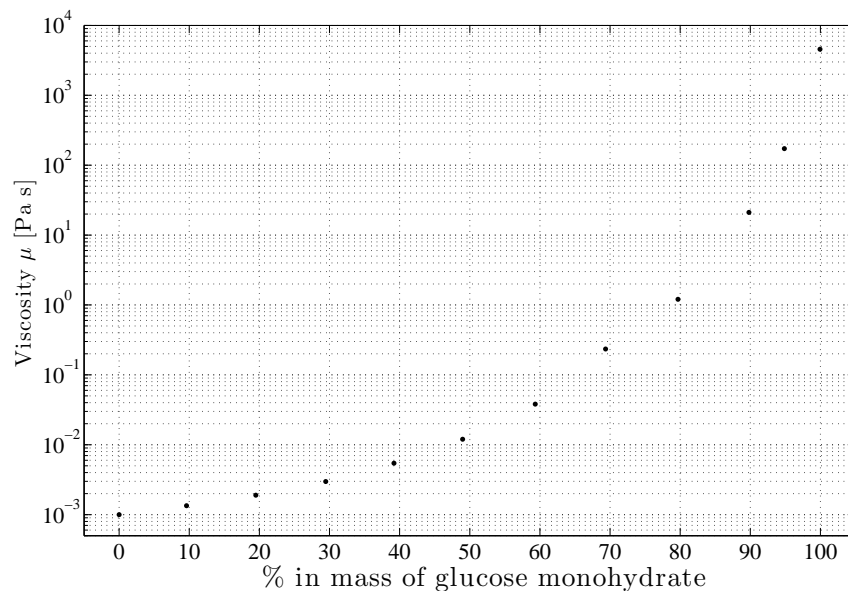
Figure A.3: Viscosity μ of a glucose-water syrup in function of the glucose mono-hydrate concentration at 20°C. After Debiane [2000].

Once the temperature of 110° reached, the solution is cooled down as fast as possible, for two reasons:

- to stop the Maillard reactions and the browning of the solution [Bostan and Boyacioglu, 1997];

- to reach an unstable over-saturated solution at 20°C. If cooled down fast glucose molecules do not have sufficient time to rearrange them-self in crystal [see Figure A.4 (d-f)]. At 20°C, the high viscosity strongly slows down the

rearrangement of the molecules into crystal. The solution it unstable and crystallises usually within 3 days. The temperature range between 30°C and 50°C favors this crystallisation and has to be avoid [see Figure A.4 (f)]. In this range, thermal agitation is strong enough to overcome viscosity; the energy needed to rearrange the molecules is low.
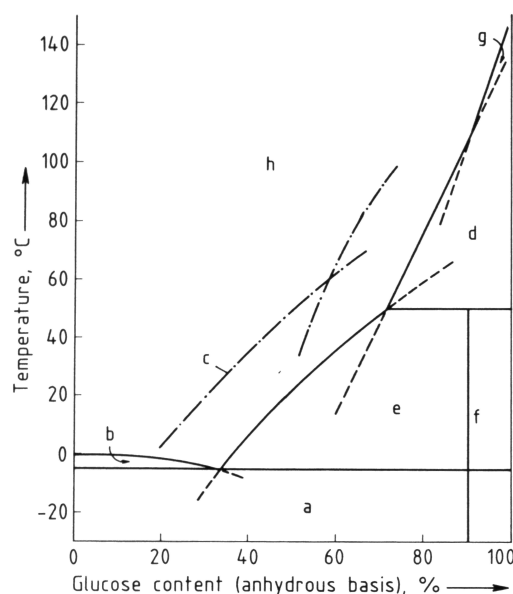
Figure A.4: Phase diagram for glucose-water solutions, a) α-glucose monohydrate and ice, b) ice and solution, c) solubility of glucose in water, before mutarotation to α-,β-equilibrium, d) anhydrous α-glucose and solution (α-, β-equilibrium), e) α-Monohydrate and solution (α-,β-equilibrium), f) α-glucose (monohydrate and anhydrous), g) β-glucose and solution, h) unsaturated solution. After Schenck [1989].

The preparation of the glucose syrup can be broken down into 13 points:

1. 50 gr of titanium dioxide were mixed with 25 kg of glucose in a 100 l steel drum and put in an oven at 130°C. The solution was often mixed to homogenised the temperature.

2. At around 60°C, when the volume of the solution was reduced, another 25 kg of glucose were added. The solution was frequently mixed.

3. Once the 50 kg at 60°C, the last 25 kg of glucose were added as well as the

demineralized water (3.3 l in our case). The solution was mixed on a regular basis.

4. Once the temperature of 110° reached, we checked that the solution was liquid and did not contain any more crystals of glucose. To ensure that there were not crystals left, the mixing propeller was carefully analysed once removed from the solution. If some crystals were found on the propeller, the solution was left for an extra-time in the oven.

5. A sample of the syrup was cooled down to 20°C and its viscosity was measured with a cone-plate rheometer (see Figure A.5). Depending of the results, water was added or removed until the desired viscosity was obtained.

6. Once the viscosity adjusted the steel drum was withdrawn from the oven and cooled down by spraying cold water. A radiator, running cold water, was also inserted into the solution to cool it down more rapidly. The radiator was necessary as the syrup had a very poor heat conductivity.

7. The drum was weighed.

8. Once the solution was cooler than 25°C, it was poured into the reservoir and left overnight with the radiator running in a closed circuit. The radiator was running with 10 l of water, which were cooled by the room temperature.

9. The radiator is removed and the solution is left at rest for a couple of hours to ensure that most bubbles were risen.

10. The drum was weighed a second time to adapt the total mass, which had been poured in the reservoir.

11. Before starting the test and releasing the syrup, the temperature was taken at different positions in the reservoir to ensure the homogeneity.

12. A final sample is tested in the rheometer.

13. The test was started by opening the dam sluice gate.
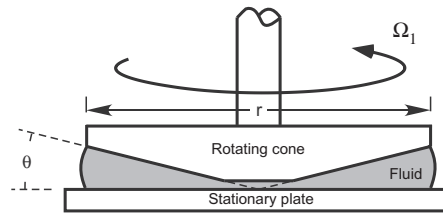
Figure A.5: Cone and plate rheometer. The fluid is contained between the stationary plate and the rotating cone. The cone plate geometry is in many instance the ideal measurement geometry; it has an almost *constant shear rate* across the gap. For a 4° cone the shear rate vary by less than 5% across the gap giving data with approx. 0.3% of error.

Glucose syrups down channels
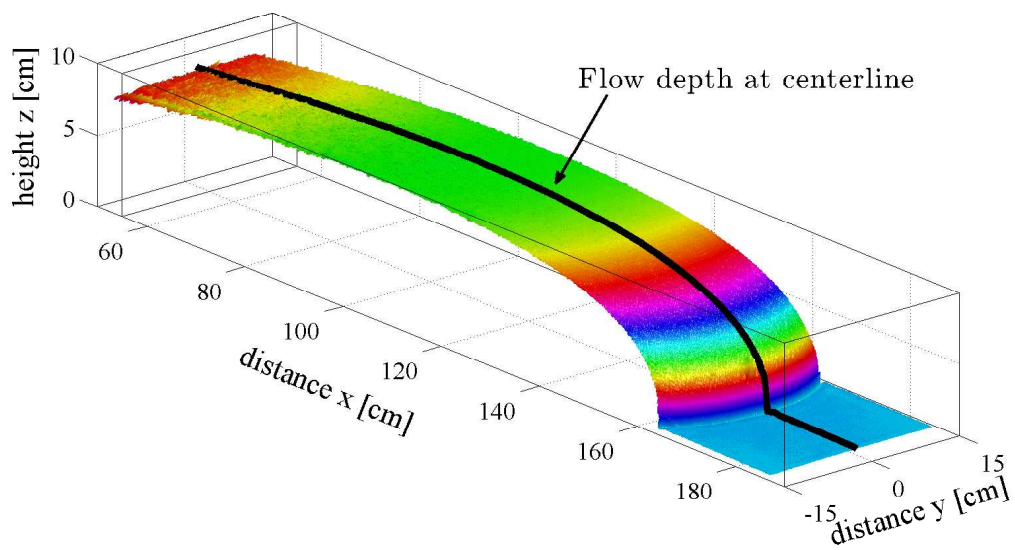
Figure B.1: 3D view of glucose syrup down a 12° inclined channel at time $t=$ 27.7 s.

α [°]	mass [kg]	h_0 [cm]	H [cm]	μ [Pa s]	ρ [Kg m^{-3}]	Figures
0	56.1	25.8	25.8	345	1420	Figures B.2 and B.3
6	56.7	26.1	28.8	352	1420	Figures B.4 and B.5
12	57.0	26.2	31.6	352	1420	Figures B.6 and B.7
18	57.6	26.5	34.8	345	1420	Figures B.8 and B.9
24	50.8	23.4	34.7	345	1420	Figures B.10 and B.11

Table B.1: Experimental parameters: h_0 is the flow depth when the canal is in horizontal position while H is the flow depth at the dam gate when the canal is inclined.

B.1 Channel slope angle: 0°
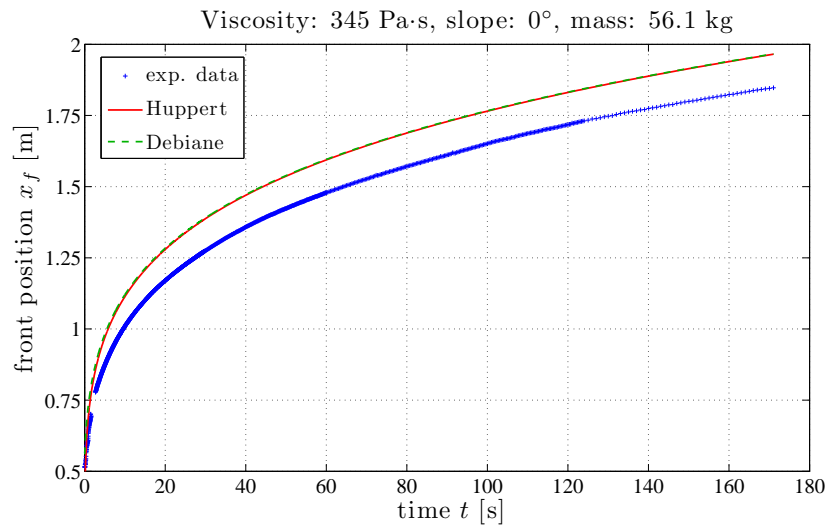
Figure B.2: 56.1 kg of glucose syrup with a viscosity of 345 Pa·s on a slope of 0°.
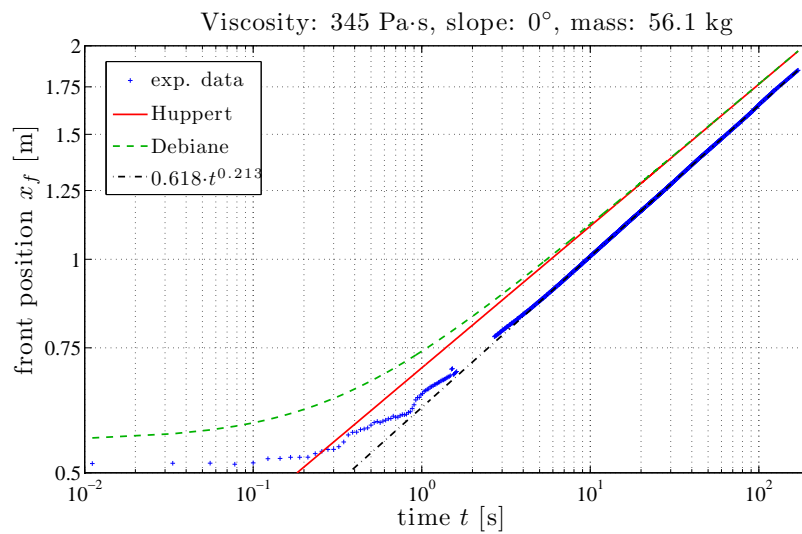
Figure B.3: 56.1 kg of glucose syrup with a viscosity of 345 Pa·s on a slope of 0°.

B.2   Channel slope angle: $6°$
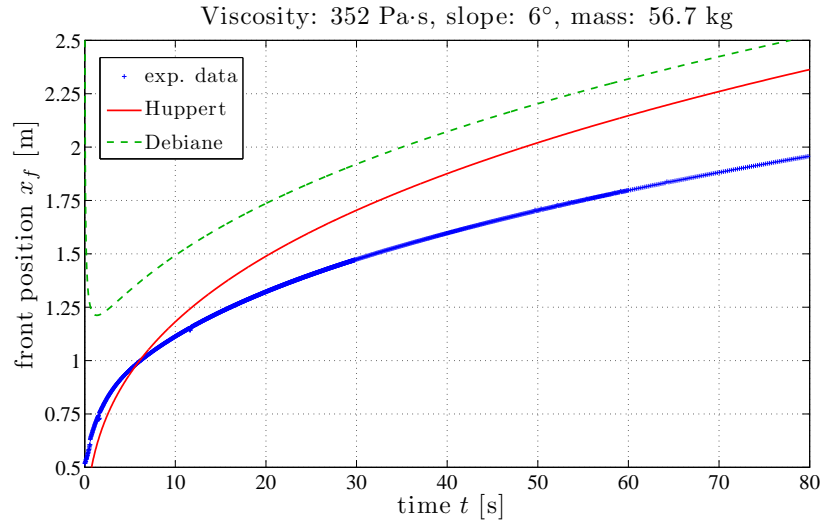
Figure B.4: 56.7 kg of glucose syrup with a viscosity of 352 Pa·s on a slope of $6°$.
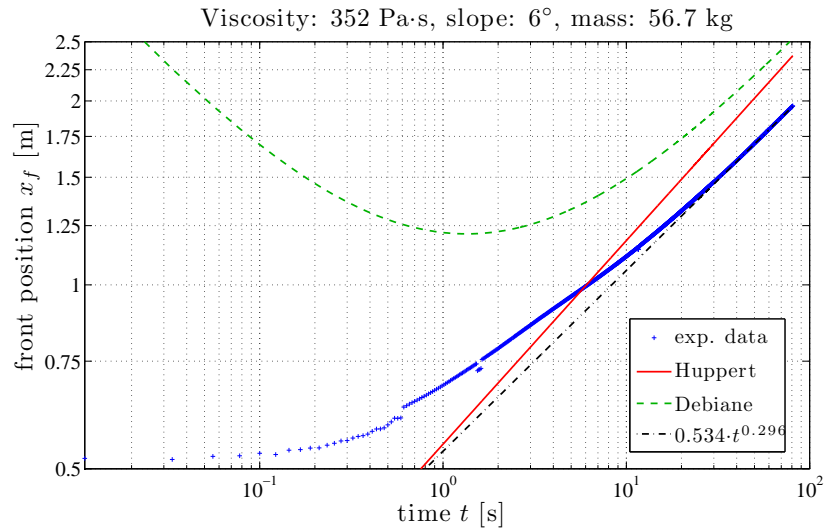
Figure B.5: 56.7 kg of glucose syrup with a viscosity of 352 Pa·s on a slope of $6°$.

B.3   Channel slope angle: 12°
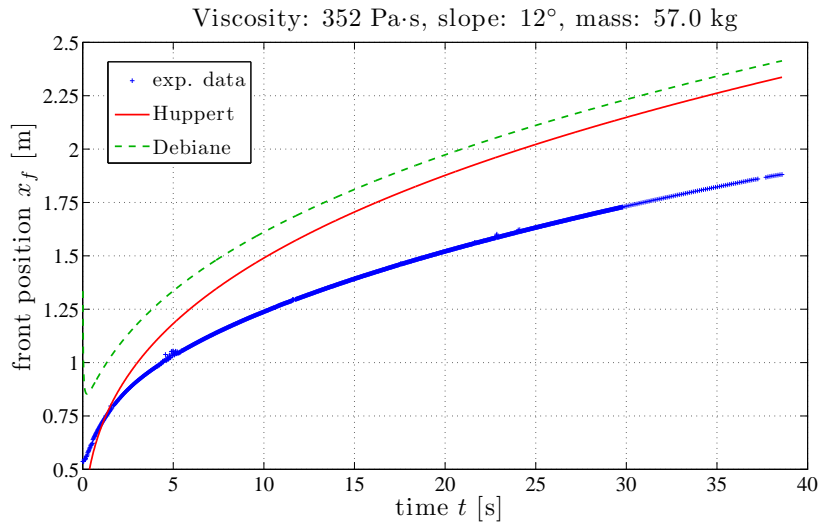
Figure B.6: 57.0 kg of glucose syrup with a viscosity of 352 Pa·s on a slope of 12°.
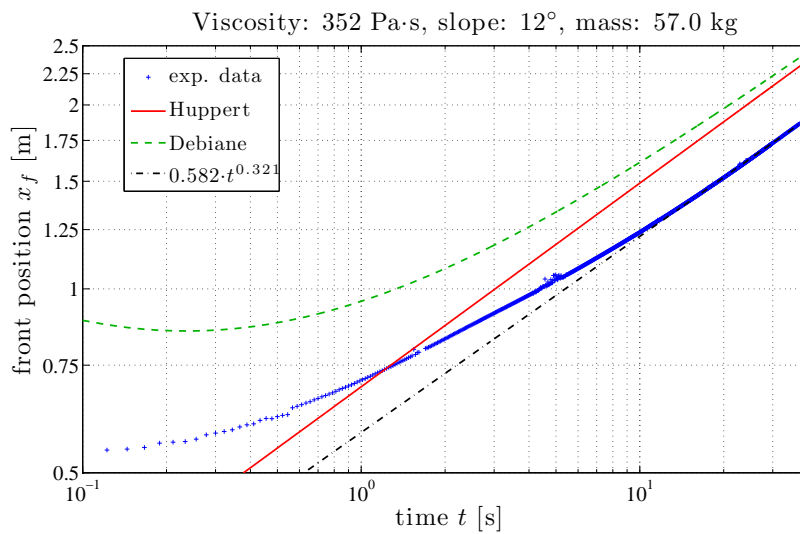
Figure B.7: 57.0 kg of glucose syrup with a viscosity of 352 Pa·s on a slope of 12°.

B.4 Channel slope angle: 18°
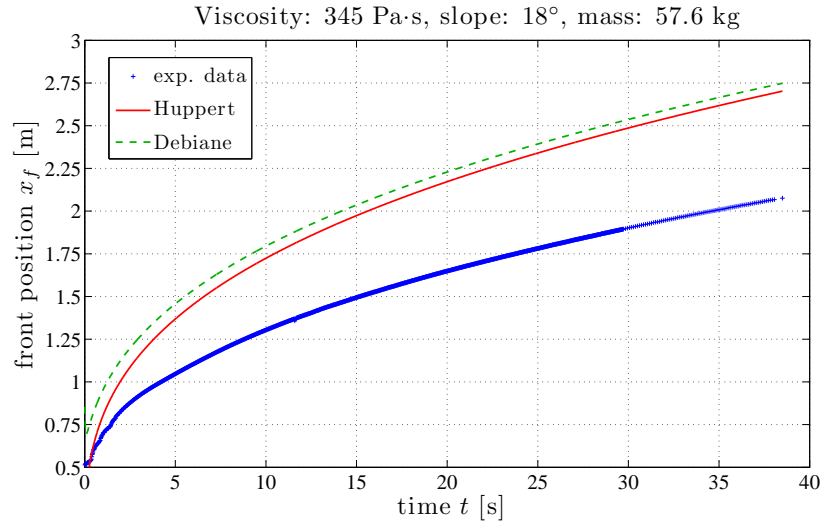
Figure B.8: 57.6 kg of glucose syrup with a viscosity of 345 Pa·s on a slope of 18°.
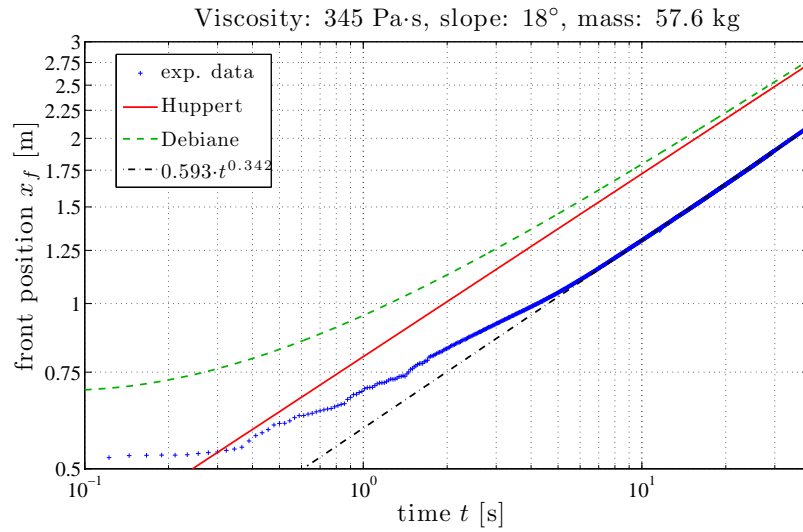
Figure B.9: 57.6 kg of glucose syrup with a viscosity of 345 Pa·s on a slope of 18°.

B.5 Channel slope angle: 24°
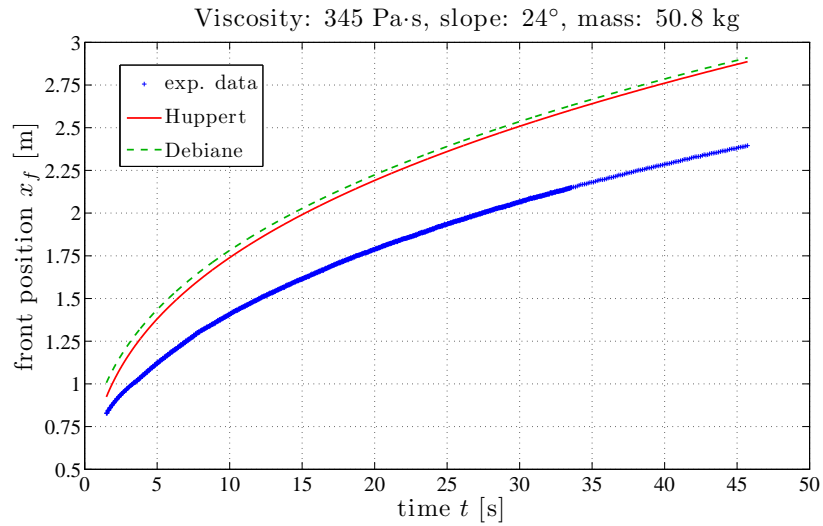
Figure B.10: 50.8 kg of glucose syrup with a viscosity of 345 Pa·s on a slope of 24°.
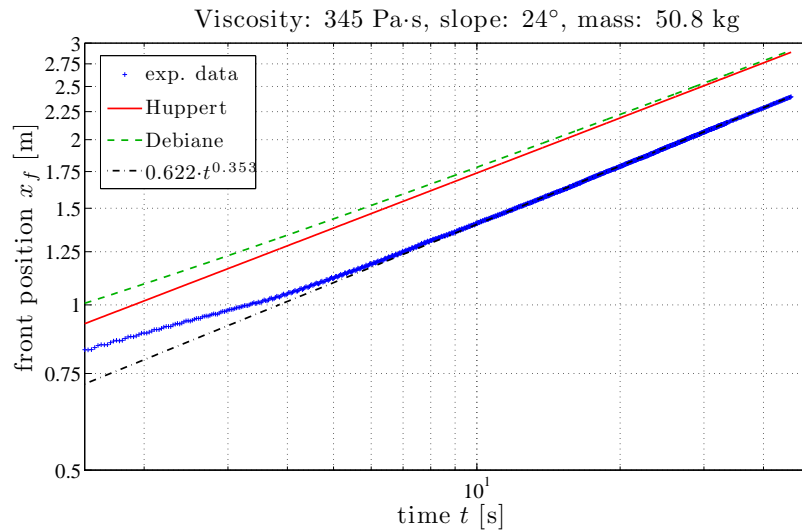
Figure B.11: 50.8 kg of glucose syrup with a viscosity of 345 Pa·s on a slope of 24°.

Ultrez 10 down channels
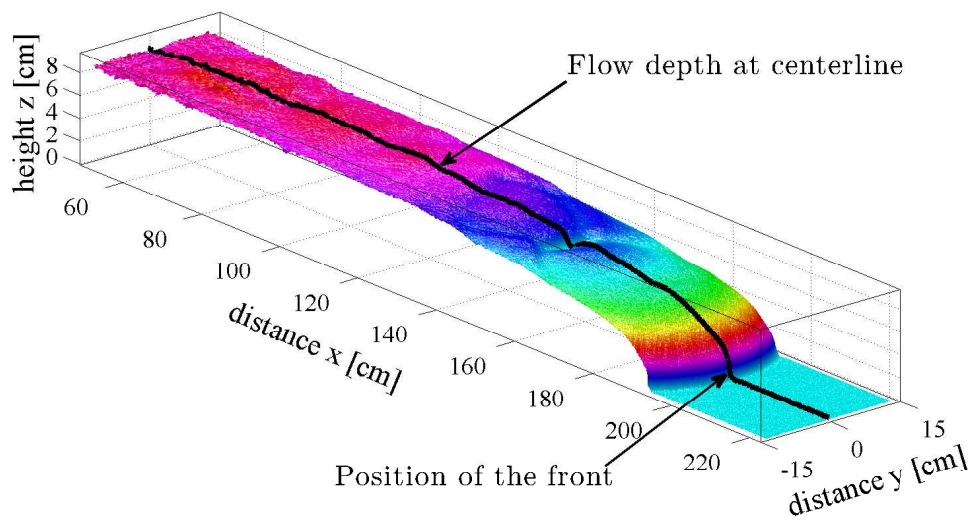
Figure C.1: 3D view of 43 kg of Ultrez 10 at a concentration C of 0.25% down a 6° inclined channel at time t= 900 s.

Slope	0°		6°		12°		18°		24°
Mass	43 kg	23 kg	43 kg	23 kg	43 kg	23 kg	43 kg	23 kg	23 kg
0.25%	C.2	C.5	C.11	C.15	C.22	C.26	C.32	C.36	C.43
0.30%	C.3	C.6	C.12	C.16	C.23	C.27	C.33	C.37	C.44
0.35%	C.4	C.7	C.13	C.17	C.24	C.28	C.34	C.38	C.45
0.40%		C.8	C.14	C.18	C.25	C.29	C.35	C.39	C.46

Table C.1: Figure reference numbers for experiments run with Carbopol Ultrez 10 down a canal.

C.1 Channel slope angle: 0°

C.1.1 Channel slope angle: 0° and mass: 43 kg
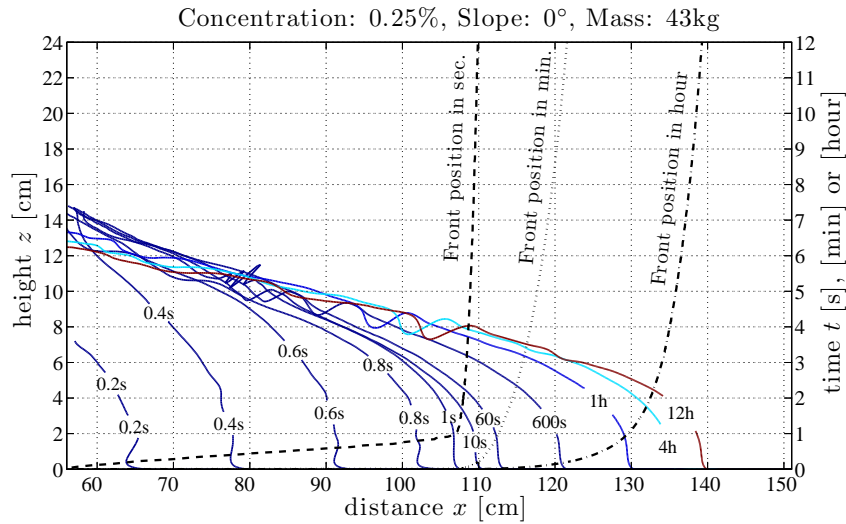
Figure C.2: 43 kg of Ultrez 10 at a concentration of 0.25% on a slope of 0°.
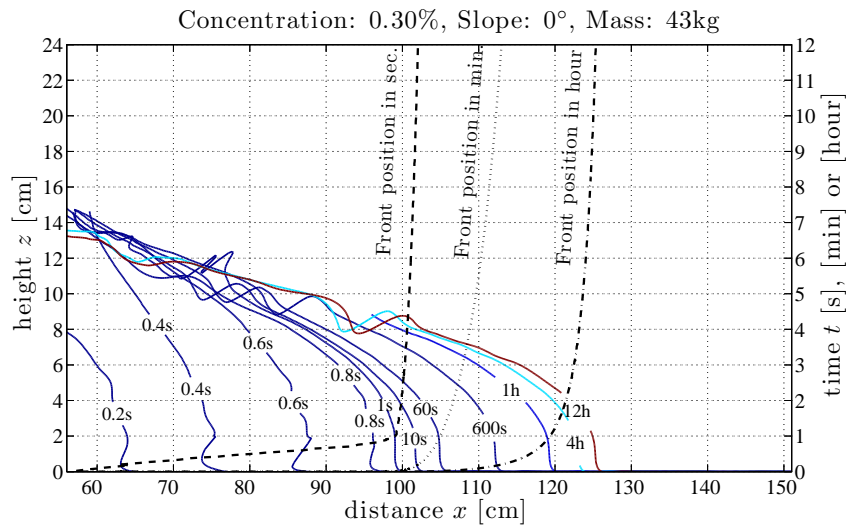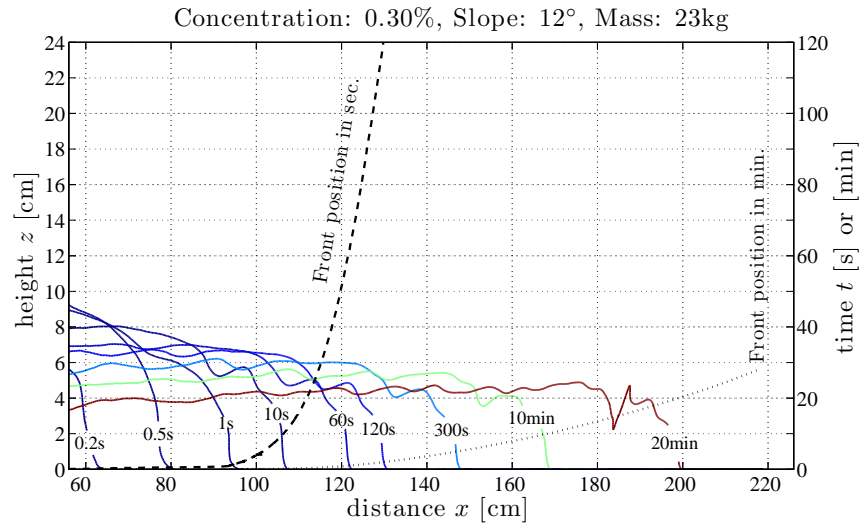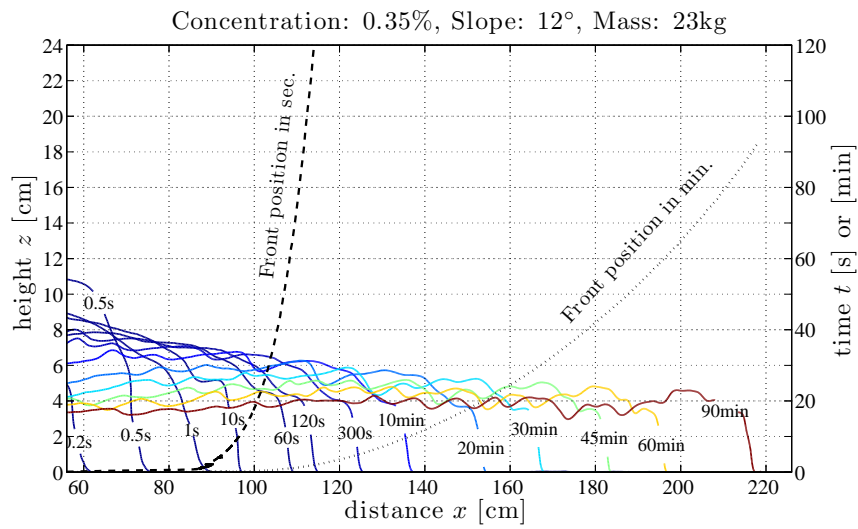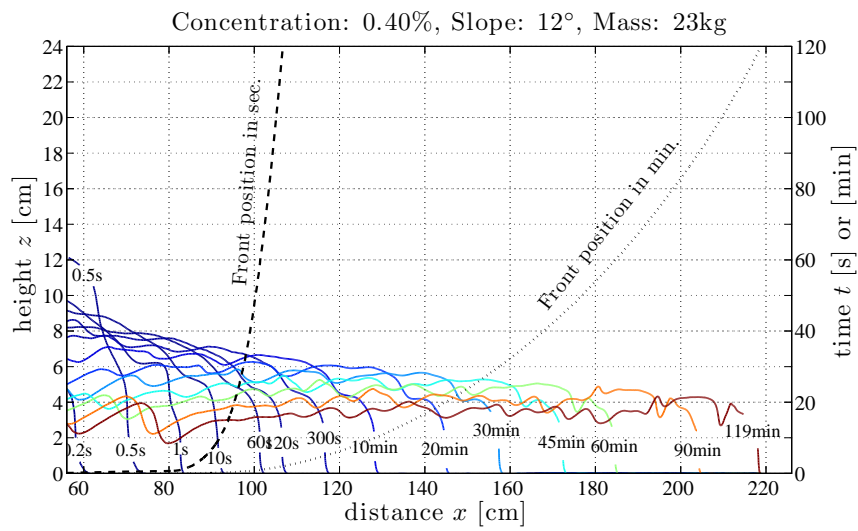

Figure C.3: 43 kg of Ultrez 10 at a concentration of 0.30% on a slope of 0°.
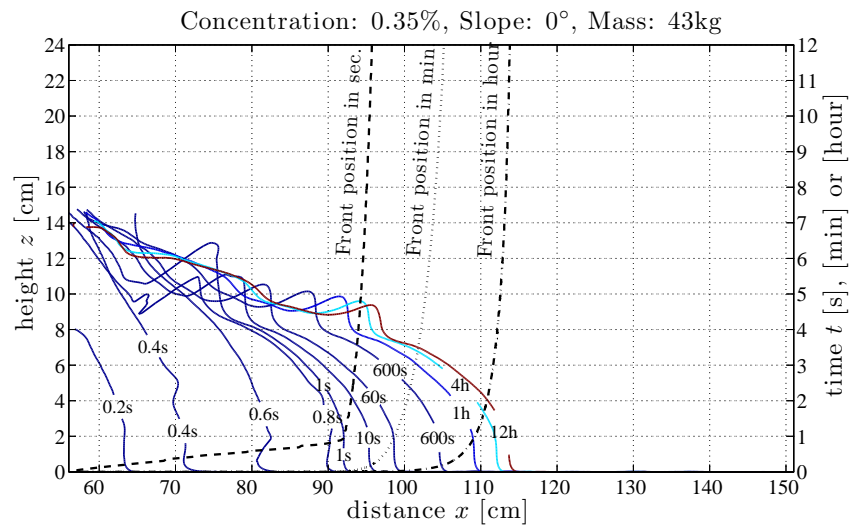
Figure C.4: 43 kg of Ultrez 10 at a concentration of 0.35% on a slope of 0°.

C.1.2 Channel slope angle: 0° and mass: 23 kg
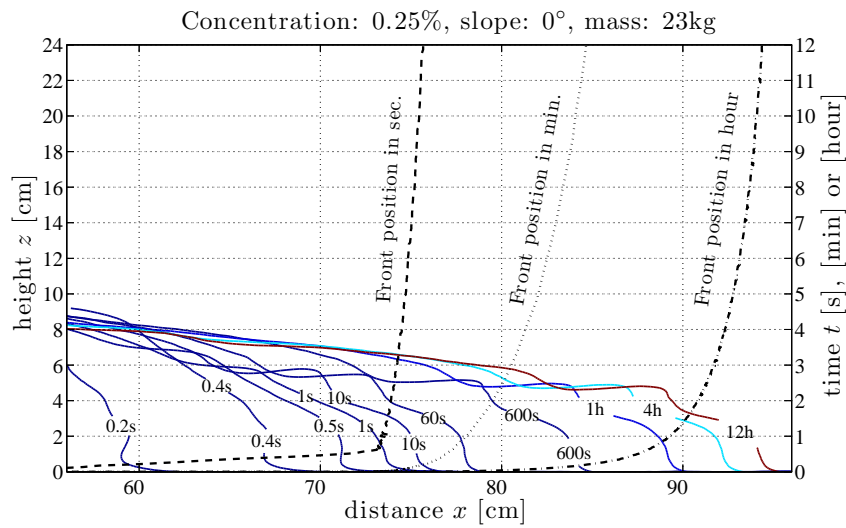
Figure C.5: 23 kg of Ultrez 10 at a concentration of 0.25% on a slope of 0°.
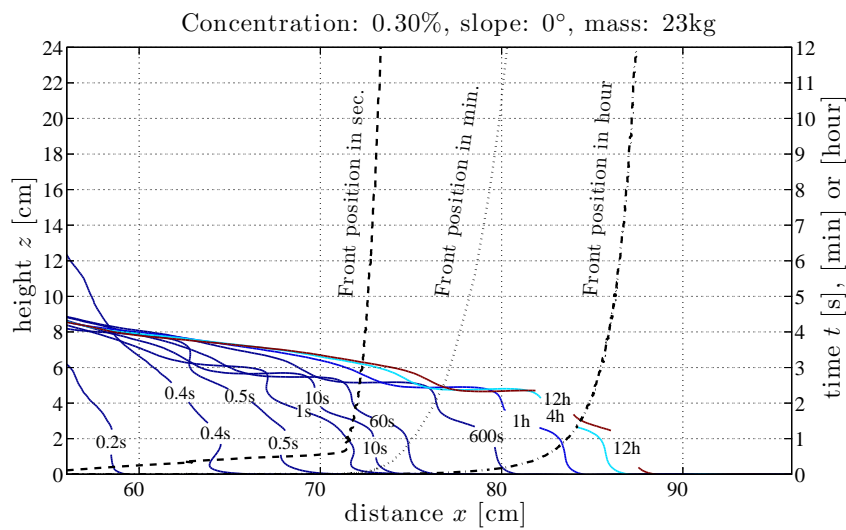
Figure C.6: 23 kg of Ultrez 10 at a concentration of 0.30% on a slope of 0°.

Concentration: 0.35%, slope: 0°, mass: 23kg
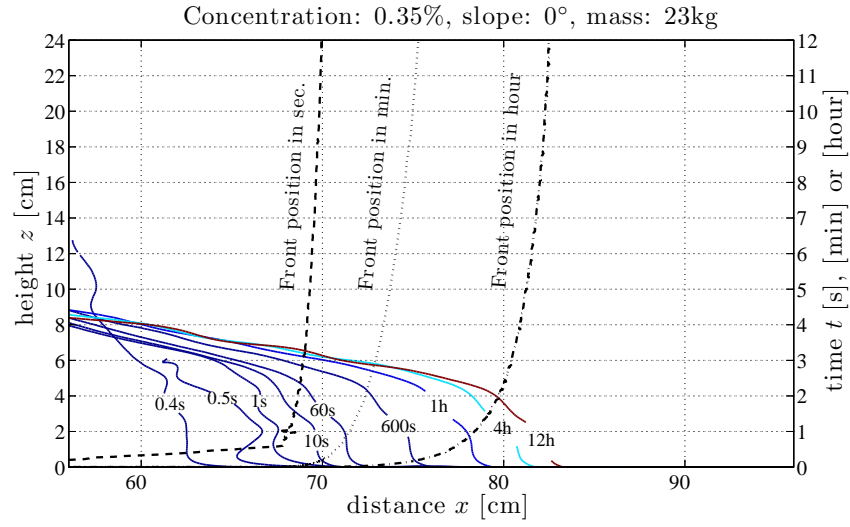
Figure C.7: 23 kg of Ultrez 10 at a concentration of 0.35% on a slope of 0°.

Concentration: 0.40%, slope: 0°, mass: 23kg
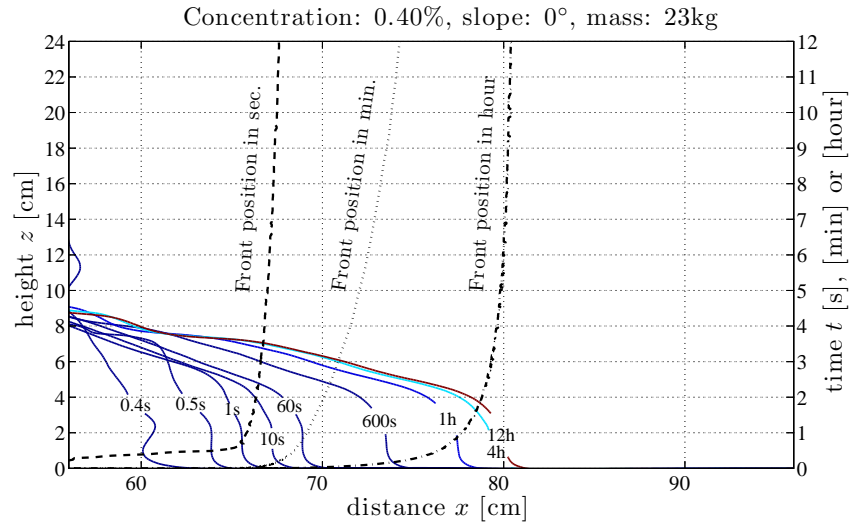
Figure C.8: 23 kg of Ultrez 10 at a concentration of 0.40% on a slope of 0°.

C.1.3 Front positions on a horizontal slope
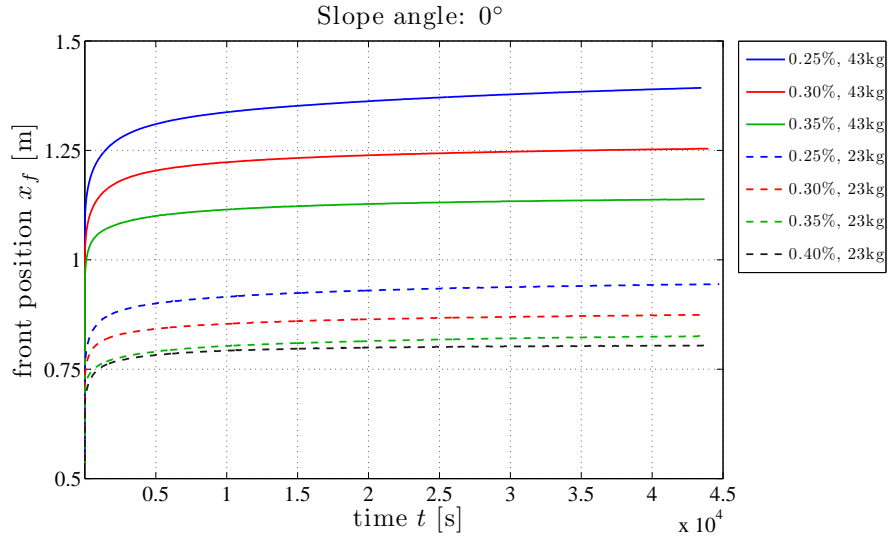
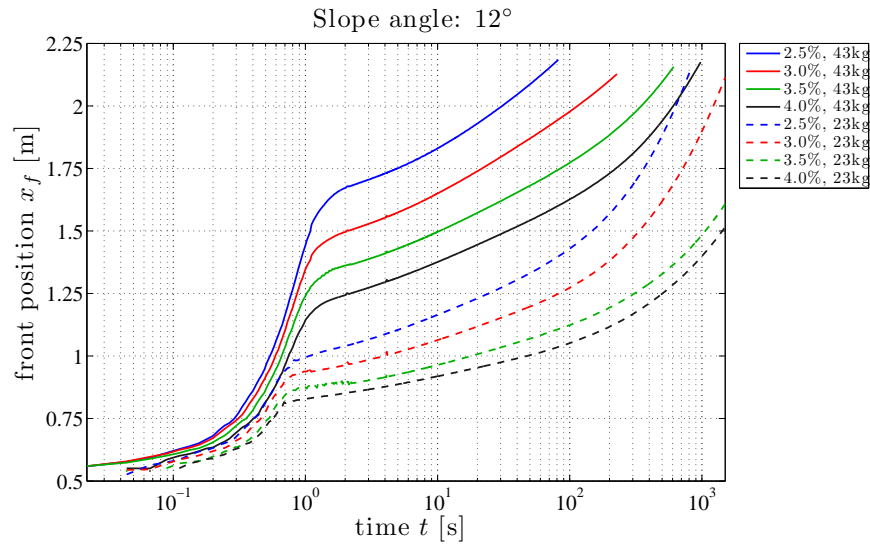Figure C.9: Comparison of the front positions x_f on a 0° inclined channel.
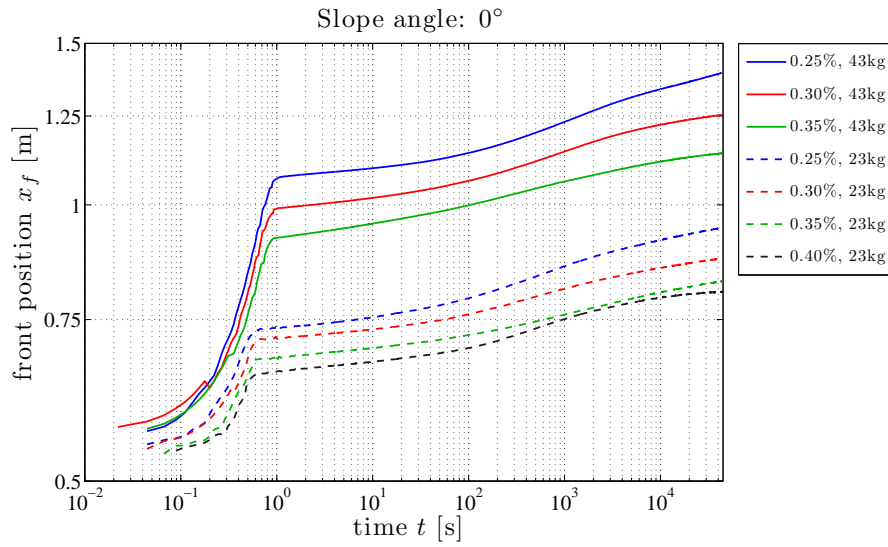
Figure C.10: Comparison of the front positions x_f on a 0° inclined channel in a semi-log plot.

C.2   Channel slope angle: 6°
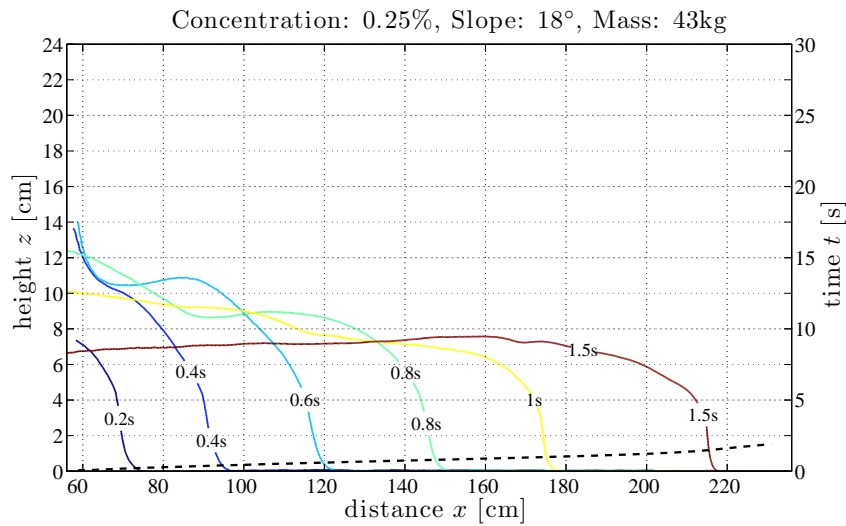
C.2.1   Channel slope angle: 6° and mass: 43 kg
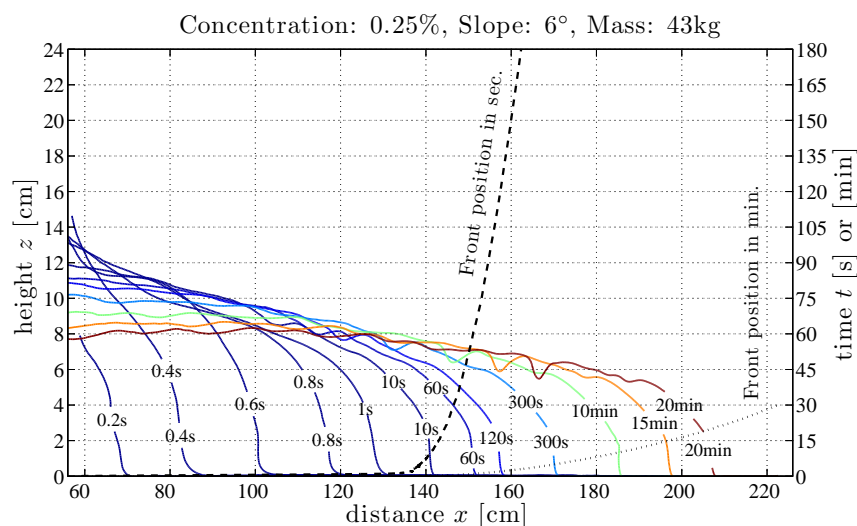
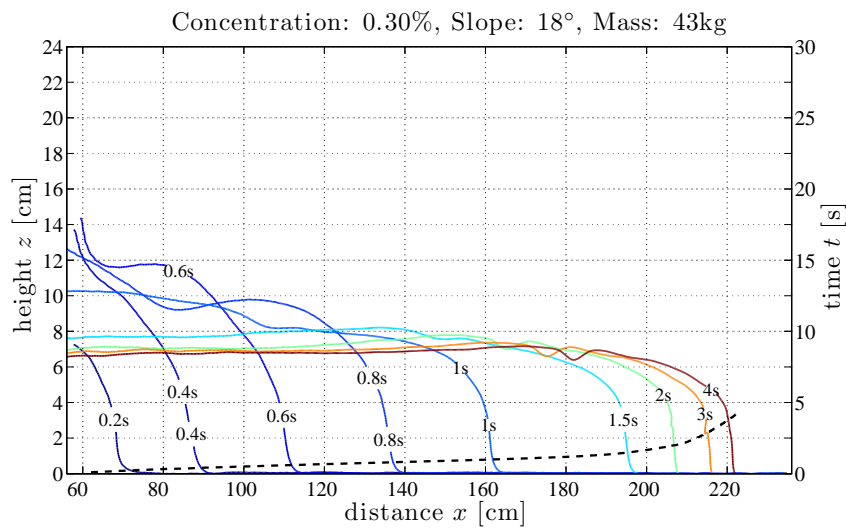Figure C.11: 43 kg of Ultrez 10 at a concentration of 0.25% on a slope of 6°.
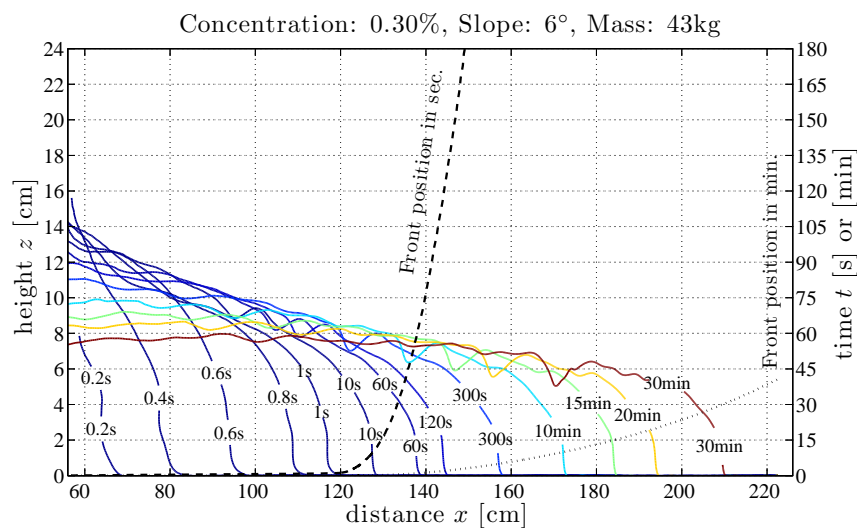
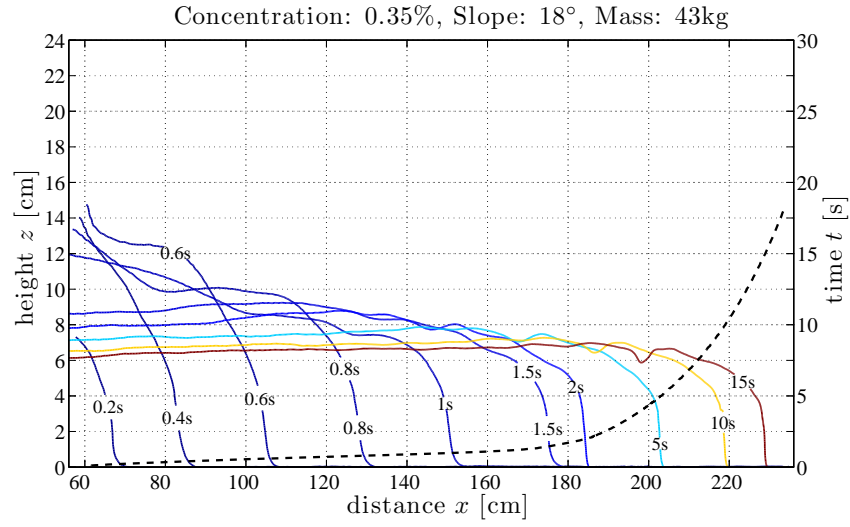Figure C.12: 43 kg of Ultrez 10 at a concentration of 0.30% on a slope of 6°.
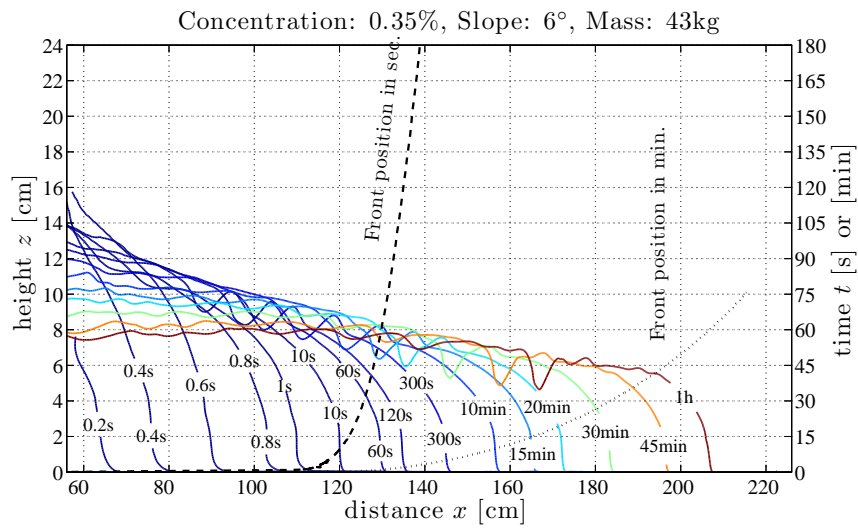
Figure C.13: 43 kg of Ultrez 10 at a concentration of 0.35% on a slope of 6°.
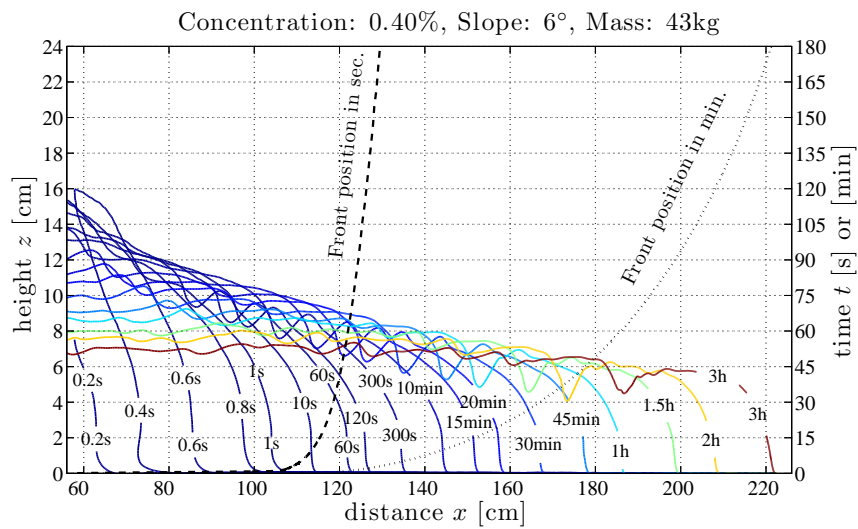
Figure C.14: 43 kg of Ultrez 10 at a concentration of 0.40% on a slope of 6°.

C.2.2   Channel slope angle: 6° and mass: 23 kg
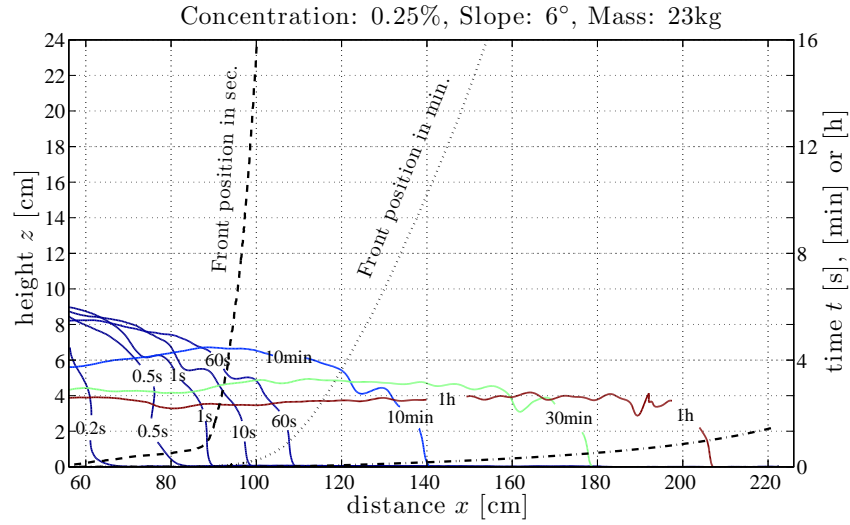
Figure C.15: 23 kg of Ultrez 10 at a concentration of 0.25% on a slope of 6°.
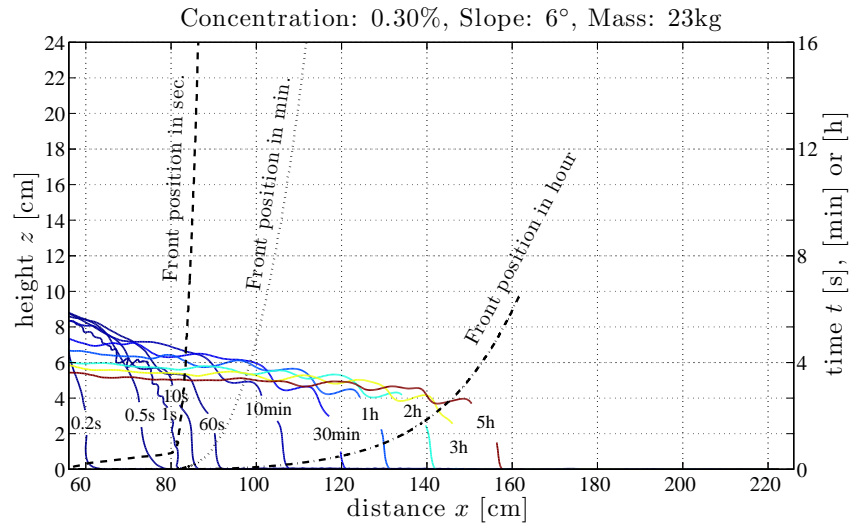
Figure C.16: 23 kg of Ultrez 10 at a concentration of 0.30% on a slope of 6°.
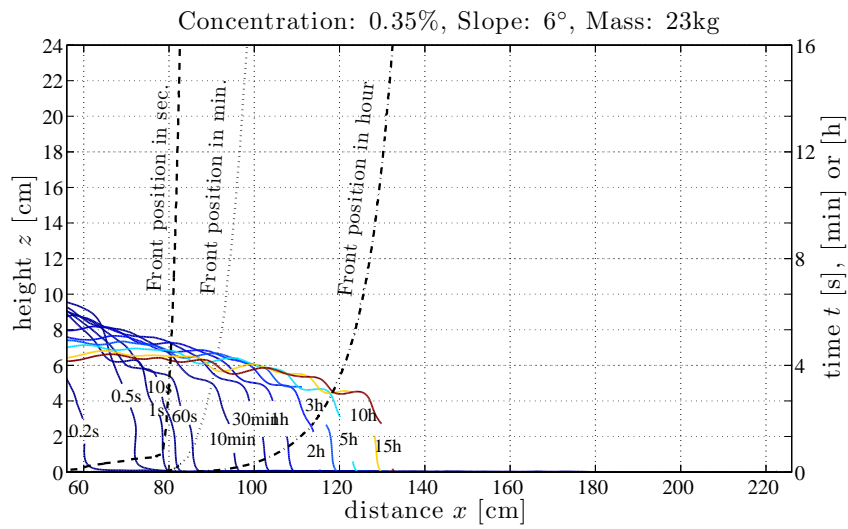
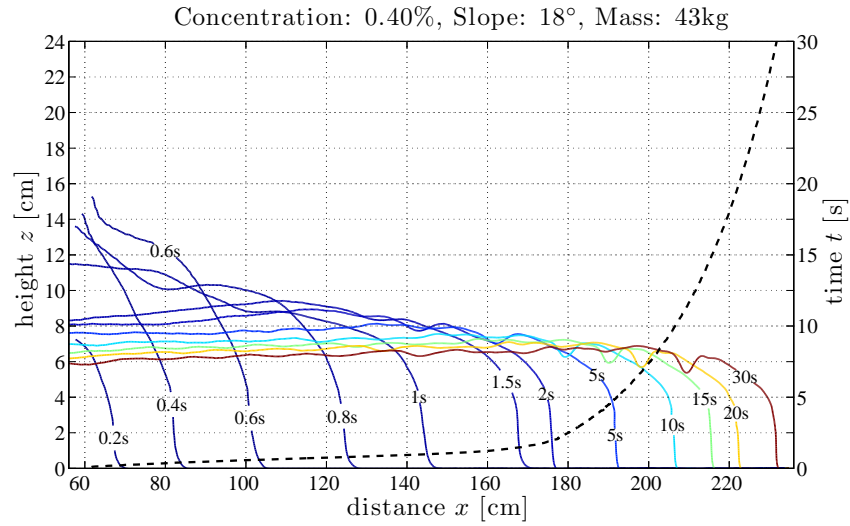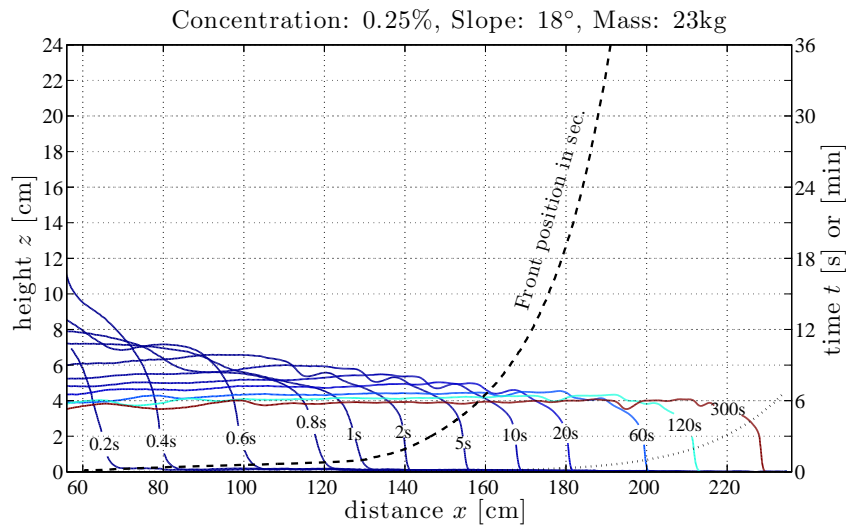Figure C.17: 23 kg of Ultrez 10 at a concentration of 0.35% on a slope of 6°.
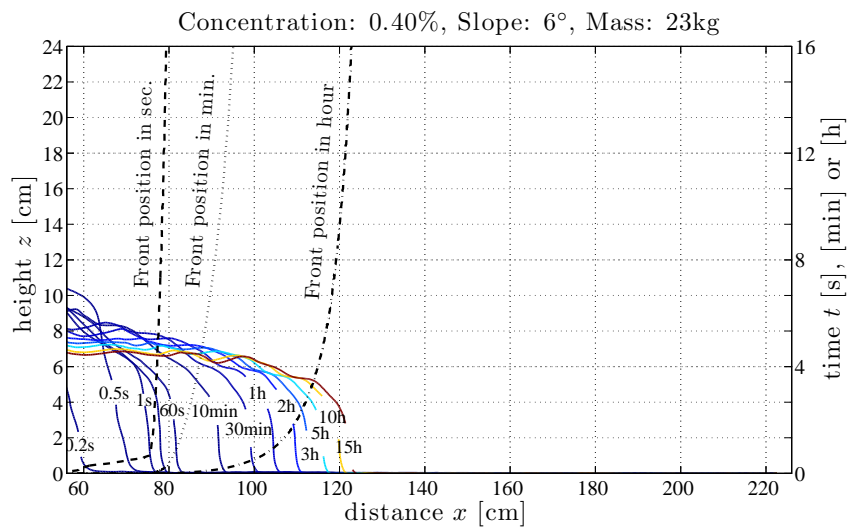
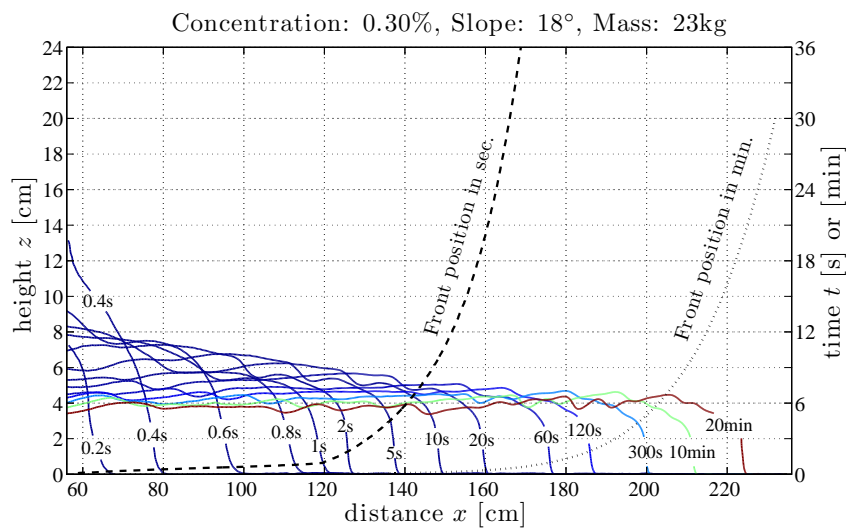Figure C.18: 23 kg of Ultrez 10 at a concentration of 0.40% on a slope of 6°.

C.2.3   Front position on a 6° slope
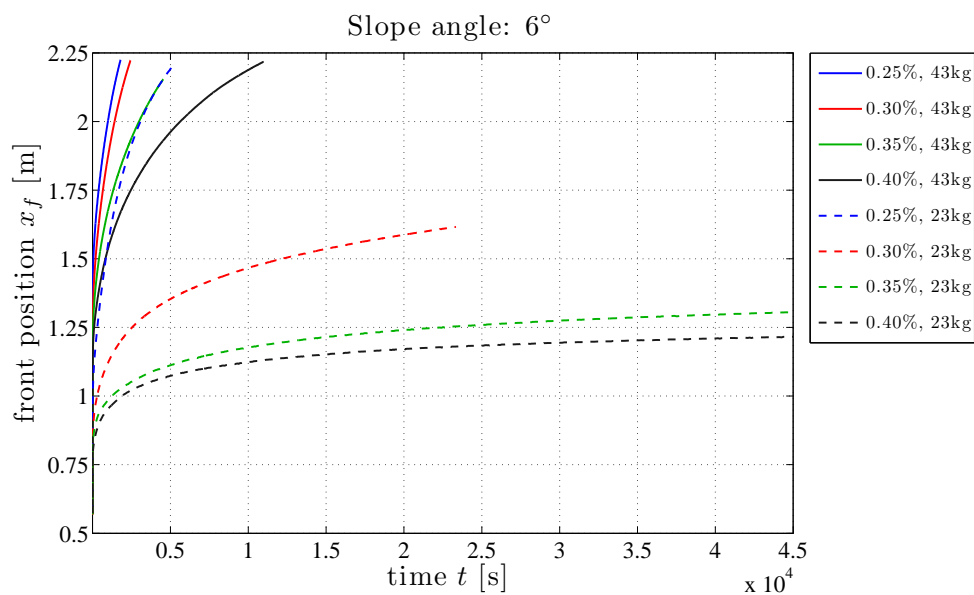
Figure C.19: Comparison of the front positions x_f on a 6° inclined channel.
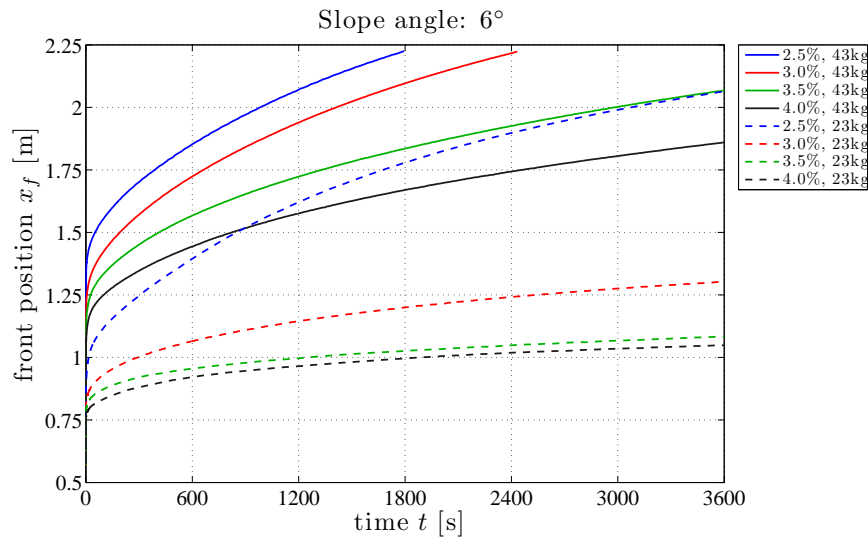
Figure C.20: Comparison of the front positions x_f on a 6° inclined channel. Zoom on the first hour.
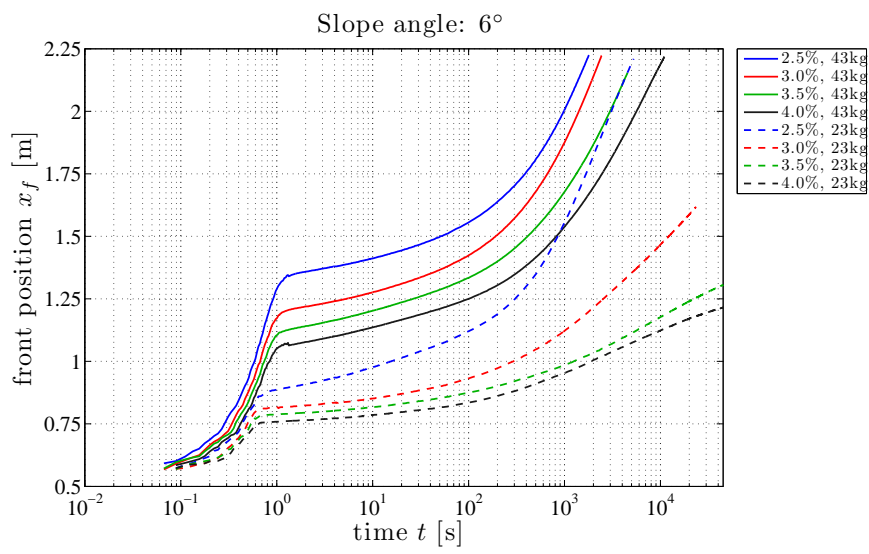
Figure C.21: Comparison of the front positions x_f on a 6° inclined channel in a semi-log plot.

C.3   Channel slope angle: 12°

C.3.1   Channel slope angle: 12° and Mass: 43 kg
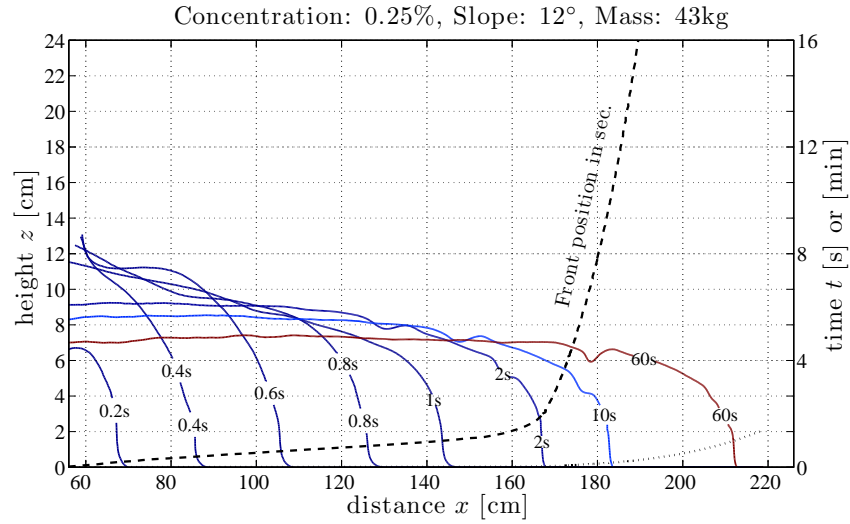
Figure C.22: 43 kg of Ultrez 10 at a concentration of 0.25% on a slope of 12°.
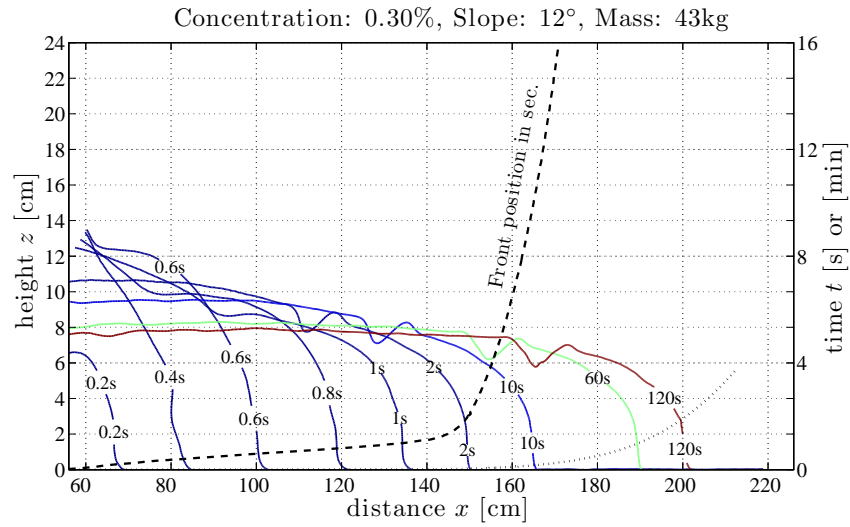
Figure C.23: 43 kg of Ultrez 10 at a concentration of 0.30% on a slope of 12°.
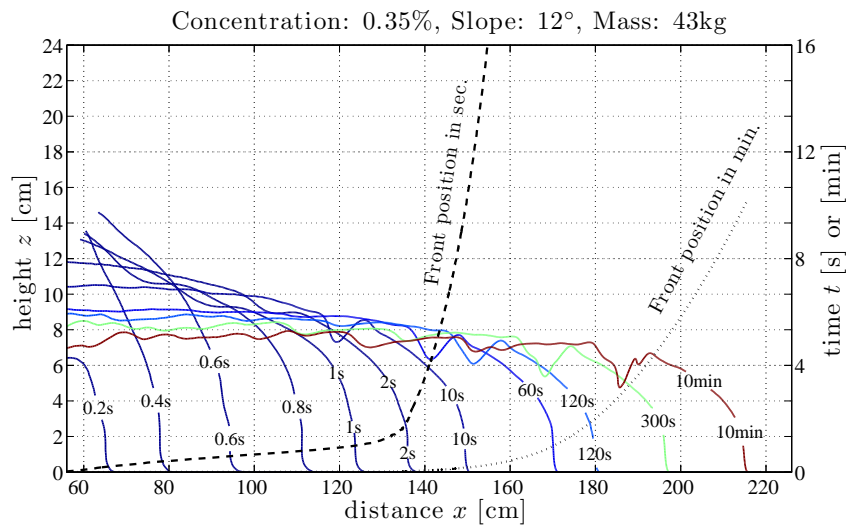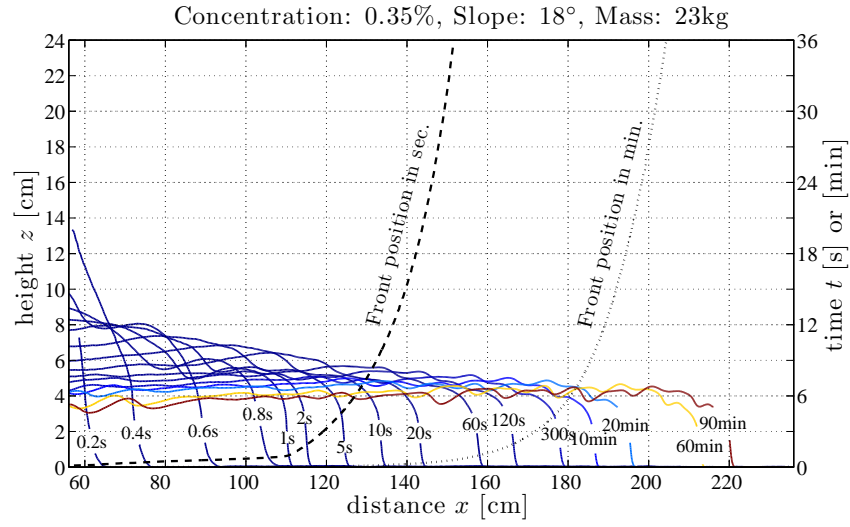
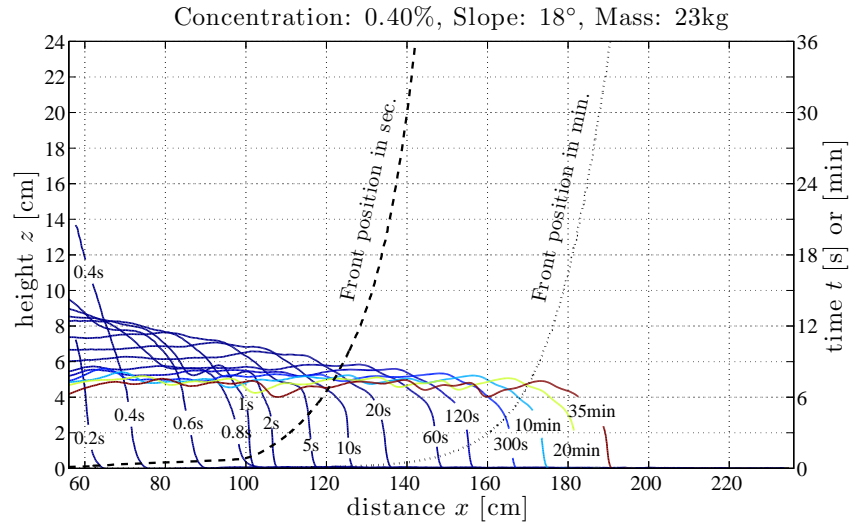Figure C.24: 43 kg of Ultrez 10 at a concentration of 0.35% on a slope of 12°.
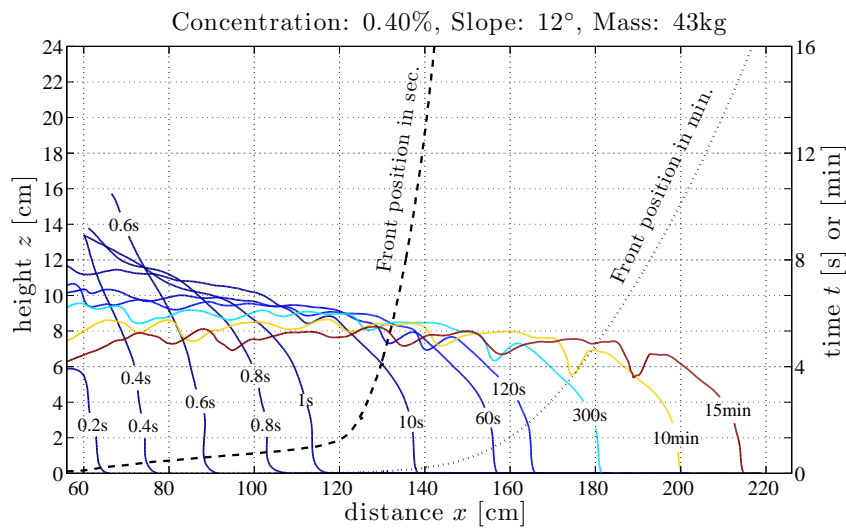
Figure C.25: 43 kg of Ultrez 10 at a concentration of 0.40% on a slope of 12°.

C.3.2   Channel slope angle: 12° and Mass: 23 kg
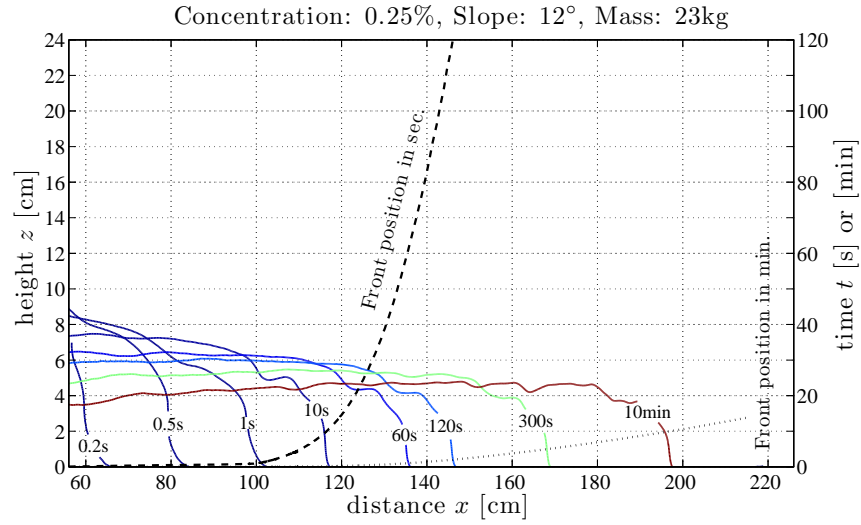
Figure C.26: 23 kg of Ultrez 10 at a concentration of 0.25% on a slope of 12°.

Figure C.27: 23 kg of Ultrez 10 at a concentration of 0.30% on a slope of 12°.

Figure C.28: 23 kg of Ultrez 10 at a concentration of 0.35% on a slope of 12°.

Figure C.29: 23 kg of Ultrez 10 at a concentration of 0.40% on a slope of 12°.
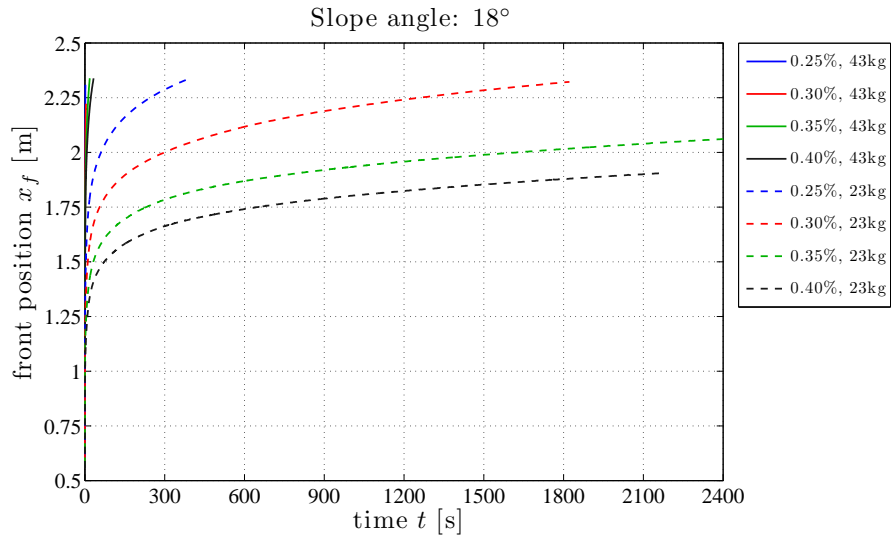
C.3.3   Front positions on a 12° slope
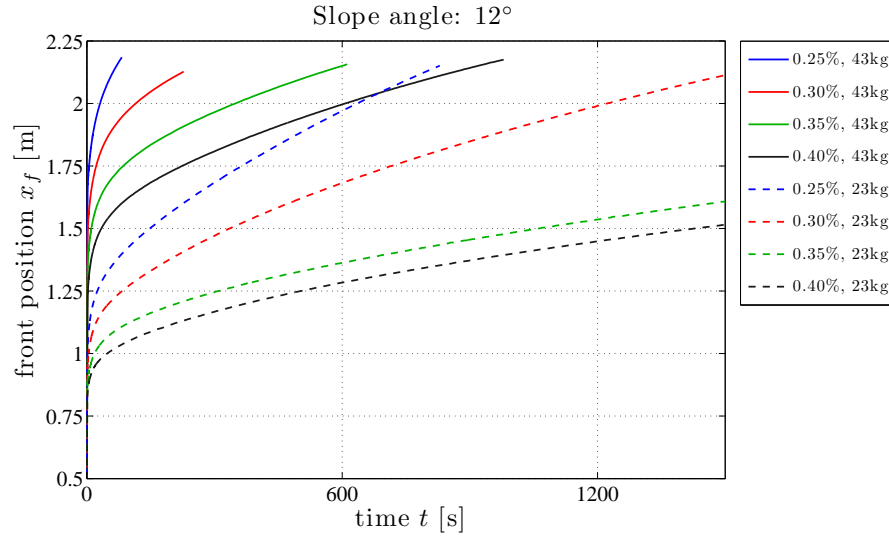
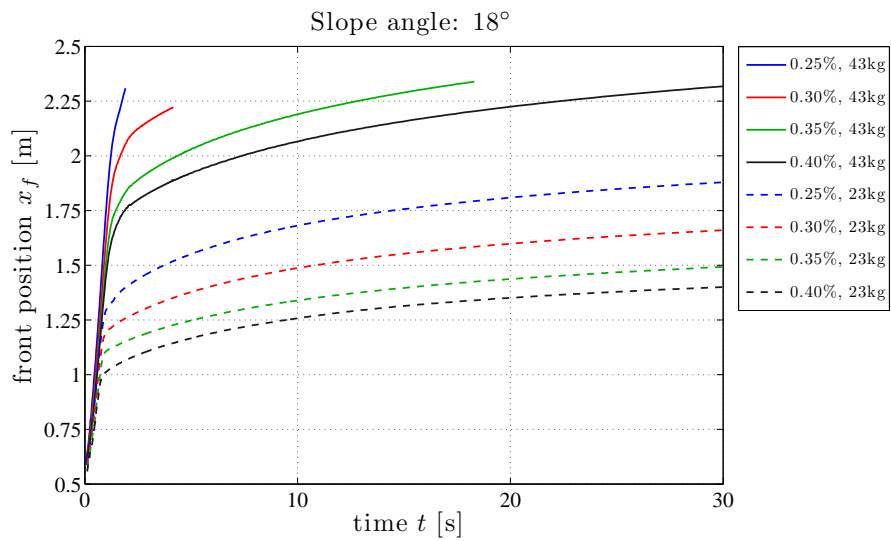Figure C.30: Comparison of the front positions x_f on a 12° inclined channel.

Figure C.31: Comparison of the front positions x_f on a 12° inclined channel in a semi-log plot.

C.4 Channel slope angle: 18°

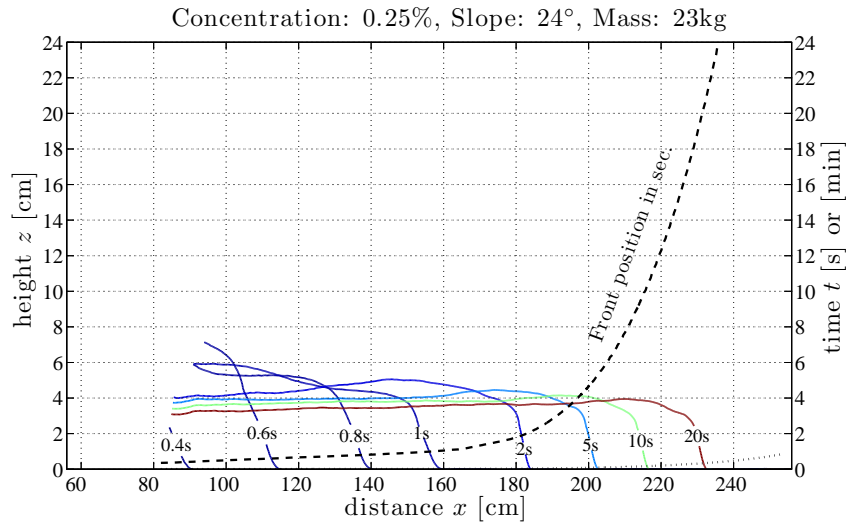## C.4.1 Channel slope angle: 18° and Mass: 43 kg

Figure C.32: 43 kg of Ultrez 10 at a concentration of 0.25% on a slope of 18°.

Figure C.33: 43 kg of Ultrez 10 at a concentration of 0.30% on a slope of 18°.

Figure C.34: 43 kg of Ultrez 10 at a concentration of 0.35% on a slope of 18°.

Figure C.35: 43 kg of Ultrez 10 at a concentration of 0.40% on a slope of 18°.

C.4.2 Slope: 18° and Mass: 23 kg

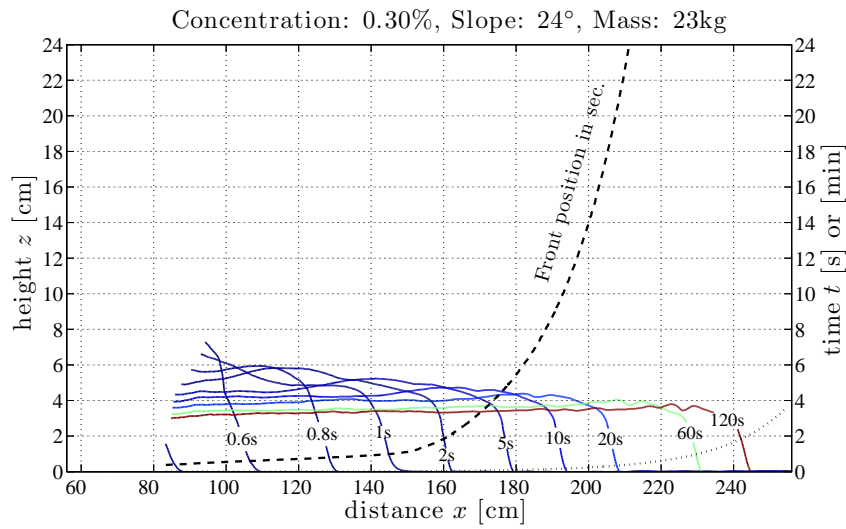Figure C.36: 23 kg of Ultrez 10 at a concentration of 0.25% on a slope of 18°.

Figure C.37: 23 kg of Ultrez 10 at a concentration of 0.30% on a slope of 18°.
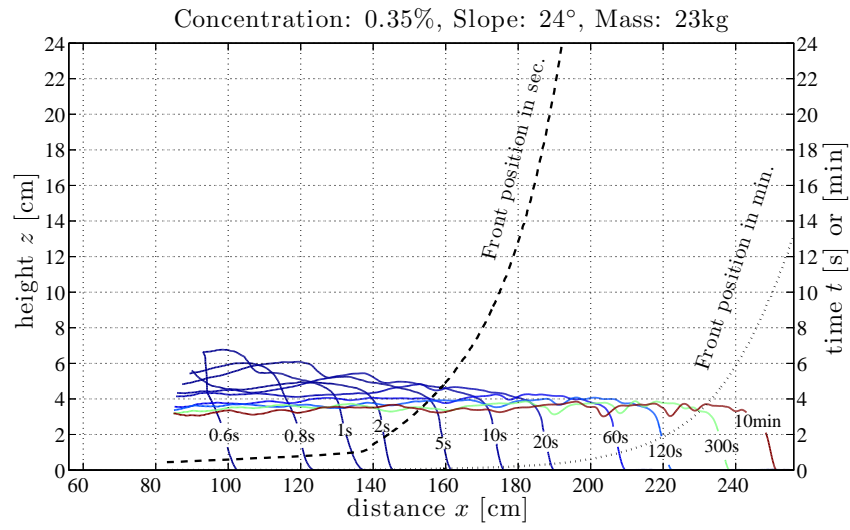
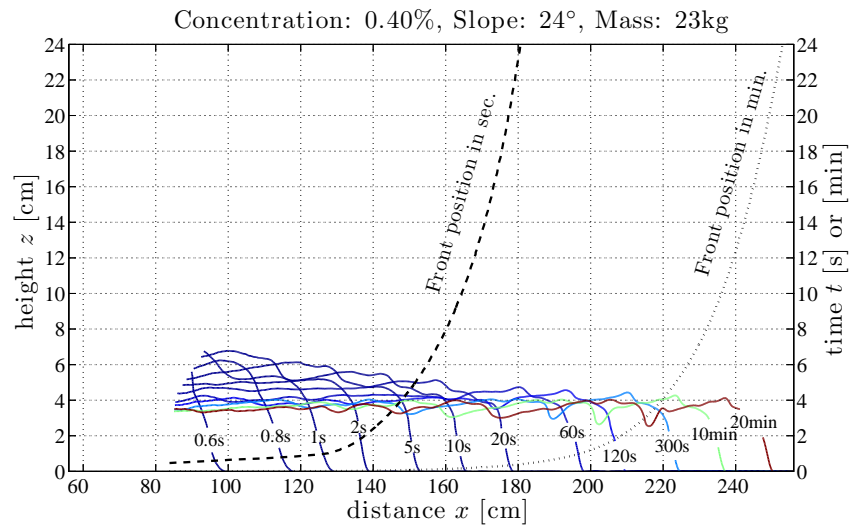Figure C.38: 23 kg of Ultrez 10 at a concentration of 0.35% on a slope of 18°.

Figure C.39: 23 kg of Ultrez 10 at a concentration of 0.40% on a slope of 18°.
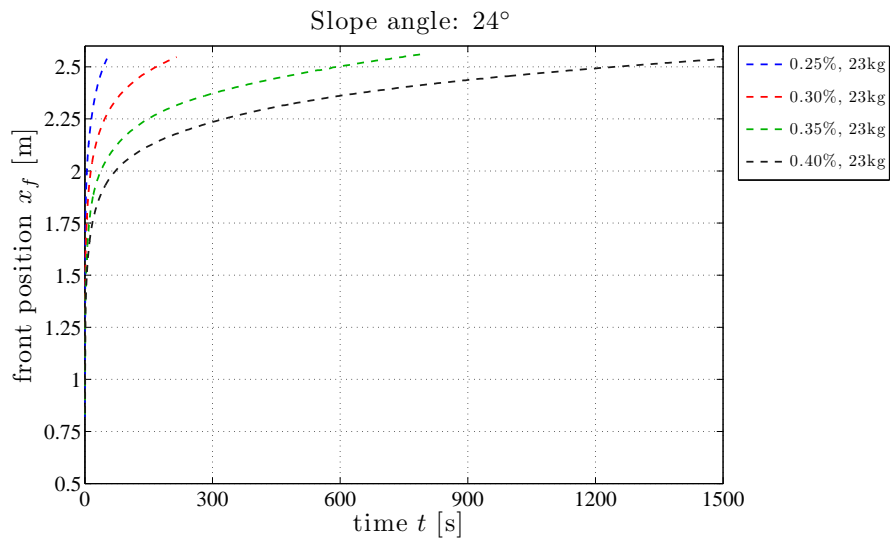
C.4.3   Front positions on a 18° slope

Figure C.40: Comparison of the front positions x_f on a 18° inclined channel.

Figure C.41: Comparison of the front positions x_f on a 18° inclined channel. Zoom on the first 30 s.
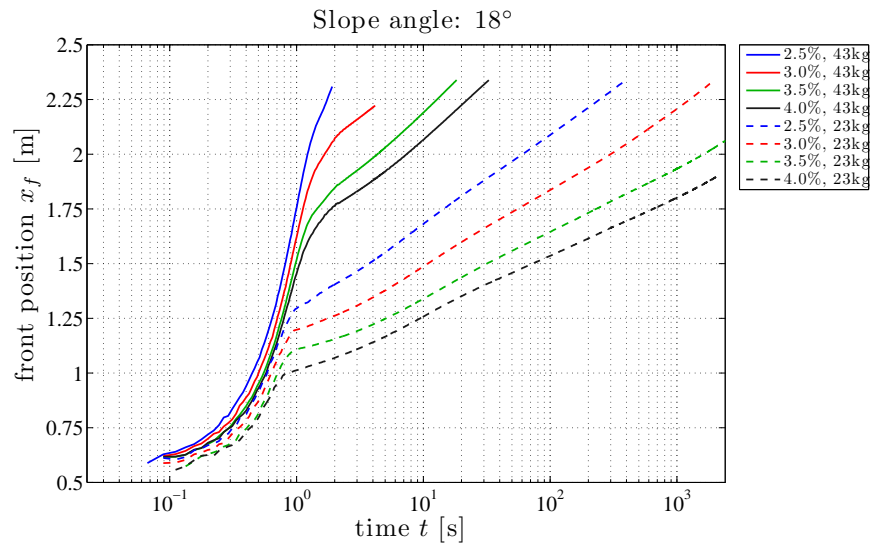
Figure C.42: Comparison of the front positions x_f on a 18° inclined channel in a semi-log plot.

C.5   Slope: 24°

C.5.1   Slope: 24° and Mass: 23 kg

Figure C.43: 23 kg of Ultrez 10 at a concentration of 0.25% on a slope of 24°.

Figure C.44: 23 kg of Ultrez 10 at a concentration of 0.30% on a slope of 24°.

Concentration: 0.35%, Slope: 24°, Mass: 23kg

Figure C.45: 23 kg of Ultrez 10 at a concentration of 0.35% on a slope of 24°.

Concentration: 0.40%, Slope: 24°, Mass: 23kg

Figure C.46: 23 kg of Ultrez 10 at a concentration of 0.40% on a slope of 24°.

C.5.2 Front positions on a 24° slope

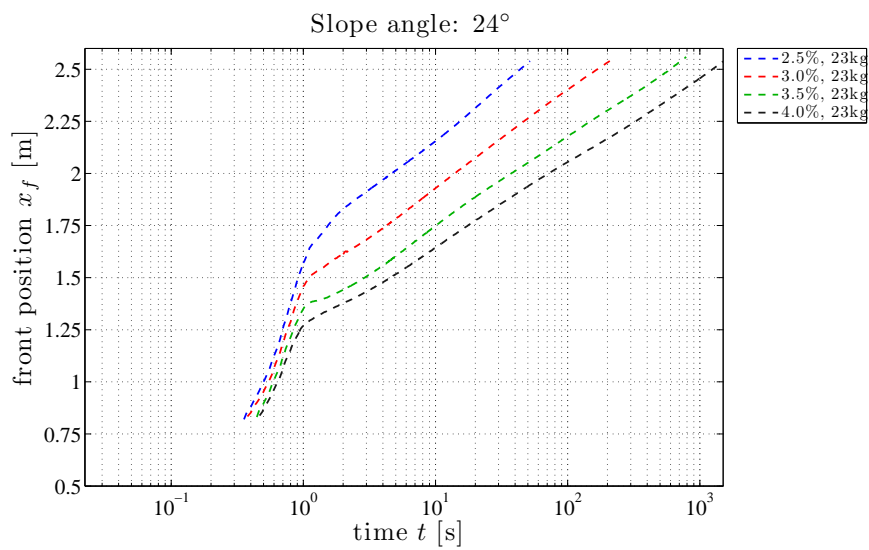Figure C.47: Comparison of the front positions x_f on a 24° inclined channel.

Figure C.48: Comparison of the front positions x_f on a 24° inclined channel in a semi-log plot.
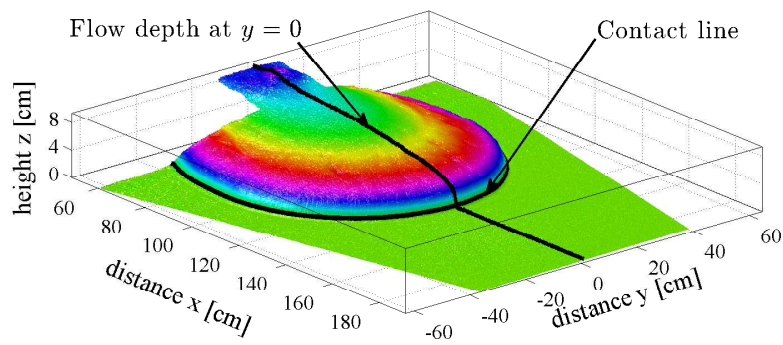
Ultrez 10 down planes

Figure D.1: 3D view of 43 kg of Ultrez 10 at a concentration C of 0.25% down a 6° inclined plane at time $t=$ 900 s.

Slope	0°	6°	12°	18°
Mass	43 kg	43 kg	43 kg	43 kg
0.25%	D.2, D.3	D.10, D.11	D.18, D.19	D.26, D.27
0.30%	D.4, D.5	D.12, D.13	D.20, D.21	D.28, D.29
0.35%	D.6, D.7	D.14, D.15	D.22, D.23	D.30, D.31
0.40%	D.8, D.9	D.16, D.17	D.24, D.25	D.32, D.33

Table D.1: Figure reference numbers for experiments run with Ultrez 10 down a inclined plane.

D.1 Plane slope angle: 0°
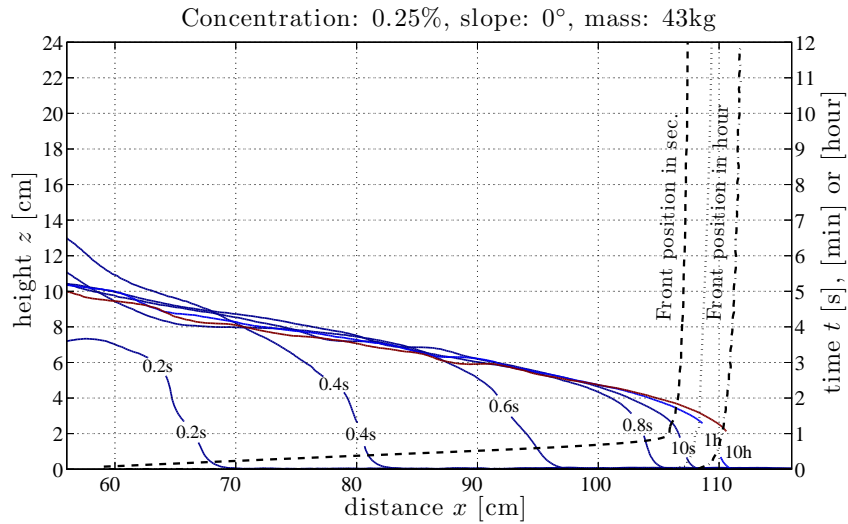
D.1.1 Plane slope angle: 0° and mass: 43 kg

Figure D.2: Flow depth of 43 kg of Ultrez 10 at $C = 0.25\%$ on a slope of 0°.

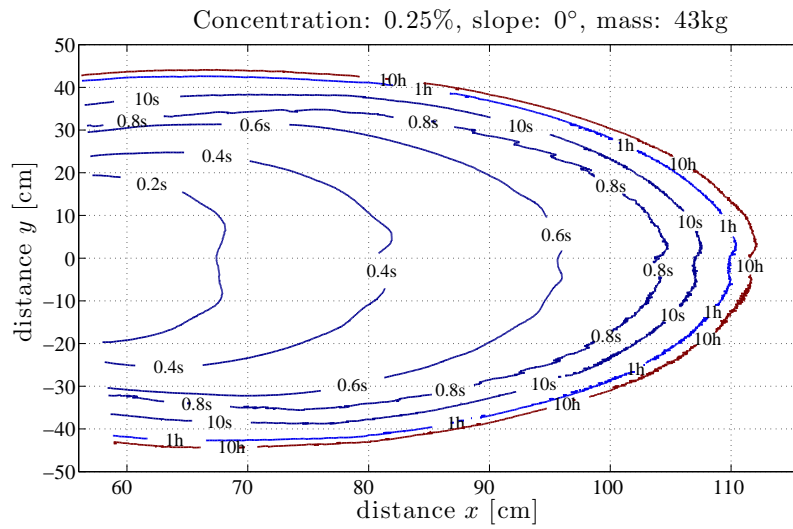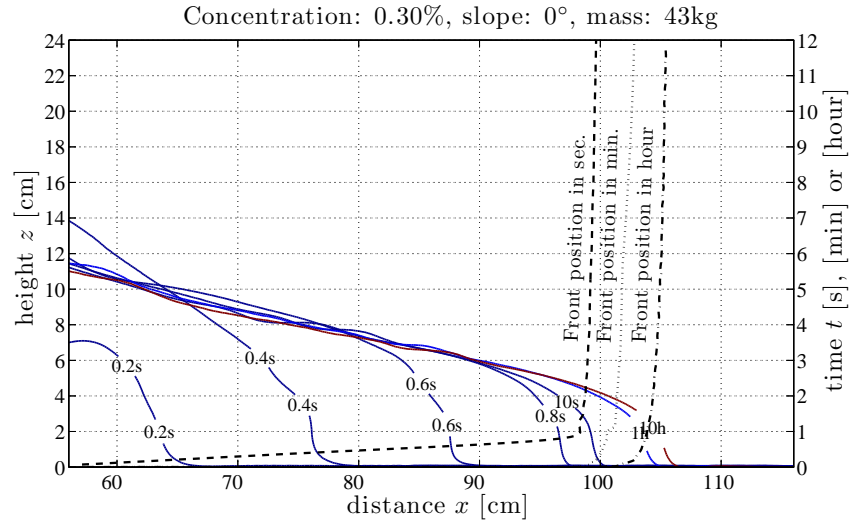Figure D.3: Contact line of 43 kg of Ultrez 10 at $C = 0.25\%$ on a slope of 0°.

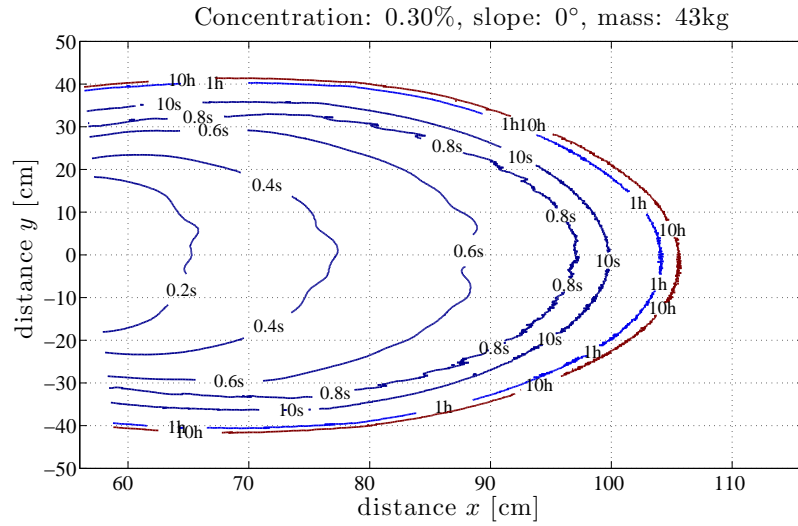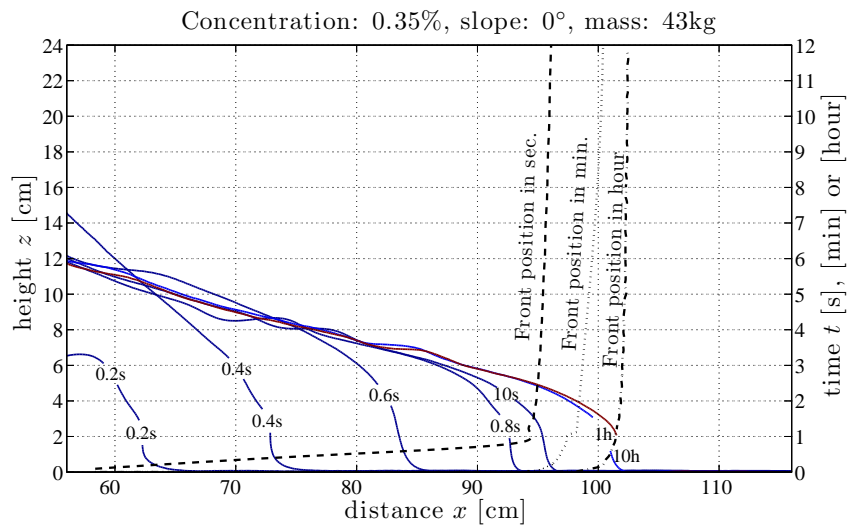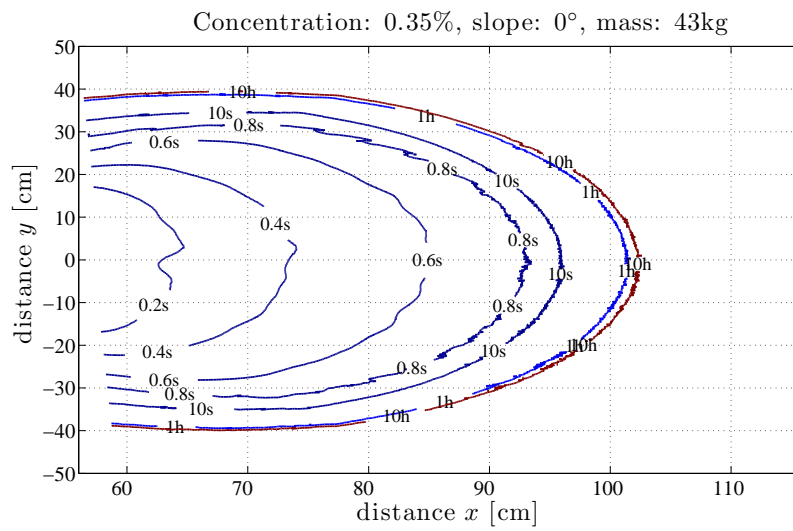Figure D.4: Flow depth of 43 kg of Ultrez 10 at $C = 0.30\%$ on a slope of $0°$.

Figure D.5: Contact line of 43 kg of Ultrez 10 at $C = 0.30\%$ on a slope of $0°$.

Concentration: 0.35%, slope: 0°, mass: 43kg

Figure D.6: Flow depth of 43 kg of Ultrez 10 at $C = 0.35\%$ on a slope of 0°.

Concentration: 0.35%, slope: 0°, mass: 43kg

Figure D.7: Contact line of 43 kg of Ultrez 10 at $C = 0.35\%$ on a slope of 0°.

Concentration: 0.40%, slope: 0°, mass: 43kg

Figure D.8: Flow depth of 43 kg of Ultrez 10 at $C = 0.40\%$ on a slope of 0°.

Concentration: 0.40%, slope: 0°, mass: 43kg

Figure D.9: Contact line of 43 kg of Ultrez 10 at $C = 0.40\%$ on a slope of 0°.

D.2   Plane slope angle: 6°

D.2.1   Plane slope angle: 6° and mass: 43 kg

Figure D.10: Flow depth of 43 kg of Ultrez 10 at $C = 0.25\%$ on a slope of 6°.

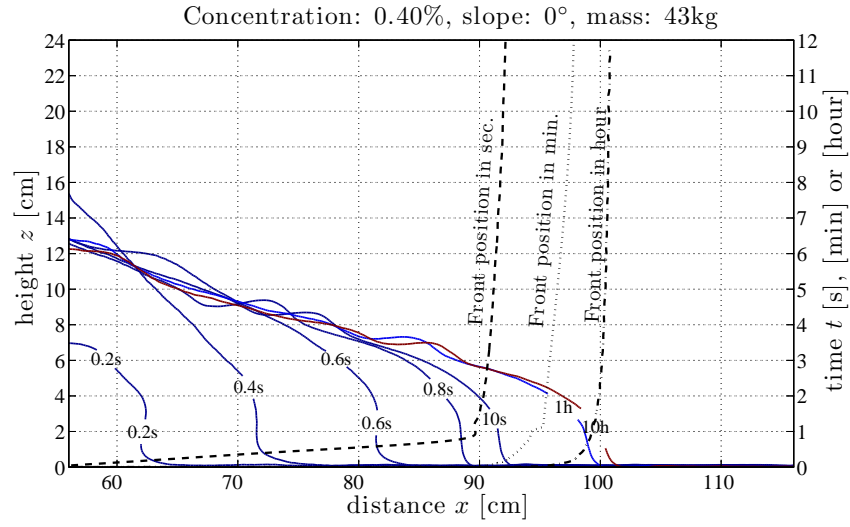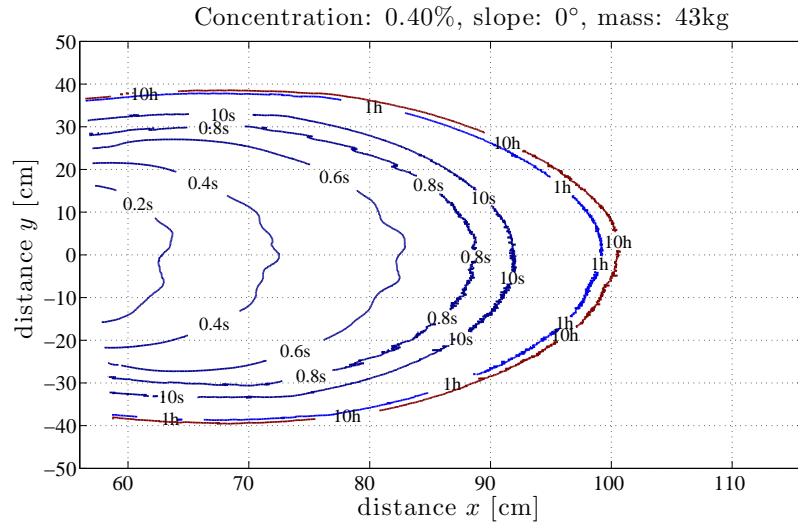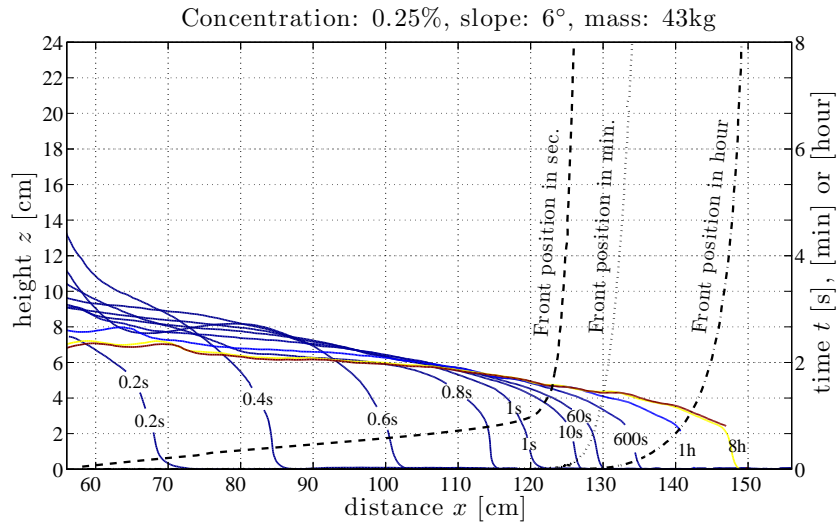Figure D.11: Contact line of 43 kg of Ultrez 10 at $C = 0.25\%$ on a slope of 6°.

Figure D.12: Flow depth of 43 kg of Ultrez 10 at $C = 0.30\%$ on a slope of $6°$.

Figure D.13: Contact line of 43 kg of Ultrez 10 at $C = 0.30\%$ on a slope of $6°$.

Concentration: 0.35%, slope: 6°, mass: 43kg

Figure D.14: Flow depth of 43 kg of Ultrez 10 at $C = 0.35\%$ on a slope of 6°.

Concentration: 0.35%, slope: 6°, mass: 43kg

Figure D.15: Contact line of 43 kg of Ultrez 10 at $C = 0.35\%$ on a slope of 6°.

Concentration: 0.40%, slope: 6°, mass: 43kg

Figure D.16: Flow depth of 43 kg of Ultrez 10 at $C = 0.40\%$ on a slope of 6°.

Concentration: 0.40%, slope: 6°, mass: 43kg

Figure D.17: Contact line of 43 kg of Ultrez 10 at $C = 0.40\%$ on a slope of 6°.

D.3 Plane slope angle: 12°

D.3.1 Plane slope angle: 12° and mass: 43 kg

Figure D.18: Flow depth of 43 kg of Ultrez 10 at $C = 0.25\%$ on a slope of 12°.

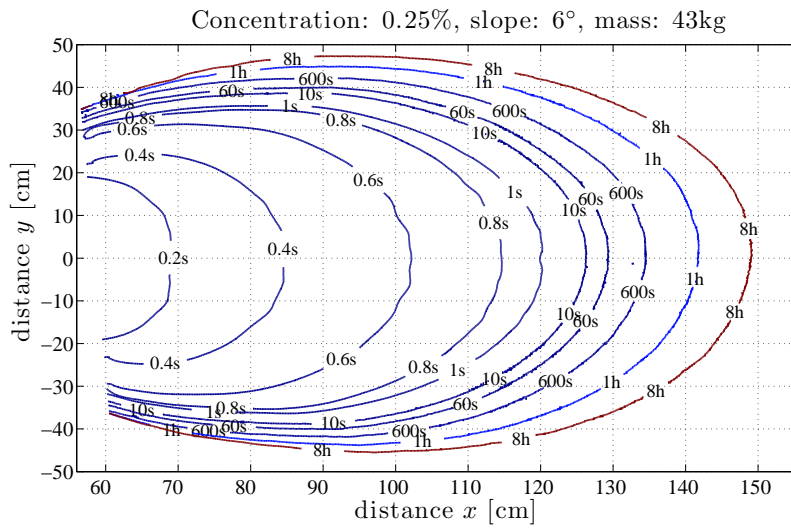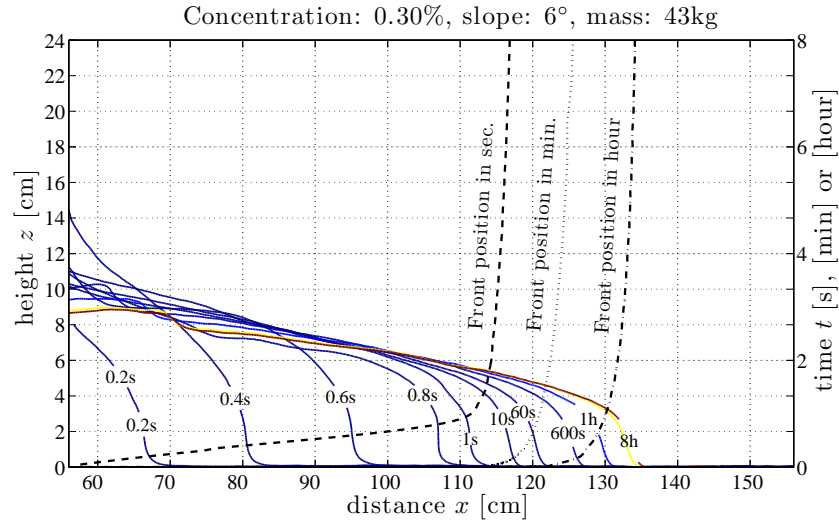Figure D.19: Contact line of 43 kg of Ultrez 10 at $C = 0.25\%$ on a slope of 12°.

Concentration: 0.30%, slope: 12°, mass: 43kg
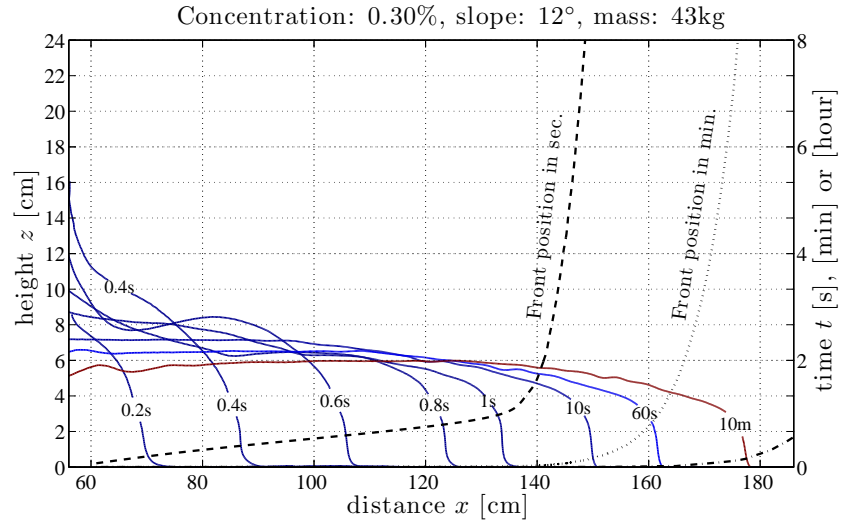
Figure D.20: Flow depth of 43 kg of Ultrez 10 at $C = 0.30\%$ on a slope of $12°$.

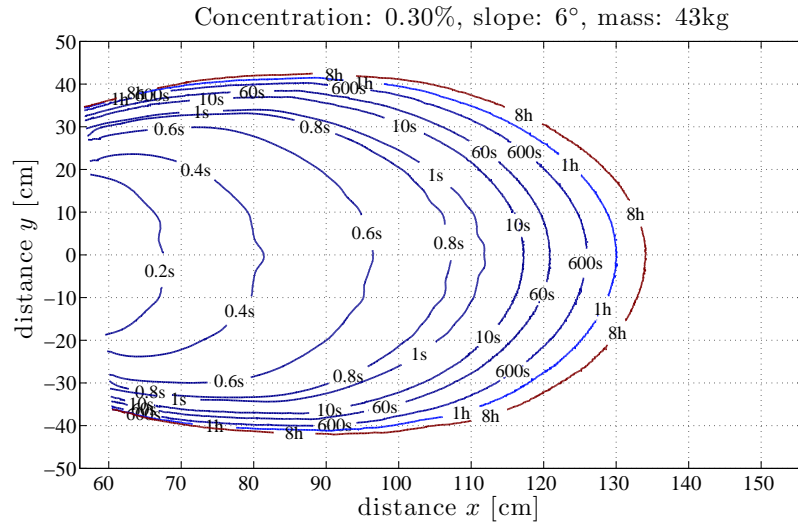Concentration: 0.30%, slope: 12°, mass: 43kg
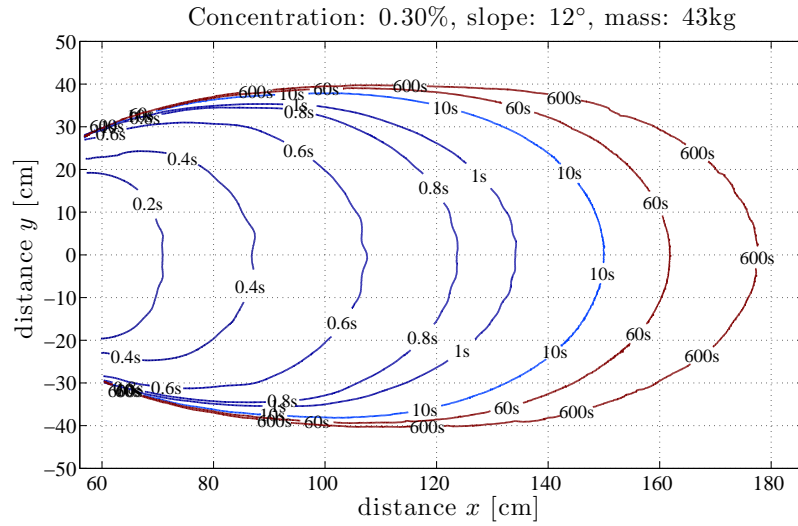
Figure D.21: Contact line of 43 kg of Ultrez 10 at $C = 0.30\%$ on a slope of $12°$.
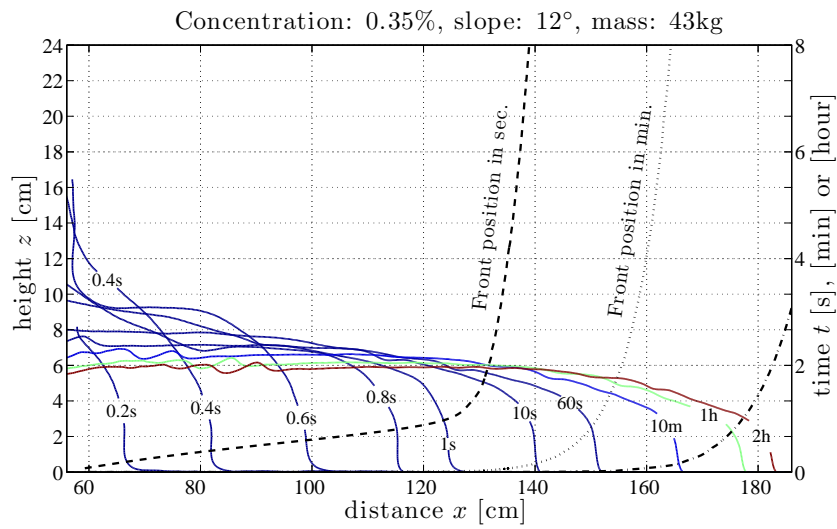
Figure D.22: Flow depth of 43 kg of Ultrez 10 at $C = 0.35\%$ on a slope of $12°$.
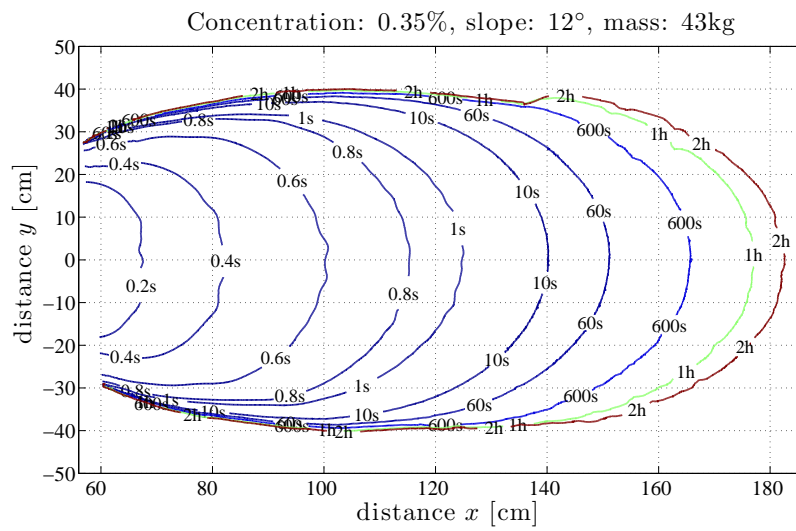
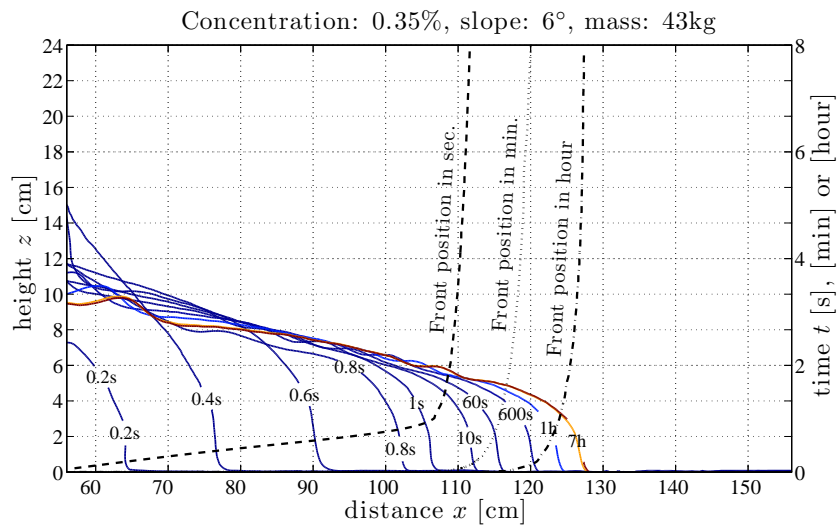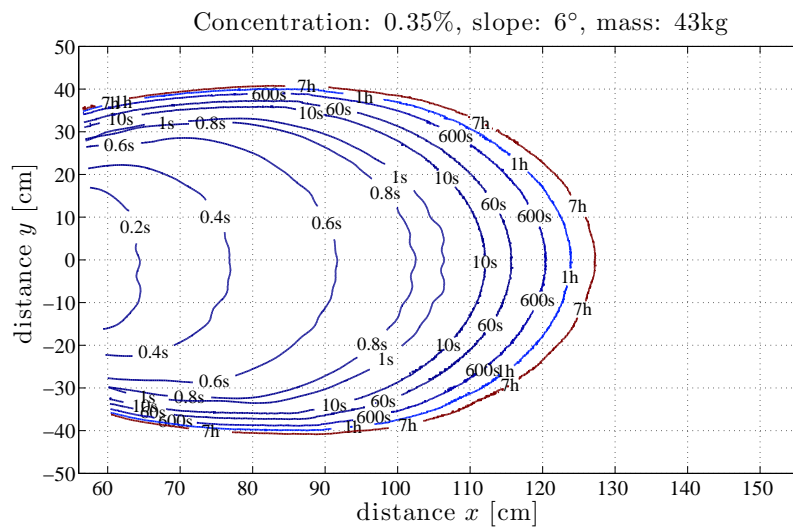Figure D.23: Contact line of 43 kg of Ultrez 10 at $C = 0.35\%$ on a slope of $12°$.

Concentration: 0.40%, slope: 12°, mass: 43kg
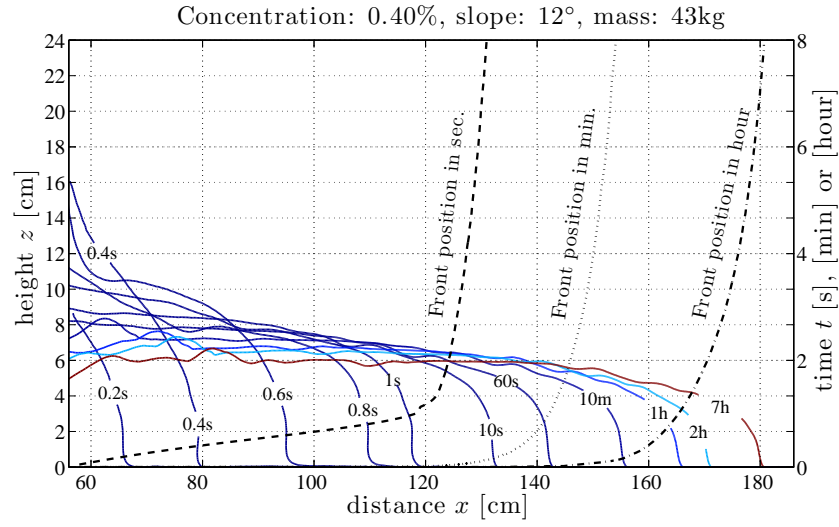
Figure D.24: Flow depth of 43 kg of Ultrez 10 at $C = 0.40\%$ on a slope of 12°.

Concentration: 0.40%, slope: 12°, mass: 43kg
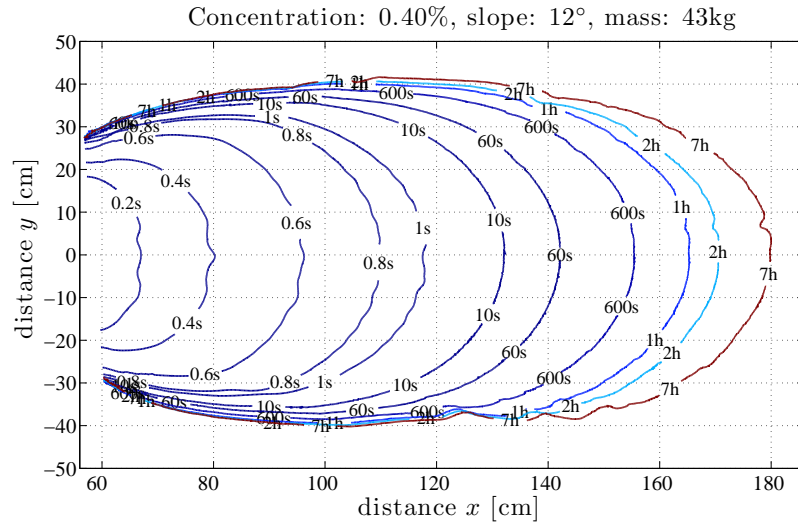
Figure D.25: Contact line of 43 kg of Ultrez 10 at $C = 0.40\%$ on a slope of 12°.

D.4 Plane slope angle: 18°

D.4.1 Plane slope angle: 18° and mass: 43 kg
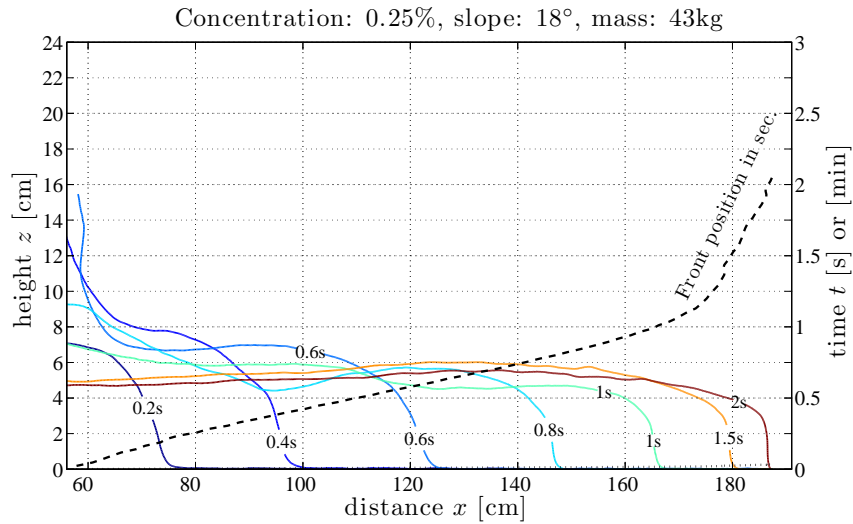
Figure D.26: Flow depth of 43 kg of Ultrez 10 at $C = 0.25\%$ on a slope of 18°.
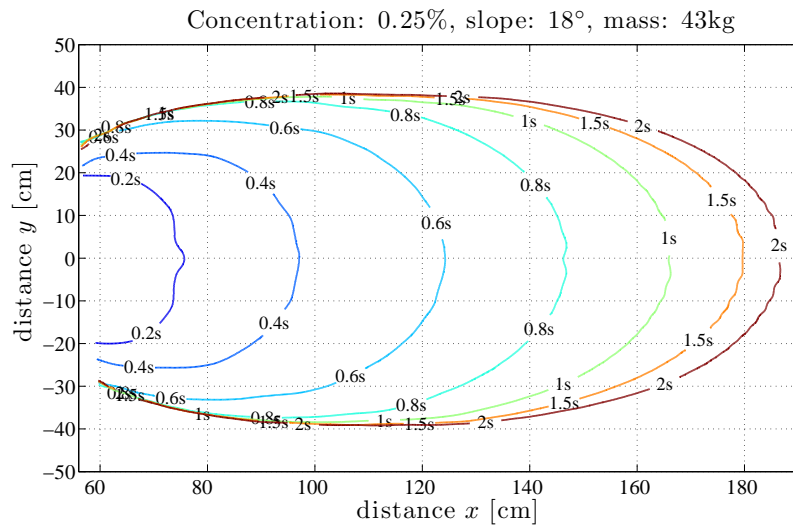
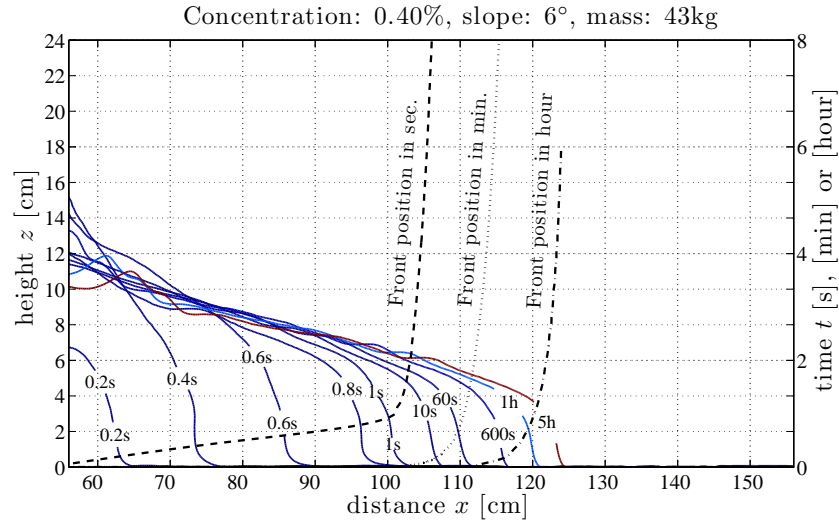Figure D.27: Contact line of 43 kg of Ultrez 10 at $C = 0.25\%$ on a slope of 18°.
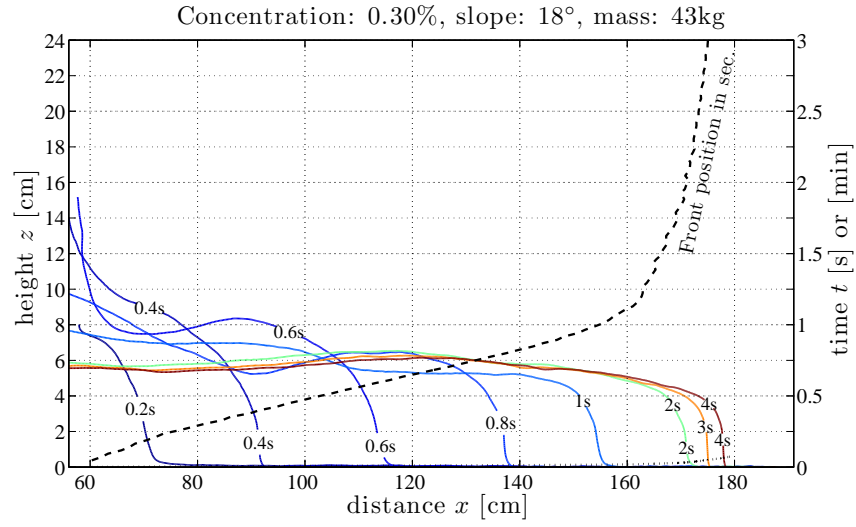
Figure D.28: Flow depth of 43 kg of Ultrez 10 at $C = 0.30\%$ on a slope of $18°$.
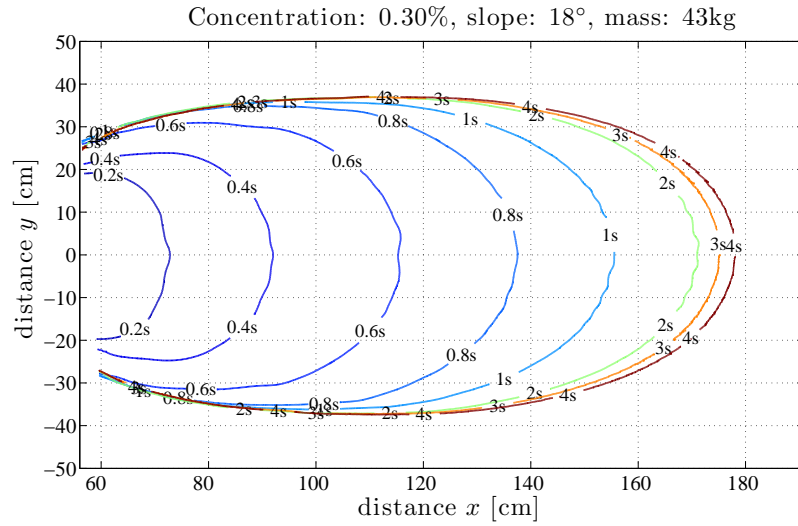
Figure D.29: Contact line of 43 kg of Ultrez 10 at $C = 0.30\%$ on a slope of $18°$.
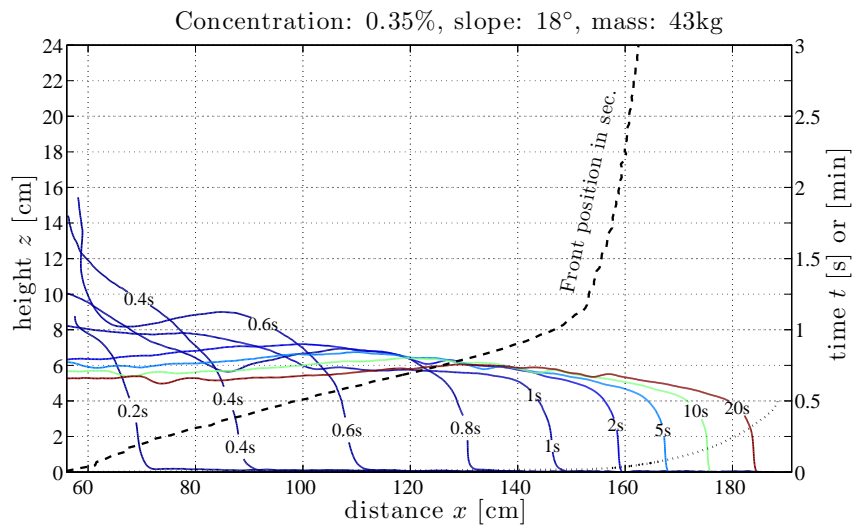
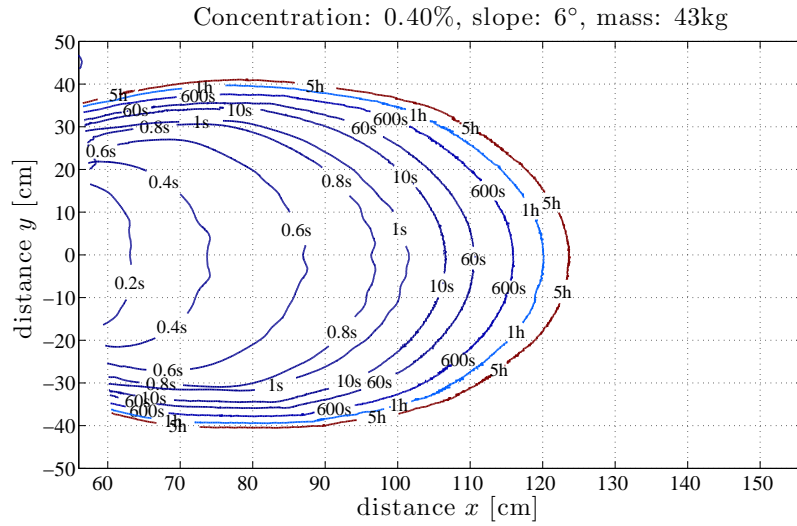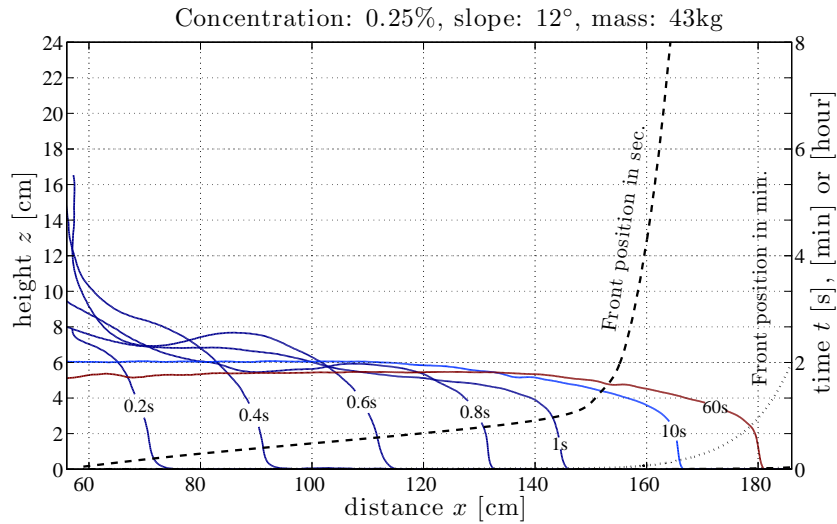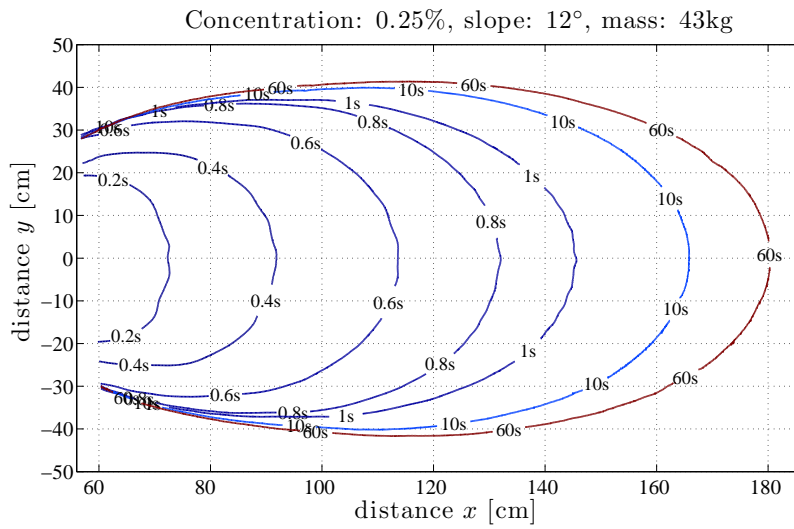Figure D.30: Flow depth of 43 kg of Ultrez 10 at $C = 0.35\%$ on a slope of 18°.
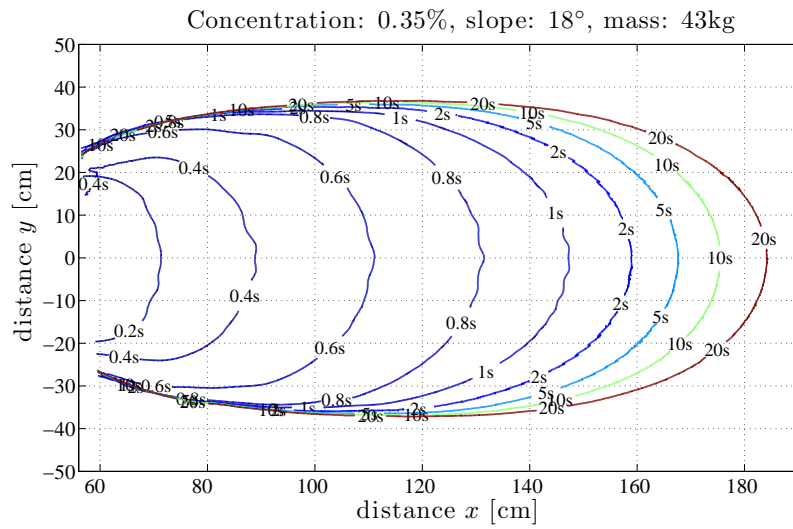
Figure D.31: Contact line of 43 kg of Ultrez 10 at $C = 0.35\%$ on a slope of 18°.

Concentration: 0.40%, slope: 18°, mass: 43kg
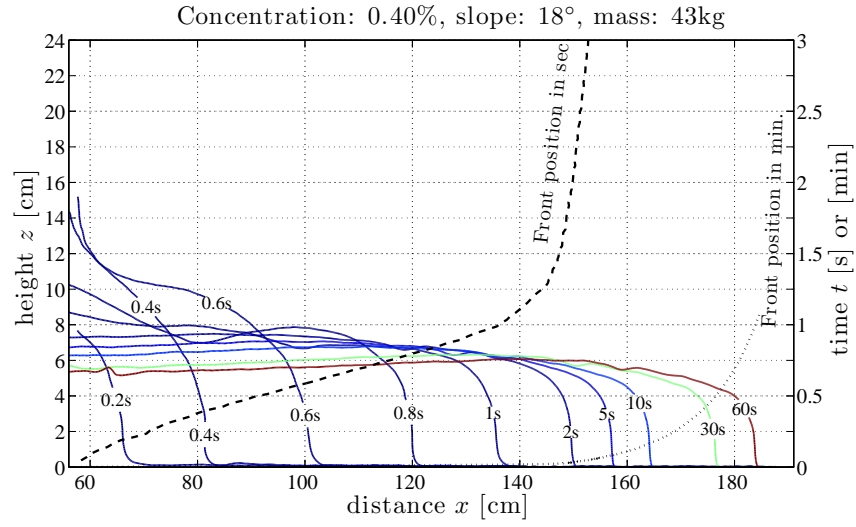
Figure D.32: Flow depth of 43 kg of Ultrez 10 at $C = 0.40\%$ on a slope of 18°.

Concentration: 0.40%, slope: 18°, mass: 43kg
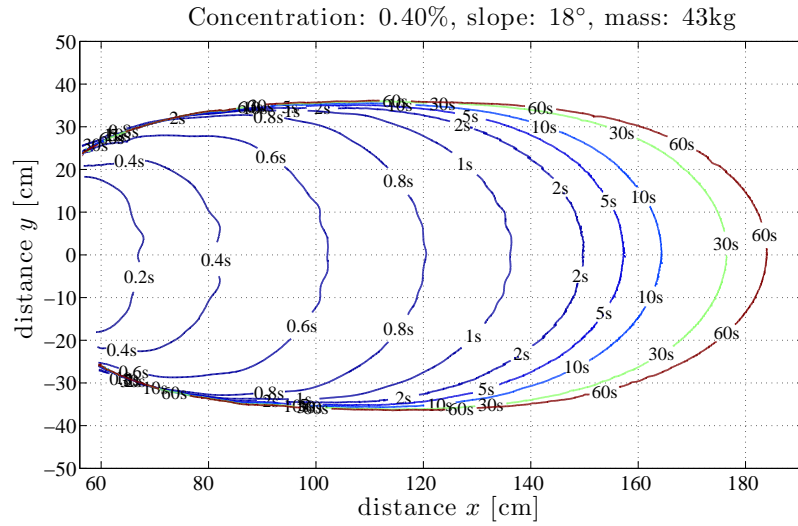
Figure D.33: Contact line of 43 kg of Ultrez 10 at $C = 0.40\%$ on a slope of 18°.

Bibliography

M. J. Adams, I. Aydin, B. J. Briscoe, and S. K. Sinha. A finite element analysis of the squeeze flow of an elasto-viscoplastic paste material. *Journal of Non-Newtonian Fluid Mechanics*, 71:41–57, 1997.

C. Ancey. Snow avalanches. In N.J. Balmforth and A. Provenzale, editors, *Geomorphological Fluid Mechanics: selected topics in geological and geomorphological fluid mechanics*, pages 319–338. Springer, 2001.

C. Ancey. Plasticity and geophysical flows: A review. *Journal of Non-Newtonian Fluid Mechanics*, 142:4–35, 2007.

D. D. Atapattu, R. P. Chabra, and P. H. T. Uhlherr. Creeping sphere motion in herschel-bulkley fluids: flow field and drag. *Journal of Non-Newtonian Fluid Mechanics*, 59:245–265, 1995.

N. J. Balmforth and R. V. Craster. A consistent thin-layer theory for bingham plastics. *Journal of Non-Newtonian Fluid Mechanics*, 84:65–81, 1999.

N. J. Balmforth, R. V. Craster, and R. Sassi. Shallow viscoplastic flow on an inclined plane. *Journal of Fluid Mechanics*, 470:1–29, 2002.

N. J. Balmforth, R. V. Craster, P. Perona, A. C. Rust, and R. Sassi. Viscoplastic dam breaks and the bostwick consistometer. *Journal of Non-Newtonian Fluid Mechanics*, 142:63–78, 2007.

H. A. Barnes. *A Handbook of Elementary Rheology*. University of Wales, 2000.

185

H. A. Barnes. A review of the slip (wall depletion) of polymer solutions, emulsions and particle suspensions in viscometers: its cause, character, and cure. *Journal of Non-Newtonian Fluid Mechanics*, 56:221–251, 1995.

H. A. Barnes. Thixotropy - a review. *Journal of Non-Newtonian Fluid Mechanics*, 70:1–33, 1997.

H. A. Barnes. The yield stress –a review or '$\pi\alpha\nu\tau\alpha\ \rho\epsilon\iota$' – everything flows? *Journal of Non-Newtonian Fluid Mechanics*, 81:213–217, 1999.

H. A. Barnes and Q. D. Nguyen. Rotating vane rheometry – a review. *Journal of Non-Newtonian Fluid Mechanics*, 98:1–14, 2001.

H. A. Barnes and K. Walters. The yield stress myth? *Rheologica Acta*, 24:324–326, 1985.

P. Bartelt, B. Salm, and U. Gruber. Calculating dense-snow avalanche runout using a voellmy-fluid model with active/passive longitudinal straining. *Journal of Glaciology*, 45:242–254, 1999.

A. Bateman, A. Granados, V. Medina, D. Velasco, and M. Nalesso. Experimental procedure to obtain 2D time-space high-speed water surface. In R.M.L. Ferreira, E.C.T.L. Alves, J.G.A.B. Leal, and A.H. Cardoso, editors, *River Flow 2006*, volume 2, pages 1879–1888. Balkema, 6-8 Septembre 2006. ISBN 0-415-40815-6.

E. C. Bingham. *Fluidity and Plasticity*. McGraw-Hill, 1922.

A. Bostan and D. Boyacioglu. Kinetics of non-enzymatic colour development in glucose syrups during storage. *Food Chemistry*, 60(4):581–585, 1997.

D. Calvetti, S. Morigi, L. Reichel, and F. Sgallari. Tikhonov regularization and the l-curve for large discrete ill-posed problems. *Journal of Computational and Applied Mathematics*, 123:423–446, 2000.

H. Chanson, S. Jarny, and P. Coussot. Dam break wave of thixotropic fluid. *Journal of Hydraulic Engineering*, 132:280–293, 2006.

L. Chen and C. Quan. Fringe projection profilometry with nonparallel illumination: a least-squares approach. *Optics Letter*, 30(16):2101–2103, August 15 2005.

D.C.-H. Cheng. Yield stress: a time-dependent property and how to measure it. *Rheologica Acta*, 25:542–554, 1986.

X. Colonna de Lega. *Deformation measurements by holographic and speckle interferometry*. PhD thesis, Ecole Polytechnique Fédérale de Lausanne, 1997.

X. Colonna de Lega and P. Jacquot. Deformation measurement with object-induced dynamic phase shifting. *Appl. Opt.*, 35(25):5115–5121, 1996.

P. Coussot, S. Proust, and C. Ancey. Rheological interpretation of deposits of yield stress fluids. *Journal of Non-Newtonian Fluid Mechanics*, 66:55–70, 1996.

P. Coussot, Q.D. Nguyen, H.T. Huynh, and D. Bonn. Avalanche behavior in yield stress fluids. *Physical Review Letters*, 88:175501, 2002.

D. De Kee and C.F. Chan Man Fong. A true yield stress? *Journal of Rheology*, 37:775–776, 1993.

A. de Waele. Viscometry and plastometry. *Oil. Color Chem. Assoc. J.*, 6:33–88, 1923.

K. Debiane. *Hydraulique des écoulements laminaires à surface libre dans un canal pour des milieux visqueux ou viscoplastiques.* PhD thesis, Université Joseph Fourier Grenoble, 2000.

A.-I. Desmangles. *Extension of the fringe projection method to large objects for shape and deformation measurement.* PhD thesis, EPFL, 2003.

N. Didden and T. Maxworthy. The viscous spreading of plane and axisymmetric gravity currents. *Journal of Fluid Mechanics*, 121:27–42, 1982.

J. Eaket, F.E. Hicks, and A.E. Petersen. Use of stereoscopy for dam break flow measurement. *Journal of Hydraulic Engineering*, 131:24–29, 2005.

T. J. Flynn. Two-dimensional phase unwrapping with minimum weighted discontinuity. *Journal of the Optical Society of America*, 14(10):2692–2701, oct 1997.

D. C. Ghiglia and M. P. Pritt. *Two-dimensional phase unwrapping: theory, algorithms, and software.* Wiley-Interscience. Wiley, cop., 1998. ISBN 0-471-24935-1.

D. C. Ghiglia and L. A. Romero. Minimum L^p-norm two-dimensional phase unwrapping. *J. Opt. Soc. Am. A*, 13(10):1–15, October 1996.

R. M. Goldstein, H. A. Zebker, and C. L. Werner. Satellite radar interferometry: two-dimensional phase unwrapping. *Radio Science*, 23(4):713–720, 1988.

T. Gregory and S. Mayers. A note on slippage during the study of the rheological behaviour of paste inks. *Surface Coatings International*, 76(2):82–86, 1993.

M. Griebel, T. Dornseifer, and T. Neunhoeffer. Numerical simulation in fluid dynamics, a practical introduction. In *SIAM, Philadelphia*, 1998.

R.W. Griffiths. The dynamics of lava flows. *Annual Review of Fluid Mechanics*, 32:477–518, 2000.

W. Herschel and R. Bulkley. Konsistenzmessungen von Gummi-Benzollösungen. *Colloid & Polymer Science*, 39(4):291–300, 1926.

C.K. Hitzenberger, M. Sticker, R. Leitgeb, and A.F. Fercher. Differential phase measurements in low-coherence interferometry without 2π ambiguity. *Optics Letter*, 26(23):1864, 2001.

A.J. Hogg and D. Pritchard. The effects of hydraulic resistance on dam-break and other shallow inertial flows. *Journal of Fluid Mechanics*, 501:179–212, 2004.

X. Huang and M.H. García. A perturbation solution for bingham-plastic mudflows. *Journal of Hydraulic Engineering*, 123:986–994, 1997.

X. Huang and M.H. García. A herschel-bulkley model for mud flow down a slope. *Journal of Fluid Mechanics*, 374:305–333, 1998.

Y. Y. Hung, L. Lin, H. M. Shang, and B. G. Park. Practical three-dimensional computer vision techniques for full-field surface measurement. *Opt. Eng*, 39(1): 143–149, January 2000.

B. Hunt. Asymptotic solution for dam-break problem. *Journal of Hydraulics Division ASCE*, 108:115–126, 1982.

B. Hunt. Dam-break solution. *Journal of Hydraulic Engineering*, 110:675–686, 1984.

B. Hunt. Newtonian fluid mechanics treatment of debris flows and avalanches. *Journal of Hydraulic Engineering*, 120:1350–1363, 1994.

J. M. Huntley and H. O. Saldner. Shape measurement by temporal phase unwrapping: comparison of unwrapping algorithms. *Meas. Sci. Technol.*, 8:989–992, 1997.

H.E. Huppert. The propagation of two-dimensional and axisymetric viscous gravity currents over a rigid horizontal surface. *Journal of Fluid Mechanics*, 121:43–58, 1982a.

H.E. Huppert. Flow and instability of viscous current down a slope. *Nature*, 300: 427–429, 2 December 1982b.

Y. Ichioka and M. Inuiya. Direct phase detecting system. *Applied Optics*, 11: 1507–1514, 1972.

R.M. Iverson. How should mathematical models of geomorphic processus to be judged? In P.R. Wilcock and R.M. Iverson, editors, *Prediction in Geomorphology*, pages 83–94. American Geophysical Union, 2003.

R.M. Iverson. The physics of debris flows. *Reviews of Geophysics*, 35:245–296, 1997.

R.M. Iverson, J.E. Costa, and R.G. LaHusen. Debris-flow flume at H.J. Andrews experimental forest, Oregon. Technical report, USGS Open-File Report 92-483, 1992.

R.M. Iverson, M. Logan, and R.P. Denlinger. Granular avalanches across irregular three-dimensional terrain: 2. experimental tests. *Journal of Geophysical Research*, 109:F01015, 2004.

A. E. James, D. J. A. Williams, and P. R. Williams. Direct measurement of static yield properties of cohesive suspensions. *Rheologica Acta*, 26(5):437–446, 1987.

M.-S. Jeong and S.-W. Kim. Color grating projection Moiré with time-integral fringe capturing for high-speed 3-D imaging. *Opt. Eng*, 41(8):1912–1917, 2002.

M.A. Kern, F. Tiefenbacher, and J.N. McElwaine. The rheology of snow in large chute flows. *Cold Regions Science and Technology*, 39:181–192, 2004.

R. C. Kerr, R. W. Griffiths, and K. V. Cashman. Formation of channelized lava flows on an unconfined slope. *Journal of Geophysical Research*, 111, 2006.

K.G. Larkin, D.J. Bone, and M.A. Oldfield. Natural demodulation of two-dimensional fringe patterns. I. general background of the spiral phase quadrature transform. *J. Opt. Soc. Am. A*, 18(8):1862, 2001.

M. Lehmann. Decorrelation-induced phase errors in phase-shifting speckle interferometry. *Appl. Opt.*, 36(16):3657–3667, 1997.

M. Liebling, T. Blu, and M. Unser. Complex-wave retrieval from a single off-axis hologram. *J. Opt. Soc. Am. A*, 21(3):367–377, mar 2004.

G.G. Lipscomb and M.M. Denn. Flow of bingham fluids in complex geometries. *Journal of Non-Newtonian Fluid Mechanics*, 14:337–346, 1984.

K.F. Liu and C.C. Mei. Slow spreading of a sheet of bingham fluid on an inclined plane. *Journal of Fluid Mechanics*, 207:505–529, 1990.

A.Y. Malkin. Non-linearity in rheology - an essay of classification. *Rheologica Acta*, 34:27–39, 1995.

W.W. Marcy. Two-dimensinal fringe-pattern analysis. *Applied Optics*, 22:3101–3105, 1983.

G.P. Matson and A. Hogg. Two-dimensional dam break flows of herschel-bulkley fluids: The approach to the arrested state. *Journal of Non-Newtonian Fluid Mechanics*, 05.03 2007.

K. L. McCarthy and J. D. Seymour. A fundamental approach for the relationship between the bostwick measurement and newtonian fluid viscosity. *Journal of Texture Studies*, 24:1–10, 1993.

P.R.S. Mendes and E.S.S. Dutra. Viscosity function for yield-stress liquids. *Applied Rheology*, 14:296–302, 2004.

M. Misiti, Y. Misiti, G. Oppenheim, and J.-M. Poggi. Wavelet toolbox 4: User's guide. Technical report, The MathWorks, 2007.

P.C.F. Møller, J. Mewis, and D. Bonn. Yield stress and thixotropy: on the difficulty of measuring yield stresses in practice. *Soft Matter*, 2:274–283, 2006.

C. Nakaya. Spread of fluid drops over a horizontal plane. *Journal of the Physical Society of Japan*, 37(2):539–543, August 1974.

C. Nakaya. Long waves on a thin fluid layer flowing down an inclined plane. *Physics of Fluids*, 18:1407–1412, 1975.

C. Niclass, A. Rochas, P.A. Besse, and E Charbon. Design and characterization of a cmos 3d image sensor based on single photon avalanche diodes. *Journal of Solid-State Circuits*, pages 1847–1854, sep 2005.

Bulletin 11 : Thickening Properties. Noveon, Inc., 9911 Brecksville Road, Cleveland, Ohio 44141-3247, U.S.A., January 2002.

R. Onodera, H. Watanabe, and Y. Ishii. Interferometric phase-measurement using a one-dimensional discrete hilbert transform. *Optical Review*, 12(1):29–36, 2005.

W. Ostwald. Ueber die geschwindigkeitsfunktion der viskosität disperser systeme. i. *Colloid & Polymer Science*, 36(2):99–117, 1925.

G. Parker, Y. Fukushima, and H.M. Pantin. Self-accelerating turbidity currents. *Journal of Fluid Mechanics*, 171:145–181, 1986.

C. Parti, M. Giani, and N. Leuratti. Sar interferometry: A 2-d phase unwrapping technique based on phase and absolute values information. In NJ IEEE Pisctaway, editor, *Geoscience and Remote Sensing Symposium, 1990. IGARSS '90.*

'Remote Sensing Science for the Nineties'., 10th Annual International, pages 2043–2046, 1990.

J.-M. Piau. Carbopol gels: Elastoviscoplastic and slippery glasses made of individual swollen sponges meso- and macroscopic properties, constitutive equations and scaling laws. *Journal of Fluid Mechanics*, 144(1):1–29, 2007.

J.-M. Piau. Flow of a yield stress fluid in a long domain. application to flow on an inclined plane. *Journal of Rheology*, 40:711–723, 1996.

O. Pouliquen and Y. Forterre. Friction law for dense granular flow: application to the motion of a mass down a rough inclined plane. *Journal of Fluid Mechanics*, 453:133–151, 2002.

D. Pritchard. On fine sediment transport by a flood surge. *Journal of Fluid Mechanics*, 5343:239–248, 2005.

M.D Pritt. Phase unwrapping by means of multigrid techniques for interferometric sar. *IEEE Transactions on Geoscience and Remote Sensing*, 34(3):728–738, 1996.

P. L. Ransom and J. Kokal. Interferogram analysis by a modified sinusoid fitting technique. *Applied Optics*, 25:4199–4204, 1986.

M. Reiner. The deborah number. *Physics Today*, 17:62, Jannuary 1964.

M. Rentschler and C. Ancey. Simulations de fluides viscoplastiques. In *18ème Congrès Français de Mécanique, Grenoble, France*, 2007.

A. Ritter. Die fortpflanzung der wasserwellen. *Zeitschrift des Vereines Deutscher Ingenieure*, 36(33):947–954, 1892.

G.P. Roberts and H.A. Barnes. New measurements of the flow-curves for carbopol dispersions without slip artefacts. *Rheologica Acta*, 40:499–503, 2001.

G.P. Roberts, H.A. Barnes, and P. Carew. Modelling the flow behaviour of very shear-thinning liquids. *Chemical Engineering Journal*, 56:5617–5623, 2001.

M.W. Roth. Phase unwrapping for interferometric sar by the least-error path. Technical report, Johns Hopkins University Applied Physics Lab Technical Report, Laurel, MD, March 30, 1995.

B. Saint Venant. Théorie du mouvement non permanent des eaux, avec application aux crues des rivières et à l'introduction des marées dans leur lit. *Comptes Rendus de l'Académie des Sciences, série I*, 173:147–154– 237–240, 1871.

B. Salm. A short and personal history of snow avalanche dynamics. *Cold Regions Science and Technology*, 39:83–92, 2004.

F.W. Schenck. Glucose and glucose-containing syrups. In Weinheim, editor, *Ullman's Encyclopaedia of Industrial Chemistry, Fifth Edition*, volume A12, pages 457–475. Wiley, 1989.

M. Sticker, C.K. Hitzenberger, R. Leitgeb, and A.F. Fercher. Quantitative differential phase measurement and imaging in transparent and turbid media by optical coherence tomography. *Optics Letter*, 26(8):518, 2001.

X. Su and W. Chen. Fourier transform profilometry: a review. *Optics and Lasers in Engineering*, 35:263–284, February 28 2001.

H. Takajo and T. Takahashi. Least-squares phase estimator from phase differences. *J. Opt. Soc. Am. A*, 5(11):1818–1827, November 1988.

M. Takeda, H. Ina, and S. Kobayashi. Fourier-transform method of fringe-pattern analysis for computer-based topography and interferometry. *Journal of the Optical Society of America*, 72(1):156 – 160, 1982.

L.R. Watkins. Phase recovery from fringe patterns using the continuous wavelet transform. *Optics and Lasers in Engineering*, 45:298–303, 2007.

C. Wu, G. Huang, and Y. Zheng. Theoretical solution of dam-break shock wave. *Journal of Hydraulic Engineering*, 125:1210–1220, 1999.

C.-S. Wu and Y.T. Kwak. Characterization of microgels by brookfield viscometry with cylindrical, t-bar, and flags impeller spindles. *Journal of Applied Polymer Science*, 71:67–74, 1999.

Z. Xiaoling, L. Yuchi, Z. Meirong, N. Xiaobing, and H. Yinguo. Calibration of a fringe projection profilometry system using virtual phase calibrating model planes. *J. Opt. A: Pure Appl. Opt*, 7:192–197, march 9 2005.

Y.L. Yeow, W.C. Ko, and P.P.P. Tang. Solving the inverse problem of couette viscometry by tikhonov regularization. *Journal of Rheology*, 44:1335–1351, 2000.

Mechanical Engineer

Steve Cochard
December 14, 1973
Swiss

Condémine 40
1814 La Tour-de-Peilz
Switzerland
Phone : +41 21 944 39 62
E-mail : steve.cochard@a3.epfl.ch

Education

2004 - 2007	**Dr. ès sciences : Measurements of time-dependent free-surface viscoplastic flows down steep slopes.** Ecole Polytechnique Fédérale de Lausanne, Lausanne, Switzerland.
1994 - 2000	**Master in mechanical engineering.** Ecole Polytechnique Fédérale de Lausanne, Lausanne, Switzerland.
Languages	French : mother language
	English : fluent. Au pair in New York (1993-1994)
	German : working knowledge

Professional experience

2004 - 2007	**Ph.D. Student**, Environmental Hydraulics Laboratory, Ecole Polytechnique Fédérale de Lausanne, Lausanne, Switzerland.

- PhD thesis : Measurements of time-dependent free-surface viscoplastic flows down steep slopes.
- Contribution on the understanding of the dynamics of gravity-driven free-surface flows, with the objective of modeling natural hazards such as debris flows, snow avalanches, turbidity currents or pyroclastic flows.
- Design, development and validation of a fringe projection system providing accurate instantaneous whole-field 3D shape measurements of the free-surface profile and the spreading rate of non-Newtonian fluids at high repetition rate. Development of the acquisition software and of the post-processing algorithms.
- Design and development of a unique test facility with an inclined plan to model the dam-break problem at different slope inclinations.
- Validation of experimental results with theoretical models.
- Development of a new procedure to prepare viscoplastic polymeric gels for non-Newtonian fluid experimental research.
- Improvement of the methods to characterize the rheological behavior of viscoplastic materials.
- Responsible for the sessions of fluid mechanics exercises for the civil engineering and environmental engineering students.
- Follow-up of three masters students.
- Doctoral school in Mechanics of Solids and Fluids.

2001 - 2004	**Project Manager in Aero-Thermodynamics of Tunnels**, Electrowatt Infra Ltd, Zürich, Switzerland

- Project leader for the development and improvement of ventilation systems for several existing tunnels or tunnel projects.
- Coordination of activities within networks of partners, contacts and clients. Development of methodologies for the optimization of the ventilation within a transdisciplinary team.
- Design, development and validation of new numerical methods to simulate smoke, toxic gases and temperature propagation in case of fire in any underground facility with different ventilation configurations.
- Responsible for the validation and use of 3D computational fluid dynamics (CFD) codes to simulate fires in complex tunnel configurations.
- Follow-up of wind-tunnel tests.

2000	**Consultant for the SNCF Research and Technology Department** (French National Railway Company), Paris, France for GESTE, PSE Parc Scientifique, Lausanne, Switzerland. – Contribution to the operational security of the TGV regarding side-wind effects on the new Mediterranean High-Speed Line. – Development of the methodology for a safe operation of trains based on meteorological characteristics. Implementation of weather stations. Development of software, using MatLab, to post-treat wind data and to detect and predict in real time the apparition of dangerous wind conditions.
1999-2000	**Internship at the SNCF Research and Technology Department**, Paris, France. 5 months, Master degree work experience. – Study of aerodynamic phenomena associated with high-speed trains entering tunnels and passing each other. Development of software, using MatLab, to analyze these phenomena and the associated aural discomfort for passengers.

Publications and proceedings

2007 : Publications

- S. Cochard, C. Ancey, Tracking the free surface of time-dependent flows : Image processing for the dam-break problem, Experiments in Fluids, 2006.
- C. Ancey, S. Cochard, S. Wiederseiner and M. Rentschler, Existence and features of similarity solutions for non-Boussinesq gravity currents, Physica D, 2007.

2007 : Proceedings

- S. Cochard, C. Ancey : Dam breaks with vicoplastic materials down steep slopes, Viscoplastic Fluids : From Theory to Application, Monte Verità, Switzerland, October 2007.

2006 : Publications

- C. Ancey, S. Cochard, S. Wiederseiner and M. Rentschler, Scaling laws for granular flows down inclined channels, submitted to Physical Review E, 2006.
- C. Ancey, S. Cochard, S. Wiederseiner and M. Rentschler, Front dynamics of supercritical non-Boussinesq gravity currents, Water Resources Research, 42, W08424, 2006.
- C. Ancey, S. Cochard, Understanding avalanches, Physics World, Vol 16 No 7, 2006

2006 : Proceedings

- S. Cochard, C. Ancey : Accurate measurements of free-surface in the dam-break problem, River Flow Conference, IHAR, Lisbonne, Portugal, September 2006.
- C. Ancey, S. Cochard, S. Wiederseiner and M. Rentschler : Front dynamics of a water surge at high Reynolds number : similarity solutions to the Saint-Venant equations, River Flow Conference, IHAR, Lisbonne, Portugal, September 2006.

2005 : Proceedings

- C. Ancey, P. Vollmoeller, S. Cochard : Rhéophysique des suspensions concentrées : cadre théorique et similitude, Congrès Français de Mécanique, Troyes, 2005.

2003 : Publications

- S. Cochard : Validation of the freeware 'Fire Dynamics Simulator Version 2.0' for simulating tunnel fires, Tunnel Management International, Vol. 6, Issue 4, 2003.

2003 : Proceedings

- J. Day, S. Cochard : Swiss Tunnels : The new design guidelines and how they are being implemented, Second International Conference on Road Tunnel Traffic and Safety. Hamburg, Germany, May 2003.

2003 : Proceedings

- S. Cochard :Validation of the freeware 'Fire Dynamics Simulator Version 2.0' for simulating tunnel fires, Fourth International Conference on Tunnel Fires, Basel, Switzerland, December 2002.

Hobbies

Sailing	Five selections for the World Championship and three for the European Championship. Sailing instructor.
Skiing	Member of the Swiss Ski Federation